UNIVERSITY OF BELGRADE

FACULTY OF CIVIL ENGINEERING

Marija D. Milojević

UNCERTAINTY APPROACH TO MODELLING PEDESTRIAN-INDUCED VIBRATIONS OF CLT FLOORS

Doctoral Dissertation

Belgrade, 2026

UNIVERZITET U BEOGRADU

GRAĐEVINSKI FAKULTET

Marija D. Milojević

MODELIRANJE VIBRACIJA CLT MEĐUSPRATNIH KONSTRUKCIJA USLED PEŠAČKOG OPTEREĆENJA PRIMENOM ANALIZE NEPOUZDANOSTI

doktorska disertacija

Beograd, 2026.

Supervisors:

Prof. Dr Vitomir Racić
University of Belgrade, Faculty of Civil Engineering

Prof. Dr Marija Nefovska-Danilović
University of Belgrade, Faculty of Civil Engineering

Examiners:

Prof. Dr Stana Živanović
University of Warwick, School of Engineering, UK

Assoc. Prof. Dr Miroslav Marjanović
University of Belgrade, Faculty of Civil Engineering

Assoc. Prof. Dr Ivan Glišović
University of Belgrade, Faculty of Civil Engineering

Viva date: _____

Acknowledgments

This dissertation marks the end of a long and important chapter of my life. It would have been very different without the people who accompanied me along the way.

First and foremost, I owe my deepest gratitude to my supervisors, Prof. Dr Vitomir Racić and Prof. Dr Marija Nefovska-Danilović. Thank you for your generosity, for sharing your knowledge so openly and for giving me the opportunity to learn from you. Thank you for giving me the freedom to develop my own ideas, while always being there to guide me when needed. Without your knowledge, patience and encouragement over these years, this dissertation would not be what it is today, neither would I be the researcher I have become.

I would also like to thank the members of the committee for taking the time to read this dissertation carefully and for their comments and suggestions. To Assoc. Prof. Dr Miroslav Marjanović, thank you for making me feel welcome from my very first day at the Faculty, for involving me in so many different activities and for always being supportive and encouraging. Your support has meant a great deal to me, not only throughout this PhD journey, but also in many other aspects of my academic and professional growth. To Prof. Stana Živanović, thank you for welcoming me to the School of Engineering at the University of Warwick and for making my research stay such a positive experience. You may not realise how much I learned during that time, but the visit had a lasting influence on my development, both professionally and personally. To Prof. Ivan Glišović, thank you for all the insightful discussions and the exchange of ideas we shared while working on the Substrate4CLT project.

My time at the Chair of Engineering Mechanics and Theory of Structures would not have been the same without my *favourite* colleagues and dear friends, Jelena Nikolić and Miloš Jočković. I am incredibly grateful that this journey brought you into my life. You have been a constant source of support, encouragement and laughter. Thank you for making both the difficult and the good days so much better simply by being there.

I am very thankful to my colleagues and friends from Office 333, Emilija Jočić and Matija Bošković, for creating such a positive and supporting environment, for always being there when needed and especially for taking over my responsibilities during my research stay in the UK. I am also thankful to Marko Radišić for helping me get started with Python and LaTeX in the early stages of my PhD, for giving the Hindu software its name and for all the valuable discussions we shared while working together at the Chair of Engineering Mechanics and Theory of Structures.

To my dearest friends, Ana, Marko, Jovana, Anđelika and Cica, thank you for always being there, for believing in me and for being my loudest cheerleaders all this time.

Finally, my deepest thanks go to my family, mother Gordana, father Dragan and sister Milica. You have always been my greatest source of strength and support. From you, I learned patience, hard work and dedication, and I carried those lessons with me through every step of this journey. Thank you for your unconditional love and care. Because of you, I was able to do this.

Belgrade, 2026

Marija Milojević

Financial support

This doctoral dissertation was supported by the Science Fund of the Republic of Serbia on Grant No.**7677448: Towards Sustainable Buildings: Novel Strategies for the Design of Vibration Resistant Cross-Laminated Timber Floors - Substrate4CLT** (project leader Prof. Dr Marija Nefovska - Danilović).

The early phase of this research was supported by the Ministry of Education, Science and Technological Development of the Republic of Serbia under Project **TR-36046** (project leader Prof. Dr Mira Petronijević). Following the completion of this project, support was continued by the Ministry of Science, Technological Development and Innovations of the Republic of Serbia through Project No. **200092**.

The author acknowledges the support of the **British Scholarship Trust**, which enabled a ten-week research visit (March 16th 2024 - May 25th 2024) at the University of Warwick, School of Engineering, United Kingdom, under the supervision of Prof. Dr Stana Živanović.

Uncertainty approach to modelling pedestrian-induced vibrations of CLT floors

Abstract:

Cross-laminated timber (CLT) is increasingly used for long-span floors, where pedestrian-induced vibrations usually govern the design. Current vibration serviceability assessment (VSA) procedures are deterministic and neglect uncertainty in structural properties and pedestrian load. This dissertation studies how these uncertainties affect CLT floor response and identifies the parameters governing its variability.

Finite element models of a three-panel CLT floor were calibrated and validated using measured modal properties. Uncertainty quantification and sensitivity analysis of modal properties were carried out using Polynomial Chaos Expansion metamodels. Pedestrian-load uncertainty was characterised using walking-force records. The Design Guide for Footfall Induced Vibration of Structures (CCIP-016) load models were extended to probabilistic formulations accounting for inter- and intra-subject variability. Simplified deterministic formulations were proposed for routine VSA. Structural and load uncertainties were integrated within a unified probabilistic framework.

Timber density, longitudinal modulus of elasticity and shear modulus govern variability of CLT floor modal properties. For floors susceptible to resonant steady-state vibrations, response variability is strongly influenced by pacing rate, timber density and longitudinal modulus of elasticity. In resonance, load amplitude and damping additionally govern response variability. For floors susceptible to series of transients due to successive footfalls, load parameters are dominant source of response variability. Inter-subject variability contributes considerably more to response variability than intra-subject variability.

Keywords: cross-laminated timber, uncertainty quantification, sensitivity analysis, finite element model updating, metamodeling, harmonic force, effective impulse, walking load variability

Scientific field: Civil Engineering
Scientific subfield: Engineering Mechanics and Theory of Structures

Modeliranje vibracija CLT međuspratnih konstrukcija usled pešačkog opterećenja primenom analize nepouzdanosti

Rezime:

Unakrsno lamelirano drvo (CLT) se sve češće primenjuje za međuspratne konstrukcije velikih raspona, kod kojih je granično stanje upotrebljivosti u pogledu vibracija (GSUV) često merodavno za dimenzionisanje. Postupci za procenu GSUV su deterministički i zanemaruju varijabilnost svojstava konstrukcije i pešačkog opterećenja. Cilj disertacije je da ispita uticaj nepouzdanosti na odgovor CLT međuspratnih konstrukcija usled hoda pešaka i definiše izvor njegove varijabilnosti.

Modeli konačnih elemenata CLT konstrukcije kalibrisani su i validirani prema merenim modalnim karakteristikama. Analiza nepouzdanosti modalnih karakteristika je sprovedena primenom *Polynomial Chaos Expansion* metamodela. Nepouzdanost pešačkog opterećenja je definisana na osnovu zapisa sile hoda. Modeli opterećenja iz *Design Guide for Footfall Induced Vibration of Structures* (CCIP-016) su prošireni da obuhvataju varijabilnost između pešaka i tokom hoda istog pešaka. Za rutinsku procenu GSUV predložene su i pojednostavljene formulacije opterećenja. Nepouzdanosti konstrukcije i opterećenja su objedinjene u jedinstvenu probabilističku proceduru za procenu GSUV.

Zapreminska masa drveta, podužni modul elastičnosti i modul smicanja diktiraju varijabilnost modalnih karakteristika. Varijabilnost odgovora konstrukcija osetljivih na rezonantne vibracije zavisi od blizine frekvencije pobude i sopstvene frekvencije, koju određuju frekvencija hoda, zapreminska masa i podužni modul elastičnosti. U rezonanciji, varijabilnost odgovora potiče od amplitude opterećenja i prigušenja, dok kod konstrukcija sa izraženim prelaznim odgovorom usled serije koraka ona potiče od frekvencije i amplitude opterećenja. Razlike u hodu pešaka više doprinose varijabilnosti odgovora od varijacija tokom hoda istog pešaka.

Ključne reči: unakrsno lamelirano drvo, kvantifikacija nepouzdanosti, analiza osetljivosti, kalibracija modela konačnih elemenata, metamodeliranje, harmonijska sila, efektivni impuls, varijabilnost pešačkog opterećenja

Naučna oblast: Građevinsko inženjerstvo
Uža naučna oblast: Tehnička mehanika i teorija konstrukcija

Contents

Acknowledgments **i**

Financial support **iii**

1 Introduction **1**

1.1 Background and motivation 1

1.2 Research aims, methodology and contribution 4

1.3 Dissertation outline 6

2 Literature review **7**

2.1 Fundamental principles in the vibration analysis of CLT floors 7

2.1.1 Walking force as vibration source 7

2.1.2 CLT floor as vibration path 12

2.1.3 Vibration receiver 14

2.1.4 Human-structure interaction 15

2.2 Design guidelines for VSA of CLT floors 15

2.3 CCIP-016 framework for VSA of the floors 16

2.3.1 Low-frequency floors 16

2.3.2 High-frequency floors 19

2.4 Recent advances and research trends in CLT floor vibrations 20

3 Uncertainty analysis **21**

3.1 Uncertainty quantification 22

3.2 Sensitivity analysis . . . 22
3.2.1 Sobol' indices method . . . 24
3.2.2 Shapley effect . . . 25
3.3 Metamodel applications in uncertainty analysis . . . 28

4 Experimental testing **31**
4.1 Modal testing . . . 31
4.2 Walking tests . . . 37

5 Numerical model of CLT floors **45**
5.1 Modelling inter-panel connections . . . 46
5.2 Initial numerical model . . . 48
5.2.1 Optimisation of mesh size . . . 50
5.2.2 Single-panel floor on elastic supports . . . 50
5.2.3 Two-panel floor on elastic supports . . . 52
5.2.4 Three-panel floor supported by GLT beams . . . 53
5.3 Finite element model updating . . . 53
5.3.1 Spearman rank correlation-based sensitivity analysis . . . 56
5.3.2 Updating elastic support and timber material properties . . . 59
5.3.3 Updating connection properties . . . 61
5.3.4 Validation . . . 63
5.4 Two dimensional numerical models . . . 64
5.4.1 Low-frequency floor . . . 65
5.4.2 High-frequency floor . . . 66
5.5 Chapter summary . . . 66

6 Uncertainty analysis of modal properties **69**
6.1 Characterisation of uncertainties . . . 69
6.2 Low-frequency floor . . . 71

6.2.1 Training and validation of PCE metamodel 71
6.2.2 Uncertainty analysis of natural frequencies 74
6.2.3 Uncertainty analysis of modal masses 77
6.2.4 Model reduction: uncertainty analysis considering three uncertain parameters 79
6.3 High-frequency floor 81
6.3.1 Training and validation of PCE metamodel 81
6.3.2 Uncertainty analysis of natural frequencies 83
6.3.3 Uncertainty analysis of modal masses 86
6.3.4 Model reduction: uncertainty analysis considering three uncertain parameters 88
6.4 Chapter summary 89

7 Modelling dynamic force **91**

7.1 Database description 92
7.2 Harmonic load model 92
7.2.1 Model formulation 93
7.2.2 Extraction of model parameters from the database 94
7.2.3 Verification through force reconstruction and SDOF response calculation 100
7.2.4 Probabilistic description of model parameters 104
7.2.5 Implementation and generation of probabilistic harmonic load 109
7.2.6 Simplified harmonic load model for deterministic calculations 111
7.3 Impulse load model 113
7.3.1 Model formulation 115
7.3.2 Extraction of model parameters 116
7.3.3 Verification through SDOF response calculation 121
7.3.4 Probabilistic description of model parameters 122
7.3.5 Implementation and generation of probabilistic impulse load 126
7.3.6 Simplified deterministic effective impulse model 128

7.3.7 Damping effect consideration . . . 131

7.4 Chapter summary . . . 132

8 Deterministic vibration response 135

8.1 Proposed simplified load models . . . 136

8.1.1 Low-frequency floors . . . 136

8.1.2 High-frequency floors . . . 138

8.2 Hindu software . . . 139

8.2.1 Computational framework and implementation . . . 139

8.2.2 Graphical user interface . . . 140

8.3 Response verification . . . 145

8.3.1 Low-frequency floors . . . 146

8.3.2 High-frequency floors . . . 150

8.4 Chapter summary . . . 152

9 Uncertainty analysis of vibration response 155

9.1 Internal stochastic variability . . . 157

9.2 Convergence study . . . 159

9.3 Low-frequency floor . . . 160

9.3.1 Uncertainty analysis of non-resonant response considering total load variability . . . 160

9.3.2 Uncertainty analysis of non-resonant response considering only inter-subject load variability . . . 164

9.3.3 Uncertainty analysis of resonant response considering total load variability 166

9.3.4 Uncertainty analysis of resonant response considering only inter-subject load variability . . . 169

9.4 High-frequency floor . . . 170

9.4.1 Uncertainty analysis of transient response considering total load variability 172

9.4.2 Uncertainty analysis of transient response considering only inter-subject load variability . . . 174

9.5 Chapter summary . . . 176

10 Concluding remarks **181**

10.1 Dissertation summary and outputs 181

10.2 Main contributions 185

10.3 General implications for VSA of CLT floors 186

10.4 Recommendations for future work 188

Biography **203**

Contributions **205**

List of Figures

1.1 Schematic view of CLT configuration. 2

1.2 Four commonly used types of CLT inter-panel connections: a) single surface spline, b) double surface splines, c) internal spline and d) half-lapped joint. . . . 3

1.3 Schematic illustration of dissertation workflow, emphasising the specific contributions delivered in each phase 5

2.1 An example of continuously measured vertical component of walking force (a) and the corresponding Fourier amplitudes (b) [40]. 8

2.2 Resonant (a) and transient (b) response types. 9

2.3 DLFs of walking force for the first four harmonics (after Kerr [49]). 10

2.4 Correlation between the R factor and root-mean-square vertical acceleration in the frequency range $1 - 100$Hz, after [90]. 14

3.1 Illustration scheme of the effect of variance of two input variables, $\mathrm{Var}[X_1]$ and $\mathrm{Var}[X_2]$, on the variance of output $\mathrm{Var}[Y]$ when inputs are uncorrelated (a) and correlated (b). 23

4.1 CLT panels for assembling single-panel floor (a), two-panel floor (b) and three-panel floor (c). All dimensions are in centimetres. 32

4.2 Dimensions and test grid for single-panel floor (a), two-panel floor (b) and three-panel floor (c). All dimensions are in centimetres. 32

4.3 Experimental setup of a single-panel floor (a), two-panel floor (b) and three-panel floor (c). 33

4.4 Detail of half-lap joint (a), elastic support (b) and panel-to-GLT beam and GLT beam-to-steel frame connection (c). 34

4.5 Boundary conditions of single and two-panel floors (a) and three-panel floor (b), steel frame that supports GLT beams and three-panel floor (c). 34

4.6 A characteristic example of a singular value decomposition of the spectral density matrices. 34

4.7 Experimentally determined rigid body mode shapes of the single-panel and two-panel floors. 35

4.8 Experimentally determined deformation mode shapes of the single-panel, two-panel and three-panel floors. 36

4.9 Two WPs and acceleration measurement points of three-panel floor. 37

4.10 Acceleration time history due to TS1 walking at $f_p = 2$Hz on three-panel CLT floor along WP1 in direction D1 (a) and corresponding Fourier amplitude spectrum (b). 38

4.11 Acceleration time history due to TS1 walking at $f_p = 2$Hz on three-panel CLT floor along WP1 in direction D2 (a) and corresponding Fourier amplitude spectrum (b). 38

4.12 Acceleration time history due to TS1 walking at $f_p = 2$Hz on three-panel CLT floor along WP2 in direction D1 (a) and corresponding Fourier amplitude spectrum (b). 39

4.13 Acceleration time history due to TS1 walking at $f_p = 2$Hz on three-panel CLT floor along WP2 in direction D2 (a) and corresponding Fourier amplitude spectrum (b). 39

4.14 Acceleration time history due to TS1 free walking on three-panel CLT floor along WP1 in direction D1 (a) and corresponding Fourier amplitude spectrum (b). . . 40

4.15 Acceleration time history due to TS1 free walking on three-panel CLT floor along WP1 in direction D2 (a) and corresponding Fourier amplitude spectrum (b). . . 40

4.16 Acceleration time history due to TS1 free walking on three-panel CLT floor along WP2 in direction D1 (a) and corresponding Fourier amplitude spectrum (b). . . 40

4.17 Acceleration time history due to TS1 free walking on three-panel CLT floor along WP2 in direction D2 (a) and corresponding Fourier amplitude spectrum (b). . . 41

4.18 Acceleration time history due to TS2 free walking on three-panel CLT floor along WP1 in direction D1 (a) and corresponding Fourier amplitude spectrum (b). . . 41

4.19 Acceleration time history due to TS2 free walking on three-panel CLT floor along WP1 in direction D2 (a) and corresponding Fourier amplitude spectrum (b). . . 41

4.20 Acceleration time history due to TS2 free walking on three-panel CLT floor along WP2 in direction D1 (a) and corresponding Fourier amplitude spectrum (b). . . 42

4.21 Acceleration time history due to TS2 free walking on three-panel CLT floor along WP2 in direction D2 (a) and corresponding Fourier amplitude spectrum (b). . . 42

5.1 Step-by-step approach to FEMU. 46

5.2 Equivalent elastic strip connection model to replace real half-lapped joint connection. 47

5.3 Behaviour of a half-lapped joint connection (a), rigid rectangle model (b), equivalent elastic strip (c). 47

5.4 Numerical models of single-panel (a), two-panel (b) and three-panel floor (c). . . 48

5.5 Timber material coordinate system with L-longitudinal, T-transversal and R-radial axes (a), layers' orientation in FE model (b). 49

5.6 Mesh size optimisation described as T/L+HLJ, where T stands for the mesh size in the transverse direction, L for the mesh size in the longitudinal direction, and HLJ for the refinement around the half-lapped joint shaped edge. 50

5.7 Experimentally (up) and numerically (down) determined mode shapes of the single-panel floor. 51

5.8 Experimentally (up) and numerically (down) determined mode shapes of the two-panel floor. 53

5.9 Experimentally (up) and numerically (down) determined mode shapes of the three-panel floor. 54

5.10 Criteria for obtaining knee point: minimum distance from equilibrium point - min dEP (a), maximum distance from boundary line - max dBL (b), maximum band angle - max β (c). 55

5.11 Spearman's correlation coefficients between timber and elastic support material properties, and single-panel floors numerical frequencies and MAC values. 57

5.12 Spearman's correlation coefficients between connection properties and two-panel floors numerical natural frequencies (up) and MAC values (down). 57

5.13 Algorithm to optimise FE modelling parameters. 58

5.14 Pareto front for updating parameters E_{supp} and ν_{LT} (up), E_T, G_{LT}, G_{RT} and ν_{LT} (down), and optimal solutions obtained using three different criteria for the "knee" point. 59

5.15 Relative errors between experimentally and numerically determined natural frequencies and MAC values for both initial and updated model of the single-panel floor. 60

5.16 Pareto front for updating connection parameters and optimal solutions obtained using three different criteria for the "knee" point. 62

5.17 Relative errors between experimentally and numerically determined natural frequencies and MAC values for both initial and updated model of the two-panel floor. 62

5.18 Relative errors between experimentally and numerically determined natural frequencies and MAC values for both initial and updated model of the three-panel floor. 63

5.19 Two-dimensional FE model with boundary conditions. For LFF L = 6m, for HFF L = 5m 65

5.20 Numerically determined mode shapes for 2D model of LFF 65

5.21 Relative errors between experimentally and numerically determined natural frequencies and MAC values for 3D and 2D models of the three-panel LFF. 66

5.22 Numerically determined mode shapes for 2D model of HFF 67

6.1 Evaluating minimal training sample size for second-order PCE metamodel. . . . 72

6.2 Evaluating minimal training sample size for third-order PCE metamodel. 73

6.3 Comparison of natural frequencies predicted by the second-order PCE metamodel (n=128) and the FE model. 73

6.4 Comparison of modal masses predicted by the second-order PCE metamodel (n=128) and the FE model. 74

6.5 Mean values and COVs of natural frequencies obtained using PCE and SFEM. . 75

6.6 PDFs of natural frequencies obtained using PCE and SFEM. 75

6.7 CDFs of natural frequencies obtained using PCE and SFEM. 76

6.8 First order and total order Sobol' indices for natural frequencies. 76

6.9 Mean values and COVs of modal masses obtained using PCE and SFEM. 77

6.10 PDFs of modal masses obtained using PCE and SFEM. 78

6.11 CDFs of modal masses obtained using PCE and SFEM. 78

6.12 First order and total order Sobol' indices for modal masses. 79

6.13 Evaluating minimal training sample size for second-order PCE metamodel with three variables. 80

6.14 Comparison of UQ and SA for the first three modes, considering three and ten uncertain parameters 80

6.15 Evaluating minimal training sample size for second-order PCE metamodel. . . . 81

6.16 Evaluating minimal training sample size for third-order PCE metamodel. 81

6.17 Comparison of natural frequencies predicted by the second-order PCE metamodel (n=128) and the FE model. 82

6.18 Comparison of modal masses predicted by the second-order PCE metamodel (n=128) and the FE model. 83

6.19 Mean values and COVs of natural frequencies obtained using PCE and SFEM. . 84

6.20 PDFs of natural frequencies obtained using PCE and SFEM. 84

6.21 CDFs of natural frequencies obtained using PCE and SFEM. 85

6.22 First order and total order Sobol' indices for natural frequencies. 85

6.23 Mean values and COVs of modal masses obtained using PCE and SFEM. 86

6.24 PDFs of modal masses obtained using PCE and SFEM. 86

6.25 CDFs of modal masses obtained using PCE and SFEM. 87

6.26 First order and total order Sobol' indices for modal masses. 87

6.27 Evaluating minimal training sample size for second-order PCE metamodel with three variables. 88

6.28 Comparison of UQ for the first four modes, considering three and ten uncertain parameters 88

6.29 Comparison of SA for the first four modes, considering three and ten uncertain parameters 89

7.1 A portion of 35s-long measured normalised force [40], corresponding 3Hz filtered signal and defined period of a single step. 94

7.2 Variability of walking frequency during a single walk. 95

7.3 COVs with corresponding mean walking frequencies. 95

7.4 Variability of DLFs during a single walk. 97

7.5 Mean values of DLFs with corresponding walking frequencies. 98

7.6 COVs of DLFs with corresponding walking frequencies. 98

7.7 Correlation between DLF mean values for six harmonics. 99

7.8 The AR coefficients ρ_{f_p} with corresponding mean walking frequencies. 100

7.9 The AR coefficients ρ_{DLF_h} with corresponding mean DLFs. 100

7.10 Measured and reconstructed force time histories (a) and corresponding Fourier amplitude spectra (b) for walking session $i = 446$. 101

7.11 Acceleration response of the SDOF oscillators [mm/s^2] induced by all 744 measured ($a^m_{rms,max}$) and reconstructed ($a^r_{rms,max}$) force signals. 101

7.12 Acceleration response of the SDOF oscillators with frequency $f = f_p$ (a), $f = 2f_p$ (b) and $f = 3f_p$ (c) induced by measured and corresponding reconstructed force signal (walking session $i = 446$). 102

7.13 Acceleration response of the SDOF oscillators with frequency $f = 4f_p$ (a), $f = 5f_p$ (b) and $f = 6f_p$ (c) induced by measured and corresponding reconstructed force signal (walking session $i = 446$). 103

7.14 Histogram of pedestrian body weight and corresponding normal distribution. . . 105

7.15 Histograms of walking frequency mean value $\mu_{f_{p,i}}$ and standard deviation $\sigma_{f_{p,i}}$, with distributions utilised to approximate μ_{f_p} and σ_{f_p}. 105

7.16 Histograms of DLF mean values $\mu_{\mathrm{DLF}_{h,i}}$ with distributions utilised to approximate μ_{DLF_h}. 106

7.17 Histograms of DLF standard deviations $\sigma_{\mathrm{DLF}_{h,i}}$ with distributions utilised to approximate σ_{DLF_h}. 106

7.18 Matrix of linear correlation coefficients for 15 force parameters. 108

7.19 Histogram of AR coefficient for walking frequency $\rho_{f_{p,i}}$ with distribution utilised to approximate ρ_{f_p}. 109

7.20 Histograms of AR coefficient for DLFs $\rho_{\mathrm{DLF}_{h,i}}$ with distribution utilised to approximate ρ_{DLF_h}. 110

7.21 Fourier amplitude spectrum of the measured force (walking session $i = 446$, $f_p = 2.04$Hz) with spectra of 200 generated walking-forces with the same mean f_p.111

7.22 Mean DLFs and corresponding CDFs, with the selected subset for simplified force modelling. 112

7.23 Relative errors between DLFs predicted by simplified force model and corresponding measured DLFs. 113

7.24 Reconstruction of a typical transient vibration response using effective impulses. 114

7.25 A portion of 35s-long measured normalised force [40], corresponding 3Hz filtered signal and defined period of a single step for f_p calculation. 116

7.26 Variability of walking frequency during a single walk. 117

7.27 COVs with corresponding mean walking frequencies. 117

7.28 Comparison of step-based and first-harmonic-based definition of walking frequency.117

7.29 Variability of I_{eff} during the walking session $i = 446$ for SDOF oscillators with different frequencies. 119

7.30 Mean value and COV of I_{eff} during walking session $i = 446$ for SDOF oscillators with different frequencies. 119

7.31 Averaged $\mu_{I_{\text{eff,i}}}$ and $\text{COV}_{I_{\text{eff,i}}}$ over 744 walking sessions for SDOF oscillators with different frequencies. 120

7.32 The AR coefficients ρ_{f_p} with corresponding mean walking frequencies. 120

7.33 The AR coefficients $\rho_{I_{\text{eff}}}$ for SDOF oscillators with different natural frequencies, with corresponding mean walking frequencies. 120

7.34 Mean value and standard deviation of the AR coefficients $\rho_{I_{\text{eff}}}$ for all walking sessions with corresponding SDOF oscillator natural frequencies. 121

7.35 Velocity response of SDOF oscillator with frequency f_n = 14Hz induced by measured force signal and corresponding reconstructed impulse load. 122

7.36 Velocity response of SDOF oscillator with frequency f_n = 14Hz induced by measured force signal and corresponding reconstructed impulse load - a detailed view. 122

7.37 Peak velocity and maximum rms value for moving average (T=1s) of all 261 SDOF oscillators induced by all 744 measured (v^m_{peak}, $v^m_{rms,max}$) and reconstructed (v^r_{peak}, $v^r_{rms,max}$) force signals. 122

7.38 Histograms of step-based walking frequency mean value $\mu_{f_{p,i}}$ and standard deviation $\sigma_{f_{p,i}}$ with distributions utilised to approximate μ_{f_p} and σ_{f_p}. 123

7.39 Histograms of mean value $\mu_{I_{\text{eff,i}}}$ and standard deviation $\sigma_{I_{\text{eff,i}}}$ of effective impulse with distributions utilised to approximate $\mu_{I_{\text{eff}}}$ and $\sigma_{I_{\text{eff}}}$, for four different SDOF oscillator frequencies. 124

7.40 Lognormal distribution parameters $\mu_{\ln}$ and $\sigma_{\ln}$ for $\mu_{I_{\text{eff}}}$ and $\sigma_{I_{\text{eff}}}$ as functions of the SDOF oscillator frequency, with the corresponding fitted trend lines. 125

7.41 Correlation coefficients between four impulse load parameters for different SDOF oscillator natural frequencies. 126

7.42 Matrix of linear correlation coefficients for four impulse load parameters. 126

7.43 Histograms of AR coefficients for f_p and I_{eff} with distributions to approximate ρ_{f_p} and $\rho_{I_{\text{eff}}}$. 127

7.44 Scatter plots of mean I_{eff} versus walking frequency f_p for four different f_n. . . . 128

7.45 Variation of coefficient $a(f_n)$ over f_n. 129

7.46 Variation of coefficient $A_{\text{CDF}}(f_n)$ over f_n for different CDF levels. 130

7.47 Predicted and database values of effective impulse (a) and calculated RMSRE for different f_n (b). 131

7.48 Predicted I^p_{eff} and database values I^d_{eff} of effective impulse taking into account different damping ratio 132

8.1 Comparison of DLFs according to CCIP-016, proposed formulation and database values for CDF= 0.75 (corresponding to CCIP-016). 137

8.2 Comparison of I_{eff} according to CCIP-016, proposed formulation and database values for CDF= 0.75, $G = 750$N and $\zeta = 3\%$ (corresponding to CCIP-016). . . 139

8.3 Hindu software main window and its components: Menu bar (a), Available modes (b), Input parameters (c), Walking path (d) and Canvas (e). 141

8.4 Floor tab - available options (a), choosing one of the listed FE software (b), displayed loaded modal properties (c). 142

8.5 Walking path window. 142

8.6 The *Model* tab with the implemented walking load models and assessment procedures (a), and the *Response diagrams* tab with the available visualisation options (b). 143

8.7 Time-domain response histories at the receiver point: contributions of individual modes (a) and the total response with the corresponding one-second running RMS history (b). 144

8.8 3D visualisation of the spatial distribution of the floor vibration response. 144

8.9 Walking paths and receiver point for LFF (a) and HFF (b). 145

8.10 Comparison of the measured peak and maximum one-second running RMS acceleration with those predicted using the CCIP-016 and proposed load models for TS1 walking at $f_p = 2$Hz along WP1 (a) and WP2 (b). 147

8.11 CDFs of the maximum one-second running RMS acceleration obtained using 76 measured walking-force signals and the proposed probabilistic formulation, for a pedestrian walking at $f_p = 2$Hz along WP1 (a) and WP2 (b). 148

8.12 Comparison of the acceleration time histories with corresponding one-second running RMS obtained using the CCIP-016 and proposed load models for pedestrian walking at $f_p = 2.1$Hz along WP1 (a) and WP2 (b). 149

8.13 CDFs of the maximum one-second running RMS acceleration obtained using 76 measured walking-force signals and the proposed probabilistic formulation, for a pedestrian walking at $f_p = 2.1$Hz along WP1 (a) and WP2 (b). 150

8.14 Comparison of the velocity time histories with corresponding one-second running RMS obtained using the CCIP-016 and proposed load models for pedestrian walking at $f_p = 2.1$Hz along WP1 (a) and WP2 (b). 151

8.15 CDFs of the maximum one-second running RMS acceleration obtained using 31 measured walking-force signals and the proposed probabilistic formulation, for a pedestrian walking at $f_p = 2.5$Hz along WP1 (a) and WP2 (b). 152

9.1 Normalised Shapley effects convergence with increasing number of permutations m 159

9.2 Empirical and best-fit distribution of non-resonant $a_{rms,max}$ considering total variability for WP1 and WP2. 161

9.3 Calculated $a_{rms,max}$ as a function of the floor fundamental-to-walking frequency ratio f_1/f_p for WP1 (a) and WP2 (b). 162

9.4 CDFs of non-resonant $a_{rms,max}$ considering total variability for WP1 and WP2 (a), with experimentally measured responses (b) and resonant responses obtained deterministically using CCIP-016 and the proposed simplified load model (c). . . 162

9.5 Internal AR(1) model variability and normalised Shapley effects of the 19 uncertain input parameters for the non-resonant responses along WP1 and WP2. . . . 163

9.6 Empirical and best-fit distribution of non-resonant $a_{rms,max}$ considering only inter-subject variability for WP1 and WP2. 165

9.7 Mean values and standard deviation of non-resonant $a_{rms,max}$, considering total and inter-subject variability cases, for WP1 and WP2. 165

9.8 Normalised Shapley effects of the 12 uncertain input parameters for the non-resonant responses along WP1 and WP2, considering only inter-subject variability. 166

9.9 Empirical and best-fit distribution of resonant $a_{rms,max}$ considering total variability for WP1 and WP2. 167

9.10 CDFs of resonant $a_{rms,max}$ considering total variability for WP1 and WP2 with resonant responses obtained deterministically using CCIP-016 and the proposed simplified load model. 167

9.11 Internal AR(1) model variability and normalised Shapley effects of the 18 uncertain input parameters for the resonant responses along WP1 and WP2. 168

9.12 Empirical and best-fit distribution of resonant $a_{rms,max}$ considering only inter-subject variability for WP1 and WP2. 169

9.13 Mean values and standard deviation of resonant $a_{rms,max}$, considering total and inter-subject variability cases, for WP1 and WP2. 169

9.14 PDFs of non-resonant and resonant $a_{rms,max}$ considering total and inter-subject variability cases for WP1 and WP2. 170

9.15 CDFs of non-resonant and resonant $a_{rms,max}$ considering total and inter-subject variability cases, for WP1 and WP2. 171

9.16 Normalised Shapley effects of the 11 uncertain input parameters for the resonant responses along WP1 and WP2, considering only inter-subject variability. 171

9.17 Empirical and best-fit distribution of transient $v_{rms,max}$ considering total variability for WP1 and WP2. 173

9.18 CDFs of transient $v_{rms,max}$ considering total variability for WP1 and WP2 with responses obtained deterministically using CCIP-016 and the proposed simplified load model. 173

9.19 Internal AR(1) variability and normalised Shapley effects of the 9 uncertain input parameters for the transient responses along WP1 and WP2. 174

9.20 Empirical and best-fit distribution of transient $v_{rms,max}$ considering only inter-subject variability for WP1 and WP2. 175

9.21 Mean values and standard deviation of transient $v_{rms,max}$, considering total and inter-subject variability cases, for WP1 and WP2. 175

9.22 PDFs and CDFs of transient response $v_{rms,max}$ considering total and inter-subject variability cases for WP1 and WP2. 176

9.23 Normalised Shapley effects of the 7 uncertain input parameters for the transient responses along WP1 and WP2, considering only inter-subject variability. 176

List of Tables

2.1 Statistical properties of human walking frequency 11

2.2 Mean and design values, and COVs of DLFs for four harmonics according to CCIP-016 [41]. 18

4.1 Experimentally measured natural frequencies of the single-panel (1pf), two-panel (2pf) and three-panel floors (3pf) and and damping ratios of the three-panel floor. 35

4.2 Walking test trials. 38

4.3 Walking test results. 43

5.1 Initial properties of elastic supports, C24 timber material and elastic strip with the bounds used in FEMU for parameters to be updated. 49

5.2 Experimentally measured and numerically determined natural frequencies and MAC values of initial model of the single-panel floor. 51

5.3 Experimentally measured and numerically determined natural frequencies and MAC values of initial model of the two-panel floor. 52

5.4 Experimentally measured and numerically determined natural frequencies and MAC values of initial model of the three-panel floor. 54

5.5 Experimentally measured and numerically determined natural frequencies and MAC values of updated model of the single-panel floor. 60

5.6 Updated properties of elastic support and C24 material and relative error compared to the initial values. 61

5.7 Updated connection properties and relative error compared to the initial values. 62

5.8 Experimentally measured and numerically determined natural frequencies and MAC values of updated model of the two-panel floor. 63

5.9 Experimentally measured and numerically determined natural frequencies and MAC values of updated model of the three-panel floor. 64

5.10 Experimentally and numerically determined natural frequencies, numerically determined modal masses and MAC values for 2D model of the three-panel LFF. 66

5.11 Numerically determined natural frequencies and modal masses for 2D model of the three-panel HFF. 67

6.1 Literature review on uncertain timber material properties. 70

6.2 Properties of uncertain modelling parameters of CLT floor. 71

6.3 Relevance of an uncertain parameter based on Sobol' indices value [173]. 77

7.1 Fitted distributions of force parameters. 107

7.2 Distribution parameters of AR coefficient. 109

7.3 Values of p-coefficients for calculating DLFs of simplified harmonic force model. . 112

7.4 Best-fit equations for the parameters of the lognormal distributions fitted to $\mu_{I_{\text{eff}}}$ and $\sigma_{I_{\text{eff}}}$. 125

7.5 Fitted distributions of impulse load parameters. 125

7.6 Values of coefficients $p_0(\text{CDF}) - p_3(\text{CDF})$ for calculating $A_{\text{CDF}}(f_n)$ of simplified impulse load model. 130

8.1 Values of p-coefficients for calculating DLFs of simplified harmonic force model. . 137

8.2 Values of coefficients $p_0(\text{CDF}) - p_3(\text{CDF})$ for calculating $A_{\text{CDF}}(f_n)$ of simplified impulse load model. 138

8.3 Comparison of peak and maximum one-second running RMS acceleration values obtained using the proposed model, CCIP-016 and experimental measurements for TS1 walking at $f_p = 2\text{Hz}$. 147

8.4 Comparison of peak and maximum one-second running RMS acceleration values of resonant response obtained using the proposed model and CCIP-016. 149

8.5 Comparison of resonant R factors obtained using the proposed model and CCIP-016. 150

8.6 Comparison of peak and maximum one-second running RMS velocity values of transient response obtained using the proposed model and CCIP-016. 151

8.7 Comparison of R factors obtained using the proposed model and CCIP-016. . . . 152

9.1 Distributions of parameters for vibration response analysis of LFF. 156

9.2 Distributions of parameters for vibration response analysis of HFF. 156

1 Introduction

Civil engineering and construction sector relies heavily on materials whose production is highly energy-demanding, such as cement, concrete and steel. It also requires large quantity of natural resources and involves processes that generate significant greenhouse-gas emissions. According to the latest global assessments, buildings and their construction together account for around one third of the total CO_2 emissions and global energy consumption [1, 2]. In Europe, this sector is responsible for approximately a half of all extracted raw materials and about 40% of greenhouse-gas emissions [3]. Recent studies [4] also show that the carbon footprint of global construction activity has doubled over the past three decades and is projected to double again by 2050 without major changes in material production and structural design. These unfavourable figures have led to a trendy shift towards more sustainable practices, including increased use of low-carbon materials, improvements in energy efficiency, strategies for recycling and re-use of building components and life-cycle-based assessment of structural systems, all aiming to substantially lower the environmental impact of civil engineering sector.

Timber as a building material satisfies all key requirements of sustainable engineering, as it is produced from a natural, renewable resource, stores biogenic carbon through its service life and requires significantly less energy to manufacture compared to steel or concrete. Although it has been used for centuries, its usage in modern construction dropped significantly with the rise of steel and reinforced concrete, which offered much higher structural performances. However, the development of advanced engineered wood products such as *cross-laminated timber* (CLT) has renewed interest in timber material, positioning it once again as a competitive and sustainable alternative, especially for low and mid-rise buildings [5, 6]. In this context, this doctoral dissertation aims to contribute to the wider use of timber material by providing deeper insight into the vibration behaviour of CLT floors, which is an essential aspect of floor performance in modern timber buildings.

1.1 Background and motivation

CLT, also known as mass timber or X-lam, was developed in Austria in the early 1990s. It rapidly gained popularity and a global acceptance - first across Europe and, subsequently, in North America and across the globe [7].

CLT is a natural composite product consisting of an odd number of layers (or lamellas), typically three to nine. Each layer is formed from multiple parallel timber boards placed (and optionally glued) edge-to-edge. The layers are glued and pressed together so that directions of their fibers are typically perpendicular [8], as illustrated in Figure 1.1. This crosswise configuration

provides CLT panels with enhanced strength and stiffness in both directions. The panel axis that aligns with the fibres of outer (top and bottom) layers is considerably stiffer and is referred to as the *major* direction, while the perpendicular axis, governed primarily by the stiffness of internal layers, is termed the *minor* direction [9].

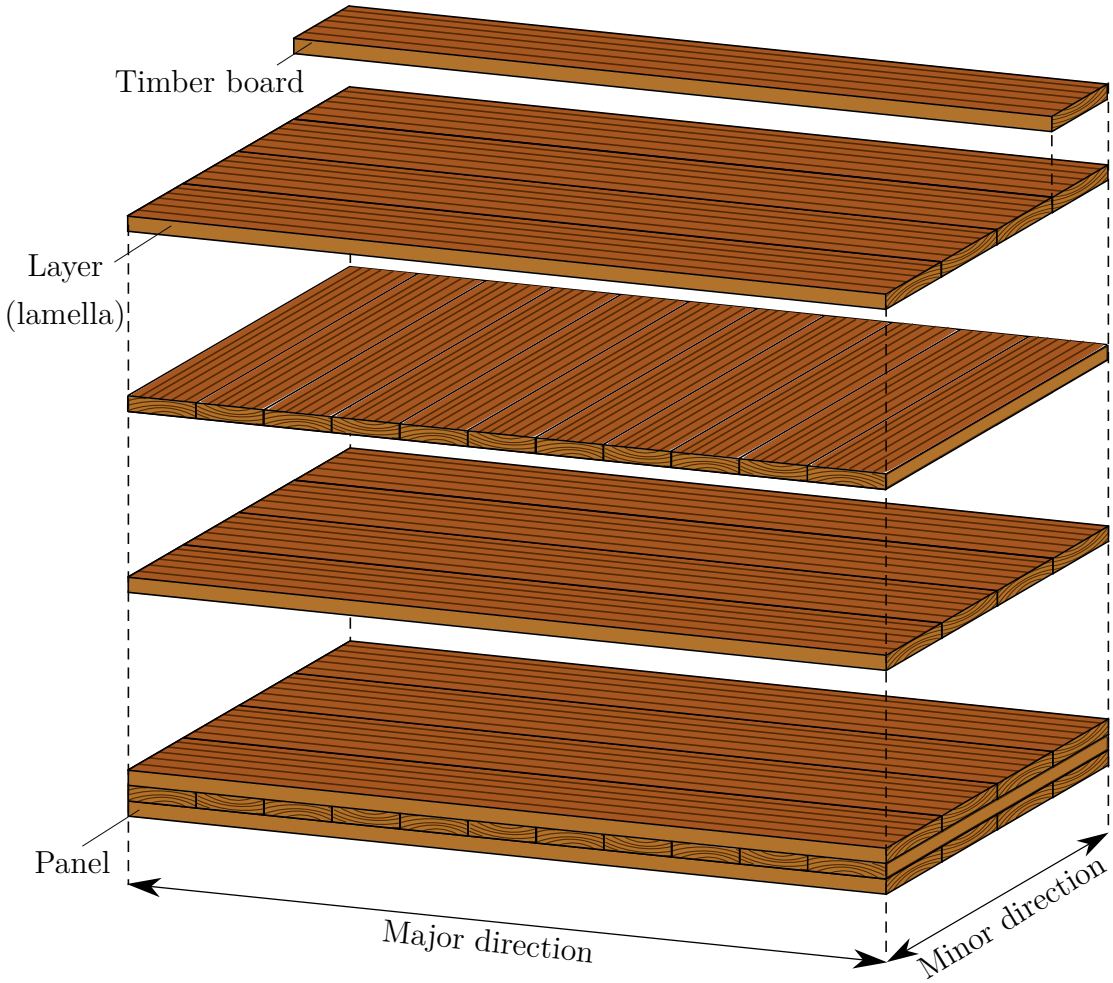

Figure 1.1: Schematic view of CLT configuration.

Generally, CLT structures are built from large panels used as structural walls, floor or roof slabs. These structural elements are manufactured under controlled factory conditions and prefabricated with precision, offering a high degree of design flexibility. The manufacturing process and transportation limit the size of CLT panels to approximately 20m in length and $3 - 4$m in width [8, 10]. Panels are then assembled on site using various type of inter-panel connections, such as single surface spline, double surface spline, internal spline and half-lapped joint presented in Figure 1.2. Due to the light weight of the timber, large dimensions and tight dimensional tolerances of prefabricated elements, CLT structures can be erected rapidly and with high construction efficiency [11].

With its favourable strength and stiffness properties, which are often comparable to those of concrete, its aesthetic appeal and reliable fire, seismic and thermal performance, CLT has proven to be highly competitive in modern structural engineering [12–14]. When viewed in the broader context of environmental sustainability, the advantages of CLT become particularly significant. Life cycle assessments consistently show that CLT buildings produce on average 40% lower greenhouse gas emissions than their concrete counterparts [15], operate with lower energy consumption [16] and allow components to be reused or recycled at the end of building's lifespan [17].

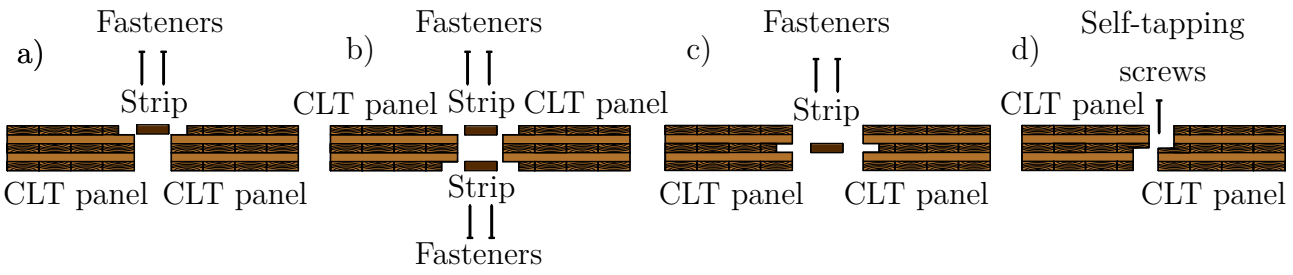

Figure 1.2: Four commonly used types of CLT inter-panel connections: a) single surface spline, b) double surface splines, c) internal spline and d) half-lapped joint.

The praising high stiffness-to-weight ratio of CLT supports design of lightweight long-span floors, but it also makes them sensitive to vibration issues [18]. Floors in residential and commercial buildings are primarily designed to accommodate human occupants. Consequently, human activities such as walking, jumping and running are generally recognised as the predominant sources of vibration in these structures [19]. Among them, walking represents the most common form of cyclic locomotion [20], and is the most relevant load case scenario for vibration serviceability assessment (VSA) of floors in general. Although human-induced vibrations rarely pose a structural safety risk, they can adversely affect occupants' comfort and may cause malfunction of vibration-sensitive equipment [21]. Nevertheless, vibration serviceability often becomes the governing design criterion for long-span CLT floors, rather than strength or deflection limits [22–24].

For many years, vibration serviceability criteria were based primarily on limiting the static deflection of the floor. They later evolved to include the control of dynamic properties, such as minimum frequency requirement. Today, the most popular approaches to VSA are based on calculating the vibration response induced by pedestrian walking and comparing it with a predefined acceptability limit [25]. Calculating the floor vibration response requires knowledge regarding two main components: floor modal properties and walking loading. In everyday design routine, due to simplicity and efficiency of dynamic response calculations, they are both typically modelled deterministically. Consequently, whether a floor is fit for use is decided through a binary fail/pass criterion evaluated for the worst case loading scenario. This approach leads to particularly conservative results for floors with low damping [26], including CLT floors. Živanović and Pavić [27] pioneered a probabilistic approach which accounts for a random nature of walking loading and quantifies the probability of response staying within or surpassing a specified vibration threshold.

Variations in wood species, growth irregularities, knots, fibre orientation, moisture content and differences in manufacturing processes inevitably lead to variability in timber material properties [28, 29]. This inherent variability introduces uncertainties into the modal properties of a timber floor [30–32]. Due to the limited amount of research and the absence of modelling guidelines, the influence of inter-panel connections on floor's modal properties, dynamic response and vibration serviceability is often neglected. Consequently, multi-panel CLT floors are commonly modelled either as monolithic systems with ideally connected panels or as a set of independent panels. Neither of these approaches accurately represents the actual behaviour of the CLT floor and may lead to significant errors in calculating modal properties and vibration response [33]. Additionally, boundary conditions and damping represent major sources of uncertainty in any floor system, and CLT floors are no exception.

Variability in pedestrian walk, and therefore in pedestrian-induced load, manifests in two ways. First, no person is capable of taking two identical consecutive steps. This phenomenon is

referred to as *intra-subject* variability. Second, differences among individuals, such as age, height, weight and body structure, result in distinct walking patterns, giving rise to *inter-subject* variability [34].

All these variabilities yield high uncertainty of floor vibration response, resulting in a wide range of possible responses that cannot be predicted by purely deterministic calculations. Using extreme values as design criteria normally leads to overly conservative solutions, while relying solely on mean values neglects the influence of rare, but potentially critical scenarios. Within this context, introducing an uncertainty and probabilistic framework into vibration analysis becomes essential. It provides a deeper insight into the distribution of potential responses and offers a possibility to assess the risk of not meeting the vibration serviceability criterion. However, there is a clear lack of research addressing the combined effects of variability in both pedestrian loading and structural properties, such as timber material properties, inter-panel connections and damping, on the vibration response of CLT floors. In other words, a comprehensive and systematic approach for identifying the key parameters and quantifying total uncertainty in the predicted response is still missing. This gap represents the central problem that this dissertation aims to address.

1.2 Research aims, methodology and contribution

The research presented in this dissertation is based on the hypothesis that probabilistic modelling of floor vibration behaviour provides a more accurate and reliable basis for VSA than conventional deterministic methods. With this in mind, the dissertation examines the extent to which variability in both structural properties and pedestrian-induced force influences the vibration behaviour of CLT floor. This will be carried out within an *uncertainty analysis* framework that integrates appropriate *uncertainty quantification* (UQ) method together with *sensitivity analysis* (SA). Finally, based on the obtained results, recommendations and guidelines for the vibration serviceability design of long-span CLT floors can be formulated. These recommendations should more accurately reflect the actual in service behaviour of floor and contribute to more cost-effective and reliable design solutions. To accomplish this objective, this dissertation is organised into five phases, each providing a distinctive contribution toward the final research aim, as illustrated in Figure 1.3.

The first phase involves developing a deterministic finite element (FE) model of a multi-panel CLT floor. A key challenge in this step was appropriately representing the inter-panel connections. A simple and pragmatic modelling approach was adopted based on literature search. Parameters required to describe this connection model were obtained by fitting the numerically calculated modal properties to match the experimentally measured modal properties of three corresponding full-scale CLT floors using an appropriate optimisation algorithm. Experimental results used for this step-by-step FE model updating (FEMU) procedure were obtained within the Substrate4CLT research project, funded by the Science Fund of the Republic of Serbia.

The second phase of this research studies how variability in structural properties influences the natural frequency and modal masses of CLT floor. Uncertainty in timber material properties, damping and inter-panel connection parameters were identified from the available literature and used as input for probabilistic UQ and SA, typically performed through stochastic FE method (SFEM) [35] and Monte Carlo (MC) simulation [36]. However, combining complex FE models with MC simulation often makes uncertainty analysis computationally demanding. To

overcome this drawback, it is common to replace the computationally expensive model with a cost-efficient metamodel [37]. Therefore, the FE model of a CLT floor was replaced with a Polynomial Chaos Expansion (PCE) metamodel [38], enabling UQ and SA of modal properties to be carried out much more efficiently. The same metamodel was subsequently employed in the final (fifth) phase as a computationally efficient replacement for the FE model.

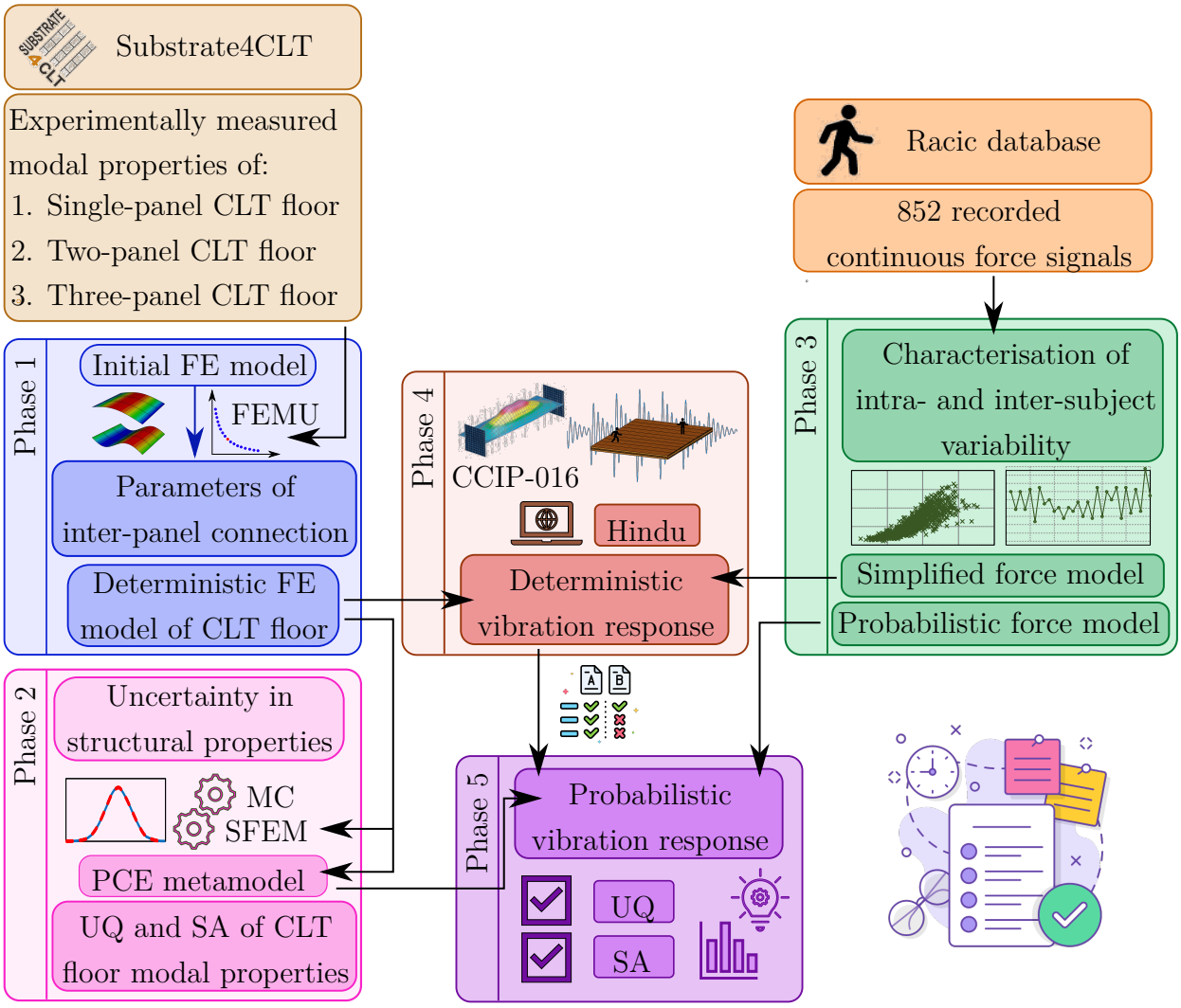

Figure 1.3: Schematic illustration of dissertation workflow, emphasising the specific contributions delivered in each phase

The third phase of this research starts from an established database of recorded continuous force signals generated by more than 70 test subjects walking individually on an instrumented treadmill collected by Racic as part of his doctoral research [39, 40]. This comprehensive database, comprising 852 recorded signals, was analysed with two main objectives. First, to characterise both intra- and inter-subject variability in the parameters that define pedestrian-induced force. Second, to identify an appropriate way to incorporate this variability into established probabilistic pedestrian force models. The analysis carried out in the later phases will determine whether all uncertain parameters contribute equally to the overall uncertainty of the dynamic response. In addition, this phase also yielded a simplified force model that is practical and efficient for use in everyday engineering design.

The fourth phase involves calculating vibration response of the CLT floor in a conventional, deterministic manner, following currently the most comprehensive and widely used Design guide for footfall induced vibration of structures (CCIP-016) [41], which is expected to inform the next

generation of Eurocodes. Additionally, vibration response was calculated using the simplified force model developed in the third phase of the dissertation. Deterministically calculated response served as a benchmark for the final phase in which vibration response was evaluated using probabilistic approach. As a part of this phase, a software tool named Hindu [42] was developed for calculating floor vibration response under pedestrian-induced dynamic excitation. Although still in early stage of development, Hindu features a user-friendly graphical interface that provides quick calculations and effective visualisation of results.

The final, fifth phase brings together the results of all preceding phases by calculating the vibration response while accounting for all identified sources of uncertainty. In this way, the total uncertainty of the vibration response was quantified. Particular emphasis was placed on assessing the influence of intra- and inter-subject variability in the pedestrian-induced force on calculated response. First, vibration response was evaluated with all force-defining parameters treated as random variables that include both intra- and inter-subject variability. Calculation was then repeated while successively removing individual variability component from each random variable. Such an approach enabled a clear assessment of the relative importance of each uncertainty source and helped to determine whether the use of a complex probabilistic force model is justified.

1.3 Dissertation outline

This dissertation is organised into ten chapters. Following this introduction, Chapter 2 provides a comprehensive literature review, starting from the fundamental principles of vibration analysis, followed by an overview of commonly used design guidelines for VSA and concluding with recent research trends in human-induced vibrations of CLT floors. Chapter 3 presents the theoretical background of uncertainty analysis, enabling readers less familiar with this modelling concept to follow the subsequent chapters. A detailed description of the full-scale CLT floors and experimental setup for measuring their modal properties and vibration response induced by pedestrian walking, are provided in Chapter 4. The majority of the first phase is summarised in Chapter 5, which describes the development of the FE model of a multi-panel CLT floor from the initial model using the results from Chapter 4 and appropriate FEMU procedure. Chapter 6 corresponds to the second phase of the research and focuses on the characterisation of uncertainties in structural properties and their influence on modal properties of the CLT floor. Starting from the available database of recorded force signals, Chapter 7 addresses the third phase, presenting the characterisation of intra- and inter-subject variability in pedestrian induced force and the development of both complex probabilistic and simplified force models. Chapter 8 outlines the deterministic calculation of vibration response according to standard practice and introduces the Hindu software developed for this purpose. The key outcome of this research, i.e. the fifth phase comprising the probabilistic vibration response analysis using the developed uncertainty framework, is presented in Chapter 9. Finally, Chapter 10 summarises the main findings and conclusions of the dissertation and provides recommendations for future work.

2 Literature review of human-induced vibrations of CLT floors

In this chapter, a comprehensive review of the current state of knowledge on vibration serviceability of CLT floors is presented. The first section outlines the fundamental principles and terminology relevant to VSA, following the well-known framework of vibration *source*, vibration *path* and vibration *receiver*, with emphasis on pedestrian-induced vibrations of CLT floors. The second section presents an overview of the existing design guidelines and code provisions commonly applied to the vibration design of timber floors, highlighting their limitations when applied to CLT floor systems. In the third section, the CCIP-016 framework for the VSA of floors is discussed separately, as it forms the basis for the methodology adopted in this dissertation. The final section reviews the latest research trends related to vibration behaviour of CLT floors. Together, these sections form the basis for identifying the key knowledge gaps addressed in the subsequent chapters of this dissertation.

2.1 Fundamental principles in the vibration analysis of CLT floors

As outlined in Introduction, walking represents the most common form of human activity, and all major guidelines utilise pedestrian-induced load as the governing load case scenario for VSA of floors (Section 2.1.1). The floor structure itself acts as a vibration path, i.e. medium for transmitting vibrations from the source to the receiver (Section 2.1.2). The criteria for floor vibration serviceability are defined according to the vibration receiver, i.e. a human occupant or equipment that may be disturbed by excessive vibration levels (Section 2.1.3).

2.1.1 Walking force as vibration source

A walking pedestrian generates a dynamic contact force between the feet and supporting structure. This force, commonly referred to as ground reaction force, consists of three orthogonal components - vertical, longitudinal and lateral [43]. Among them, the vertical component has by far the largest magnitude and is therefore regarded as only relevant in vibration analysis of floor structures. Hence, in the remainder of this dissertation, the terms walking force, walking load and pedestrian-induced force/load will refer to the vertical component of the ground reac-

tion force. An example of one continuously measured walking force is presented in Figure 2.1a. As person walks, the left and right foot alternately contact the ground. The supporting foot generates essentially the entire force, while the opposite foot is in the air. During the short double-support phase, both feet are in contact with the ground and contribute to the total force [20]. This repeating left-right stepping pattern results in a near-periodic, narrow-band force, characterised by distinctive peaks in the amplitude spectrum centered at the pedestrian's walking frequency and its integer multiples, i.e. harmonics (Figure 2.1b). Due to the non-perfect periodicity of the step cycle, energy spread around these frequencies is observed.

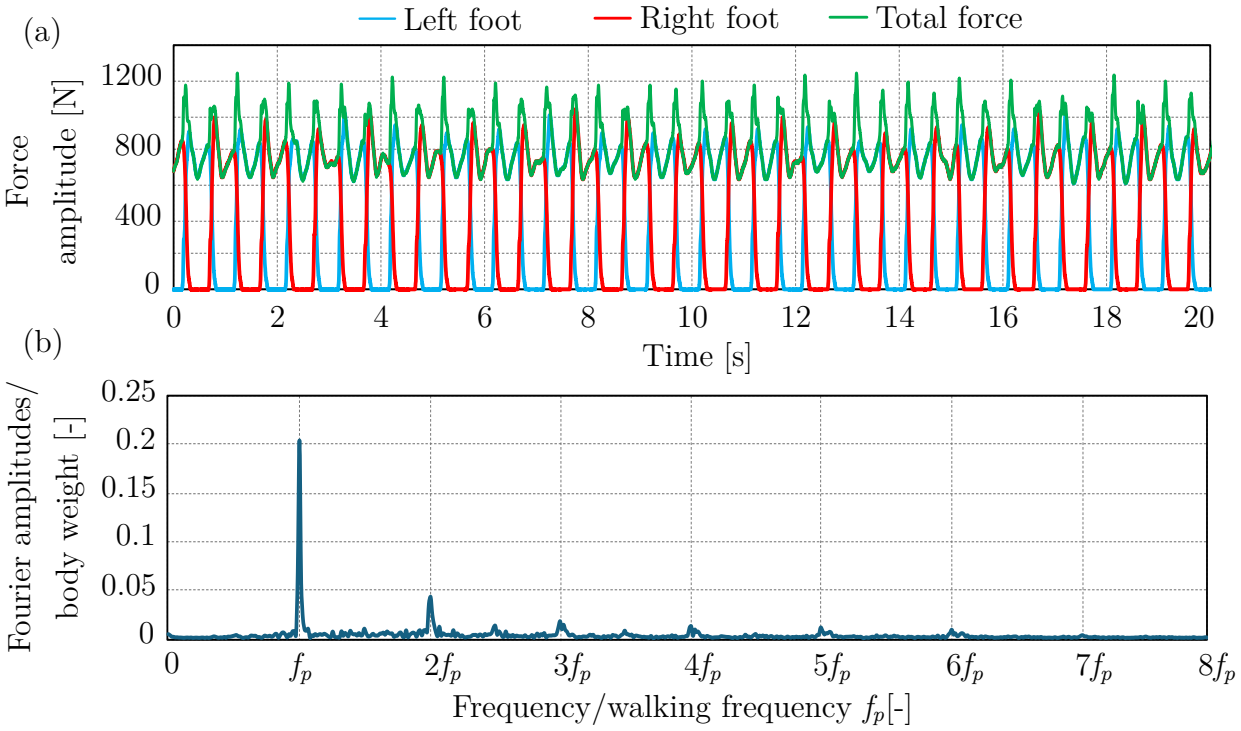

Figure 2.1: An example of continuously measured vertical component of walking force (a) and the corresponding Fourier amplitudes (b) [40].

A floor's response to walking excitation depends on the relationship between the walking force, i.e. its frequency spectrum, and the floor's modal properties. In this context, measured pedestrian-induced vibrations of floors have revealed two characteristic types of dynamic response: resonant and transient. The resonant response typically occurs when the pedestrian's walking frequency, or one of its harmonics, matches the natural frequency of one or more vibration modes of the floor. In such cases, the energy input from each step accumulates, causing the vibration amplitude to grow progressively over time (Figure 2.2a). Floor's response also depends on the amplitude of walking force component at the frequency of the relevant harmonic. If the floor's fundamental frequency lies far above the walking frequency range, this amplitude is small (higher harmonics in Figure 2.1b), therefore walking force component carries very little energy. Consequently, resonant build-up cannot develop even if the frequencies match, due to floor's damping. In this case, a transient response occurs, characterised by a high amplitude peak generated by each step, followed by a rapid decay before the next step (Figure 2.2b).

Wyatt [44] was the first to distinguish floors according the type of the response they are likely to exhibit. He established this classification based on floors fundamental frequency. So-called *low-frequency floors* (LFFs) are considered prone to resonant response (Figure 2.2a), whereas *high-frequency floors* (HFFs) generally exhibit a transient response (Figure 2.2b). According to Wyatt [44], a floor is considered LFF if its fundamental frequency is less than three times

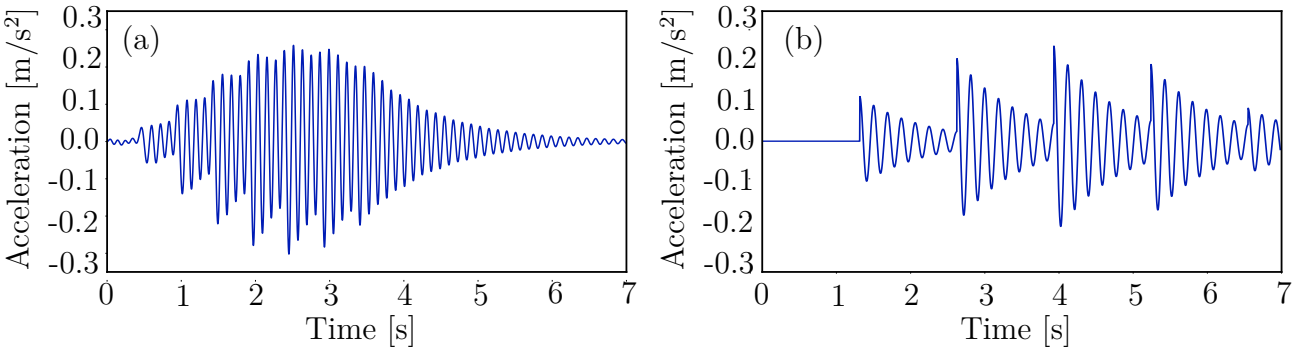

Figure 2.2: Resonant (a) and transient (b) response types.

the walking frequency. In contrast, floors whose fundamental frequency exceeds this value are classified as HFF. The definition of the cut-off frequency separating LFFs and HFFs varies across different guidelines. Nowadays, the most commonly adopted limit is the fourth harmonic of walking frequency, as it is generally accepted that, above this level, walking force harmonic does not have sufficient energy to induce resonance [45]. As normal human walking frequency falls within relatively narrow range, typically between 1.5 and 2.5Hz, this corresponds to a threshold of approximately 10Hz.

The fundamental difference between the resonant and transient vibration responses has led to developing two conceptually distinct walking force models, each tailored to the design requirements of LFFs and HFFs. This need for two force models simply reflect the fact that no single model is currently capable to describe the complete amplitude spectrum of walking force. The force model capable of reproducing resonant response is generally assumed to be perfectly periodic [43], and can therefore be expressed in the form of a Fourier series:

$$F_p(t) = \mathrm{G}\left(1 + \sum_{i=1}^{n} \mathrm{DLF}_i \sin\left(2\pi i f_p t - \varphi_i\right)\right) \tag{2.1}$$

where G is pedestrian's weight, f_p is walking frequency, DLF_i is Fourier coefficient of the ith harmonic, also known as dynamic load factor, φ_i is phase angle of ith harmonic, i is the harmonic number and n is the total number of contributing harmonics. The main challenge of this model lies in determining appropriate DLFs and selecting a sufficient number of harmonics to adequately represent both the dynamic force and dynamic response of the structure.

Early studies introduced force models comprising only the first harmonic [46]. Such an approach was reasonable, given that the research was primarily focused on pedestrian bridges, whose fundamental frequencies typically fall within the range of pedestrian walking frequencies. Following models [47] included more harmonics with the constant DLFs and independent of walking frequency. A major step forward was made by Rainer, Pernica and Allen in 1988 [48], who measured the vertical component of dynamic force generated by test subjects walking at frequencies ranging from 1Hz to 3Hz. They proposed a force model comprising four harmonics, with DLFs defined as functions of the pedestrian walking frequency. However, their study was based on a limited experimental dataset, involving only three test subjects and a small number of tests. When working on his doctoral dissertation, Kerr [49] conducted comprehensive experimental measurements of vertical component of pedestrian-induced dynamic forces, involving more then 40 test subjects walking at frequencies in the range $1 - 3$Hz, resulting in over 1000 recorded force signals. A clear positive correlation was observed between the walking frequency and the first DLF, with the mean trend of DLF_1 increasing with walking frequency and being well described by a third-order polynomial (Figure 2.3). This trend is consistent with the find-

ings reported by Rainer et al. [48]. On the other hand, there was no correlation between the walking frequency and DLFs of the second, third and fourth harmonic. A large scatter in the measured DLF_2, DLF_3 and DLF_4 was observed (Figure 2.3), highlighting an extremely high degree of variability in the forces generated by different pedestrians. Consequently, they are modelled as constants, represented by their mean values. The amplitudes of higher harmonics were difficult to identify in the experimental data, due to both limited precision of measurements and their low magnitudes, which make them hard to distinguish from the measurement noise. Apart from establishing the correlation between the walking frequency and the DLFs, Kerr [49] did not investigate whether the correlation exist among DLFs themselves, e.g. if DLFs 2-4 could be determined directly from the value of DLF_1. Based on several databases of recorded force signals, Willford, Young and Field [50] proposed a force model comprising four harmonics, in which each DLF is expressed as a linear function of the pedestrian walking frequency. The DLFs calculated in this manner have a 25% probability of being exceeded. This represents the first systematic attempt to account for the stochastic nature of human walking, i.e. inter-subject variability. This model was developed in-house by Arup Consulting and it has been incorporated into CCIP-016 design guide [41]. At present, it remains the best most widely adopted commercially available harmonic force model.

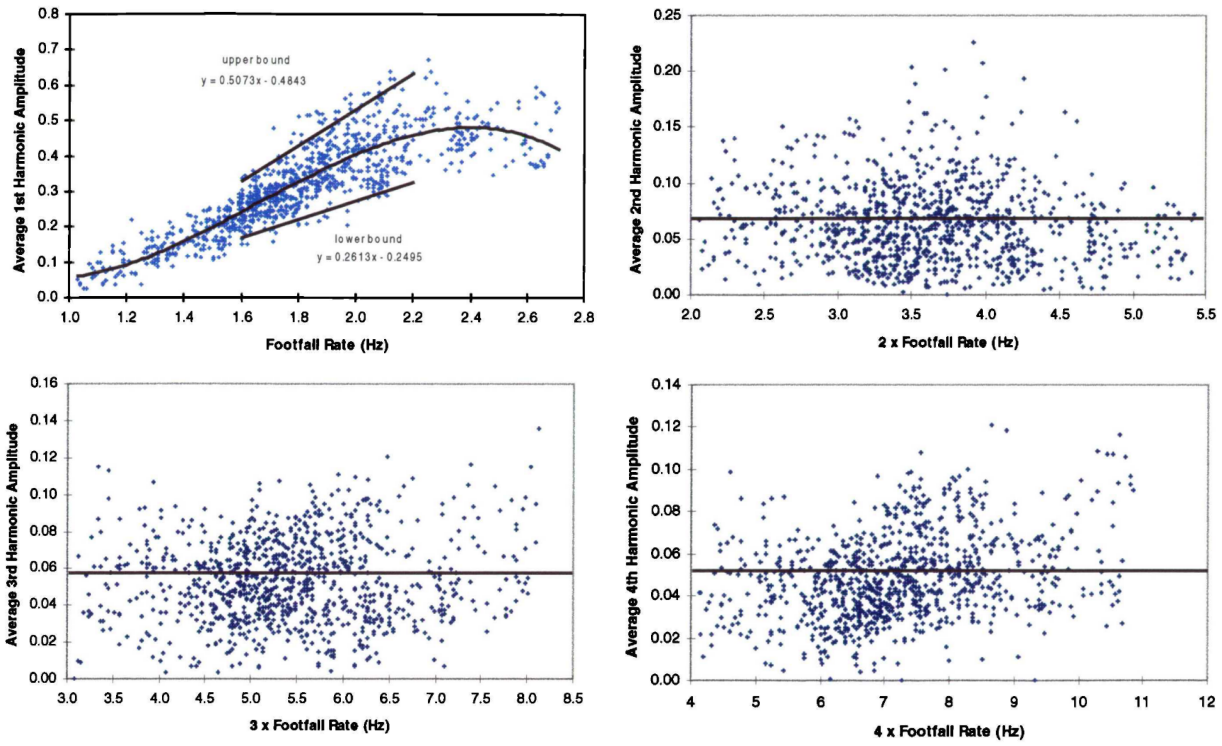

Figure 2.3: DLFs of walking force for the first four harmonics (after Kerr [49]).

The transient response is most effectively represented by modelling footfall as an equivalent impulse. The method first published by the Concrete Society [51] and later incorporated into CCIP-016 design guide [41] relies on calculating the floor's response to so-called *effective impulse*, derived from a database of measured footfall signals [49]. It has been proved as the most accurate method up to date [45, 50].

With the use of more precise equipment for measuring dynamic forces and structural responses, it has been observed that some floors exhibit significant vibration responses within frequency ranges both bellow and above 10Hz [27]. Furthermore, resonant response can occur at frequencies above this threshold and higher modes of LFFs may be impulsively excited that can dominate local response [52]. In such cases, neither harmonic nor impulse load model provides

reliable prediction of the actual response. Developing a unified force model that accounts for the complete frequency content of walking forces, and therefore is able to reproduce both response types, would eliminate the current distinction between LFFs and HFFs and reduce the likelihood of errors in the predicted response [40]. Having this in mind, Živanović and Pavić [27] combined their earlier harmonic force model [53] with the effective impulse approach [41, 51]. The resulting model applies to both LFFs and HFFs. Additionally, it accounts for inter-subject variability in the walking force. However, Middleton [52] showed that inter-subject variability plays a relatively minor role compared to step-to-step variations in walking frequency and ignoring this variation can lead to response overestimation by up to 40% for HFFs.

A main challenge in developing a simple load model suitable for routine design procedure of both LFFs and HFFs is the extremely high intra- and inter-subject variability of the forces generated by pedestrians. To illustrate inter-subject variability, Table 2.1 summarises the mean values and standard deviations of pedestrian walking frequencies compiled by Racic, Pavić and Brownjohn [20], from various measurement campaigns reported in the literature. All studies consistently indicate that walking frequency follows a normal distribution, with mean values typically ranging between 1.8 and 2.0Hz. These findings are in agreement with the measurement conducted later by Racic and Brownjohn [40], who reported mean walking frequencies in range $1.88 - 1.98$Hz.

Table 2.1: Statistical properties of human walking frequency

Source	**Mean value** [Hz]	**St. dev.** [Hz]	**Note**
Y. Matsumoto, T. Nishioka, H. Shiojiri, K. Matsuzaki [54]; Y. Matsumoto [55]	1.99	0.173	Sample of 505 people free walking
S. Živanović, A. Pavić, P. Reynolds [53]	1.87	0.186	1976 people crossing bridge in Podgorica
S.C. Kerr, N.W.M. Bishop [56]	1.90	–	
A. Pachi, T. Ji [57]	1.80	0.110	Over 800 measurements, 100 men and 100 women walking across 2
	2.00	0.130	bridges and inside 2 shopping malls
C. Sahnaci, M. Kasperski [58]	1.92	0.134	227 people, 38 women and 189 men walking on 16m long platform

Variability in dynamic load may be incorporated into the force model and response calculation through a probabilistic framework. Živanović, Pavić and Reynolds [53] included inter-subject variability by modelling the walking frequency and step length as independent, normally distributed random variables, with mean values of 1.87Hz and 0.71m, respectively, and coefficient of variation (COV) of 10%. Mean values and standard deviations of the DLFs for the five harmonics were determined from measurements reported in [49, 59]. Besides five (main) harmonics, this force model comprises five subharmonics. Subharmonics appear as peaks between the main harmonics in the frequency spectrum and arise from differences in forces generated by left and right foot. Mean DLF values for subharmonics were calculated from dynamic force signals collected by [59] and expressed as functions of DLF_1. Chen, Ding and Živanović [60] proposed a stochastic model representing one walking stride, consisting of two consecutive steps made by left and right foot, i.e single footfall trace model. To reproduce the characteristic "M"-shaped form of the walking stride, the authors used eight harmonics. The pedestrian's weight

and walking frequency were treated as random variables [53], while the mean values of DLFs were expressed as functions of walking frequency. Inter- and intra-subject variability were taken into account by multiplying the DLFs by two dimensionless coefficients. Both coefficients were assumed normally distributed with mean of 1, while standard deviations were derived from a comprehensive database of 4841 recorded walking strides.

Magdaleno et al. [61] developed a stochastic data-driven model in which the vertical ground reaction forces generated by the left and right feet were modelled separately as characteristic "M"-shaped footfall waveforms. Variability in the footfall shape was described using correlated normally distributed force ordinates, while step duration and double-support time were introduced as additional random variables. Their statistical properties were derived from a database comprising a total of 481 footfalls recorded at four prescribed pacing rates: 110, 120, 130 and 140 steps per minute, corresponding to 1.82, 1.99, 2.15 and 2.32Hz, respectively. However, the database contains measurements from only one test subject and therefore characterises intra-subject variability only. In addition, the subject walked at four prescribed pacing rates rather than at a freely selected pace, limiting the applicability of the resulting models to these four walking frequencies. Finally, the total walking force was reconstructed from separately measured left- and right-foot insole signals and therefore depends on accurate synchronisation between the two measurement systems.

In addition to time-domain models, in the early 1980s Ohlsson [62] introduced a then novel concept for the mathematical modelling of walking forces by analysing their auto-spectral density and treating the excitation as a stationary random process. He addressed the frequency content in the range $6 - 50$Hz, while Eriksson [63] extended this approach to frequencies below 6Hz. Based on continuously measured walking forces, Eriksson [63] demonstrated that the excitation energy is not concentrated exclusively at discrete frequencies corresponding to the force harmonics, but is instead spread over finite frequency bands around them, i.e. the harmonic peaks exhibit a certain width in the spectrum. This provided clear evidence that walking excitation is a narrow-band random rather than a perfectly periodic process. Brownjohn et al. [59] further reported that this energy spread becomes more prominent for higher harmonics, indicating their greater randomness. Subsequent studies have further developed power-spectral-density-based models of pedestrian loading and implemented them within random vibration analyses of floors and footbridges [64–68]. Despite these developments, the Fourier-series representation remains widely used for modelling walking loads because it provides a direct physical description of the dominant harmonic components of the walking force. Its parametric form also enables the variability of the quantities governing individual harmonics to be introduced explicitly. For HFFs, effective impulses provide a more practical representation of the transient response than a detailed spectral description of the walking force.

2.1.2 CLT floor as vibration path

Timber is an orthotropic material with three principal material axes (longitudinal - L, radial - R and tangential - T). Explicit formulas based on isotropic plate representation cannot reliably provide natural frequencies of CLT floors apart from the fundamental [69]. Consequently, in engineering practice, CLT floor modal properties are obtained using the FE method. A FE model that is sufficiently simple, yet provides an accurate description of reality is essential for a reliable VSA. In most engineering applications, it is sufficiently accurate to model CLT structures using two-dimensional (2D) FEs based on simple equivalent single-layer theories [70].

Given that the CLT panel is significantly stiffer in the major than the minor direction, CLT floors behave as one-way plates under static loading, regardless of the floor width-to-span ratio. Consequently, the design of CLT floors for static loads is typically based on the analysis of a 1m-wide strip, while the minor direction is neglected. However, in dynamic analysis, the floor width and the boundary conditions in the minor direction become extremely important. They not only affect natural frequencies but significantly alter the floor mode shapes, which, in turn, directly influence the pedestrian-induced modal forces in vibration response calculations. Changing the boundary conditions of a CLT floor from simply supported on two opposite edges (SFSF) to simply supported on all four edges (SSSS) can increase its fundamental frequency anywhere between 13 and 200%, depending on the floor width [71]. Similar trend was observed for the higher natural frequencies as well. Supporting the CLT floor on timber instead of steel beams resulted in $5-11\%$ lower natural frequencies, whereas clamping the edges increased the frequencies by up to 25% [71–74]. On the other hand, perfectly simply supported boundary conditions are rarely achieved in reality, particularly when floors are supported by walls. Jarnerö, Brandt and Olsson [75] demonstrated that adding storeys and increasing load on the walls enhances the degree of clamping between the floor and the wall. Furthermore, Zhang et al. [76] proposed an analytical formula for calculating the fundamental frequency of a CLT floor elastically clamped into a wall. Later, they extended their research by analysing the influence of various parameters on clamping degree and its effect on vibration serviceability of mass timber floor systems [77, 78]. In addition to the boundary conditions along the floor perimeter, Lago and Doudak [79] showed that even intermediate non-bearing supports can substantially modify the modal properties of CLT floors. Depending on the support location and screw spacing, increases of $45-224\%$ in fundamental frequencies were reported.

Inter-panel connections, which are a distinctive feature of CLT floors, exhibit considerably lower bending stiffness than adjacent panels, typically between 1% and 6% of the panel stiffness [80, 81]. Consequently, a multi-panel CLT floor possesses lower overall stiffness than a corresponding monolithic floor of the same dimensions. Current research [69, 71, 79, 82–84] distinguish three approaches to modelling inter-panel connections: (i) a series of springs with translation stiffness in three orthogonal directions, (ii) a series of rotational springs with translation stiffness equal to that of the CLT panel, and (iii) an equivalent elastic strip, rigidly connected to the adjacent panels. Macpherson et al.[84] proposed an analytical expression for calculating rotational stiffness of half-lapped joint connection based on a rigid rectangle model with four linear springs. Nevertheless, this expression was validated using deflections of beam elements, where the measured displacements are substantially larger than those potentially induced by people walking on real long-span floors. Furthermore, connection models comprising a series of translation or rotational springs are not viable solution for routine engineering applications, as their implementation depends on the type of commercial software used for structural modelling and analysis. Paolini et al.[83] introduced an equivalent elastic strip to represent the single-surface spline connection, with strip properties derived by matching displacement and rotation of the real and modelled connection. However, the model was verified only against experimentally measured natural frequencies of short-span floor-wall structure. Although this model is straightforward and easy to implement in any commercial software, the stiffness properties of the elastic strip relevant to VSA of long-span floors have not yet been established.

Additional floor layers, partition walls and additional mass from furniture are often overlooked in the VSA of CLT floor. These non-structural elements undoubtedly influence modal properties and vibration response of CLT floors, and their effect can be either beneficial or detrimental [75, 82, 85–88]. However, existing design guidelines are generally unclear in providing recommendation on how such effects should be accounted for.

2.1.3 Vibration receiver

ISO 10137 [89] distinguishes three types of vibration receivers: human occupants, building contents and building structures. When the receiver is the building structure, excessive vibration may cause minor damage to structural and non-structural elements. As structural damage does not fall within domain of vibration serviceability, the building structure as receiver is out of the scope of this dissertation. If the receiver is the building contents, the vibration levels should be limited to ensure the proper functioning of sensitive equipment. The upper limit is normally defined by manufacturers of such equipment. Finally, when humans are the receiver, excessive vibration levels can adversely affect their comfort, life quality and working efficiency.

The acceptable vibration level for human occupants depends on their environment and activity. Base curves representing vibration magnitudes that cause approximately equal human reaction in different environment were defined in BS 6472:1992 [90]. Vibration levels above the base curve increases the likelihood of adverse comments, whereas complaints are uncommon when vibration magnitudes remain below the base curve. As a measure of vibration level, BS 6472:1992 [90] introduced so-called *response* factor (or R factor), which represents the estimated dynamic response normalised by the perception threshold of an average healthy person. Figure 2.4 presents an example of the correlation between the R factor and the root-mean-square (rms) vertical acceleration, illustrating that humans are most sensitive to vibrations in the frequency range of $4 - 8$Hz, where perception threshold is approximately 0.005m/s^2. This perception threshold is inherently subjective, varying with individual sensitivity, physical condition, activity and environment. However, quantitative data describing this variability do not exist and R factors defined in [90] remain the best-known and most widely used indicators for assessing human perception of floor vibrations.

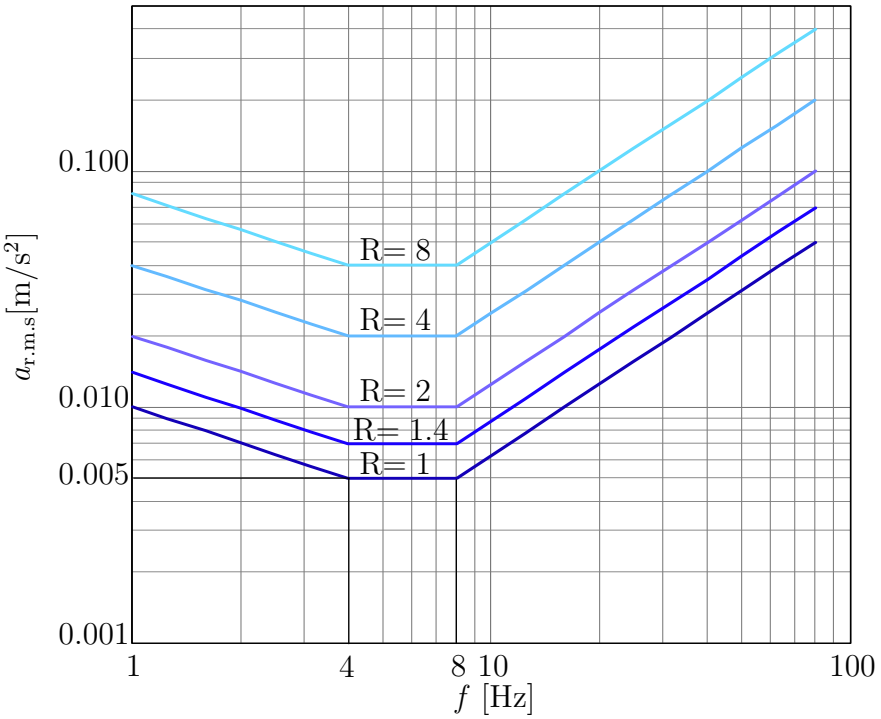

Figure 2.4: Correlation between the R factor and root-mean-square vertical acceleration in the frequency range $1 - 100$Hz, after [90].

2.1.4 Human-structure interaction

Although the pedestrian load, walking path and vibration receiver have been considered separately in the preceding subsections, they are all components of the same dynamic system. It is now widely known that the pedestrian and structure may interact dynamically, giving rise to the phenomenon known as *human-structure interaction* (HSI) [43]. HSI generally manifests in two ways. First, the presence and motion of a human can alter the modal properties of the structure. The most commonly reported effect is typically an increase in damping of the coupled human-structure system compared with that of the empty structure [91]. Second, structural vibrations can affect pedestrian gait and consequently modify the generated walking forces through changes in pacing rate, balance or synchronisation with the motion of the structure [92].

Although these interaction mechanisms are well recognised, their accurate representation remains challenging. Human dynamic properties vary considerably with factors such as posture, gait and walking frequency, while the influence of structural motion on pedestrian forces is still not fully understood. HSI is therefore commonly represented by modelling the human body as a spring-mass-damper system or as a rigid bipedal system with controlled step frequency [93].

The significance of HSI associated with changes in structural modal properties generally decreases as the pedestrian-to-structure mass ratio decreases. Therefore, such effects are of particular concern for lightweight and flexible floors, including timber and CLT floors. For the full-scale floors analysed in this dissertation, however, the pedestrian-to-structure mass ratio is relatively low, suggesting that these effects are less pronounced than in very lightweight floor systems. In addition, vibration levels measured during the Substrate4CLT research project were sufficiently low that no noticeable influence on pedestrian gait was observed. Accordingly, HSI is not explicitly considered in this dissertation, and pedestrian loading is assumed to act independently of the structural response.

2.2 Design guidelines for VSA of CLT floors

For a long period in the absence of more specific guidelines, design of CLT floors in Europe has been governed by Eurocode 5 (EC5) [94], which was primarily developed for traditional timber joist floors. With respect to VSA of floors, EC5 limits the fundamental frequency to 8Hz. This limit is effectively equivalent to the commonly adopted boundary of 10Hz separating LFFs and HFFs, implying that EC5 implicitly promotes floor designs with fundamental frequencies in the HFF range. As a result, pedestrian-induced vibrations are expected to be predominantly transient rather than resonant. If the fundamental frequency exceeds 8Hz, VSA is based on calculating static deflection under a 1kN point load and vibration velocity resulting from a unit impulse, considering only the fundamental mode of vibration. Swedish CLT handbook [95] adopts the same methodology for VSA as EC5, with minor adaptation for CLT floors. On the other hand, Canadian CLT handbook [96] states that CLT floors are heavier and exhibit lower damping compared to traditional timber joist floors. Therefore, recommendations and guidelines developed for the VSA of joist floors are not directly applicable to CLT floors. According to this handbook, the criterion for VSA is defined through the so-called vibration-control span limit. In other words, if the floor span is shorter than this limit, the vibration levels are considered acceptable. However, this criterion merely represent another attempt to increase floor stiffness sufficiently to avoid resonant vibrations.

Contemporary literature considers resonance-avoidance approach outdated and overly conservative for two main reasons. First, studies [34] have shown that resonant vibrations can occur at frequencies up to 14Hz. Increasing floor stiffness to ensure that the fundamental frequency exceeds this value may lead to overdesign and excessive material use, contradicting the fundamental principles of sustainable engineering. Second, and more importantly, even if resonant vibrations occur, they do not necessarily lead to unacceptable vibration responses. This was demonstrated by Hamm, Richter and Winter [97], who were the first to recommend allowing limited resonance in the vibrations of timber structures. After a comprehensive experimental testing campaign conducted on more than 100 real timber floors, they critically evaluated the EC5 guidelines and suggested allowing resonant vibrations, provided that the resulting acceleration magnitudes remain controlled and limited. Alongside [97], Abeysekera et al.[98] and Schirén et al.[99] are among the main proponents of the so-called *vibration performance* approach for VSA of timber floors. This approach evaluates whether floor is fit for use based on its predicted, not necessarily resonant, response and it has been employed in guidelines for VSA of concrete and steel-concrete composite floors since 1989 [41, 44, 51, 100]. Among these publications, the most comprehensive and widely adopted is the Concrete Centre Design Guide CCIP-016 [41], developed by the Concrete Society [51]. Although originally published for concrete structures, it is founded on fundamental principles of dynamics and can therefore be applied to floors made of any material, including timber [101]. The CCIP-016 design guideline is already an integral part of the latest American Mass Timber design guide [102] and will be incorporated into the next generation of EC5.

This dissertation adopts the CCIP-016 framework for the VSA of CLT floors and further develops its proposed load models for both LFFs and HFFs. Therefore, the framework is briefly outlined in the following section to provide the necessary background for the analyses presented in the subsequent chapters.

2.3 CCIP-016 framework for VSA of the floors

In CCIP-016, the boundary between low- and high-frequency floors is approximately 10Hz. This limit follows from the adopted four-harmonic walking force model and the maximum walking frequency of 2.5Hz, giving the highest excitation frequency of 10Hz. Floors with a fundamental frequency above this value are assessed using the effective impulse approach. For floors with a fundamental frequency close to this 10Hz boundary, both resonant and transient responses should be evaluated and compared.

2.3.1 Low-frequency floors

All modes with natural frequencies up to 15Hz may contribute significantly to the response and should therefore be included. The response of each relevant mode to each of four force harmonic must be calculated and subsequently combined, as presented in Algorithm 1.

Modal properties, including the natural frequency f_n, modal mass m_n, damping ratio ζ_n and mode shape, for all modes (n) with frequency up to 15Hz should be identified. They may all be obtained using simplified expressions or FE analysis, except for the damping ratios, which should be determined experimentally or adopted based on previous experience or recommendations provided in relevant guidelines. CCIP-016 assumes that the pedestrian force is stationary

Algorithm 1 Algorithm for VSA of LFF according to CCIP-016 [41].

Find all modes with $f_n < 15\text{Hz}$
For each mode determine $f_n, m_n, \zeta_n, \mu_{e,n}, \mu_{r,n}$
Select f_p
for $h = 1$ to 4 **do**
    $f_h = h \cdot f_p$
    Calculate DLF_h at f_h according to Table 2.2
    Calculate $F_h = \text{DLF}_h \cdot \text{G}$
    for $n = 1$ to maximum included n **do**
        Calculate $A_n = 1 - \left(\frac{f_h}{f_n}\right)^2$
        Calculate $B_n = 2\zeta_n \frac{f_h}{f_n}$
        Calculate $\rho_{h,n} = 1 - e^{-2\pi\zeta_n N_{\text{step}}}$, where $N_{\text{step}} = 0.55h\frac{L}{l_{\text{step}}}$
        Calculate real component $\text{Re}\, a_{h,n} = \left(\frac{f_h}{f_n}\right)^2 \cdot \frac{F_h \mu_{r,n}\mu_{e,n}\rho_{h,n}}{m_n} \cdot \frac{A_n}{A_n^2 + B_n^2}$
        Calculate imaginary component $\text{Im}\, a_{h,n} = \left(\frac{f_h}{f_n}\right)^2 \cdot \frac{F_h \mu_{r,n}\mu_{e,n}\rho_{h,n}}{m_n} \cdot \frac{B_n}{A_n^2 + B_n^2}$
    end for
    Sum the real components in all modes: $\text{Re}\, a_h = \sum_n \text{Re}\, a_{h,n}$
    Sum the imaginary components in all modes: $\text{Im}\, a_h = \sum_n \text{Im}\, a_{h,n}$
    Find the magnitude of the acceleration $|a_h| = \sqrt{(\text{Re}\, a_h)^2 + (\text{Im}\, a_h)^2}$
    Calculate baseline peak acceleration for $R = 1$, $a_{R=1,h}$:
    if $f_h < 4\text{Hz}$ **then**
        $a_{R=1,h} = \frac{0.0141}{\sqrt{f_h}} \text{m/s}^2$
    else if $4\text{Hz} < f_h < 8\text{Hz}$ **then**
        $a_{R=1,h} = 0.0071 \text{m/s}^2$
    else
        $a_{R=1,h} = 2.82\pi f_h \cdot 10^{-4} \text{m/s}^2$
    end if
    Calculate response factor for this harmonic $R_h = \frac{|a_h|}{a_{R=1,h}}$
end for
Calculate the total response factor $R = \sqrt{R_1^2 + R_2^2 + R_3^2 + R_4^2}$

and applied at the most adverse location on the floor. Therefore, the mode shape amplitudes at both the excitation point $\mu_{e,n}$, and the receiver location $\mu_{r,n}$ are required. The walking frequency f_p is selected within the realistic range of $1.5 - 2.5\text{Hz}$ such that one of its harmonics coincides with the natural frequency of a relevant (usually the first) mode and induces resonance.

For each of the four harmonics h with harmonic frequency $f_h = hf_p$, the DLF_h is determined according to Table 2.2. CCIP-016 provides both mean and design values of the DLFs, which correspond to a probability of exceedance of approximately 25% [50]. The force amplitude F_h is obtained by multiplying DLF_h by the pedestrian weight G. The theoretical steady-state acceleration $a_{h,n}$ of each mode n to each force harmonic h is calculated using the complex formulation of the standard dynamic magnification factor (DMF) for steady-state response:

$$a_{h,n} = \left(\frac{f_h}{f_n}\right)^2 \cdot \frac{F_h \mu_{r,n} \mu_{e,n}}{m_n} \cdot \mathrm{DMF}_{h,n} \tag{2.2}$$

where

$$\mathrm{DMF}_{h,n} = \frac{1}{\left[1 - \left(\frac{f_h}{f_n}\right)^2\right] + i\left[2\zeta_n \frac{f_h}{f_n}\right]} \tag{2.3}$$

and $i = \sqrt{-1}$.

Table 2.2: Mean and design values, and COVs of DLFs for four harmonics according to CCIP-016 [41].

h	$\mathbf{f_h}$[Hz]	$\mathbf{DLF_{mean}}$	**COV**	$\mathbf{DLF_{design}}$
1	$1 - 2.8$	$0.37(f_h - 0.95) \leq 0.5$	0.17	$0.41(f_h - 0.95) \leq 0.56$
2	$2 - 5.6$	$0.054 + 0.0044 f_h$	0.40	$0.069 + 0.0056 f_h$
3	$3 - 8.4$	$0.026 + 0.0050 f_h$	0.40	$0.033 + 0.0064 f_h$
4	$4 - 11.2$	$0.010 + 0.0051 f_h$	0.40	$0.013 + 0.0065 f_h$

Two factors may prevent the theoretical steady-state response from being fully developed. First, the pedestrian moves across the floor, so successive footfalls are applied at different positions and do not continuously excite the most critical point of the mode shape. Second, particularly for lightly damped structures, the number of loading cycles during a single crossing may be insufficient for the resonant response to reach its steady-state value. To account for these effects, the DMF is scaled by a reduction factor ρ, defined as:

$$\rho_{h,n} = 1 - e^{-2\pi\zeta_n N_{\mathrm{step}}}, \qquad N_{\mathrm{step}} = 0.55h\frac{L}{l_{\mathrm{step}}} \tag{2.4}$$

where L is the floor span and l_{step} is the step length.

For each harmonic, the total response at the receiver location is obtained by combining the contributions of all relevant modes. Since the modal responses generally differ in phase, their amplitudes cannot be added directly. Instead, the real and imaginary components of the complex response are summed separately over all modes. The magnitude of the resulting response is then calculated as the square root of the sum of the squares (SRSS) of the total real and imaginary components:

$$|a_h| = \sqrt{\left(\sum_n \mathrm{Re}\, a_{h,n}\right)^2 + \left(\sum_n \mathrm{Im}\, a_{h,n}\right)^2} \tag{2.5}$$

The response factor R_h is calculated separately for each harmonic. First, the baseline peak acceleration corresponding to R=1 is determined at the harmonic frequency f_h. This baseline value is obtained from the frequency-dependent base curve specified in [90], which represents the approximate threshold of vibration perception for an average healthy person. The R factor for each harmonic is then calculated as the ratio of the predicted peak acceleration to the corresponding baseline acceleration. Finally, the contributions of all harmonics are combined using the SRSS method to obtain the total response factor:

$$R = \sqrt{\sum_h R_h^2} \tag{2.6}$$

which should be compared against the criteria given in [89].

2.3.2 High-frequency floors

The procedure presented in Algorithm 2 is applicable to structures with a fundamental vertical frequency above 4Hz. All modes n with natural frequencies below twice the fundamental vertical frequency should be included in the calculation. Therefore, modal properties f_n, m_n, ζ_n and mode shape for these modes should be determined. The procedure evaluates the velocity time history generated by a single footfall applied at a specified location on the floor. Accordingly, the mode shape amplitudes at the excitation point $\mu_{e,n}$ and at the receiver location $\mu_{r,n}$ are also required for each mode. The f_p should be selected as the highest value that can reasonably be expected for the considered structure and its intended use. For example, higher walking frequencies are generally anticipated in corridors than in office areas or residential rooms.

Algorithm 2 Algorithm for VSA of HFF according to CCIP-016 [41].

1: Find all modes with $f_n < 2 \cdot f_1$
2: Determine $f_n, m_n, \zeta_n, \mu_{e,n}, \mu_{r,n}$
3: Select f_p
4: **for** $n = 1$ to maximum included n **do**
5: Calculate $I_{\text{eff,n}}$ according to Eq. (2.8)
6: Calculate the peak velocity $v_{n,peak} = \mu_{e,n}\mu_{r,n}\dfrac{I_{\text{eff,n}}}{m_n}$
7: Calculate the velocity response $v_n(t) = v_{n,peak}e^{-2\pi\zeta_n f_n t}\sin(2\pi f_n t)$
8: **end for**
9: Sum the velocity responses in all modes: $v(t) = \sum_n v_n(t)$
10: Calculate a RMS response over the period of one footfall T: $v_{rms} = \sqrt{\dfrac{1}{T}\int_0^T v(t)^2 dt}$
11: Calculate baseline RMS velocity for $R = 1$, $v_{R=1}$:
12: **if** $f_1 < 8$Hz **then**
13: $v_{R=1} = \dfrac{5 \cdot 10^{-3}}{2\pi f_1}$m/s
14: **else**
15: $v_{R=1} = 1 \cdot 10^{-4}$m/s
16: **end if**
17: Calculate the response factor $R = \dfrac{v_{rms}}{v_{R=1}}$

For each mode n, the effective impulse is calculated from the selected walking frequency f_p and the corresponding natural frequency f_n. As in the case of the harmonic load model, CCIP-016 provides both mean (Eq. (2.7)) and design effective impulse values (Eq. (2.8)), with the latter corresponding to a probability of exceedance of approximately 25%:

$$\text{Mean} \quad I_{\text{eff,n}} = 42\frac{f_p^{1.43}}{f_n^{1.30}} \quad [\text{Ns}] \tag{2.7}$$

$$\text{Design} \quad I_{\text{eff,n}} = 54\frac{f_p^{1.43}}{f_n^{1.30}} \quad [\text{Ns}] \tag{2.8}$$

From this, peak velocity can be calculated as

$$v_{n,peak} = \mu_{e,n}\mu_{r,n}\frac{I_{\text{eff,n}}}{m_n} \tag{2.9}$$

and complete velocity time history as

$$v_n(t) = v_{n,peak}e^{-2\pi\zeta_n f_n t}\sin(2\pi f_n t) \tag{2.10}$$

The total response $v(t)$ is obtained by summing the velocity time histories of all relevant modes, after which a RMS velocity is calculated over one footfall period $T = 1/f_p$:

$$v_{rms} = \sqrt{\frac{1}{T}\int_0^T v(t)^2 dt} \tag{2.11}$$

The baseline RMS velocity corresponding to $R = 1$ is determined at the frequency f_p from the frequency-dependent base curve specified in [90]. Finally, R factor is determined as:

$$R = \frac{v_{rms}}{v_{R=1}} \tag{2.12}$$

and compared against the criteria given in [89].

2.4 Recent advances and research trends in CLT floor vibrations

Current body of literature suggests that uncertainty-based and probabilistic modelling approach has already emerged in the VSA of pedestrian bridges and various floor systems [103–108].

Regarding timber and CLT floors, there is only a limited body of research on influence of variability in structural properties on their modal properties and dynamic response. A majority of rare existing studies have focused on vibration behaviour in higher frequency range, typically associated with acoustic performance [109, 110]. In contrast, for lower frequency range relevant to pedestrian-induced vibrations, Lim et al. [111] reported a significant COV of 16.5% in the fundamental frequency of a traditional timber joist floor arising from variability in joists density. Similarly, Ge et al. [112] demonstrated that material variability could result in a timber joist floor with a mean fundamental frequency of 8.18Hz falling below the 8Hz requirement in approximately 30% of cases. Milojević et al. [113] employed MC simulation to evaluate the effects of uncertainty in four material parameters, namely timber density, longitudinal modulus of elasticity and two shear moduli, on the natural frequencies and modal masses of a CLT floor. A 10% COV in these parameters yielded natural frequency COVs of $6 - 7.5\%$. Modal masses exhibited a uniform COV of 10%, demonstrating that their uncertainty arises solely from variability in timber density. Nonetheless, the study considered only a single-panel CLT floor, neglecting high level of uncertainty in inter-panel connections.

Almost all studies on the pedestrian-induced vibration response of CLT floors have been based on deterministic calculations [71, 114, 115]. To date, the only study that evaluated the dynamic response of CLT floor using probabilistic approach is the work by Aloisio et al. [116], who employed a probabilistic model of pedestrian force proposed by Chen et al. [60]. Nevertheless, the structural parameters, such as timber material properties, inter-panel connections and boundary conditions, therefore the modal properties of CLT floor, were still modelled as deterministic.

3 Theoretical background of uncertainty analysis

This chapter aims to enable readers who are unfamiliar with uncertainty modelling concept to follow the rest of this dissertation. It explains why deterministic analyses are no longer sufficient for modern engineering problems and introduces the core elements of uncertainty analysis: representing variability (as random variables/field/processes), quantifying it (UQ) and identifying key input parameters (SA). Practical tools for uncertainty analysis are outlined and Sobol' indices and Shapley effect methods, used in the following study, are elaborated in more details. The special attention is given to the two global SA methods, Sobol' indices and Shapley effect, and their implementation. As MC simulation performed on high-fidelity FE models is usually computationally demanding, this chapter also introduces the concept of metamodeling and justifies the choice of PCE metamodel for this study. Technical and methodological details are provided only to the level needed for understanding later chapters.

Uncertainty encountered during numerical modelling can arise from various sources and is commonly categorised into aleatory and epistemic uncertainties [117]. Aleatory uncertainty refers to the inherent randomness of a system that cannot be reduced by acquiring additional information. A typical example is the natural variation in timber material properties resulting from differences in wood species, growth conditions and internal defects. Epistemic uncertainty, on the other hand, stems from limited knowledge, insufficient data and/or modelling simplification. Uncertainty in boundary conditions in FE models represents such a case. A key characteristic of epistemic uncertainty is that it can be reduced through improved measurements, additional experimental data and/or more detailed modelling. This dissertation focuses on aleatory uncertainties in modelling parameters of CLT floors and pedestrian-induced load. Epistemic uncertainties in the numerical model are reduced, though not fully eliminated, through validation against the experimental results in Section 5. Moreover, the use of an extensive database comprising 852 measured pedestrian force signals is assumed to minimise epistemic uncertainty related to load modelling.

Uncertainties can be represented mathematically using random variables, or, when variability changes over space and time, through random field and stochastic processes, respectively [118]. They are further propagated through the numerical model in order to quantify their influence on output of interest (e.g. vibration response). This process is known as uncertainty quantification (UQ). When a model contains a large number of uncertain parameters, sensitivity analysis (SA) is utilised in parallel to identify the most influential variables and to reduce model complexity by eliminating the insignificant parameters [119]. Together, UQ and SA form the foundation of

the uncertainty analysis framework, and their overviews are provided in Sections 3.1 and 3.2, respectively. Section 3.3 then outlines the metamodeling concept, commonly employed in uncertainty analysis, and presents the mathematical formulation of Polynomial Chaos Expansion (PCE) metamodel used in this dissertation.

3.1 Uncertainty quantification

Conventional deterministic modelling approach treats all input parameters as fixed values and does not take into account their natural variability. As a result, it provides only a single predicted output, offering no insight into possible range or likelihood of calculated outputs. Therefore, probabilistic methods play essential role in UQ, as they allow input variability to be represented explicitly. In engineering mechanics, probabilistic methods are generally divided into three categories, based on the output information they provide [120]. *Response variability methods* yield only the basic statistical measures of the output, such as mean value and variance. *Structural reliability methods* quantify the probability that output surpasses a predefined threshold, e.g. a failure criterion, while *stochastic finite element methods* (SFEMs) aim to describe the entire probability density function (PDF) of the predicted output. The SFEM is a powerful tool in computational stochastic mechanics that extends the traditional deterministic FE method by modelling uncertain parameters as random variables, fields or processes [35]. Within this dissertation, structural properties of CLT floor were modelled as random variables (Section 6), while the walking force was represented as stochastic process whose parameters were treated as random variables (Section 7).

To address the high computational demands of SFEM, cost-efficient surrogate models are used as alternatives to detailed FE models [121]. Although terms "surrogate model" and "metamodel" are often used interchangeably, they are not synonyms. A surrogate model refers broadly to any simplified approximation of a complex numerical model, whereas a metamodel is a specific type of a surrogate constructed using a defined mathematical or statistical modelling technique. In this dissertation, a PCE metamodel was adopted as the surrogate replacing the FE model of the CLT floor, which will be described in Section 5. The choice of a PCE metamodel was motivated by its well-established efficiency in uncertainty analysis [120], as further discussed in Section 3.3. Once the FE model was replaced by the PCE metamodel, UQ was carried out using the metamodel instead of SFEM. However, SFEM results were retained for validation purposes.

3.2 Sensitivity analysis

Generally, SA methods can be classified into two categories [120]: local and global. Local SA examines how a small perturbation in a single input parameter, taken around a specific reference point, affects the model output, while all other input parameters remain fixed. It is computationally inexpensive and can provide insight into the behaviour of the model in the vicinity of the reference point. However, its results depend on the chosen reference point and it cannot capture interactions between input variables or effects that occur across the full range of their variability. On the other hand, global SA evaluates the influence of each input parameter on the model output while all inputs vary simultaneously. It provides insight into the model behaviour across the entire input space and offers a more comprehensive and realistic

assessment of the output. Certain global SA methods are also capable of quantifying the effect of interaction between input parameters. However, this broader applicability comes at a higher computational cost, as global SA is typically more demanding than local SA and requires more advanced analytical or numerical techniques.

Global SA methods can be broadly classified into two categories [120]: regression-based and variance-based methods. Regression-based methods approximate the model output using a fitted (usually linear) regression model and then employ statistical indicators to quantify the influence of each input parameter on the output. Typical examples include the Pearson and Spearman rank correlation methods, which use correlation coefficients and standardised regression coefficients, respectively, as sensitivity measures [122]. The use of these coefficients provides a straightforward, interpretable measure of the linear (Person) or monotonic (Spearman) relationship between an input parameter and the output. However, because these methods rely on linear or monotonic dependence between input and output, they may not perform well for highly non-linear models. In addition, although they can handle limited interaction effects, more advanced variance-based methods are generally better suited for capturing complex interactions between input variables. In variance-based methods, the total variance of the model output is decomposed into contributions from individual input parameters and their interactions. These methods are conceptually related to analysis of variance (ANOVA) techniques, as they follow the same principle of partitioning the total variance into additive components. Compared with regression-based methods, their performance is not constrained by linear or monotonic relationship between inputs and the model output, making them suitable for highly non-linear systems. The Sobol' method [123] is the most widely adopted variance-based global SA technique. It quantifies the contribution of each input parameter and their interactions to the output variability using so-called Sobol' indices. However, Sobol' indices require the input parameters to be statistically independent. If variables are correlated, the results may become misleading, because correlated inputs tend to vary together and their shared influence (surface c in Figure 3.1b) is either double-counted or incorrectly assigned to a single variable. To overcome this challenge, the Shapley effect [124] has been introduced. It fairly distributes the shared contribution of correlated or interacting inputs among all variables involved. In other words, instead of ignoring correlations, the Shapley effect splits the combined influence of a group of inputs and assigns an appropriate portion to each individual input, providing an unbiased measure of their importance.

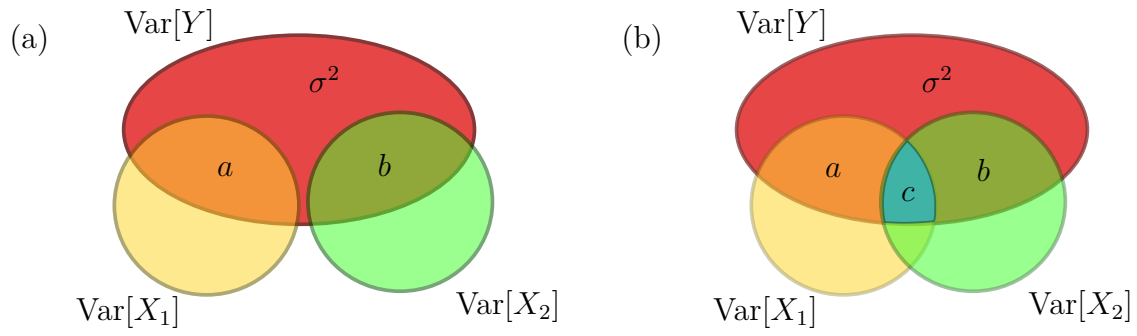

Figure 3.1: Illustration scheme of the effect of variance of two input variables, $\mathrm{Var}[X_1]$ and $\mathrm{Var}[X_2]$, on the variance of output $\mathrm{Var}[Y]$ when inputs are uncorrelated (a) and correlated (b).

All SA methods have their own domains of applicability, balancing computational efficiency and the level of insight they provide. Accordingly, this dissertation employed three different global SA approaches in three separate phases, selecting each method based on its suitability for the specific objective. At the early stage of the dissertation, during FEMU of the CLT floor

in the first phase, the Spearman rank correlation coefficient was employed as a screening tool to exclude timber material and connection properties that showed no meaningful relationship with the floor modal properties (Section 5.3.1). This step was intended only to identify and eliminate non-influential parameters, not to quantify their contribution to output variability. By reducing the number of parameters, the dimensionality of the FEMU problem was reduced, which in turn improved the efficiency and robustness of the FE model development. All input parameters representing the uncertain structural properties of CLT floor were assumed to be statistically independent. Consequently, a global SA based on Sobol' indices was carried out as a part of uncertainty analysis of the floor's modal properties in the second phase (Chapter 6). Once the input parameters associated with pedestrian-induced force were characterised (Chapter 7), it became evident that many of them were strongly correlated. Accordingly, the final uncertainty analysis of the vibration response in the fifth phase (Chapter 9) employed a global SA using the Shapley effect, which is suitable for handling correlated inputs. Following subsections present summaries of the Sobol' indices methods (Section 3.2.1) and Shapley effect (Sections 3.2.2) used throughout this dissertation. As the Spearman rank correlation coefficient is a standard, straightforward and widely understood method, its formulation is not detailed.

3.2.1 Sobol' indices method

A mathematical model with d input parameters gathered in an input vector $\mathbf{x}$ and a scalar output y is represented by:

$$y = f(\mathbf{x}), \quad \mathbf{x} \in K^d, \tag{3.1}$$

where the input parameters are defined on the d-dimensional unit cube K^d:

$$K^d = \Big\{\mathbf{x} : 0 \leq x_i \leq 1, \quad i = 1, ..., d\Big\}. \tag{3.2}$$

The Sobol' decomposition [123] of $f(\mathbf{x})$ into summands of increasing dimensions is defined as:

$$f(x_1, ..., x_d) = f_0 + \sum_{i=1}^{d} f_i(x_i) + \sum_{1 \leq i < j \leq d} f_{ij}(x_i, x_j) + ... + f_{1,2,...,d}(x_1, ..., x_d), \tag{3.3}$$

where f_0 is a constant. The integral of each summand in Eq.(3.3) over any of its independent variables is zero, i.e.:

$$\int_0^1 f_{i_1,...i_s}(x_{i_1}, ..., x_{i_s}) dx_{i_m} = 0, \quad \text{for} \quad 1 \leq m \leq s. \tag{3.4}$$

Consequently, all summands in Eq.(3.3) are orthogonal to each other:

$$\int_{K^d} f_{i_1,...i_s}(x_{i_1}, ..., x_{i_s}) \int_{K^d} f_{j_1,...j_s}(x_{j_1}, ..., x_{j_t}) d\mathbf{x} = 0 \quad \text{for} \quad \Big\{i_1, ..., i_s\Big\} \neq \Big\{j_1, ..., j_t\Big\}, \tag{3.5}$$

where $d\mathbf{x}$ stands for $dx_1, ..., dx_d$. Total number of summands in Eq.(3.3) is $2^d - 1$. Furthermore, from Eq.(3.4) it follows that the constant f_0 is the mean value of $f(\mathbf{x})$, i.e.:

$$f_0 = \int_{K^d} f(\mathbf{x}) d\mathbf{x}. \tag{3.6}$$

Sobol' [123] showed that decomposition in Eq.(3.3) is unique whenever $f(\mathbf{x})$ is integrable over K^d, and the terms in the decomposition can be obtained analytically. Univariate and bivariate terms read:

$$\begin{aligned} f_i(x_i) &= \int_{K^{d-1}} f(\mathbf{x}) d\mathbf{x}_{\sim i} - f_0 \\ f_{ij}(x_i, x_j) &= \int_{K^{d-2}} f(\mathbf{x}) d\mathbf{x}_{\sim ij} - f_i(x_i) - f_0 \end{aligned} \tag{3.7}$$

where symbol $\sim$ stands for "complementary of", so $\int_{K^{d-1}} d\mathbf{x}_{\sim i}$ and $\int_{K^{d-2}} d\mathbf{x}_{\sim ij}$ denote integration over all parameters except x_i, and x_i and x_j, respectively. Analogous expressions can be derived for higher order members as well.

If the input parameters $\mathbf{x} = \left\{x_1, ..., x_d\right\}$ are independent random variables $\mathbf{X} = \left\{X_1, ..., X_d\right\}$, characterised by joint PDF $\mathbf{G}_{\mathcal{K}}$, then the output $Y = f(\mathbf{X})$ is also a random variable. In that case, variance of the output D, often denoted as total variance, is defined as:

$$D = \mathrm{Var}[Y] = \int_{K^d} f^2(\mathbf{X}) d\mathbf{X} - f_0^2, \tag{3.8}$$

while partial variances are computed from each of terms in Eq.(3.3):

$$\begin{gathered} D_{i_1,...,i_s} = \int_{K^s} f^2_{i_1,...,i_s}(X_{i_1}, ..., X_{i_s}) dX_{i_1}, ..., X_{i_s}, \\ 1 \leq i_1 < ... < i_s \leq d, \quad s = 1, ..., d \end{gathered} \tag{3.9}$$

By squaring and integrating Eq.(3.3) over K^d and using Eq.(3.5), total variance D can be decomposed as follows:

$$D = \sum_{i=1}^{d} D_i + \sum_{1 \leq i < j \leq d} D_{ij} + ... + D_{1,2,...,d}. \tag{3.10}$$

A sensitivity measure, i.e. Sobol' sensitivity indices, can be defined as:

$$S_{i_1,...,i_s} = \frac{D_{i_1,...,i_s}}{D} \tag{3.11}$$

Each index $S_{i_1,...,i_s}$ quantifies the contribution of uncertainties in the set of input parameters $\left\{i_1, ..., i_s\right\}$ to the total variance. The first order sensitivity indices S_i account for the individual influence of each uncertain parameter X_i, while higher order indices account for possible interaction and combined effect of multiple parameters. To evaluate the total effect of an input parameter X_i (both the individual effect and interactions with other parameters), the total sensitivity indices S_{T_i} are defined as the sum of all indices $S_{i_1,...,i_s}$ involving parameter i:

$$S_{T_i} = \sum_{\mathfrak{I}_i} S_{i_1,...,i_s}, \quad \mathfrak{I}_\mathfrak{i} = \left\{(i_1, ..., i_s) : \exists m, 1 \leq m \leq s, i_m = i\right\}. \tag{3.12}$$

By their definition, Eq.(3.11), and according to Eq.(3.10), Sobol' indices satisfy:

$$\sum_{i=1}^{d} S_i + \sum_{1 \leq i < j \leq d} S_{ij} + ... + S_{1,2,...,d} = 1. \tag{3.13}$$

It can be easily shown that

$$S_{T_i} = 1 - S_{\sim i}, \tag{3.14}$$

where $S_{\sim i}$ is the sum of all indices excluding parameter i.

3.2.2 Shapley effect

In cooperative game theory, the Shapley value quantifies the "fair share" of each player in the total payoff of a game, i.e. in the outcome produced by the entire group of players [124, 125].

A d-player game with the set of players $\mathcal{K} = \{1, 2, ..., d\}$ is defined through a real-valued cost (or value) function:

$$c : 2^{\mathcal{K}} \to \mathbb{R}, \qquad c(\emptyset) = 0. \tag{3.15}$$

where $c(\mathcal{J})$ is the cost associated with the coalition of players $\mathcal{J} \subseteq \mathcal{K}$. The Shapley value of player i is defined as:

$$v_i = \sum_{\mathcal{J} \subseteq \mathcal{K} \setminus \{i\}} \frac{(d - |\mathcal{J}| - 1)!|\mathcal{J}|!}{d!} \Big(c(\mathcal{J} \cup \{i\}) - c(\mathcal{J}) \Big), \tag{3.16}$$

where $|\mathcal{J}|$ denotes the number of elements in the set $\mathcal{J}$. By definition, v_i represents the incremental contribution of player i when added to a subset $\mathcal{J} \subseteq \mathcal{K} \setminus \{i\}$. The coefficient associated with each expansion member in Eq.(3.16) can be written as [126]:

$$\frac{(d - |\mathcal{J}| - 1)!|\mathcal{J}|!}{d!} = \frac{1}{d} \binom{d-1}{|\mathcal{J}|}^{-1}. \tag{3.17}$$

This expression shows that the Shapley value assigns an equal weight of $\frac{1}{d}$ to each of d possible coalition sizes ($\mathcal{J} = 0, 1, 2..., d-1$) and an equal weight $\binom{d-1}{|\mathcal{J}|}^{-1}$ to all subsets of a size $\mathcal{J}$. In practical terms, this means that any interaction effect is evenly distributed among all variables participating in that interaction.

In the context of global SA, the players correspond to the input variables $\mathbf{X} = \{X_1, ..., X_d\}$, and the cost function $c(\mathcal{J})$ measures the variance of $Y = f(\mathbf{X})$ caused by uncertainty of the inputs in $\mathcal{J} \subseteq \mathcal{K}$. Song, Nelson and Staum [126] introduced a cost function that satisfies $c(\emptyset) = 0$ and $c(\mathcal{K}) = \mathrm{Var}[Y]$:

$$c(\mathcal{J}) = \mathrm{E}[\mathrm{Var}[Y|\mathbf{X}_{-\mathcal{J}}]], \tag{3.18}$$

where $\mathbf{X}_{-\mathcal{J}} = \mathbf{X}_{\mathcal{K} \setminus \mathcal{J}}$. This quantity represents the expected amount of variance that remains in Y when all variables outside the subset $\mathcal{J}$ are known. It is analogous to the interpretation of the total sensitivity index S_{T_i} defined by Eq.(3.12).

The *Shapley effect* of the ith input Sh_i is obtained by substituting the cost function (3.18) into the Shapley value definition (3.16). Shapley effects possess two important properties that make them highly suitable as dependency-aware importance measures [127]:

$$Sh_i \geq 0, \quad \sum_{i=1}^{d} Sh_i = \mathrm{Var}[Y]. \tag{3.19}$$

In words, they provide a non-negative measure of how much each input variable contributes to the total output variance, taking into account individual effects, interactions and the effects of the input dependence. Shapley effects may be normalised by $\mathrm{Var}[Y]$, yielding dimensionless indices that sum to one [128]:

$$\tilde{Sh}_i = \frac{Sh_i}{\mathrm{Var}[Y]}, \quad \sum_{i=1}^{d} \tilde{Sh}_i = 1. \tag{3.20}$$

These normalised Shapley effects (often named Shapley indices or Shapley-based importance indices) represent the fraction of output variability attributed to each input variable, similar to Sobol' sensitivity indices.

The greatest challenge in using Shapley effect lies in its extremely high computational cost [129]. Computing Shapley value given by Eq.(3.16) requires evaluating cost function (3.18)

for 2^{d-1} possible subsets $\mathcal{J}$ of the input parameters. Furthermore, calculating each of 2^{d-1} cost functions requires numerous MC simulations. To make this computation more efficient, Castro, Gómes and Carzola [130] introduced an approximation algorithm ApproShapley. It relies on the permutation representation of the Shapley value, an equivalent formulation to the so-called "subset-based" definition presented in Eq.(3.16). This alternative formulation expresses the Shapley value as the average marginal contribution of variable i across all $d!$ possible permutations of the input variables.

For a given permutation π, let $P_i(\pi)$ denote the set of variables appear before i in the ordering in π. The marginal contribution of variable i in permutation $P_i(\pi)$ is then $c(P_i(\pi)\cup\{i\})-c(P_i(\pi))$. By averaging this quantity over every permutation of the d variables, the Shapley value (3.16) can be re-written as:

$$v_i = \sum_{\pi\in\Pi(\mathcal{K})} \frac{1}{d!}\Big(c(P_i(\pi)\cup\{i\}) - c(P_i(\pi))\Big), \tag{3.21}$$

where $\Pi(\mathcal{K})$ denotes the set of all $d!$ permutations of variables in $\mathcal{K}$. Calculating the exact value of Shapley effect by using expression (3.21) now requires computing the cost function (3.18) for all $d!$ permutations. At first glance, calculating the cost function $d!$ times appears significantly more demanding than computing it 2^{d-1} times. However, Castro et al. [130] demonstrated that it is not necessary to consider all $d!$ permutations and that Shapley effects can be estimated by using only m randomly generated permutations $\pi_1, \pi_2, ..., \pi_m$ in $\mathcal{K}$:

$$v_i = \frac{1}{m}\sum_{l=1}^{m}\Big(c(P_i(\pi_l)\cup\{i\}) - c(P_i(\pi_l))\Big). \tag{3.22}$$

Song et al. [126] further adapted ApproShapley by introducing MC simulation to evaluate the cost function (3.18), as presented in Algorithm 3. First, N_V samples of input variables are generated according to their joint PDF $\mathbf{G}_\mathcal{K}$ to estimate mean value $\bar{Y}$ and total variance $\mathrm{Var}[Y]$ (lines 2-6). Next, for each of m generated permutations (while *counter* $< m$, line 7), the marginal contribution of a given variable to the output variance is computed (line 24). In order to do so, an inner loop of N_I samples (lines 15-18) is used to approximate the conditional variance $\mathrm{Var}(Y|\mathbf{X}_{-\mathcal{J}})$ (lines 19-20). Then, the conditional expectation $\mathrm{E}[\mathrm{Var}(Y|\mathbf{X}_{-\mathcal{J}})]$ is evaluated over N_O conditional variances (lines 13-22). Finally, averaging the calculated marginal contribution across all m permutation yield the Shapley effect estimate (Output, line 30). By introducing the parameter *prevC*, which stores the cost of the current subset (line 26) and reuses this value when computing the marginal cost for the next variable (line 24), the algorithm avoids recalculating the same quantity. This adaptation made by Song et al. [126] reduces the computational load of ApproShapley [130] by approximately half.

Ultimately, total computation of Shapley effect using Algorithm 3 requires evaluating $N_V + mN_IN_O(d-1)$ MC simulations. To obtain a reliable estimate of $\mathrm{Var}[Y]$, the sample size N_V should be chosen sufficiently large. Moreover, for a fixed computational budget, there is a trade-of between increasing the number of permutations m and improving the accuracy of the cost function estimates through larger values of N_I and N_O. Song et al. [126] demonstrated that an efficient strategy is to set $N_I = 3$, $N_O = 1$ and to allocate the remaining budget to maximising m.

Algorithm 3 Algorithm to estimate the Shapley effects, after Song et al. [126]

Choose m, N_V, N_O, N_I; set $\widehat{Sh}_i = 0$ for $i = 1, \ldots, d$; $counter = 0$
for $q = 1$ to N_V **do**
  Sample $\mathbf{X}_{\mathcal{K}}^{(q)} \sim \mathbf{G}_{\mathcal{K}}$
  Evaluate $Y^{(q)} = f(\mathbf{X}_{\mathcal{K}}^{(q)})$
end for
$\bar{Y} = N_V^{-1} \sum_{q=1}^{N_V} Y^{(q)}$; $\widehat{\mathrm{Var}}[Y] = (N_V - 1)^{-1} \sum_{q=1}^{N_V} \left(Y^{(q)} - \bar{Y}\right)^2$
while $counter < m$ **do**
  Generate $\pi \in \Pi(\mathcal{K})$; $prevC = 0$
  for $j = 1$ to d **do**
    if $j = d$ **then**
      $\hat{c}(P_{\pi(j)} \cup \{\pi(j)\}) = \widehat{\mathrm{Var}}[Y]$
    else
      for $l = 1$ to N_O **do**
        Sample $\mathbf{X}^{(l)}_{-P_{\pi(j+)}(\pi)} \sim \mathbf{G}_{-P_{\pi(j+)}(\pi)}$
        for $h = 1$ to N_I **do**
          Sample $\mathbf{X}^{(l,h)}_{P_{\pi(j+1)}(\pi)} \sim \mathbf{G}_{P_{\pi(j+1)}(\pi)}$
          Evaluate $Y^{(l,h)} = f(\mathbf{X}^{(l,h)}_{P_{\pi(j+1)}(\pi)}, \mathbf{X}^{(l)}_{-P_{\pi(j+1)}(\pi)})$
        end for
        Calculate $\bar{Y}^{(l)} = N_I^{-1} \sum_{h=1}^{N_I} Y^{(l,h)}$
        Calculate $\widehat{\mathrm{Var}}\left[Y \mid \mathbf{X}^{(l)}_{-P_{\pi(j+1)}(\pi)}\right] = (N_I - 1)^{-1} \sum_{h=1}^{N_I} \left(Y^{(l,h)} - \bar{Y}^{(l)}\right)^2$
      end for
      Calculate $\hat{c}(P_{\pi(j+1)}(\pi)) = N_O^{-1} \sum_{l=1}^{N_O} \widehat{\mathrm{Var}}\left[Y \mid \mathbf{X}^{(l)}_{-P_{\pi(j+1)}(\pi)}\right]$
    end if
    Calculate $\widehat{\Delta}_{\pi(j)} c(\pi) = \hat{c}(P_{\pi(j+1)}(\pi)) - prevC$
    Update $\widehat{Sh}_{\pi(j)} = \widehat{Sh}_{\pi(j)} + \widehat{\Delta}_{\pi(j)} c(\pi)$
    $prevC = \hat{c}(P_{\pi(j+1)}(\pi))$
  end for
  $counter = counter + 1$
end while
Output: $\widehat{Sh}_i = \widehat{Sh}_i / m$ for $i = 1, \ldots, d$

3.3 Metamodel applications in uncertainty analysis

In their most general form, metamodels are black-box approximations that establish a relationship between an input vector $\mathbf{x}$ and an output $y = f(\mathbf{x})$, allowing fast and computationally costless evaluation of the output [131]. The construction of a metamodel typically involves three steps. First, a set of design points, i.e. strategically chosen input vector that span the domain of interest, is generated, typically using some of the sampling methods, such as Pseudo-random number generator, Optimal design, Latin-Hypercube sampling, Sobol' sequence etc [106]. Second, the complex numerical model is evaluated at each of these points, producing a set of outputs. The resulting input-output pairs serve as the training data from which the metamodel is built. Finally, the last step involves metamodel validation against another set of input-outputs generated by a complex model.

There is a wide variety of metamodeling techniques, such as response surface model, most commonly implemented through polynomial regression (PR), Kriging model, support vector machines and neural networks [132–137]. Each of them relies on different mathematical formulation. However, no single metamodel is universally optimal, as its performance depends strongly on the type and complexity of the analysed problem, and selecting the right one is a challenging task. The selected metamodel should be efficient, robust and well suited for the problem at hand.

Dey et al. [106] evaluated ten different metamodeling techniques for UQ of the first three natural frequencies of laminated composite plates. Their results showed that PR required the fewest design points (64) to achieve adequate accuracy for eight input variables, followed by PCE and multivariate adaptive regression splines (MARS), each requiring 128 design points. However, their comparison considered only UQ performance and did not address the computational demands of subsequent global SA. PR and MARS metamodels require extensive MC simulations to estimate Sobol' indices, leading to high computational cost, especially for high number of input variables. By contrast, PCE enables analytical evaluation of Sobol' indices directly from its expansion coefficients, eliminating the need for MC simulations. Therefore, PCE was selected in this dissertation as the most suitable metamodeling technique, offering a balanced combination of accuracy and efficiency, particularly for use in uncertainty analysis.

PCE is a spectral decomposition method that models the input-output relationship of a system as a series of orthogonal polynomials, each corresponding to the probability distribution of the input variables [38]. Let a $\mathbf{X} \in \mathbb{R}^d$ be a random input vector with independent components and a joint PDF. Let f denote a computationally expensive-to-run model, and define the output $Y = f(\mathbf{X})$ with a finite variance. The PCE of $f(\mathbf{X})$ is defined as:

$$Y = f(\mathbf{X}) = \sum_{\boldsymbol{\alpha} \in \mathbb{N}^d} c_{\boldsymbol{\alpha}} \Psi_{\boldsymbol{\alpha}}(\mathbf{X}) \tag{3.23}$$

where $\Psi_{\boldsymbol{\alpha}}$ are the multivariate polynomials of order α with respect to input PDF, $\boldsymbol{\alpha} \in \mathbb{N}^d$ is a set of d-dimensional indices mapping to the components of $\Psi_{\boldsymbol{\alpha}}$, and $c_{\boldsymbol{\alpha}}$ are the coefficients of PCE. For independent inputs, multivariate polynomials are tensor product of univariate polynomials $\phi^{(i)}_{\alpha_i}(X_i)$ with respect to the ith variable in degree α_i:

$$\Psi_{\boldsymbol{\alpha}}(\mathbf{X}) = \prod_{i=1}^{d} \phi^{(i)}_{\alpha_i}(X_i) \tag{3.24}$$

The original homogeneous chaos expansion was first proposed by Wiener [138], where $\Psi_{\boldsymbol{\alpha}}$ are Hermite polynomials and random variables are normally distributed. Afterwards, a generalisation of the original Wiener-chaos expansion was introduced in order to deal with random variables that follow different distribution types. In that case, the polynomial basis is formed following the so-called Askey scheme [139] (e.g., Hermite polynomials correspond to Gaussian distributions, Legendre to Uniform, Laguerre to Gamma, Jacobi for Beta).

In practice, the infinite expansion (3.23) is truncated to total degree p,

$$f(\mathbf{X}) \approx f^{PC}(\mathbf{X}) = \sum_{\boldsymbol{\alpha} \in \mathcal{A}^{p,d}} c_{\boldsymbol{\alpha}} \Psi_{\boldsymbol{\alpha}}(\mathbf{X}), \quad \mathcal{A}^{p,d} \equiv \left\{ \boldsymbol{\alpha} \in \mathbb{N}^d : \|\boldsymbol{\alpha}\|_1 \leq p \right\} \tag{3.25}$$

where $\|\boldsymbol{\alpha}\|_1 = \sum_{i=1}^{d} \alpha_i$. As a result, the total number of terms in the truncated PCE is $\dfrac{(d+p)!}{d!p!}$.

The coefficients $c_{\boldsymbol{\alpha}}$ can be calculated using various methods, broadly classified into intrusive and non-intrusive approaches. Among the non-intrusive methods, projection and regression techniques are commonly utilised [120]. This dissertation employed the Chaospy package [140] in

Python [141] to construct the PCE metamodel. PCE coefficients were estimated non-intrusively, through a least-squares regression, which minimises the sum of squared residuals between the truncated PCE and the models's exact output.

Once the PCE coefficients are computed, due to the orthogonality of polynomial basis, model output statistic and Sobol' indices can be determined analytically via the straightforward post-processing of the PCE coefficients. The mean value μ and variance σ^2 are given as:

$$\mu = c_0, \quad \sigma^2 = \sum_{j=1}^{M} c_i^2, \tag{3.26}$$

where $M = \Big(\frac{(d+p)!}{d!p!} - 1\Big)$, while first-order and total Sobol' indices can be computed as:

$$S_i = \frac{\sum_{k \in \mathcal{L}_i} c_k^2 \langle \Psi_k, \Psi_k \rangle}{\sum_{k=1}^{M} c_k^2 \langle \Psi_k, \Psi_k \rangle}, \quad S_{T_i} = \frac{\sum_{k \in \mathcal{L}_{T_i}} c_k^2 \langle \Psi_k, \Psi_k \rangle}{\sum_{k=1}^{M} c_k^2 \langle \Psi_k, \Psi_k \rangle} \tag{3.27}$$

where $\mathcal{L}_i = \Big\{k \in \mathcal{A}^{p,d} : k_i > 0, k_l = 0, l \neq i\Big\}$ and $\mathcal{L}_{T_i} = \Big\{k \in \mathcal{A}^{p,d} : k_i > 0\Big\}$.

4 Experimental testing

This chapter describes the tested floor structures and experimental setup. The assembly and testing of a three full-scale CLT floors were carried out at the Faculty of Civil Engineering, University of Belgrade in collaboration with a research team from the Faculty of Civil Engineering, University of Zagreb, within Substrate4CLT research project. Experimental tests included measuring modal properties of the full-scale CLT floors and their acceleration response due to pedestrians walking. As the PhD candidate assisted in the experimental data collection, these tests do not count as an intellectual contribution of this dissertation. Nevertheless, they provided high-quality, full-scale measurement data that are essential for development and validation of the numerical models used later in this research (Chapter 5). Parts of the material presented in this chapter have been published in *Milojević M. et al. (2024) Characterization of inter-panel connections in CLT floors using finite element model updating. Journal of Building Engineering. 97, pp.110682.*[142]

The experimental campaign comprised measurements of the modal properties of three floor configurations, consisting of one, two, and three CLT panels (Section 4.1). The results obtained for each configuration were subsequently used in a three-step FEMU procedure, described in detail in Chapter 5. In addition, the acceleration response of the three-panel floor, induced by two pedestrians walking individually at different pacing rates, was measured (Section 4.2). These results illustrated the variability of human walk and resulting vibration response, and were used to validate the probabilistic pedestrian force model developed in Chapter 7.

4.1 Modal testing

Floors were assembled using 5-ply CLT panels with a total thickness of 15cm, made from C24 strength-class timber, as illustrated in Figure 4.1. The outer layers of the floors were oriented in the span direction. The overall dimensions of the tested floors, together with the corresponding measurement point grids adopted for modal testing are presented in Figure 4.2, while photographs of the three experimental setups are shown in Figure 4.3.

The half-lapped joint connections between adjacent panels (Figure 4.4a) were secured using 140mm long self-tapping screws spaced at 250mm. The single-panel and two-panel floors were supported on two neoprene foam rubber sheets, each 2.5cm thick and 12cm wide (Figures 4.4b and 4.5a), positioned at 67cm and 62.5cm from the shorter edges of the respective floors. These elastic supports were located close to the floor and aligned with one of the measurement point

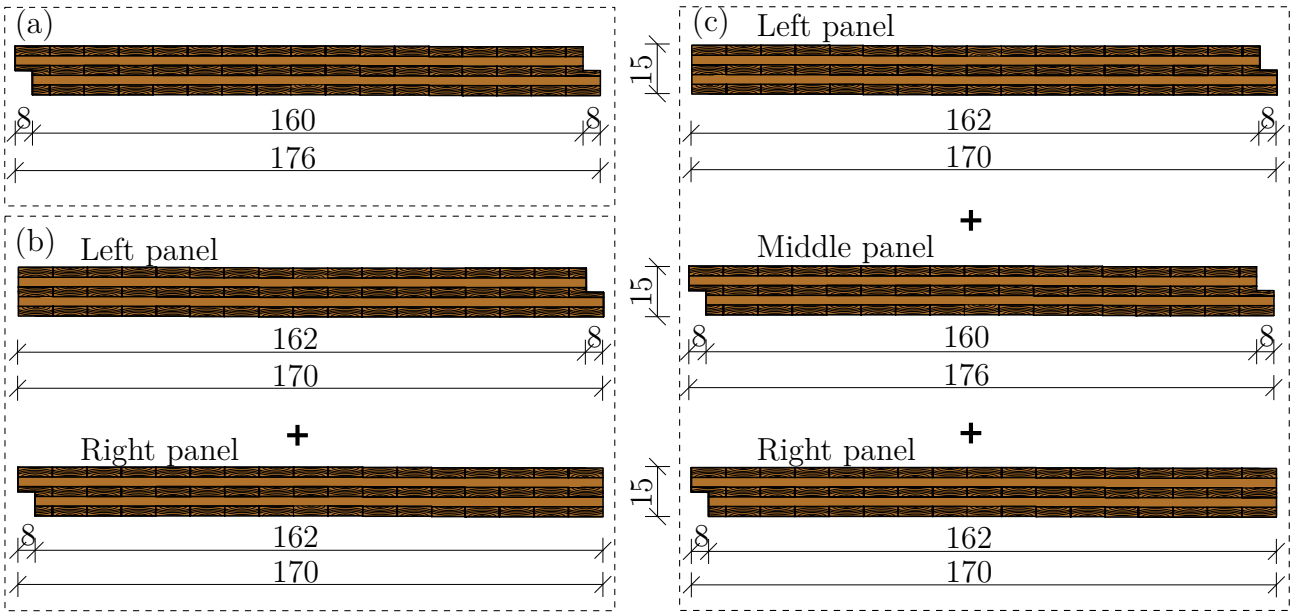

Figure 4.1: CLT panels for assembling single-panel floor (a), two-panel floor (b) and three-panel floor (c). All dimensions are in centimetres.

lines, as illustrated in Figure 4.2. Simply supported boundary conditions for the three-panel floor were achieved by screwing its shorter edges to glued-laminated timber (GLT) beams using 200mm long screws spaced at 250mm, as shown in Figures 4.4c and 4.5b. The GLT beams were fastened to a massive steel frame placed on a heavy laboratory floor (Figure 4.5c), ensuring a sufficiently stiff support.

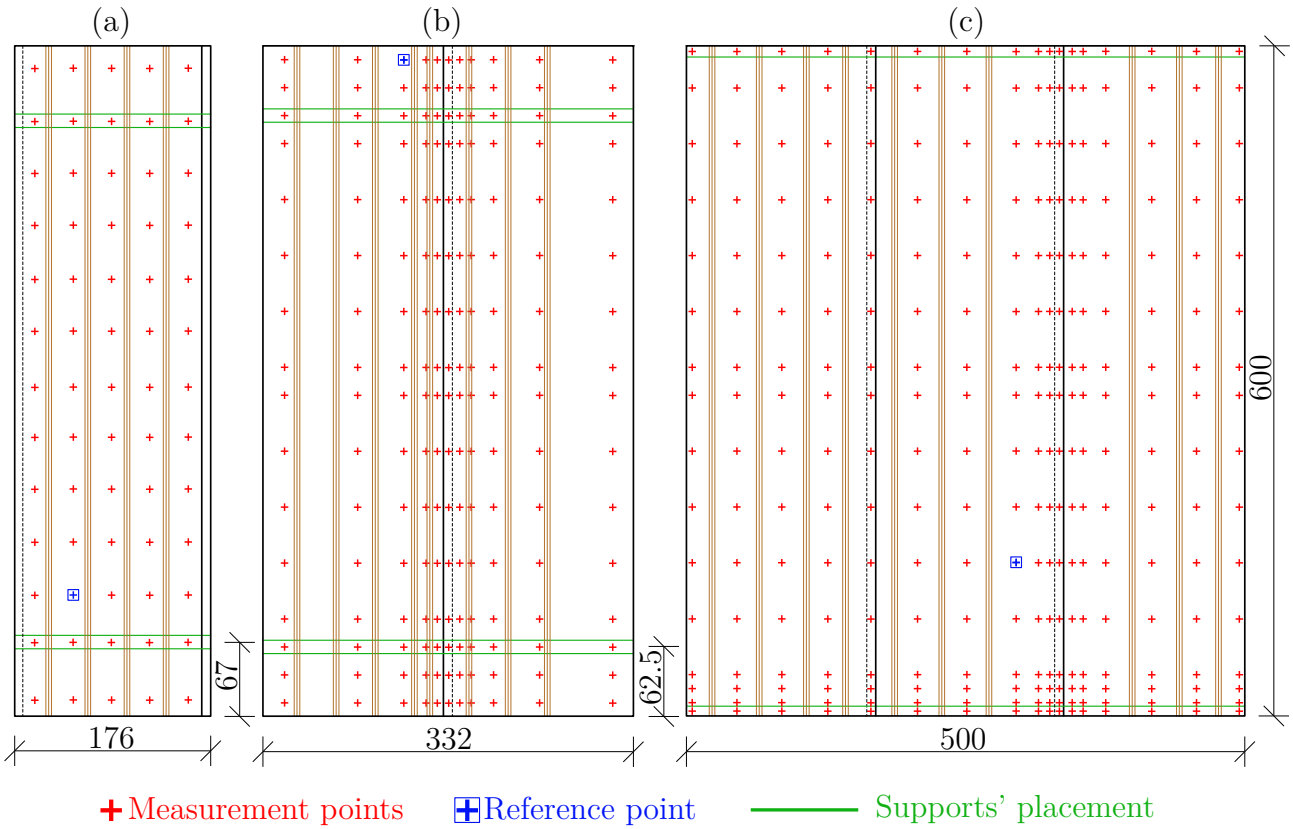

Figure 4.2: Dimensions and test grid for single-panel floor (a), two-panel floor (b) and three-panel floor (c). All dimensions are in centimetres.

(a)

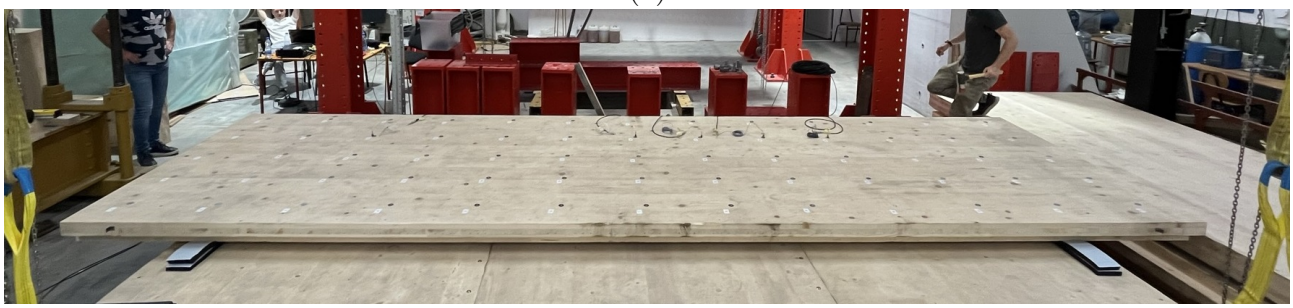

(b)

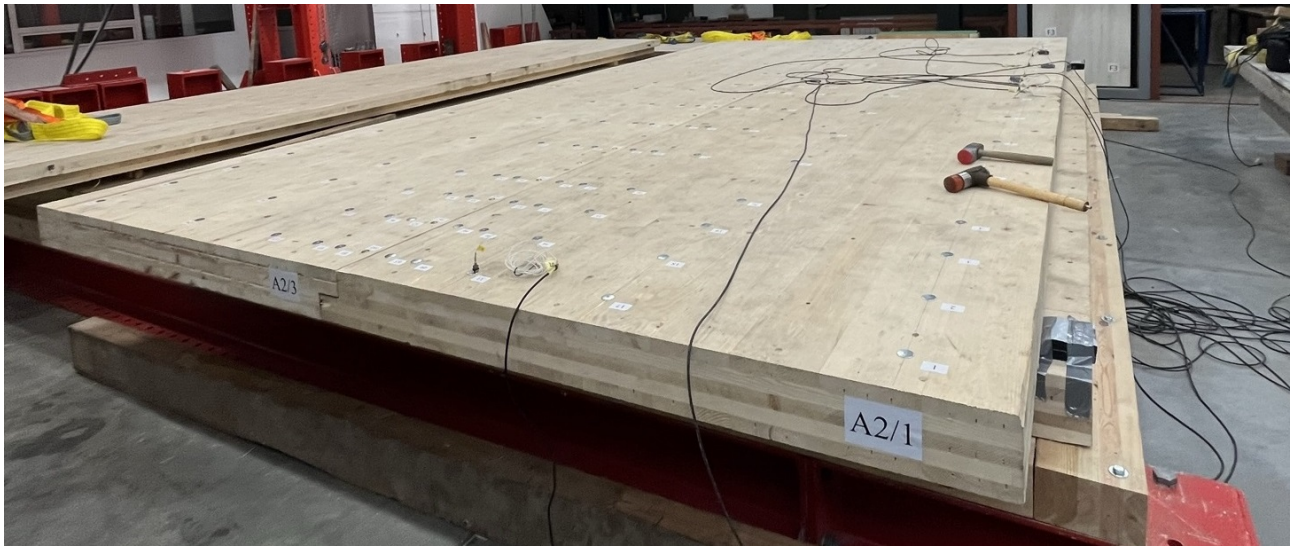

(c)



Figure 4.3: Experimental setup of a single-panel floor (a), two-panel floor (b) and three-panel floor (c).

The floors were excited in a random manner by gently tapping their top surface with two or three rubber impact hammers, applied individually at different locations (Figure 4.3c). It was assumed that the resulting vibration response could be treated as ambient, characterised by a broad-band random nature. Each floor configuration was instrumented with a dense measurement grid, comprising 65 measurement points for the single-panel floor, 176 for the two-panel floor and 272 for the three-panel floor (Figure 4.2). The grid was refined in the vicinity of the inter-panel connections and around the supports in the case of the three-panel floor to more

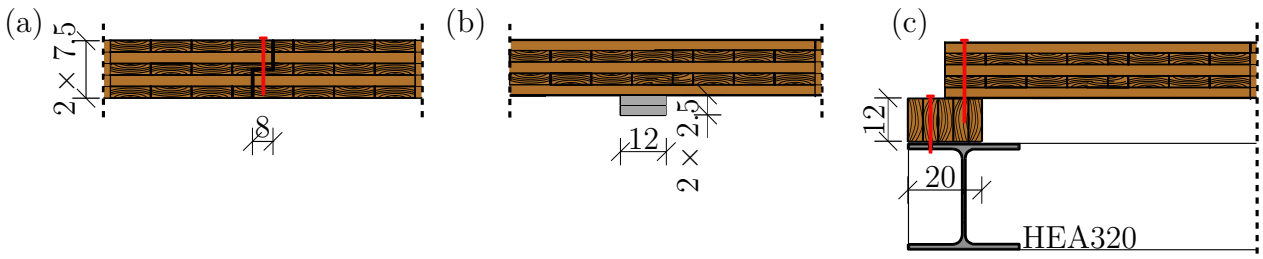

Figure 4.4: Detail of half-lap joint (a), elastic support (b) and panel-to-GLT beam and GLT beam-to-steel frame connection (c).

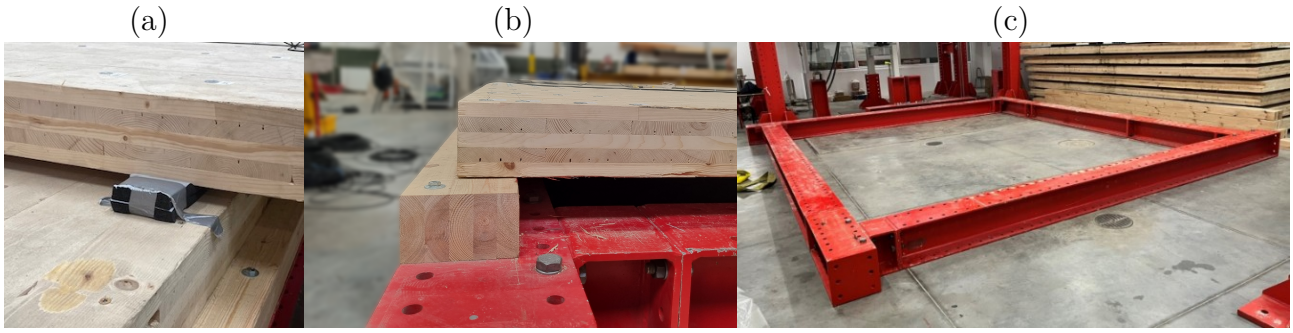

Figure 4.5: Boundary conditions of single and two-panel floors (a) and three-panel floor (b), steel frame that supports GLT beams and three-panel floor (c).

precisely capture the local deformations near the connections and supports. Acceleration responses were recorded using five Brüel&Kjær 4508-B accelerometers [143], each with a nominal sensitivity od 100mV/g. Data acquisition was performed in multiple measurement swipes, employing four roving accelerometers, while one accelerometer remained fixed and served as the reference (see Figure 4.2). In each swipe, vibration responses were recorded over a duration of 64s at sampling frequency of 2048Hz. The recorded acceleration data were processed using the commercial software ARTeMIS Modal Pro for Operational Modal Analysis [144], applying the Enhanced Frequency Domain Decomposition technique to extract the modal properties. Figure 4.6 illustrates an example of the singular value decomposition of the spectral density matrices employed for vibration modes identification.

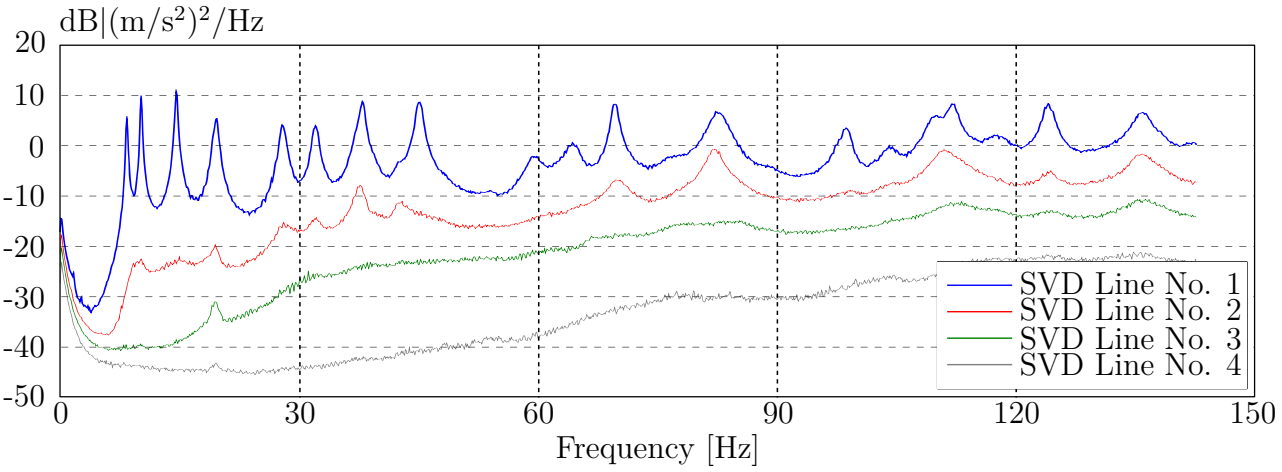

Figure 4.6: A characteristic example of a singular value decomposition of the spectral density matrices.

The extracted natural frequencies and damping ratios (ζ) are listed in Table 4.1, while corresponding mode shapes are illustrated in Figures 4.7 and 4.8. Damping ratios are provided only for the three-panel floor, as they are used later in response calculations in Chapters 8 and 9.

Table 4.1: Experimentally measured natural frequencies of the single-panel (1pf), two-panel (2pf) and three-panel floors (3pf) and and damping ratios of the three-panel floor.

Mode #	$\boldsymbol{f_{1pf}}$ [Hz]	$\boldsymbol{f_{2pf}}$ [Hz]	$\boldsymbol{f_{3pf}}$ [Hz]	$\boldsymbol{\zeta_{3pf}}$ [%]
RBM 1	6.50 ± 0.12	$5.70\pm$	–	–
RBM 2	7.25 ± 0.09	$7.40\pm$	–	–
RBM 3	9.75 ± 0.07	7.38 ± 0.22	–	–
RBM 4	–	$9.60\pm$	–	–
1	19.50 ± 0.16	13.25 ± 0.10	8.40 ± 0.03	1.04
2	20.33 ± 0.07	20.00 ± 0.09	10.20 ± 0.03	1.48
3	39.25 ± 0.02	20.63 ± 0.20	14.60 ± 0.44	0.89
4	49.00 ± 0.01	26.75 ± 0.03	19.60 ± 0.77	1.52
5	68.75 ± 0.01	39.63 ± 0.03	28.00 ± 0.08	1.43
6	87.00 ± 1.02	48.13 ± 0.04	32.20 ± 0.36	*
7	108.25 ± 0.03	55.00 ± 0.08	38.00 ± 0.45	1.33
8	119.25 ± 0.49	69.50 ± 0.07	45.20 ± 0.61	*
9	123.50 ± 0.04	80.13 ± 0.32	69.80 ± 0.08	0.63
10	–	83.25 ± 0.05	98.80 ± 0.18	0.75
11	–	87.25 ± 0.20	124.25 ± 0.94	0.38
12	–	93.50 ± 0.07	–	–
13	–	107.88 ± 0.73	–	–
14	–	114.13 ± 0.32	–	–
15	–	121.50 ± 0.55	–	–
16	–	125.88 ± 0.20	–	–

* Damping values could not be determined.

Single-panel and two-panel floors were placed on elastic supports, resulting in the first several rigid body vibration modes (RBMs), presented in Figure 4.7. The three RBMs of single-panel floor of the single-panel floor comprise the vertical translation of the panel (RBM 1), rotation about its longitudinal axes (RBM 2) and rotation about its transverse axis (RBM 3). These modes correspond to RBM 1, RBM 2 and RBM 4 of the two-panel floor, respectively. RBM 3 of

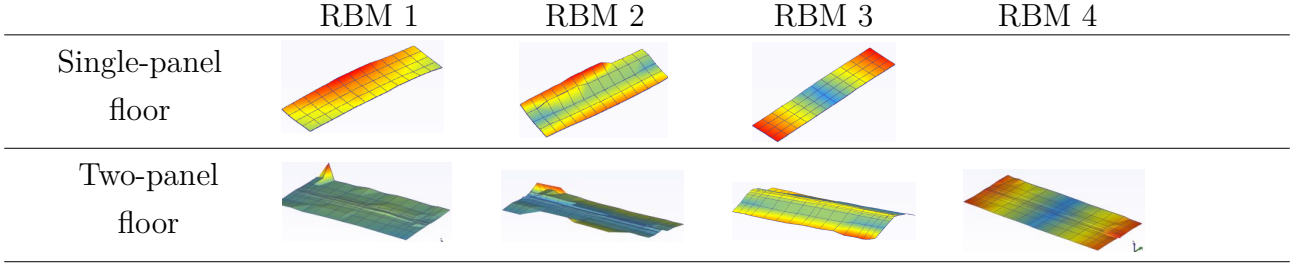

Figure 4.7: Experimentally determined rigid body mode shapes of the single-panel and two-panel floors.

	Single-panel floor	Two-panel floor	Three-panel floor
Mode 1	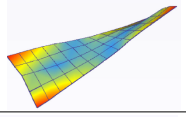	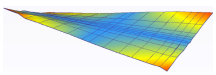	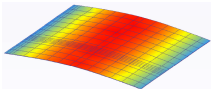
Mode 2	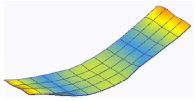	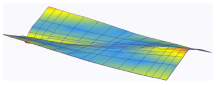	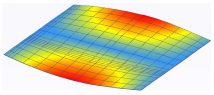
Mode 3	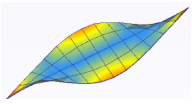	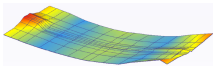	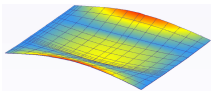
Mode 4	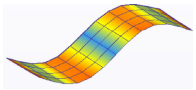	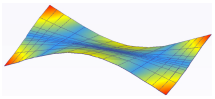	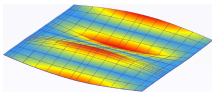
Mode 5	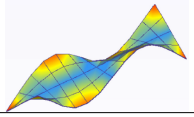	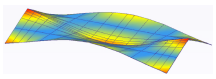	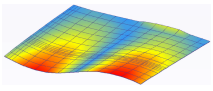
Mode 6	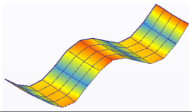	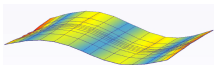	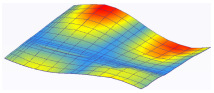
Mode 7	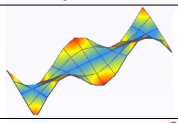	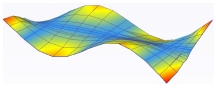	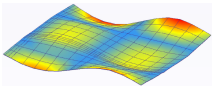
Mode 8	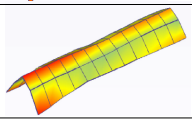	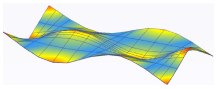	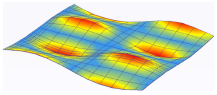
Mode 9	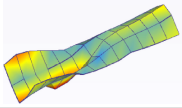	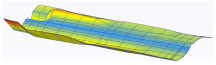	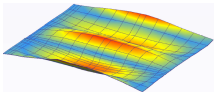
Mode 10		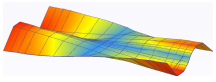	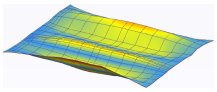
Mode 11		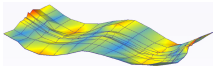	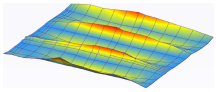
Mode 12		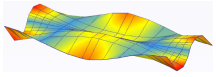	
Mode 13		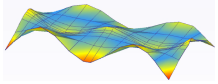	
Mode 14		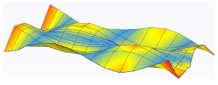	
Mode 15		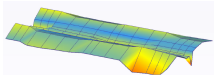	
Mode 16		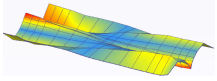	

Figure 4.8: Experimentally determined deformation mode shapes of the single-panel, two-panel and three-panel floors.

the two-panel floor represents a rigid relative rotation of the two panels about the connection line. Following the RBMs, deformation vibration modes (i.e. bending and torsional modes) up to 130Hz were identified for all three floor configuration (Figure 4.8). Although not all of these modes are directly relevant to human-induced floor vibrations, they were included in FEMU process presented in Section 5.3 in order to enhance its robustness and reliability. For completeness, the corresponding modal properties are restated in Section 5.2 together with the results of the initial FE modelling.

4.2 Walking tests

Two test subjects, TS1 (male, body mass 48 kg) and TS2 (female, body mass 51 kg), participated in the walking tests on the three-panel CLT floor. TS1 performed walking tests under two pacing conditions: a prescribed walking frequency of 2.0, Hz, controlled by a metronome, and free walking at his/her natural pacing frequency. TS2 walked only at his/her natural walking frequency. Both test subjects walked along two predefined walking paths (WPs), denoted as WP1 and WP2, as illustrated in Figure 4.9. For each combination of walking path and pacing condition, two trials were conducted: one in the direction WPiD1 and one in the opposite direction WPiD2. This resulted in a total of 12 walking trials, summarised in Table 4.2. During each trial, the vertical acceleration at the floor mid-span (Figure 4.9) was recorded. The resulting time-history responses and their corresponding amplitude spectra are illustrated in Figures 4.10-4.21. Additionally, the one-second running root-mean-square (RMS) acceleration was calculated for each trial and presented on the corresponding acceleration time history.

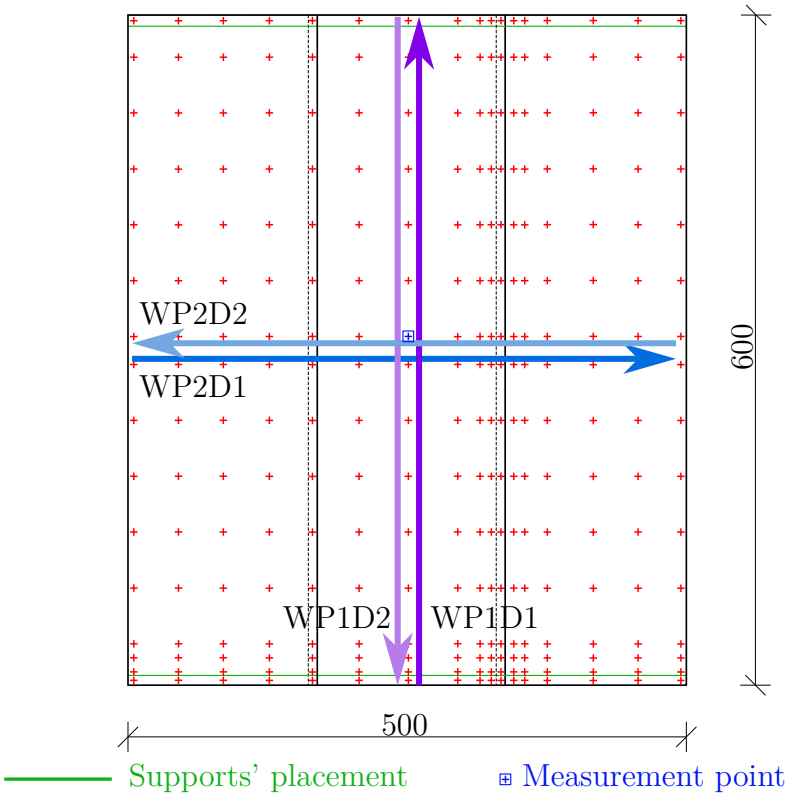

Figure 4.9: Two WPs and acceleration measurement points of three-panel floor.

An initial visual comparison of the measured responses obtained along the same WP in opposite directions indicates that the test subjects were unable to reproduce identical walking excitation

Table 4.2: Walking test trials.

Trial	Test subject	Walking path	Direction	Pacing conditions
1	TS1	WP1	D1	$f_p = 2.0$Hz
2	TS1	WP1	D2	$f_p = 2.0$Hz
3	TS1	WP2	D1	$f_p = 2.0$Hz
4	TS1	WP2	D2	$f_p = 2.0$Hz
5	TS1	WP1	D1	Free walking
6	TS1	WP1	D2	Free walking
7	TS1	WP2	D1	Free walking
8	TS1	WP2	D2	Free walking
9	TS2	WP1	D1	Free walking
10	TS2	WP1	D2	Free walking
11	TS2	WP2	D1	Free walking
12	TS2	WP2	D2	Free walking

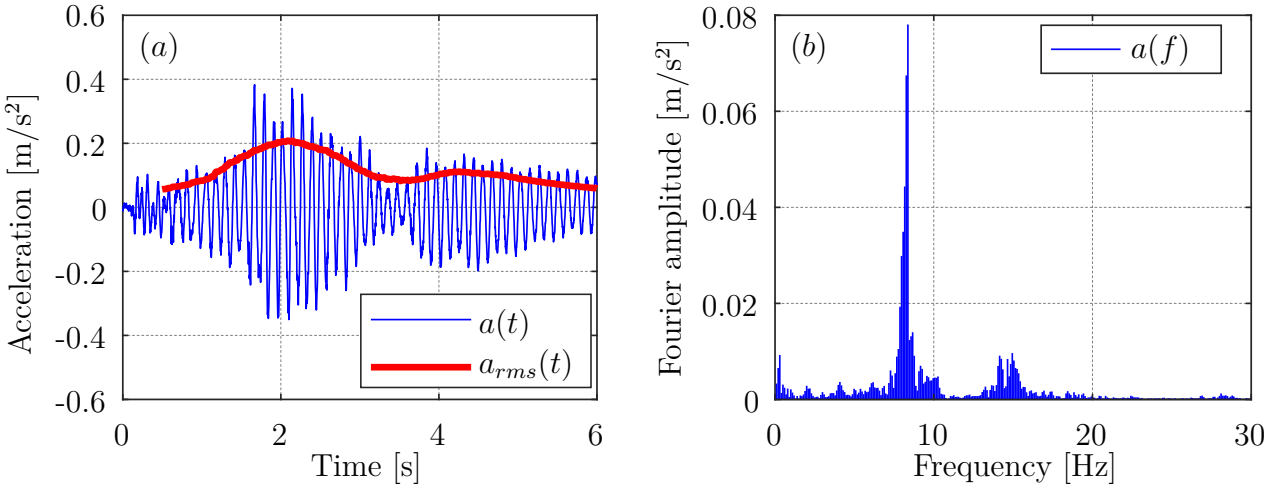

Figure 4.10: Acceleration time history due to TS1 walking at $f_p = 2$Hz on three-panel CLT floor along WP1 in direction D1 (a) and corresponding Fourier amplitude spectrum (b).

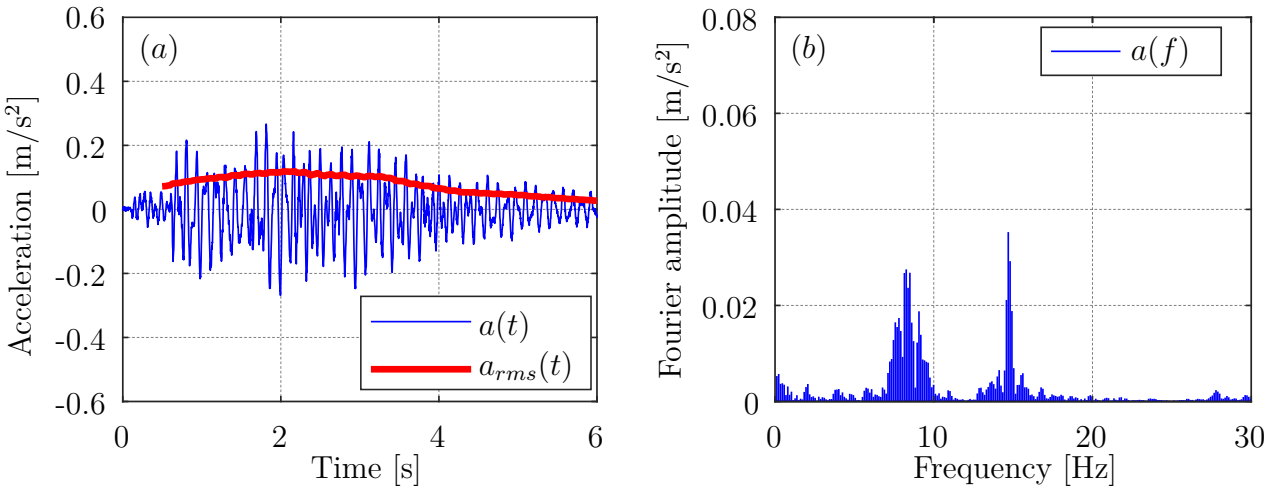

Figure 4.11: Acceleration time history due to TS1 walking at $f_p = 2$Hz on three-panel CLT floor along WP1 in direction D2 (a) and corresponding Fourier amplitude spectrum (b).

between successive trials, even when a metronome was used. Since the relevant mode shapes are symmetric along the considered walking paths, reversing the walking direction should theoretically produce a comparable structural response, provided that the footfall forces, step timing and footfall locations are identical. The observed differences between directions therefore primarily reflect the inherent variability of pedestrian walking.

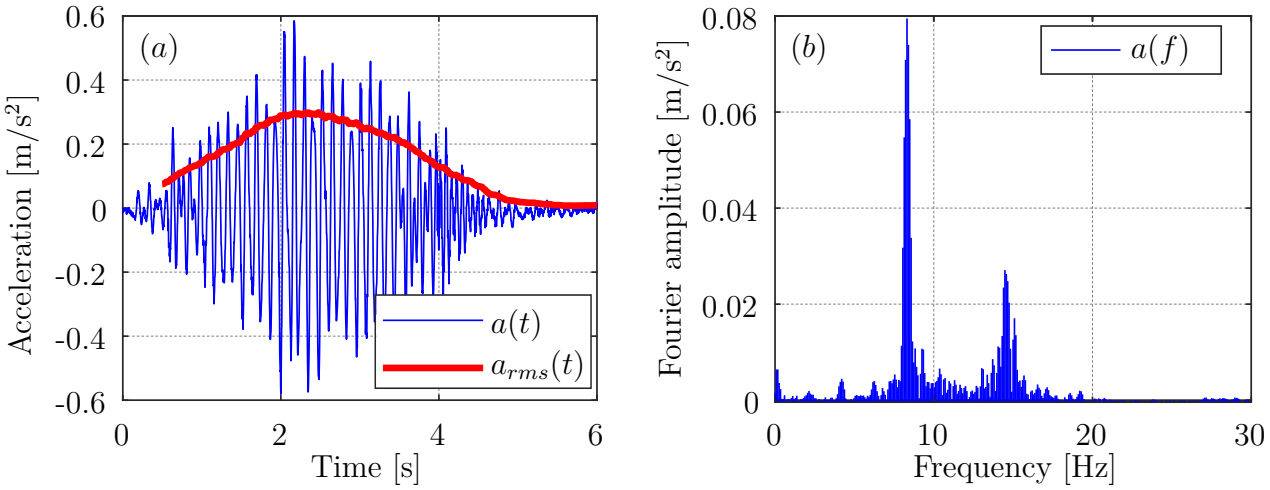

Figure 4.12: Acceleration time history due to TS1 walking at $f_p = 2$Hz on three-panel CLT floor along WP2 in direction D1 (a) and corresponding Fourier amplitude spectrum (b).

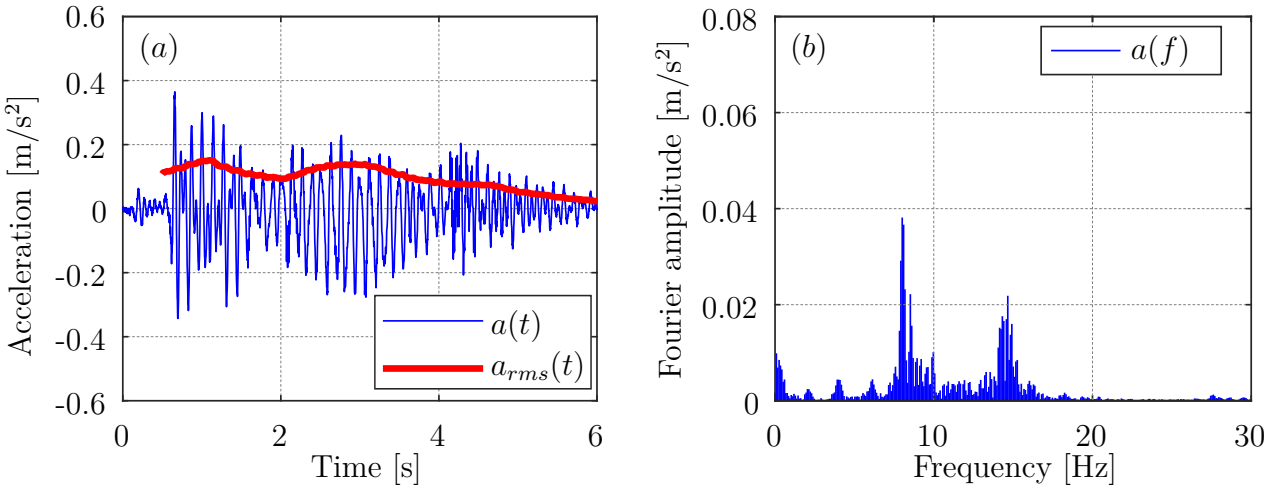

Figure 4.13: Acceleration time history due to TS1 walking at $f_p = 2$Hz on three-panel CLT floor along WP2 in direction D2 (a) and corresponding Fourier amplitude spectrum (b).

In most cases, the Fourier amplitude spectra exhibit two pronounced peaks corresponding approximately to the first and third vibration modes of the floor. However, the relative amplitudes of these peaks vary between repeated trials, further demonstrating the limited repeatability of pedestrian excitation. For TS1 walking at a nominal frequency of 2Hz, contribution of the first mode is dominant along WP1 in direction D1 (Figure 4.10) and along WP2 in direction D1 (Figure 4.12). A pronounced first–mode contribution is also observed during free walking by TS1 along WP2 in directions D1 and D2 (Figures 4.16 and 4.17). The dominance of the first mode response suggests that the fourth harmonic of the walking force was close to the fundamental frequency of the floor. This would correspond to a walking frequency of approximately 2.1Hz. Nevertheless, the response spectra identify the dominant structural response frequencies rather than directly measuring the walking frequency, and this interpretation should therefore be regarded as indicative.

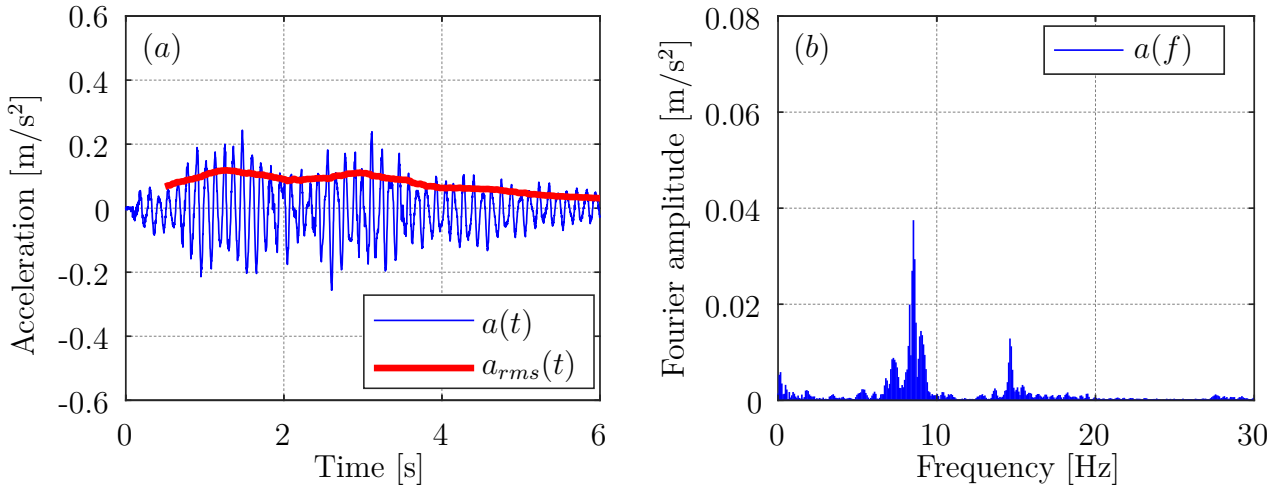

Figure 4.14: Acceleration time history due to TS1 free walking on three-panel CLT floor along WP1 in direction D1 (a) and corresponding Fourier amplitude spectrum (b).

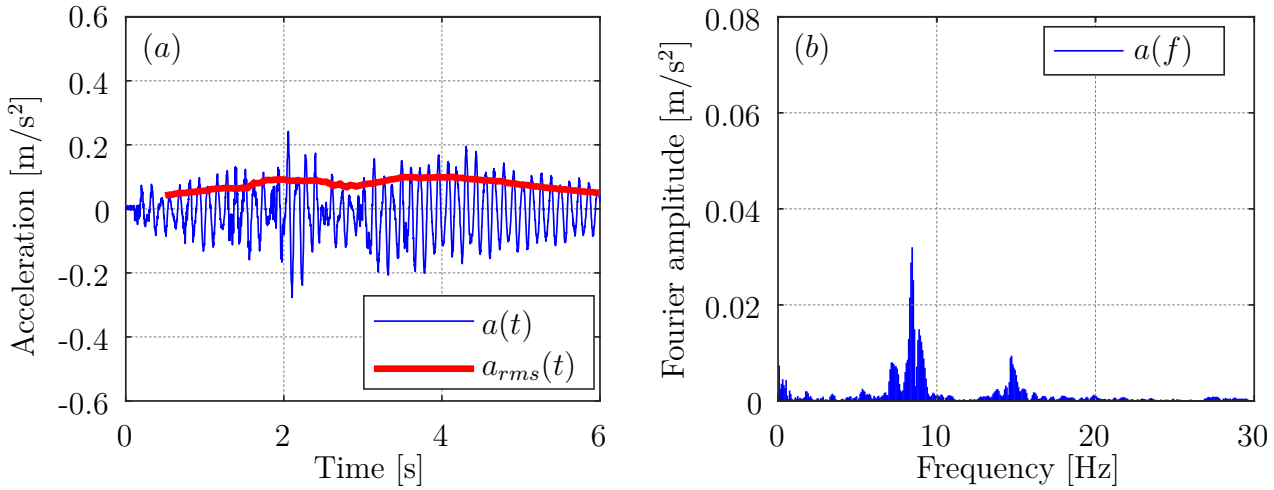

Figure 4.15: Acceleration time history due to TS1 free walking on three-panel CLT floor along WP1 in direction D2 (a) and corresponding Fourier amplitude spectrum (b).

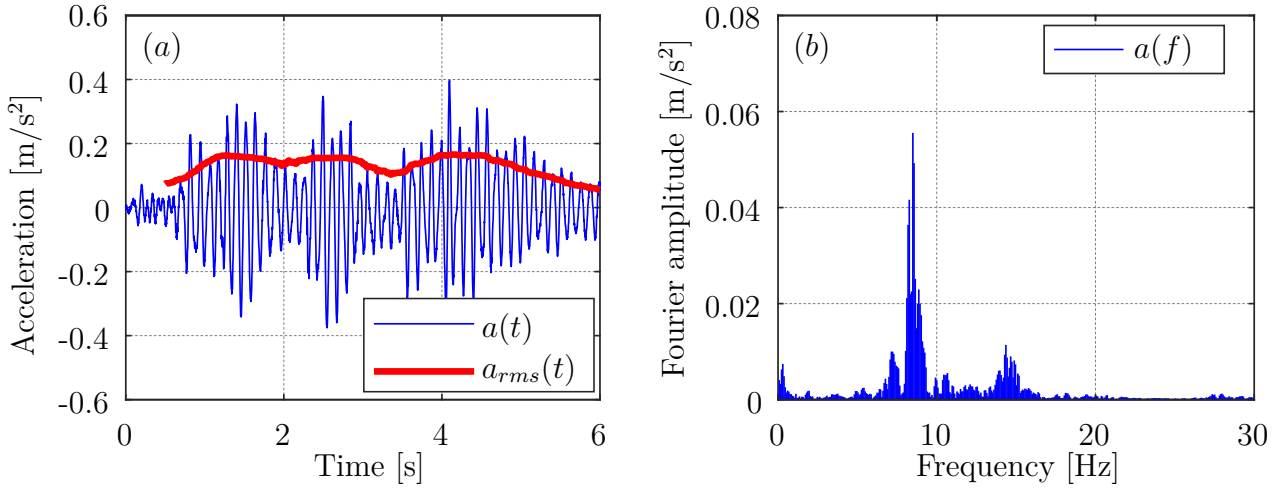

Figure 4.16: Acceleration time history due to TS1 free walking on three-panel CLT floor along WP2 in direction D1 (a) and corresponding Fourier amplitude spectrum (b).

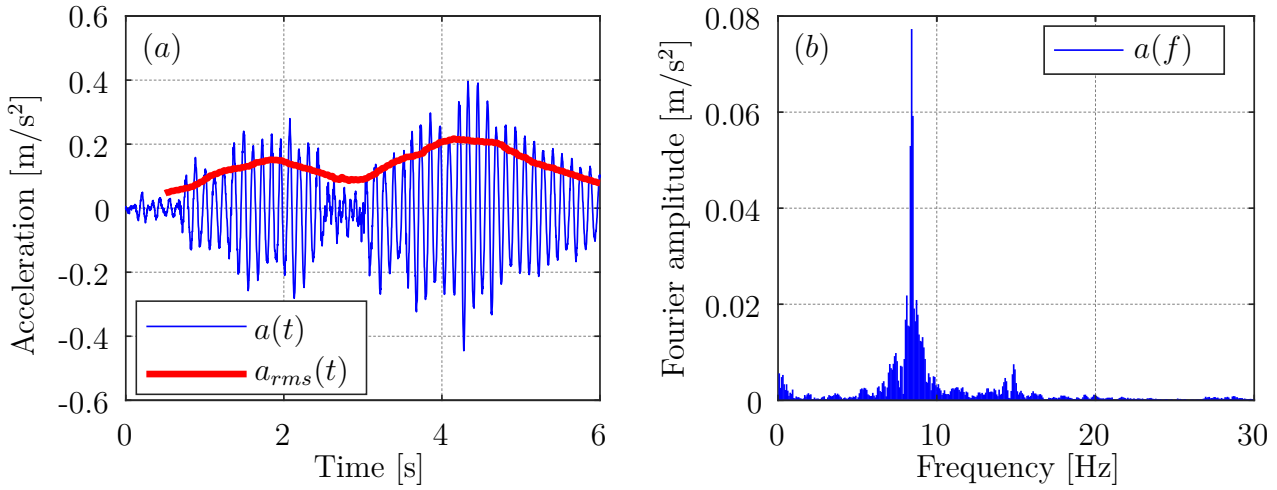

Figure 4.17: Acceleration time history due to TS1 free walking on three-panel CLT floor along WP2 in direction D2 (a) and corresponding Fourier amplitude spectrum (b).

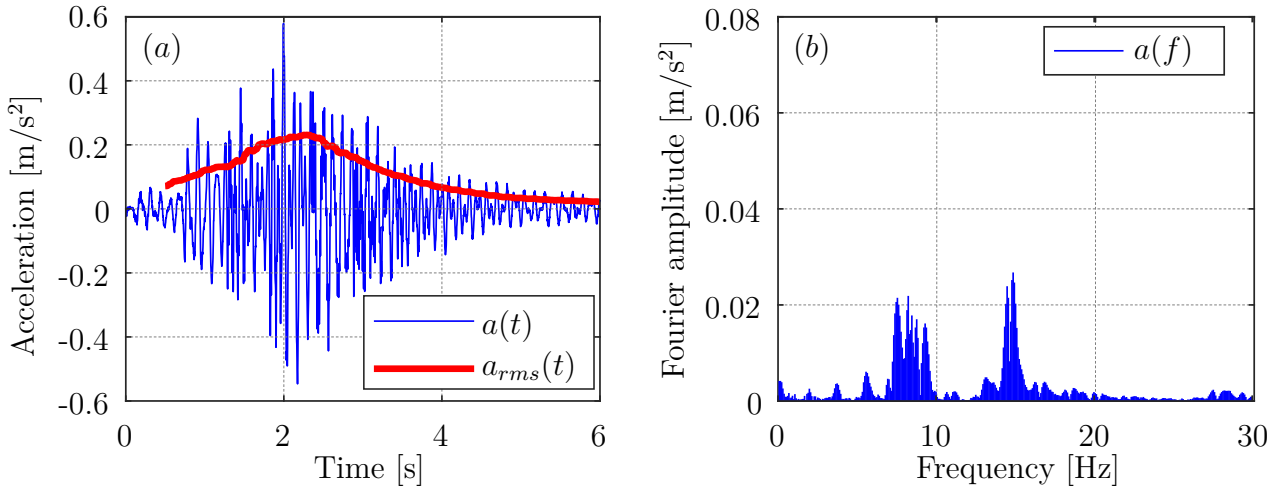

Figure 4.18: Acceleration time history due to TS2 free walking on three-panel CLT floor along WP1 in direction D1 (a) and corresponding Fourier amplitude spectrum (b).

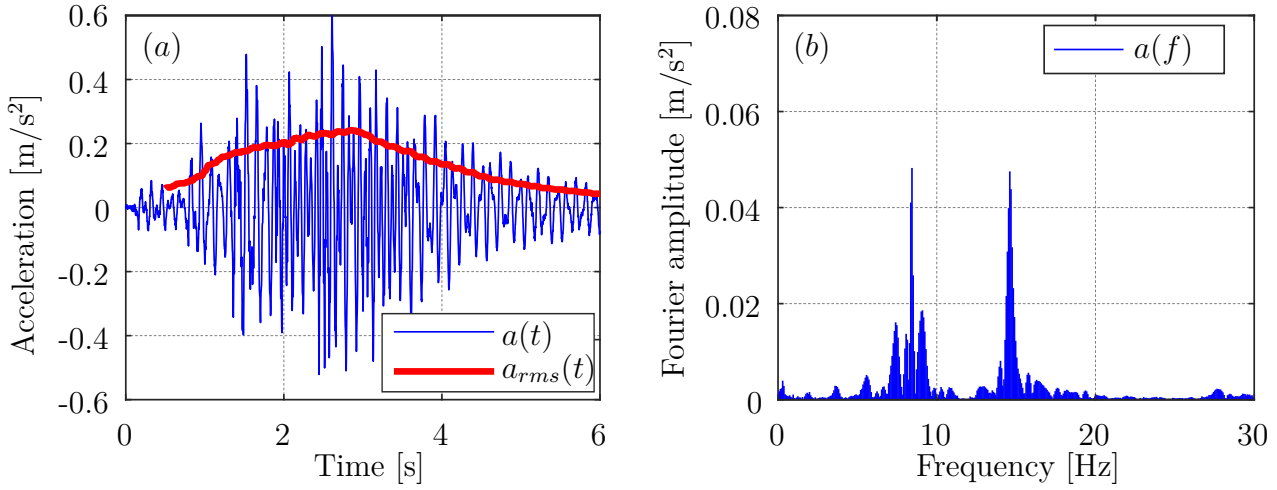

Figure 4.19: Acceleration time history due to TS2 free walking on three-panel CLT floor along WP1 in direction D2 (a) and corresponding Fourier amplitude spectrum (b).

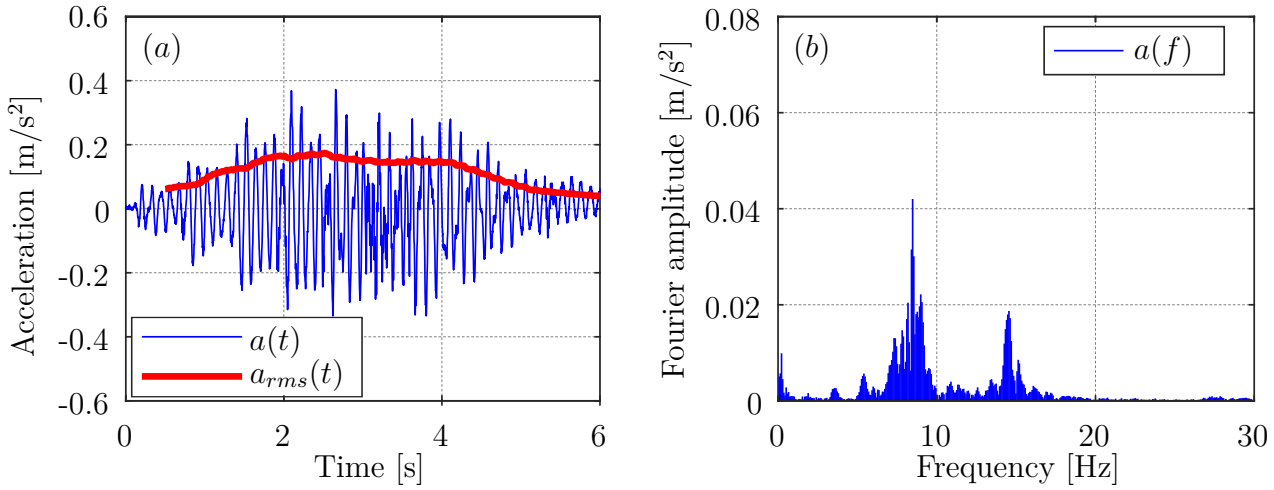

Figure 4.20: Acceleration time history due to TS2 free walking on three-panel CLT floor along WP2 in direction D1 (a) and corresponding Fourier amplitude spectrum (b).

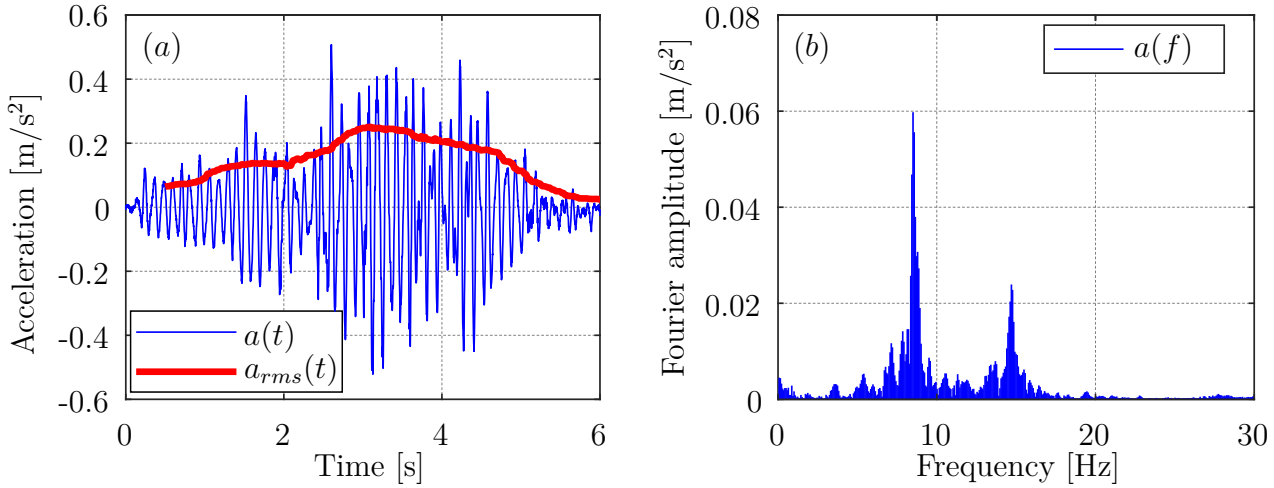

Figure 4.21: Acceleration time history due to TS2 free walking on three-panel CLT floor along WP2 in direction D2 (a) and corresponding Fourier amplitude spectrum (b).

The results of all walking trials, expressed in terms of the peak acceleration a_{peak} and the maximum one-second running RMS acceleration $a_{rms,max}$, are summarised in Table 4.3. The first four trials, in which TS1 walked at a prescribed frequency of $f_p = 2$Hz, are subsequently used for comparison with the deterministic LFF responses in Chapter 8. The remaining trials 5–12 are used in the probabilistic response assessment presented in Chapter 9.

It should be emphasised that the experimental dataset, comprising only two TSs walking along two paths, is insufficient for deriving representative response statistics. In addition, both test subjects had body masses below the population average, namely 48kg and 51kg, which is expected to result in lower walking-force amplitudes and, consequently, lower structural responses than those produced by an average pedestrian. The measured responses are therefore used only as indicative reference values, primarily to examine their position within the distributions of probabilistically predicted responses rather than to provide a statistically representative basis for model validation.

In addition to the modal and walking testing, a series of static tests was conducted on small CLT specimens within the Substrate4CLT research project. These test provided values of the

Table 4.3: Walking test results.

	Trial	**Pacing conditions**	a_{peak} [m/s^2]	$a_{rms,max}$ [m/s^2]
1	TS1-WP1-D1	$f_p = 2.0$Hz	0.3676	0.1997
2	TS1-WP1-D2	$f_p = 2.0$Hz	0.2576	0.1143
3	TS1-WP2-D1	$f_p = 2.0$Hz	0.5617	0.2882
4	TS1-WP2-D2	$f_p = 2.0$Hz	0.3502	0.1449
5	TS1-WP1-D1	Free walking	0.2559	0.1182
6	TS1-WP1-D2	Free walking	0.2722	0.1024
7	TS1-WP2-D1	Free walking	0.3972	0.1657
8	TS1-WP2-D2	Free walking	0.4452	0.2171
9	TS2-WP1-D1	Free walking	0.5791	0.2310
10	TS2-WP1-D2	Free walking	0.6414	0.2417
11	TS2-WP2-D1	Free walking	0.3723	0.1740
12	TS2-WP2-D2	Free walking	0.5214	0.2509

longitudinal modulus of elasticity E_L and timber density ρ. As the static testing programme is beyond the scope of this dissertation, it is not discussed in detail here. Nevertheless, the measured mean values of $E_L = 11242$MPa and $\rho = 424$kg/m^3 were adopted as initial input parameters for the FEMU procedure elaborated in Section 5.3.

5 Numerical model of CLT floors

This chapter focuses on the development and validation of numerical models of multi-panel CLT floors, with particular attention payed to modelling the inter-panel connections as equivalent elastic strips. These models form the basis for metamodel training and subsequent uncertainty analyses. Full-scale experimental modal testing of the three floor configurations (Chapter 4) supported a step-by-step FEMU procedure, enabling reliable identification of elastic support, timber material and elastic strip properties, as well as validation of the final numerical model. Following validation of the complex 3D model, it is demonstrated that simplified 2D models can reproduce the experimentally obtained floor modal properties with comparable accuracy. A major part of the work presented in this chapter has been published in the papers *Milojević M. et al. (2023) Influence of inter-panel connections on vibration response of CLT floors due to pedestrian-induced loading. Engineering Structures. 277 (), pp.115432*[33] and *Milojević M. et al. (2024) Characterization of inter-panel connections in CLT floors using finite element model updating. Journal of Building Engineering. 97 (), pp.110682*[142].

In MC-based SFEM, uncertainty in model output is evaluated by performing multiple deterministic FE analyses with modelling parameters varied according to their distribution and statistical properties. Accordingly, the SFEM-based uncertainty analysis workflow necessarily begins with development and validation of a deterministic FE model. As outlined in Section 3.1, uncertainty analysis in this dissertation was performed using a surrogate model, instead of directly applying SFEM. Nevertheless, developing a deterministic FE model was still required for two main purposes: (i) to generate the training data needed to construct the PCE metamodel and (ii) to perform SFEM combined with MC simulation for validation of the PCE-based uncertainty analysis of the floor natural frequencies and modal masses. Therefore, as in the deterministic approach, a reliable FE model is essential to carry out a probability-based VSA of any structure, including floors.

Existing research [72, 73] consistently indicates that inter-panel connections, often neglected in modelling, are essential for a reliable representation of the multi-panel CLT floors. In this dissertation, the half-lapped joint connections were modelled as a continuous elastic strip rigidly connected to adjacent panels, following the approach proposed by Paolini et al. [83], while its rotational stiffness was initially estimated based on recommendations by Macpherson et al. [84] (Section 5.1). To develop a reliable numerical model of the actual full-scale floor, elastic strip parameters were updated and validated using experimental data from the Chapter 4. This was achieved through a step-by-step fitting of the modal properties of the FE models of one- and two-panel CLT floors against the corresponding experimental measurements. The RBMs of the single-panel floor were used only to update the modelling parameters of the elastic supports

(Section 5.3.2). The deformation modes of the single-panel floor were then used to update the timber material properties (Section 5.3.2), whereas the properties of the relevant elastic strip representing the inter-panel connection were updated using both rigid body and deformation modes of the two-panel floor (Section 5.3.3). Finally, the results od the FEMU were validated against the measured modal properties of the three-panel floor supported by two GLT beams (Section 5.3.4). This step-by-step procedure is illustrated in Figure 5.1.

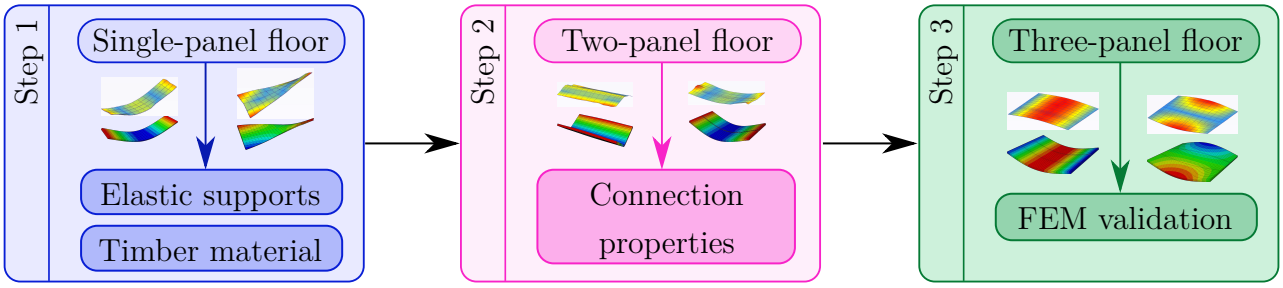

Figure 5.1: Step-by-step approach to FEMU.

This chapter begins with a description of modelling the inter-panel connections, according to Paolini et al. [83], and calculation of rotational stiffness of half-lapped joint as per Macpherson et al. [84] (Section 5.1). Development of initial numerical models of the three CLT floors is described in Section 5.2. Section 5.3 outlines principles behind the FEMU method and presents results of the adopted step-by-step FEMU procedure. Section 5.4 presents the resulting two-dimensional numerical models of the three-panel CLT floors, which are used in subsequent analyses throughout the dissertation. Finally, Section 5.5 summarises all the key finding of this chapter.

5.1 Modelling inter-panel connections

The equivalent elastic strip model was selected to represent the inter-panel connections for several practical and methodological reasons: (i) it is a simple element that provides an efficient way to incorporate inter-panel connections into FE models of multi-panel CLT floors, (ii) it can be readily implemented in any commercial FE software, (iii) it is compatible with both three-dimensional (3D) and two-dimensional (2D) FE formulations, and (iv) it results in relatively low computational cost. Accordingly, the elastic strip model offers clear advantages over commonly used spring-based connection models [69, 71, 82], particularly in the development of both 2D and 3D FE models.

Paolini et al. [83] originally proposed this model for the single-surface spline connection type illustrated in Figure 1.2. In this dissertation, it was used to represent the half-lapped joint connection. The strip's height h was adopted to match the CLT cross-section, while its width (a_{conn}) was initially assumed equal to the width of the half-lapped joint (a_{hl}), as illustrated in Figure 5.2. Any other (reasonable) initial value could have been chosen, but this was considered a fairly logical choice. This value was later updated in the FEMU process in Section 5.3. To achieve the reduced stiffness of the connection, while maintaining the same cross-sectional height, the elastic constants of the material must differ from those of the timber.

The initial modulus of elasticity of the equivalent elastic strip was derived to match rotational stiffness of the actual connection. Macpherson et al. [84] assumed that the region between the

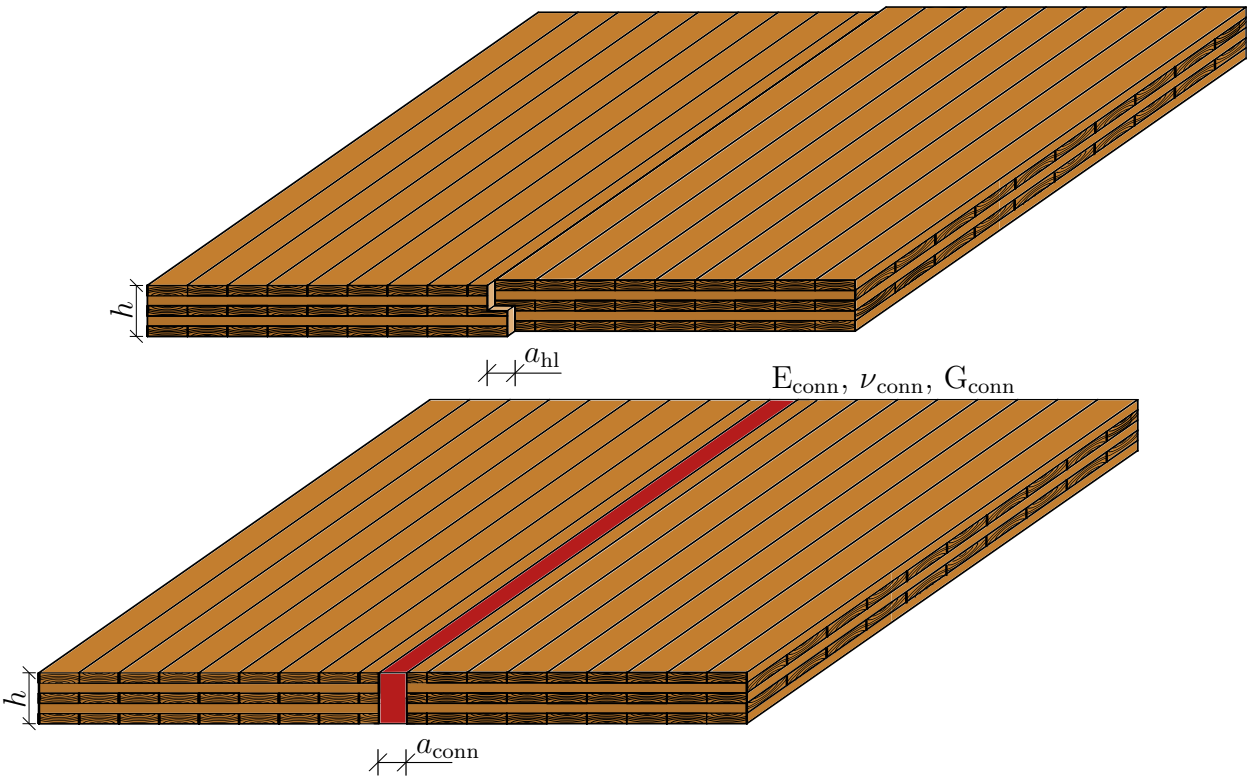

Figure 5.2: Equivalent elastic strip connection model to replace real half-lapped joint connection.

screw and the upper tip (marked orange in Figure 5.3a) is a rigid rectangle. Determination of rotational stiffness of the half-lapped joint involves calculating the stiffness of four springs arranged as illustrated in Figure 5.3b. The stiffness' k_{shear} and k_{axial} correspond to the shear and axial stiffness of the screw, while k_{top} and k_{bottom} are related to the compression of the timber at the half-lap corners. Subsequently, rotational stiffness R_{hl} of the half-lapped joint can be calculated as:

$$R_{hl} = \frac{M}{\varphi} = \frac{2h^2 k_{shear} k_{top}}{k_{shear} + k_{top}} + \frac{2l^2 k_{axial} k_{bottom}}{k_{axial} + k_{bottom}}, \tag{5.1}$$

where M is the bending moment and φ the corresponding rotation.

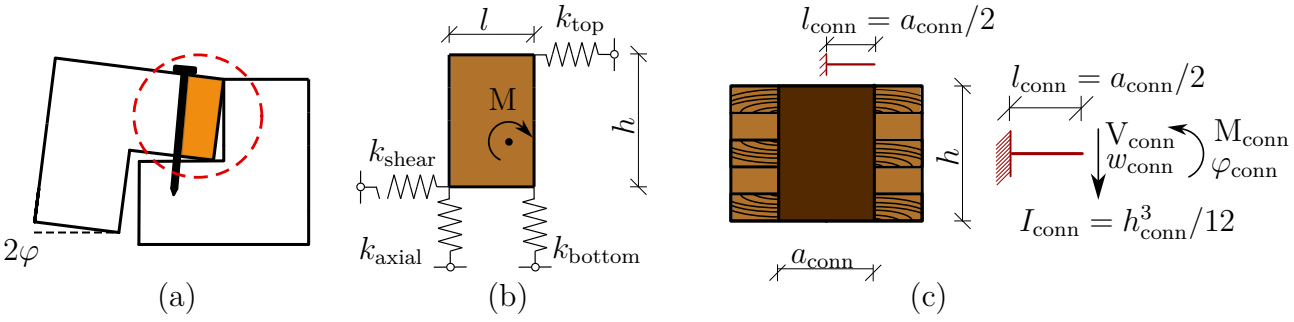

Figure 5.3: Behaviour of a half-lapped joint connection (a), rigid rectangle model (b), equivalent elastic strip (c).

The bending behaviour of the equivalent elastic strip was modelled as a cantilever beam with span $l_{conn} = a_{conn}/2$, as recommended by Paolini et al. [83] and illustrated in Figure 5.3c. Rotational stiffness of elastic strip R_{conn} is defined as the ratio between the bending moment

M_{conn} and the rotation φ_{conn}:

$$R_{conn} = \frac{M_{conn}}{\varphi_{conn}} = \frac{E_{conn} I_{conn}}{l_{conn}} \tag{5.2}$$

Finally, by evening up R_{hl} and R_{conn}, the initial value of the elastic modulus of the equivalent elastic strip was obtained:

$$E_{conn} = R_{hl} \frac{l_{conn}}{I_{conn}} = \frac{l_{conn}}{I_{conn}} \left(\frac{2h^2 k_{shear} k_{top}}{k_{shear} + k_{top}} + \frac{2l^2 k_{axial} k_{bottom}}{k_{axial} + k_{bottom}} \right) \tag{5.3}$$

The half-lapped joint was presumed to transfer the full shear force, i.e. there is no reduction in shear stiffness compared to the CLT cross-section. Consequently, the shear modulus of the strip G_{conn} was calculated as the shear modulus of the homogeneous cross-section equivalent to the actual 5-layered CLT cross-section. The Poissons ratio of elastic strip ν_{conn} was presumed to be equal to the in-plane Poissons ratio of the C24 class timber.

5.2 Initial numerical model

Initial numerical models of the three floor configurations were developed in the FE software Abaqus/CAE [145]. All floor slabs and supports were modelled using 20-node quadratic brick elements with reduced integration C3D20R as presented in Figure 5.4. This element type exhibited more efficient and stable convergence of the CLT slab natural frequencies compared to the 8-node linear brick element with reduced integration (C3D8R) [146]. The FE mesh size was selected based on a mesh optimisation study, which is described in the following subsection. Although 3D FE modelling is not commonly used in routine floor design, the numerical models in this dissertation featured a full 3D representation of the tested floors. This approach was primarily adopted to describe as accurately as possible the L-shaped edges of the single panel floor (Figure 4.1a), and thereby to minimise geometric discrepancies between the actual floor and the FE model. The capability of a 2D model to provide results as good as 3D model is examined in Section 5.4.

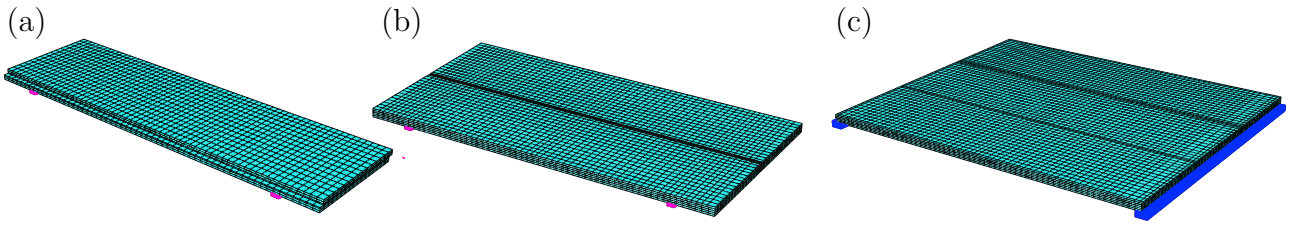

Figure 5.4: Numerical models of single-panel (a), two-panel (b) and three-panel floor (c).

Each layer of the CLT slab was modelled as an individual homogeneous lamina with orthotropic material properties [147]. Timber boards within a single lamina were assumed to be perfectly bonded, with no gaps between adjacent boards. As CLT panels consist of cross-wise oriented layers, each lamina in the FE model was rotated by 90° relative to the adjacent layers (Figure 5.5). Bonding between layers was assumed perfectly rigid and was modelled using the tie-constraints [145].

An extensive set of recommended C24 timber material properties reported by Wallner-Novak et al.[148] was used to complement the experimentally measured longitudinal modulus of elasticity

E_L and the density ρ of tested samples. Together, these values define the initial timber material properties (Table 5.1) adopted for the FEMU procedure presented in Section 5.3. The neoprene foam supports were assumed to be ideally elastic, with the initial material properties listed in Table 5.1. The initial modulus of elasticity was estimated from the measured deformation of the single-panel floor under self-weight. Density was adopted from the manufacturer's catalogue, while the Poisson's ration was assumed in the absence of any prior data. GLT beams supporting the three-panel floor were modelled as homogeneous beams with C24 material properties [148].

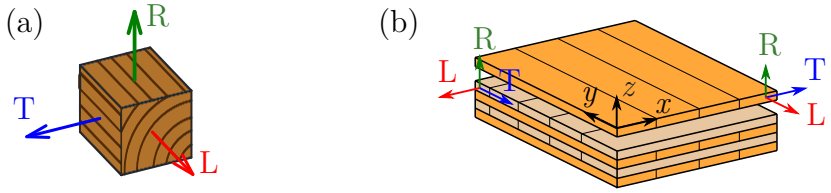

Figure 5.5: Timber material coordinate system with L-longitudinal, T-transversal and R-radial axes (a), layers' orientation in FE model (b).

Table 5.1: Initial properties of elastic supports, C24 timber material and elastic strip with the bounds used in FEMU for parameters to be updated.

Modelling parameter	**Label**	**Initial value**	**Lower/upper bound**
Neoprene foam support			
Modulus of elasticity	E_{supp}	67337 Pa	60636/74110 Pa
Density	ρ_{supp}	90 kg/m^3	
Poisson's ration	ν_{supp}	0.47	0.423/0.49
C24 timber material			
Density	ρ	424 kg/m^3	
Longitudinal modulus of elasticity	E_L	11242 MPa	10118/12366 MPa
Transversal modulus of elasticity	E_T	370 MPa	259/481 MPa
Radial modulus of elasticity	E_R	370 MPa	
Poissons ratio in LT plane	ν_{LT}	0.49	0.363/0.637
Poissons ratio in LR plane	ν_{LR}	0.39	
Poissons ratio in RT plane	ν_{RT}	0.64	
Shear modulus in LT plane	G_{LT}	690 MPa	483/897 MPa
Shear modulus in LR plane	G_{LR}	690 MPa	
Shear modulus in RT plane	G_{RT}	50 MPa	30/70 MPa
Elastic strip			
Width	a_{conn}	80 mm	40/80 mm
Modulus of elasticity	E_{conn}	8.823 MPa	-/- MPa
Poissons ratio	ν_{conn}	0.49	-/- MPa
Shear modulus	G_{conn}	306 MPa	-/- MPa

As outlined in previous Section, connection width was initially assumed equal to the width of the half-lapped joint (i.e. 80 mm). Initial value of elasticity modulus was estimated using Eq. (5.3), shear modulus was calculated as the shear modulus of the homogeneous cross-section equivalent to the actual 5-layered CLT cross-section and Poissons ratio of elastic strip was presumed to be equal to the in-plane Poissons ratio of the C24 class timber (Table 5.1).

5.2.1 Optimisation of mesh size

The FEMU process requires a large number of repeated numerical simulations. Therefore, prior to the FEMU, it was necessary to ensure that the numerical model was both computationally time efficient and sufficiently accurate. Accordingly, in this subsection, a mesh sensitivity analysis was carried out on the single-panel floor, using Modal Strain Energy (MSE) criterion to identify the optimal mesh size. The height of C3D20R elements was kept constant and equal to the thickness of a single layer (i.e. 30mm), while the element dimensions in the longitudinal and transverse directions were varied. In some cases, additional mesh refinement was applied in the vicinity of the half-lapped joint edges (Figure 5.6).

The results indicated that MSE was most sensitive to mesh variations in the transverse direction, and that reducing the in-plane element size below 100mm did not result in a significant change in the MSE values. Based on these findings, a uniform 100 × 100mm mesh without local refinement around the panel edges was adopted for the FE models of all three floors.

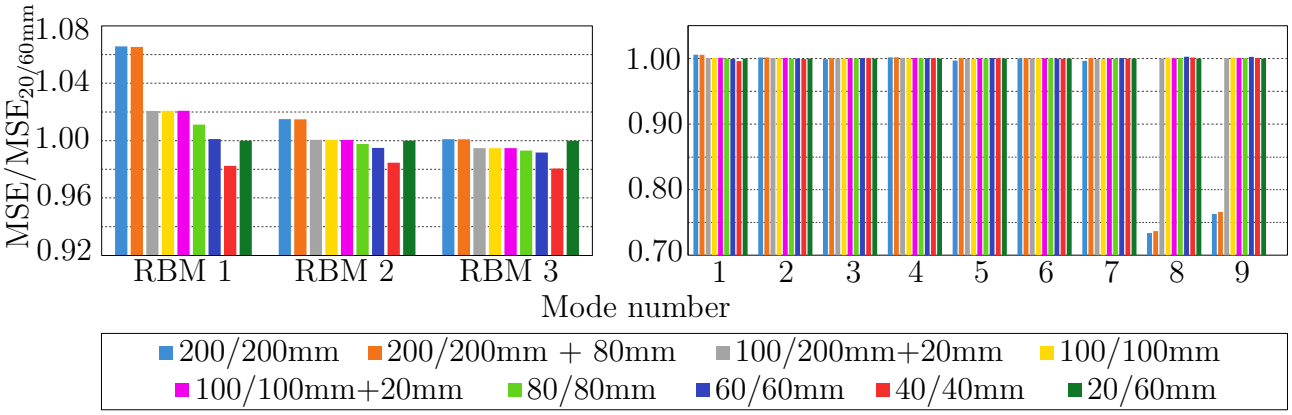

Figure 5.6: Mesh size optimisation described as T/L+HLJ, where T stands for the mesh size in the transverse direction, L for the mesh size in the longitudinal direction, and HLJ for the refinement around the half-lapped joint shaped edge.

5.2.2 Single-panel floor on elastic supports

Numerically calculated and experimentally measured natural frequencies of the single-panel floor with corresponding Modal Assurance Criterion (MAC) values [149] are listed in Table 5.2, while the corresponding mode shapes are illustrated in Figure 5.7.

Closer examination of the single-panel floor RBMs (Figure 5.7) revealed that they were not perfectly rigid-bodies, as a slight but noticeable bending of the panel was observed in RBMs 1 and 2, in both experimental and numerical results. This resulted from the asymmetry of the cross-section due to the half lap edges (see Figure 4.1a), rendering RMBs 1 and 2 neither symmetric nor antisymmetric. Furthermore, a high level of mode shape complexity [150] was obtained in these modes. While the numerically predicted natural frequencies of the RBMs 1 and 2 show good agreement with the experimental resuls, the corresponding MAC values are relatively low. In addition, the off-diagonal entries of MAC matrix associated with these two modes are almost as high as diagonal terms, indicating poor mode shape correlation and strong mode coupling. In contrast, RBM 3 exibits a MAC value of 0.997, negligible off-diagonal MAC values and low mode shape complexity, hence is recognised as a pure rigid-body mode.

Consequently, only RBM 3 was selected for the FEMU procedure, alongside with deformation modes 1-9.

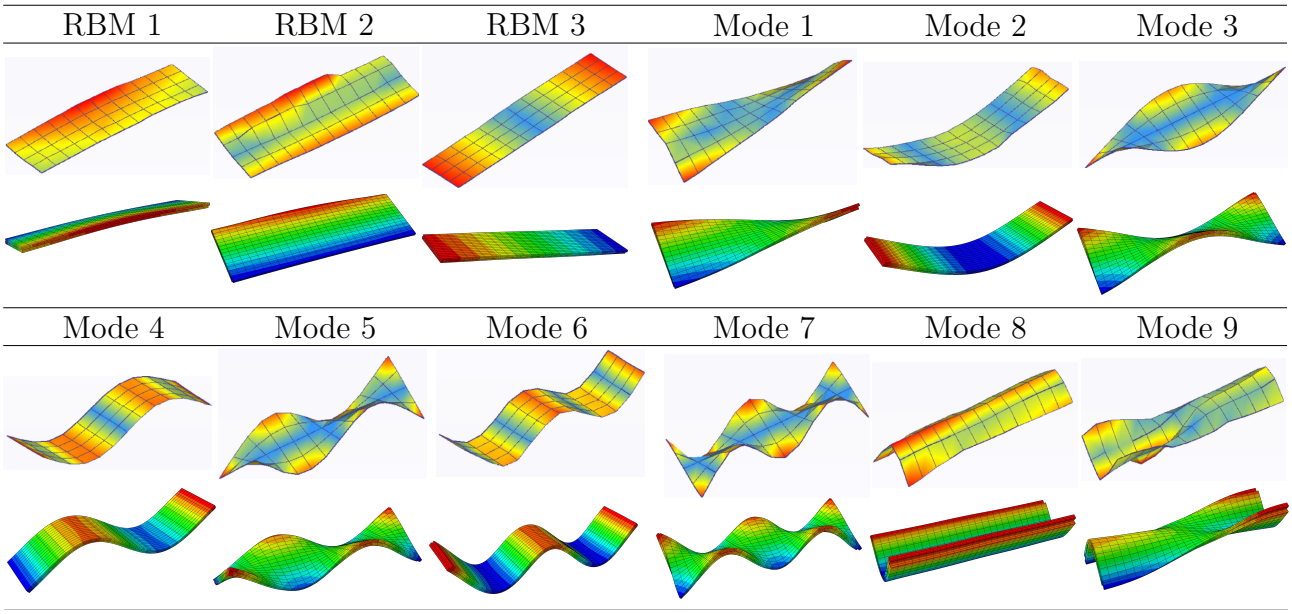

Figure 5.7: Experimentally (up) and numerically (down) determined mode shapes of the single-panel floor.

The MAC values for deformation modes 1-8 exceed 0.93, indicating strong correlation between the numerically predicted and experimentally identified mode shapes. The comparatively lower MAC of 0.776 obtained for mode 9 is likely due to the measurement inaccuracies, as suggested by visual inspection of the corresponding mode shapes (Figure 5.7). All initial natural frequencies of vibration modes up to 80Hz differ by less than 3% from their experimentally measured counterparts. Such agreement is considered more than acceptable for an initial model, particularly given that vibration modes above 80Hz are not relevant for VSA of floors [90].

Table 5.2: Experimentally measured and numerically determined natural frequencies and MAC values of initial model of the single-panel floor.

Mode #	f_{exp} [Hz]	$f_{initial}$ [Hz]	**Error***[%]	$\mathbf{MAC_{initial}}$
RBM 1	6.50	6.50	0.06	0.500
RBM 2	7.25	7.07	−2.51	0.585
RBM 3	9.75	9.60	−1.53	0.997
1	19.50	19.99	2.53	0.934
2	20.33	20.42	0.42	0.954
3	39.25	39.79	1.38	0.998
4	49.00	48.13	−1.79	0.995
5	68.75	67.17	−2.29	0.998
6	87.00	84.55	−2.81	0.984
7	108.25	100.91	−6.78	0.996
8	119.25	112.87	−5.35	0.946
9	123.50	116.34	−5.80	0.776

* Error $= (f_{initial} - f_{exp}) \times 100 / f_{exp}$ [%]

5.2.3 Two-panel floor on elastic supports

Numerically calculated and experimentally measured natural frequencies of the two-panel floor are summarised in Table 5.3, while the corresponding mode shapes are illustrated in Figure 5.8. Similar to the single-panel floor configuration, four RBMs have been identified (Figure 4.8). The RBMs 1,2 and 4 are not relevant for the present study, as the inter-panel connection and the panels do not deform relative to each other. Consequently, only the RBM 3 was considered further (hereafter referred to as RBM), as it was used together with deformation modes to update the modelling parameters of the elastic strip representing inter-panel connection (Section 5.3).

Table 5.3: Experimentally measured and numerically determined natural frequencies and MAC values of initial model of the two-panel floor.

Mode #	f_{exp} [Hz]	$f_{initial}$ [Hz]	**Error***[%]	$\mathbf{MAC_{initial}}$
RBM	7.38	14.29	93.76	0.855
1	13.25	13.46	1.59	0.995
2	20.00	23.92	19.61	0.885
3	20.63	20.24	−1.87	0.912
4	26.75	27.37	2.33	0.991
5	39.63	42.59	7.48	0.995
6	48.13	47.98	−0.31	0.945
7	55.00	54.34	−1.20	0.960
8	69.50	69.86	0.51	0.973
9	80.13	81.35	1.53	0.795
10	83.25	84.80	1.87	0.976
11	87.25	84.70	−2.93	0.747
12	93.50	95.26	1.88	0.926
13	107.88	104.17	−3.43	0.928
14	114.13	113.74	−0.34	0.919
15	121.50	119.88	−1.33	0.882
16	125.88	123.35	−2.01	0.897

* Error $= (f_{initial} - f_{exp}) \times 100 / f_{exp}$ [%]

The numerically predicted natural frequency of the RBM is 94% higher than corresponding experimentally measured natural frequency. This indicates that the initial stiffness assigned to the inter-panel connection was significantly overestimated. Furthermore, among deformation modes $1-16$, the largest relative errors between the experimental and numerical natural frequencies occur for modes involving combined longitudinally and laterally bending along the connection line, i.e. modes 2 and 5. Corresponding relative errors are 20% for 2nd and 7.5% for 5th natural frequency. This discrepancies can again be attributed to the exceptionally high stiffness of the elastic strip assumed in the initial FE model. The remaining modes exhibit good agreement with the experimental results. Although the MAC values are generally lower than those obtained for the single-panel floor, an average value of 0.916 indicates that the initial numerical model provides and adequate representation of the experimentally identified mode shapes.

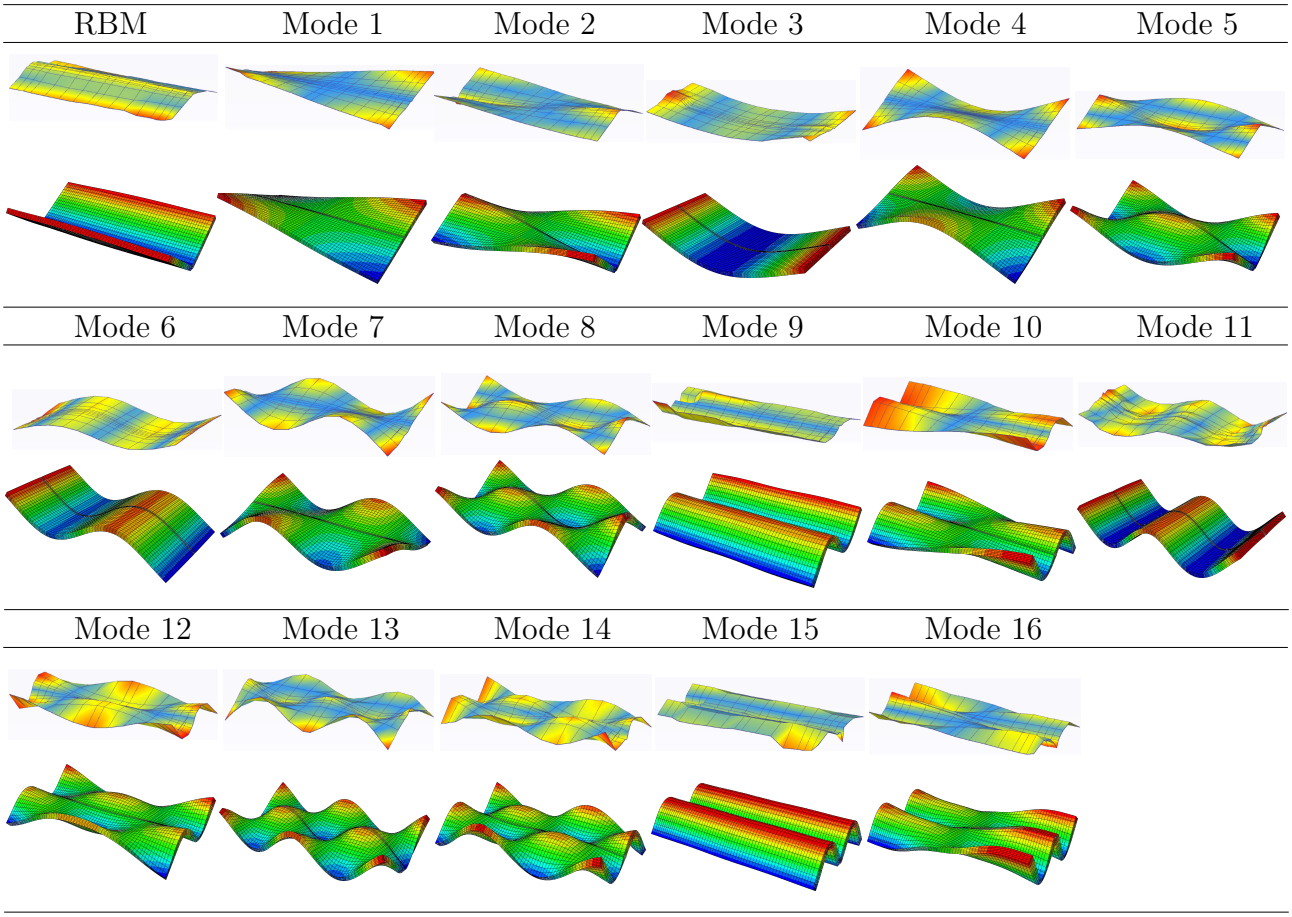

Figure 5.8: Experimentally (up) and numerically (down) determined mode shapes of the two-panel floor.

5.2.4 Three-panel floor supported by GLT beams

Natural frequencies obtained from the experimental measurements and numerical simulations of the three-panel floor are presented in Table 5.4 and the corresponding mode shapes are illustrated in Figure 5.9. Additional experimental modes with the natural frequencies up to 130Hz were identified. However, these were excluded from the present study due to their high levels of complexity. Low MAC values were obtained for modes 5 and 6, which is most likely due to imperfections in the support conditions. This interpretation is supported by apparent support displacements in these modes, as illustrated in Figure 5.9. In contrast, MAC values of all remaining modes are exceptionally high, indicating a good agreement between the numerical and experimental mode shapes. The largest discrepancies between the numerically predicted and experimentally measured natural frequencies are for modes 3 and 4, as the inter-panel connections play a dominant role. A notable difference is also observed for mode 5, due to the previously mentioned support displacements.

5.3 Finite element model updating

Broadly speaking, a FEMU represents an optimisation problem aimed at finding the values of selected modelling parameters that minimise differences between the experimental and nu-

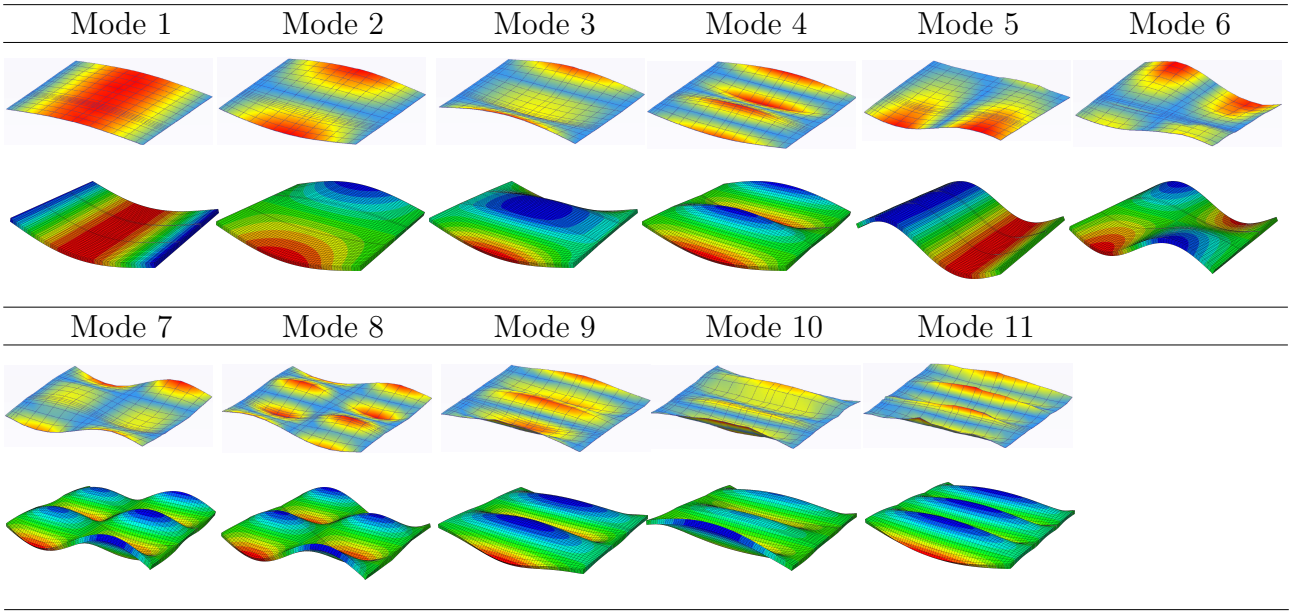

Figure 5.9: Experimentally (up) and numerically (down) determined mode shapes of the three-panel floor.

Table 5.4: Experimentally measured and numerically determined natural frequencies and MAC values of initial model of the three-panel floor.

Mode #	f_{exp} [Hz]	$f_{initial}$ [Hz]	**Error***[%]	$\mathbf{MAC_{initial}}$
1	8.40	8.32	−0.95	0.999
2	10.20	10.43	2.24	0.995
3	14.60	15.94	9.16	0.990
4	19.60	23.77	21.30	0.989
5	28.00	30.60	9.26	0.757
6	32.20	32.84	1.99	0.725
7	38.00	38.37	0.99	0.959
8	45.20	45.97	1.71	0.975
9	69.80	70.84	1.49	0.967
10	98.80	100.98	2.21	0.962
11	124.25	123.72	−0.43	0.931

* Error $= (f_{initial} - f_{exp}) \times 100 / f_{exp}$ [%]

merical response of a structure. In the modal analysis, this difference is commonly expressed through frequency (r_f) and mode shapes (r_m) residuals, which can be defined as [151]:

$$r_{f,i} = \left| \frac{f_{i,num} - f_{i,exp}}{f_{i,exp}} \right|, \qquad r_{m,i} = \sqrt{\frac{\left(1 - \sqrt{\mathrm{MAC}(\phi_{i,num}, \phi_{i,exp})}\right)^2}{\mathrm{MAC}(\phi_{i,num}, \phi_{i,exp})}} \tag{5.4}$$

where $f_{i,num}$ and $f_{i,exp}$ are the numerically and experimentally obtained natural frequencies, respectively, while $\phi_{i,num}$ and $\phi_{i,exp}$ are the corresponding mode shapes for the ith mode.

Two general approaches can be adopted to minimise residuals in FEMU: single-objective and multi-objective optimisation approach [152]. Compared to the single-objective approach, multi-objective optimisation explores the parameter search space more comprehensively, improves computational efficiency and provides a more balanced treatment of the residual sets defined in Eq. (5.4) [153]. For these reasons, a bi-objective optimisation strategy [154] was adopted in this research, with the objective functions defined as:

$$f_1 = 0.5 \sum_{i=1}^{n} r_{f,i}, \qquad f_2 = 0.5 \sum_{i=1}^{n} r_{m,i} \tag{5.5}$$

where n denotes the number of considered vibration modes.

Solving a bi-objective optimisation problem results in a set of potential optimal solutions, commonly referred to as the "Pareto front". A key challenge is to identify a single representative solution from this set, often called the "knee" point, which corresponds to the best balance between two objective functions, i.e. residuals. Several criteria have been proposed in the literature for identifying this "knee" point, including [155]: (i) the minimum distance to the equilibrium point (Figure 5.10a), (ii) the maximum distance from the boundary line (Figure 5.10b) and (iii) the maximum band angle (Figure 5.10c).

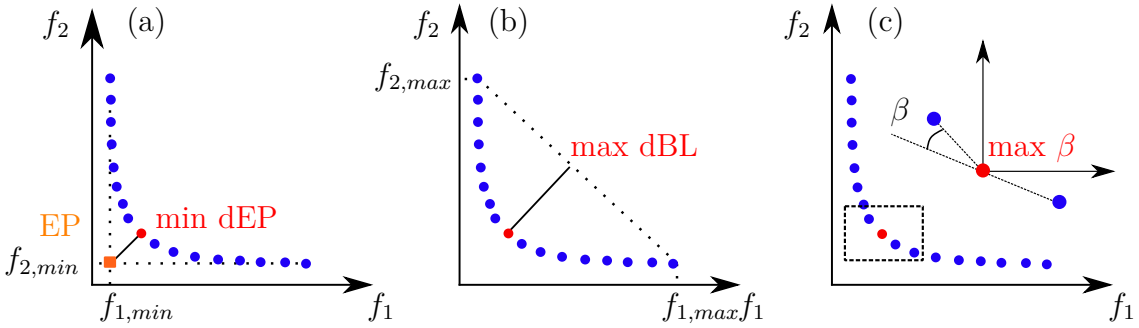

Figure 5.10: Criteria for obtaining knee point: minimum distance from equilibrium point - min dEP (a), maximum distance from boundary line - max dBL (b), maximum band angle - max β (c).

In this study, the harmony search algorithm [156] (HSA) was utilised to obtain the Pareto front. HSA is a metaheuristic optimisation algorithm inspired by musicians' efforts to create a piece of music with perfect harmony. When improvising, a musician can do so in three ways: (i) reproducing a known tune from memory, (ii) playing a variation of a known tune (by slightly adjusting the pitch, i.e. the frequency) or (iii) composing new, i.e. random, notes. These three methods correspond to the three components of the HSA optimization process: harmony memory usage, pitch adjustment and randomisation. Like other metaheuristic algorithms, HSA employs high-level strategies combined with lower-level techniques (such as trial and error) for exploring and exploiting the search space. A crucial aspect is achieving a good balance between exploring potential new solutions (diversification) and exploiting past solutions to select promising ones (intensification). In HSA, intensification is represented by the harmony memory accepting rate, meaning that good solutions from the memory are more likely to be selected or inherited. Diversification is driven by pitch adjustment and randomisation. Essentially, pitch adjustment refines a local solution, both memory consideration and pitch adjustment ensure that good local solutions are retained, while randomisation enables the algorithm to explore the global search space more widely [156].

HSA-based optimisation approach was adopted due to its high efficiency and low computational cost compared to other metaheuristic algorithms [151]. The optimisation procedure was imple-

mented using Python scripting [141] coupled with the FE analysis in Abaqus/CAE [145]. Control parameters for HSA were set as follows: harmony memory consideration rate HMCR = 0.9, pitch adjustment rate PAR = 0.3 and initial harmony memory size HMS = 50. In each new iteration, 25 new harmonies (HM) were generated. The optimisation would terminate after 100 iterations.

In the following subsections, the described FEMU procedure is applied to align the modal properties of the initial numerical models with their experimentally measured counterparts. The set of updating parameters includes material properties of the elastic supports (three parameters: E_{supp}, ρ_{supp}, ν_{supp}), timber material properties (nine parameters: E_L, E_T, E_R, ν_{LT}, ν_{LR}, ν_{RT}, G_{LT}, G_{LR}, G_{RT}) and inter-panel connection properties, comprising one geometric parameter of the elastic strip (a_{conn}) and three material parameters (E_{conn}, G_{conn}, ν_{conn}). In total, 16 modelling parameters were considered in the FEMU process. The density of C24 timber was excluded from the updating, as it was considered reliably determined from experimental measurements. Global SAs based on Spearman rank correlation coefficients, presented in the subsequent Subsection 5.3.1, will reveal the extent to which each of these 16 parameters affects the natural frequencies and MAC values of the numerical models. Low sensitivity parameters will be excluded from the FEMU to reduce model complexity and computational cost.

5.3.1 Spearman rank correlation-based sensitivity analysis

Two global SAs were carried out independently. The first studied the material properties of the elastic supports and the selected C24 timber properties of the single-panel floor, while the second focused on the geometric and material properties of the elastic strip. All 16 modelling parameters were assumed to be statistically uncorrelated and normally distributed, with mean values specified in Table 5.1 and a common COV of 15%. Note that this simplified representation of the modelling parameters was adopted solely for the purpose of these two global SAs. More realistic characterisation of the parameters' variability is investigated in Section 6.1. Latin Hypercube Sampling (LHS) method [157] was used to generate 500 samples for each of the considered parameters. Two matrices containing Spearman correlation coefficients are illustrated in Figures 5.11 and 5.12. Spearman rank coefficients of 1 and -1 indicate a perfect monotonic relationship between a modelling parameter and the corresponding natural frequency or mode shape, with positive and negative signs denoting increasing and decreasing trends, respectively. Parameters with the Spearman coefficient between -0.2 and $+0.2$ exhibit negligible monotonic relationship with corresponding modal properties. They were considered non-effective [158], so they were excluded for a better perception and clarity of the results.

Figure 5.11 shows that several modelling parameters exhibit negligible Spearman rank correlation with the modal properties of the single-panel floor. In particular, no meaningful monotonic relationship is observed for the elasticity modulus E_R, Poissons coefficients ν_{LR} and ν_{RT}, shear modulus G_{LR} and elastic support density ρ_{supp}. In contrast, a strong monotonic relationship is identified between elasticity modulus of support E_{supp} and Poissons coefficient ν_{supp} and both the natural frequency and mode shape of the RBM 3, as well as MAC values of several deformation modes. However, these support parameters do not influence natural frequencies of deformation modes. Transverse elasticity modulus E_T and Poissons coefficient ν_{LT} exhibit notable rank correlation only with higher mode shapes, specifically the 6th, 8th, and 9th. The most influential parameters are the longitudinal elasticity modulus E_L and shear moduli G_{LT} and G_{RT}, which show consistently high Spearman correlation with both natural frequencies and MAC values of deformation modes. This observation is in line with the findings reported

in a previous numerical study [113]. C24 timber properties generally exhibit no influence on the RBM 3, except the shear modulus G_{LT} which affects its mode shape. Notably, the natural frequency and MAC value of the second mode are influenced only by E_L.

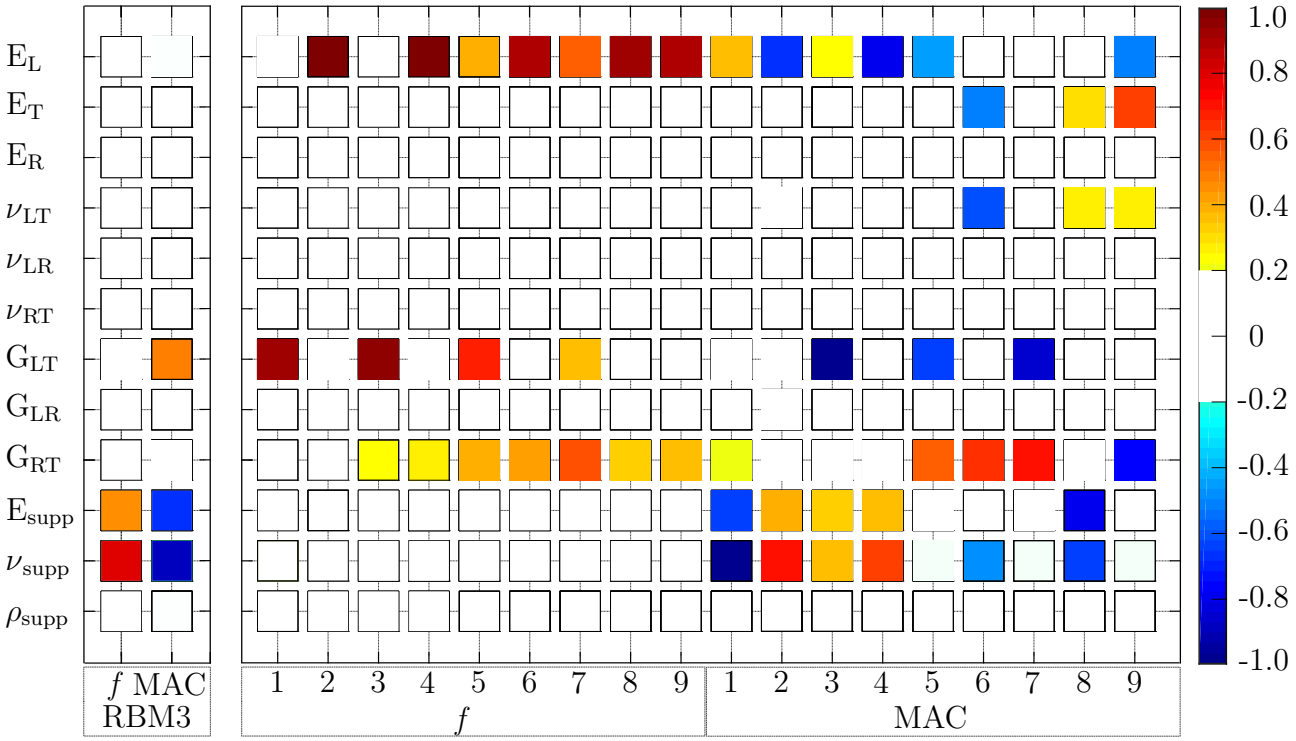

Figure 5.11: Spearman's correlation coefficients between timber and elastic support material properties, and single-panel floors numerical frequencies and MAC values.

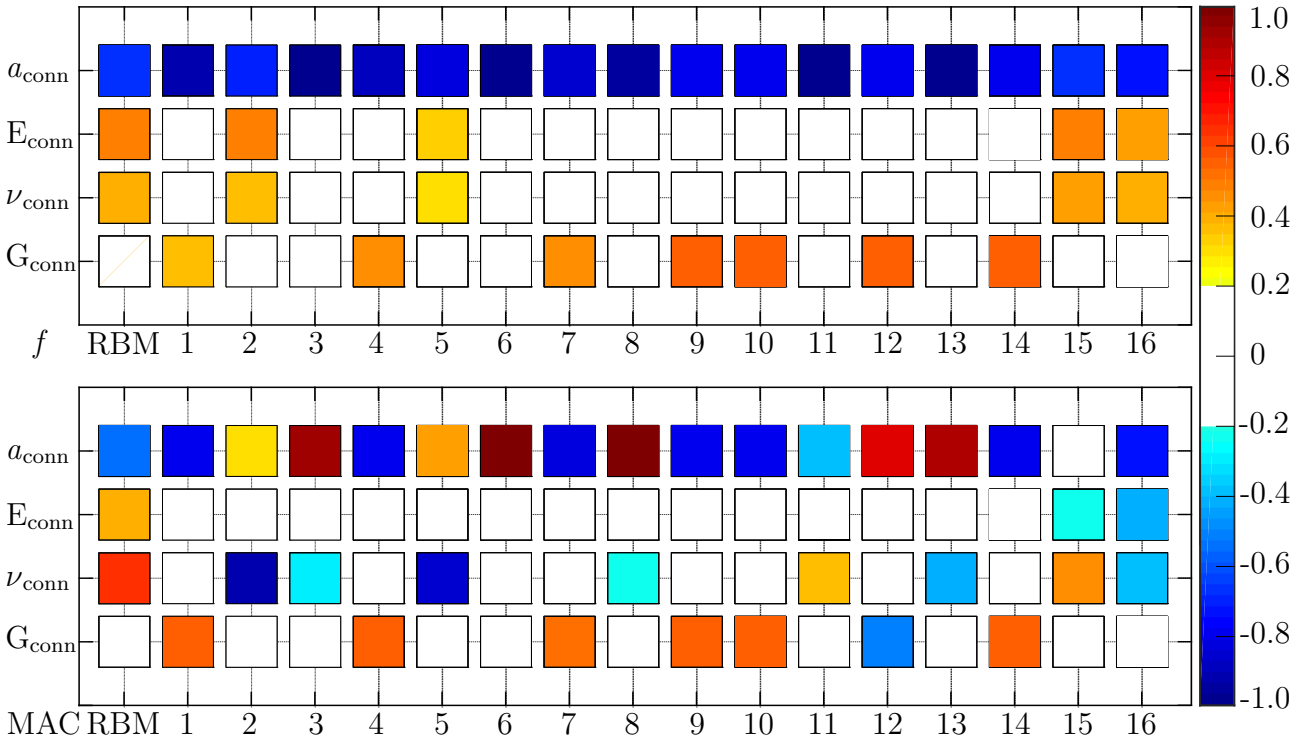

Figure 5.12: Spearman's correlation coefficients between connection properties and two-panel floors numerical natural frequencies (up) and MAC values (down).

Figure 5.12 indicates that the width of elastic strip a_{conn} is the most influential connection parameter. It exhibits a strong monotonic relationship with nearly all natural frequencies of the

two-panel floor, affecting them in a relatively uniform manner. The corresponding Spearman rank coefficients are consistently negative, indicating that a reduction in the elastic strip's width increases the overall stiffness of the connection and, consequently, increases the natural frequencies. In addition, a_{conn} shows pronounced influence on the MAC values of almost all modes. The shear modulus of elastic strip G_{conn} demonstrates a notable monotonic influence on both natural frequencies and mode shapes of modes 1, 4, 7, 9, 10, 12, and 14. In contrast, these modes show negligible sensitivity to changes in the elastic modulus E_{conn} and Poisson's ratio ν_{conn}. Conversely, the natural frequencies of the RBM and modes 2, 5, 15, and 16 are primarily affected by E_{conn} and ν_{conn}, while exhibiting little to no sensitivity to changes in G_{conn}.

Insights gained from the global SAs guided the formulation of a step-by-step FEMU procedure for the single-panel and two-panel floors (Figure 5.13), presented in Sections 5.3.2 and 5.3.3. The values of non-influential parameters E_R, ν_{LR}, ν_{RT}, G_{LR} and ρ_{supp} were fixed at their initial values listed in Table 5.1. The remaining sensitive modelling parameters of both the elastic supports and timber material were updated using the experimentally measured modal properties of the single-panel floor (Section 5.3.2). Specifically, the initial values of E_{supp} and ν_{supp} were updated based on the natural frequency and MAC value of the RBM 3. E_L was then updated using the modal properties of the second deformation mode, while E_T, G_{LT}, G_{RT} and ν_{LT} were calibrated using deformation mode 1 and modes $3-9$. In the second step, the optimised parameters obtained for the single-panel floor were transferred to the numerical model of the two-panel floor, which became the initial model for the FEMU featuring optimisation of the elastic strip parameters. An initial attempt was made to optimise the elastic strip parameters in two stages: first the strip width and G_{conn} by fitting modes 1, 4, 7, 9, 10, 12 and 14 and subsequently E_{conn} and ν_{conn} by fitting the RBM and modes 2, 3, 5, 6, 8, 11, 13, 15, and 16. However, this two-stage FEMU led to unrealistic deviation of elasticity modulus E_{conn} from its initial value and caused

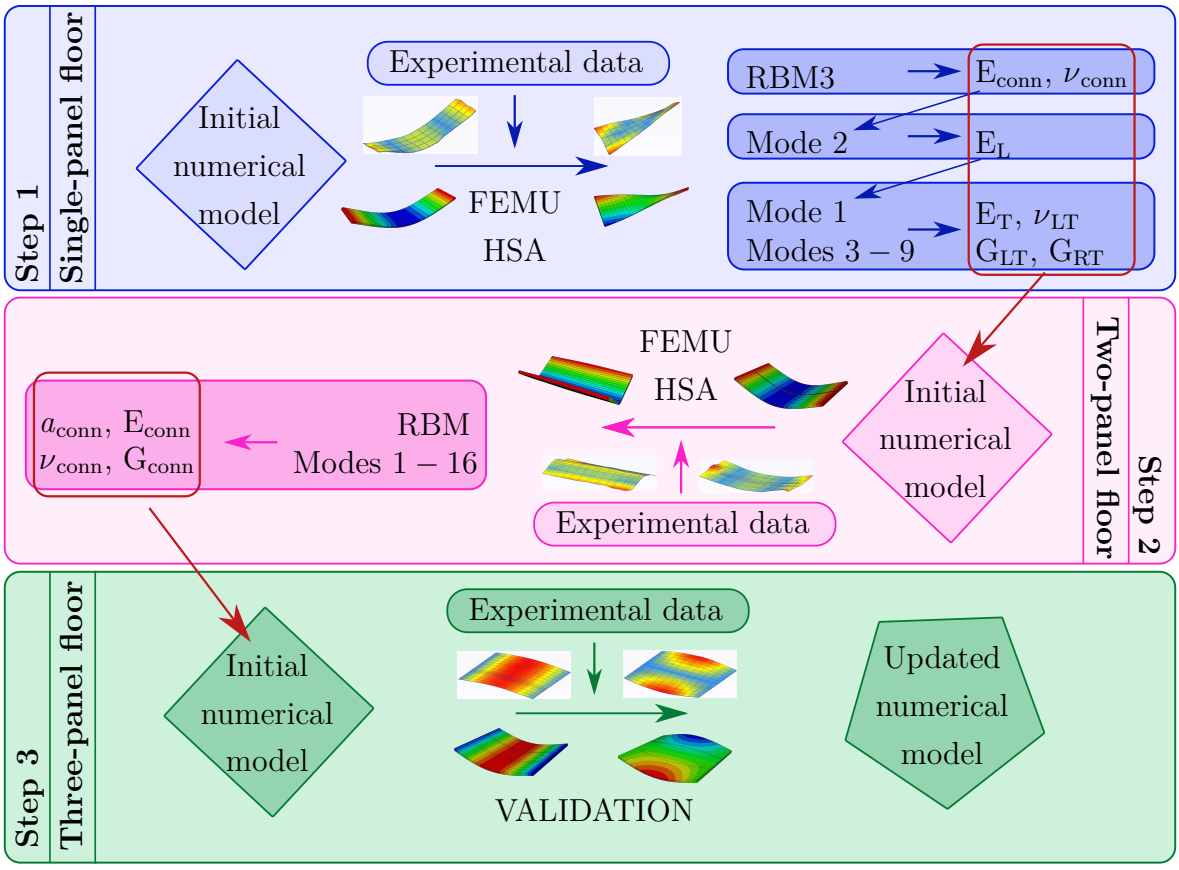

Figure 5.13: Algorithm to optimise FE modelling parameters.

unintended changes in natural frequencies that the second global SA marked as insignificant. For this reason, the FEMU presented in Section 5.3.3 was carried out by optimising all four parameters simultaneously. Finally, in the third step, the parameters updated through the first two steps were validated against the experimentally measured modal properties of the three-panel floor (Section 5.3.4).

5.3.2 Updating elastic support and timber material properties

Modelling parameters were varied within the bounds specified in Table 5.1. The material properties of the elastic supports were allowed to deviate within ±10% of their mean values, resulting in ranges $6063 - 7411\text{N/m}^2$ for E_{supp} and $0.423 - 0.517$ for ν_{supp}. As Poisson's ratio of an ideally elastic material cannot exceed 0.5, the upper limit of ν_{supp} was set to 0.499. Due to the substantial uncertainty in timber material, bounds of ±30% around the mean values were adopted for these parameters, leading to ranges of $259 - 481\text{MPa}$, $0.343 - 0.637$ and $483 - 897\text{MPa}$ for E_T, ν_{LT}, and G_{LT}, respectively. Note that timber is orthotropic material for which Poisson's ratio may exceed 0.5. Two exceptions were made to the ±30% bounds. Experimentally determined value of E_L was allowed to deviate within ±10%, resulting in a range of $10118 - 12366\text{MPa}$. In contrast, G_{RT}, considered to be the most uncertain parameter [159], was assigned a wider interval of $30 - 70\text{MPa}$, corresponding to a deviation of ±40%.

Changes in a material parameters may lead to change in the mode order. The reference mode order was defined based on the experimentally identified modes. At each FEMU iteration, numerical modes were matched to experimental ones using the maximum MAC value. The dense measurement grid (Figure 4.2) yielded well-resolved mode shapes and, consequently, reliable MAC values, allowing unambiguous mode identification.

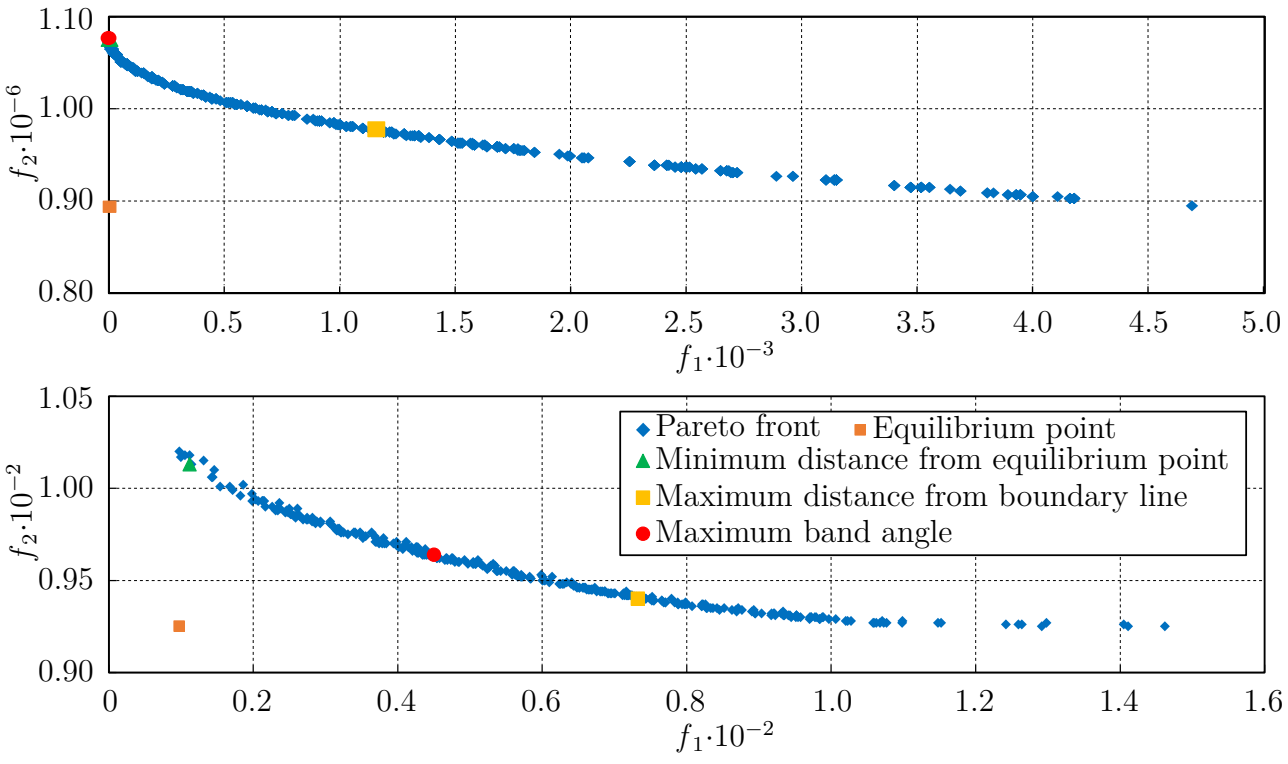

Figure 5.14: Pareto front for updating parameters E_{supp} and ν_{LT} (up), E_T, G_{LT}, G_{RT} and ν_{LT} (down), and optimal solutions obtained using three different criteria for the "knee" point.

The Pareto fronts obtained during FEMU of E_{supp} and ν_{LT}, as well as E_T, G_{LT}, G_{RT} and ν_{LT} are shown in Figure 5.14. The optimisation process led to negligible changes in objective function f_2, whereas a substantial reduction was achieved in f_1. Applying previously mentioned three different criteria for identifying the "knee" point resulted in three candidate optimal solutions, as illustrated in 5.14. Given that changes in f_2, associated with mode shapes, were minor compared to changes in f_1, associated with natural frequencies, the solution corresponding to the minimum f_1 among these candidates was selected as the best optimal solution for each stage of this optimisation step.

Natural frequencies and MAC values of the updated single-panel floor model are reported in Table 5.5. For easier comparison of the results, relative errors between the experimentally measured and numerically predicted natural frequencies and MAC values for both initial and updated models are illustrated in Figure 5.15. The FEMU procedure had a negligible effect on already high initial MAC values. On the other hand, a close agreement between the updated numerical and experimentally obtained natural frequencies was achieved, indicating a substantial improvement of the initial numerical model. For the first four deformation modes and RBM 3, the relative error of the updated model is bellow 1%. The largest error remains for mode 7, but reduced from 6.78% to 4.06%.

Table 5.5: Experimentally measured and numerically determined natural frequencies and MAC values of updated model of the single-panel floor.

Mode #	f_{exp} [Hz]	$f_{updated}$ [Hz]	$\mathbf{Error_{updated}}^*$[%]	$\mathbf{MAC_{updated}}$
RBM 3	9.75	9.75	0.01	0.997
1	19.50	19.66	0.83	0.934
2	20.33	20.49	0.79	0.955
3	39.25	39.35	0.26	0.999
4	49.00	49.07	0.15	0.995
5	68.75	67.74	−1.47	0.998
6	87.00	87.85	0.98	0.984
7	108.25	103.86	−4.06	0.997
8	119.25	117.57	−1.41	0.946
9	123.50	120.96	−2.19	0.774

* Error = $(f_{updated} - f_{exp}) \times 100 / f_{exp}$ [%]

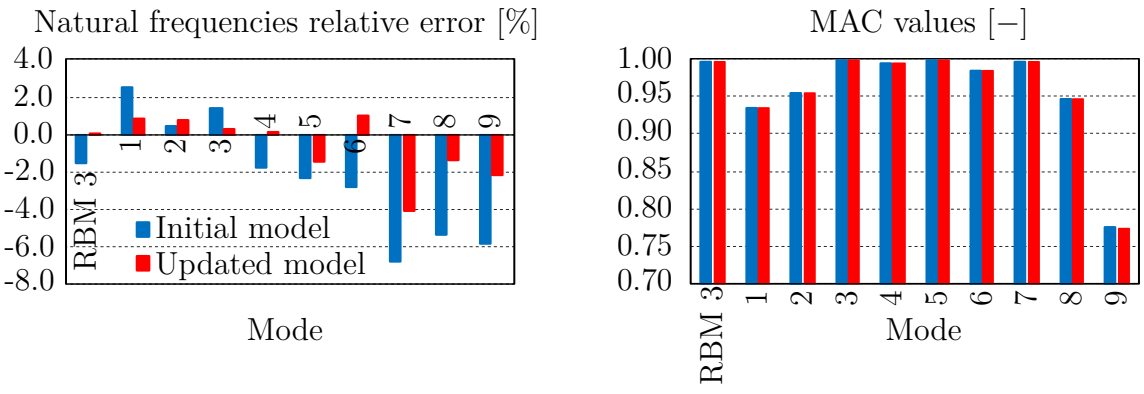

Figure 5.15: Relative errors between experimentally and numerically determined natural frequencies and MAC values for both initial and updated model of the single-panel floor.

Updated parameters obtained in the first FEMU step, together with the relative error with respect to their initial values are listed in Table 5.6. As expected, the smallest relative error (1.4%) corresponds to the experimentally determined E_L. In contrast, the shear modulus G_{RT} exhibits the largest relative error, exceeding 33%, and reaching the upper bounds of the values documented in [159]. Referring to the results of global SA shown in Figure 5.11, E_T and ν_{LT} were identified as the least sensitive of all studied parameters. Consequently, substantial adjustments of their initial values were required to induce noticeable changes in the floors modal properties, leading to deviations exceeding 25% for E_T and 17% for ν_{LT}. Furthermore, FEMU led to 8.6% reduction in G_{LT}, causing the relative error of the first natural frequency to drop from 2.53% to 0.83%. The elastic modulus E_{supp} increased by 6.3% relative to its initial value, while the corresponding Poissons ratio ν_{supp} was slightly reduced.

Table 5.6: Updated properties of elastic support and C24 material and relative error compared to the initial values.

$\mathbf{E_{supp}}$ [Pa]	$\nu_{\mathbf{supp}}$ [−]	$\mathbf{E_L}$ [MPa]	$\mathbf{E_T}$ [MPa]	$\nu_{\mathbf{LT}}$ [−]	$\mathbf{G_{LT}}$ [MPa]	$\mathbf{G_{RT}}$ [MPa]
71639	0.466	11084.34	464.45	0.407	630.72	66.56
+6.3%	−0.86%	−1.4%	+25.5%	−17%	−8.6%	+33.1%

5.3.3 Updating connection properties

In the FEMU procedure, the width of the elastic strip was constrained to vary within the range of $40 - 80$mm, while E_{conn}, G_{conn} and ν_{conn} were allowed to vary without the predefined bounds. These parameters represent effective material properties of the equivalent elastic strip and therefore have fictitious rather than physical values. Obtained Pareto front featuring three candidate "knee" points is illustrated in Figure 5.16. In this case, both objective functions f_1 and f_2 exhibit comparable sensitivity to changes in the connection properties. All three criteria used to identify the "knee" point resulted in similar optimal solutions. The best optimal solution was selected to best match vibration modes up to 30Hz, which are the only relevant for human-induced vibration analysis. This solution corresponds to the "knee" point identified using the maximum band angle criterion.

Values of the updated connection parameters are summarised in Table 5.7. The updated elastic modulus E_{conn} is reduced by more than 96% compared to its initial estimate. As discussed in Section 5.1, the initial value of E_{conn} was derived based on the rotational stiffness expression proposed by Macpherson et al [84], which is based on static load-deflection test of half-lapped joints in beam specimens. Measured vertical displacements in those tests, ranging from 4 to 12mm, are several orders of magnitude larger than the vibration amplitudes typically observed in long-span floors [160]. Therefore, this expression is not suitable for representing connection stiffness under vibration serviceability conditions. The updated Poissons ratio of the elastic strip ν_{conn} is 24.5% lower than the initial value listed in Table 5.1. In contrast, the relative error between the updated and initial shear modulus G_{conn} is negligible, supporting the presumption that connection transfers the full shear force.

Experimentally measured and numerically calculated modal parameters after the two FEMU steps are compared in Table 5.8. Relative errors between experimentally and numerically determined natural frequencies and MAC values for both initial and updated model are depicted in Figure 5.17. Relative errors between the RBM, 2th and 5th natural frequencies of the initial numerical model and their experimental counterparts exhibited the most notable reduction

after the second FEMU step. The values of these errors decreased from 93.76%, 19.61% and 7.48% to 4.03%, 1.75% and 2.14%, respectively. On the other hand, the relative error between the numerically calculated and experimentally measured natural frequencies of modes 6, 9, 10, 12, and 14 increased after the FEMU. However, given that the highest relative error of the updated natural frequency is still less than 3%, this increase can be neglected. Similar as in case of the single-panel floor, MAC values are less sensitive to changes in the material and connection properties than corresponding natural frequencies. For modes 1, 4, 7 and 15, MAC values remain unchanged, while MAC values for the RBM and modes 11 and 12 of the updated model are a bit lower than their initial counterparts.

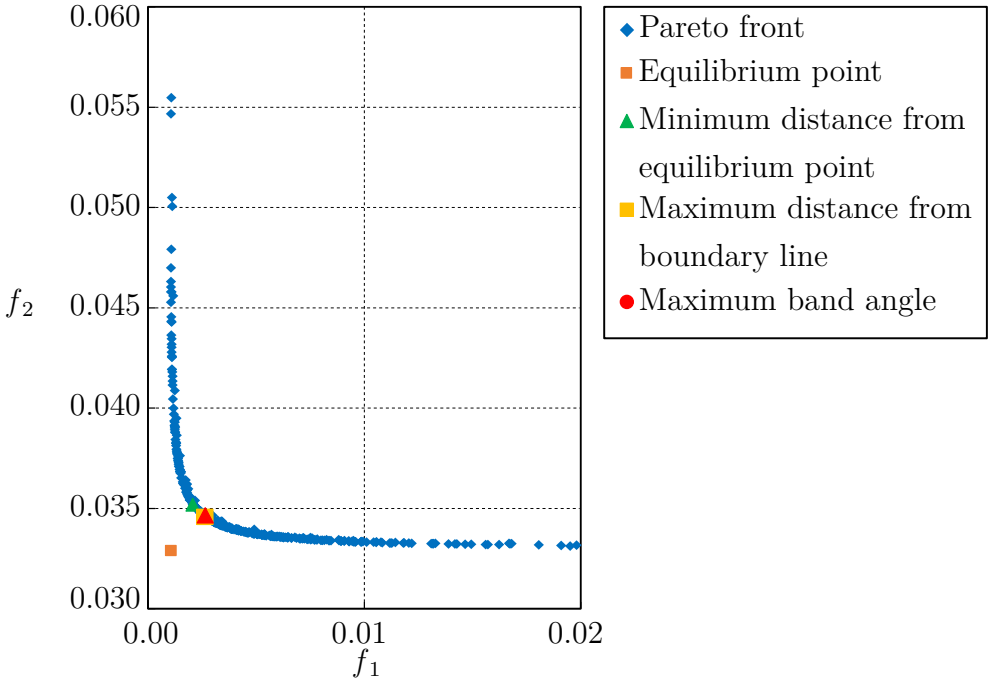

Figure 5.16: Pareto front for updating connection parameters and optimal solutions obtained using three different criteria for the "knee" point.

Table 5.7: Updated connection properties and relative error compared to the initial values.

$\boldsymbol{a}_{\mathbf{conn}}$ [mm]	$\mathbf{E}_{\mathbf{conn}}$ [MPa]	$\nu_{\mathbf{conn}}$ [−]	$\mathbf{G}_{\mathbf{conn}}$ [−]
40	0.34	0.36995	306.53
−50%	−96.16%	−24.50%	+0.17%

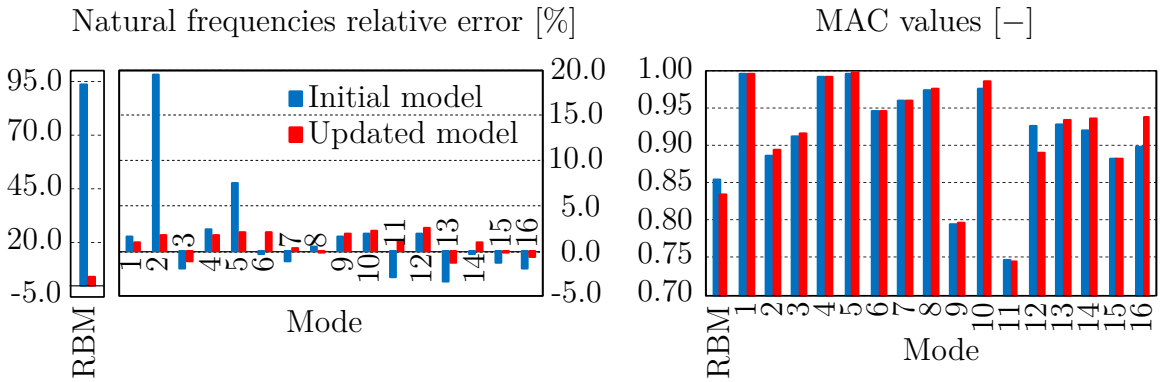

Figure 5.17: Relative errors between experimentally and numerically determined natural frequencies and MAC values for both initial and updated model of the two-panel floor.

Table 5.8: Experimentally measured and numerically determined natural frequencies and MAC values of updated model of the two-panel floor.

Mode #	f_{exp} [Hz]	$f_{updated}$ [Hz]	$\mathbf{Error_{updated}}^{*}$[%]	$\mathbf{MAC_{updated}}$
RBM	7.38	7.67	4.03	0.834
1	13.25	13.38	1.01	0.995
2	20.00	20.35	1.75	0.893
3	20.63	20.40	−1.09	0.916
4	26.75	27.22	1.76	0.991
5	39.63	40.47	2.14	0.998
6	48.13	49.10	2.02	0.946
7	55.00	55.18	0.32	0.960
8	69.50	69.46	−0.06	0.975
9	80.13	81.71	1.98	0.796
10	83.25	85.16	2.29	0.986
11	87.25	88.19	1.08	0.745
12	93.50	95.91	2.58	0.889
13	107.88	106.49	−1.29	0.933
14	114.13	115.27	1.01	0.936
15	121.50	121.48	−0.02	0.882
16	125.88	123.03	−0.67	0.937

* $\text{Error}_{\text{updated}} = (f_{updated} - f_{exp}) \times 100 / f_{exp}$ [%]

5.3.4 Validation

The modelling parameters updated in Sections 5.3.2 and 5.3.3 were subsequently implemented in the numerical model of the three-panel floor. The resulting natural frequencies are compared with the experimentally identified counterparts in Table 5.9, while the relative errors between experimentally and numerically determined natural frequencies for both the initial and the updated model are illustrated in Figure 5.18.

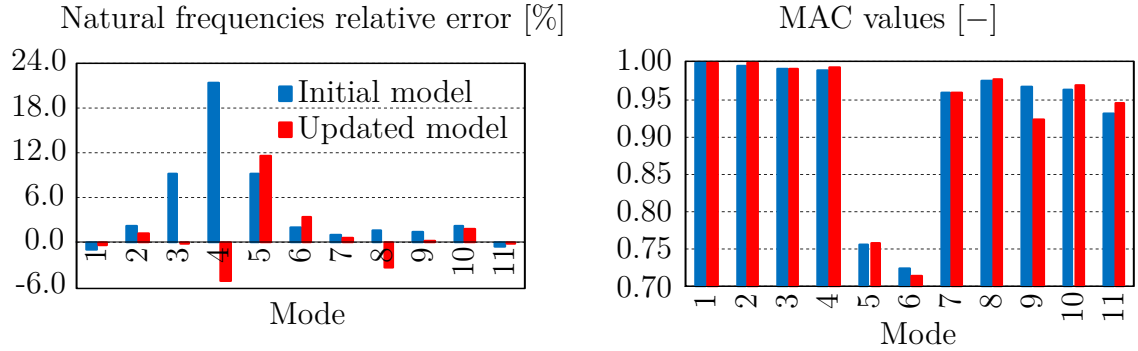

Figure 5.18: Relative errors between experimentally and numerically determined natural frequencies and MAC values for both initial and updated model of the three-panel floor.

The relative error between the fundamental frequency of the initial numerical model and the experimentally measured value, already small at 0.95% was further reduced to 0.24% after the FEMU. The most evident reduction in relative errors after the FEMU can be observed for modes

3 and 4, in which the inter-panel connections were most actively engaged, indicting a substantial improvement in modelling their stiffness. Larger relative errors persist between the updated and experimental natural frequencies is for modes 5 and 6, i.e. 11.52% and 3.53%, respectively. These errors are even greater than for the initial model. However, as already discussed in Section 5.2.4, modes 5 and 6 are affected by experimental imperfections and these errors can be disregarded. Apart from modes 5 and 6, an increase in relative error is observed only for mode 8, while all remaining modes exhibit reduced errors following FEMU. The corresponding MAC values remain unchanged or slightly improved for all modes, with minor reductions observed only for modes 6, 7 and 9.

Table 5.9: Experimentally measured and numerically determined natural frequencies and MAC values of updated model of the three-panel floor.

Mode #	$\boldsymbol{f_{exp}}$ [Hz]	$\boldsymbol{f_{updated}}$ [Hz]	$\mathbf{Error_{updated}}^{*}$[%]	$\mathbf{MAC_{updated}}$
1	8.40	8.38	−0.24	0.999
2	10.20	10.33	1.27	0.998
3	14.60	14.60	−0.03	0.990
4	19.60	18.60	−5.09	0.993
5	28.00	31.23	11.52	0.758
6	32.20	33.34	3.53	0.714
7	38.00	38.27	0.70	0.958
8	45.20	43.70	3.33	0.976
9	69.80	69.91	0.16	0.924
10	98.80	100.60	1.82	0.969
11	124.25	124.11	−0.11	0.945

* $\text{Error}_{\text{updated}} = (f_{updated} - f_{exp}) \times 100 / f_{exp}$ [%]

5.4 Two dimensional numerical models

The floor models examined so far featured the 3D representation of the actual floor. However, such detailed 3D FE models are computationally inefficient for uncertainty analysis. Therefore, further analyses in this dissertation employ 2D representation of multi-panel floors. The three-panel floor was re-modelled in Abaqus/CAE using S4R finite element, i.e. conventional 4-node shell element with reduced integration and a composite layer section. The 2D model incorporated the timber and connection properties updated in Sections 5.3.2 and 5.3.3. Simply supported boundary conditions were applied along the two parallel edges as illustrated in Figure 5.19. Obtained results are then compared to both experimental and that of a 3D numerical model in Section 5.4.1.

The considered three-panel floor has experimental fundamental frequency of 8.4Hz and is therefore classified as a low-frequency floor (LFF) [41]. In order to achieve a comprehensive uncertainty analysis of CLT floors, both low- and high-frequency floors (HFF) should be addressed. Accordingly, an additional HFF configuration was derived by reducing the span of the three-panel LFF model, while keeping all other floor properties unchanged (Section 5.4.2). It should be noted that this numerical HFF floor does not have its experimental counterpart. Finally,

resulting LFF and HFF models presented in the following subsections constitute the final numerical models used in the subsequent uncertainty analyses of modal properties (Chapter 6) and pedestrian-induced vibration response (Chapter 9).

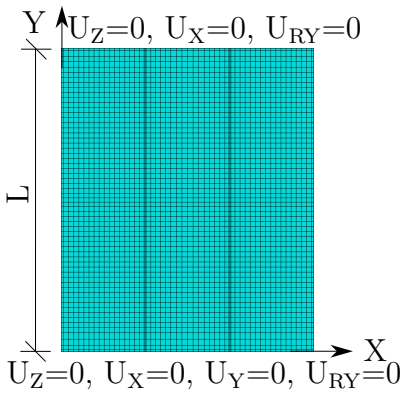

Figure 5.19: Two-dimensional FE model with boundary conditions. For LFF L = 6m, for HFF L = 5m

.

5.4.1 Low-frequency floor

Natural frequencies obtained using a 2D model of three-panel LFF are compared with the experimentally measured counterparts in Table 5.10, along with the calculated MAC values. Numerically calculated modal masses m_{2D} for each mode, needed for further analyses in Chapters 6 and 9, are provided in Table 5.10 as well. The corresponding mode shapes are illustrated in Figure 5.20.

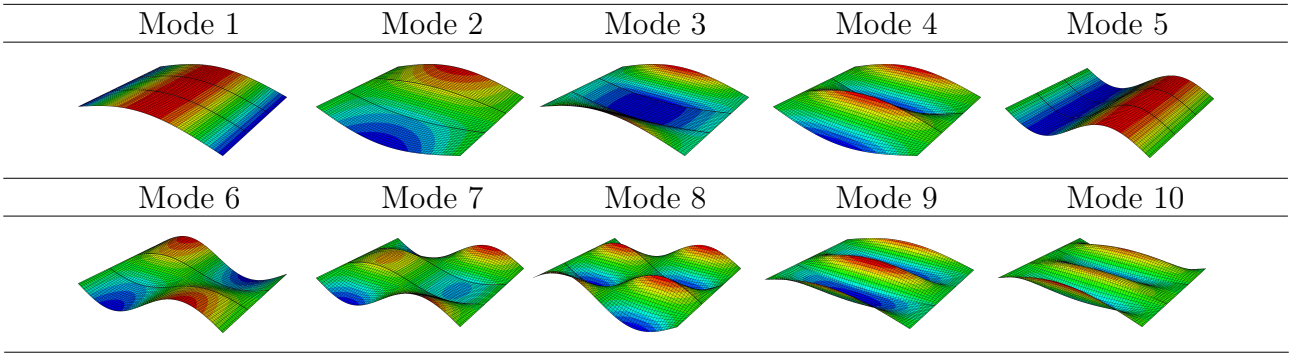

Figure 5.20: Numerically determined mode shapes for 2D model of LFF

Relative errors between the experimentally and numerically determined natural frequencies and the MAC values for 3D and 2D models are shown in Figure 5.21. Note that only modes up to 100Hz are listed, as their uncertainty will be evaluated in Chapter 6. The relative error between the experimentally measured and numerically predicted natural frequencies obtained using the 2D model is below 1% for four out of the ten identified modes. Excluding modes 5 and 6, which are affected by measurement imperfections and exhibit the largest discrepancies, the maximum remaining error is 3.36% for mode 4. The average absolute relative error across all ten vibration modes is 2.73% for the 2D model, compared to 2.77% for the 3D model. When modes 5 and 6 are excluded, the average errors reduce to 1.21% and 1.58% for the 2D and 3D models, respectively. The mean MAC value is 0.93 for both models, increasing to 0.97 when modes 5 and 6 are omitted. Overall, these results indicate that 2D and 3D numerical models provide an equally accurate representation of the experimentally measured modal properties.

Table 5.10: Experimentally and numerically determined natural frequencies, numerically determined modal masses and MAC values for 2D model of the three-panel LFF.

Mode #	f_{exp} [Hz]	$f_{\mathbf{2D}}$ [Hz]	**Error$_{\mathbf{2D}}$***[%]	**MAC$_{\mathbf{2D}}$**	$m_{\mathbf{2D}}$ [kg]
1	8.40	8.42	0.24	0.999	939.0
2	10.20	10.10	−1.03	0.998	398.1
3	14.60	14.67	0.50	0.990	245.0
4	19.60	18.94	−3.36	0.993	320.9
5	28.00	31.79	13.53	0.748	908.6
6	32.20	33.52	4.10	0.708	408.0
7	38.00	38.83	2.17	0.953	260.0
8	45.20	44.80	−0.89	0.974	321.2
9	69.80	69.80	−0.01	0.963	331.0
10	98.80	100.26	1.48	0.966	223.9

* $\text{Error}_{2D} = (f_{2D} - f_{exp}) \times 100 / f_{exp}$ [%]

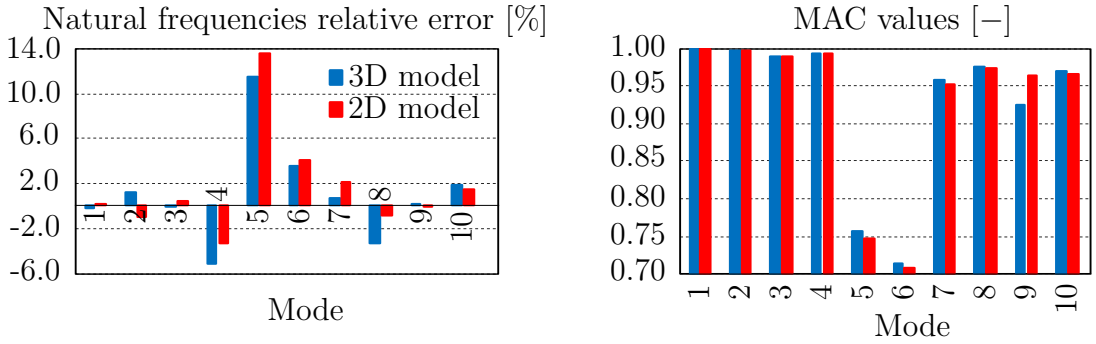

Figure 5.21: Relative errors between experimentally and numerically determined natural frequencies and MAC values for 3D and 2D models of the three-panel LFF.

5.4.2 High-frequency floor

The numerical model of the HFF was obtained by modifying the previously developed two-dimensional three-panel floor model, reducing the span from 6m to 5m. In addition, the thickness of each layer was increased from 3cm to 5cm, resulting in a total floor thickness of 25cm. The resulting natural frequencies and modal masses are summarised in Table 5.11, while the corresponding mode shapes are illustrated in Figure 5.22. With a fundamental frequency of 19.06Hz, the floor is indeed classified as a HFF according to CCIP-016 [41]. Although only 8 modes with frequency lower than 100Hz were identified, all modes corresponding to the previously developed LFF model (modes $1-9$ and 15) are further analysed for consistency.

5.5 Chapter summary

In this chapter, the FE models of the low- and high-frequency floors were developed, starting with three 3D FE models of CLT floors comprising one, two, and three panels. The inter-panel connections were modelled as an equivalent elastic strip, as recommended by Paolini et al. [83], while the initial values of the parameters describing this strip were estimated follow-

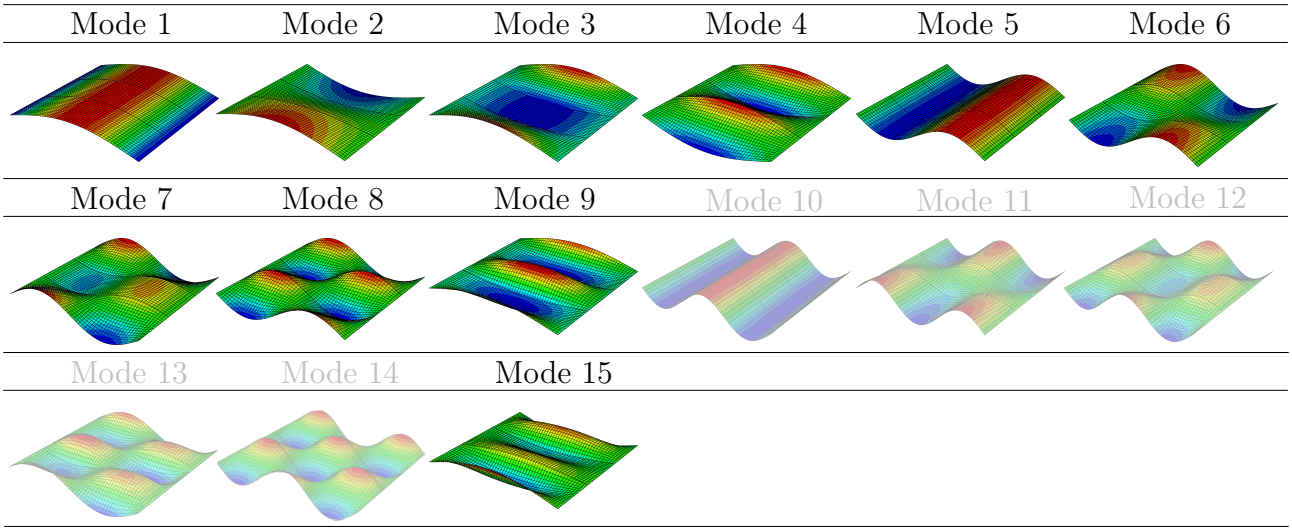

Figure 5.22: Numerically determined mode shapes for 2D model of HFF

Table 5.11: Numerically determined natural frequencies and modal masses for 2D model of the three-panel HFF.

Mode #	$\boldsymbol{f_{2D}}$ [Hz]	$\boldsymbol{m_{2D}}$ [kg]
1	19.06	1311.0
2	21.69	552.0
3	28.91	349.9
4	35.86	458.1
5	63.61	1251.0
6	65.90	549.8
7	73.09	387.7
8	81.83	476.1
9	101.08	459.4
10	116.70	1096.0
11	118.52	533.9
12	124.91	444.8
13	124.98	490.8
14	134.17	508.0
15	140.21	368.8

ing Macpherson et al. [84]. The unknown parameters of the LFF numerical model, i.e. the boundary conditions, timber material properties, and inter-panel connection properties, were identified, and the model was validated through a three-step FEMU procedure using experimentally measured modal properties of the three considered floor configurations (Chapter 4).

A Spearman rank correlation-based sensitivity analysis revealed that the timber material parameters E_R, ν_{LR}, ν_{RT} and G_{LR} have negligible influence on the natural frequencies and mode shapes of the single- and two-panel floors. Consequently, their values were kept as recommended by [148]. The first step of the three-step FEMU procedure involved determining the material properties of the elastic supports and selected timber material properties by fitting the natural frequencies and mode shapes of the single-panel FE model to their experimental counterparts.

The modulus of elasticity and Poisson's ratio of the elastic supports were identified by fitting the natural frequency and mode shape of RBM 3. Furthermore, fitting the 2nd natural frequency and mode shape yielded the timber longitudinal modulus of elasticity. Matching the numerical natural frequencies and mode shapes of modes 1 and $3-9$ to the experimental ones resulted in values of the timber material parameters E_T, ν_{LT}, G_{LT} and G_{RT}. The second step included updating the width of the elastic strip and its modulus of elasticity, Poisson's ratio and shear modulus such that the natural frequencies and mode shapes of the two-panel floor FE model matched the corresponding experimentally measured ones. Finally, validation was performed by comparing the natural frequencies and mode shapes of the three-panel floor FE model with the measured results.

The modulus of elasticity of the elastic strip, i.e. the parameter governing its rotational stiffness, was found to be significantly lower, by 96%, than the initial value calculated according to Macpherson et al. [84]. This discrepancy may arise because Macpherson et al. [84] derived the stiffness from static deflection tests, where displacement amplitudes are several orders of magnitude larger than those typical of vibration response. Moreover, the shear modulus of the half-lapped joint connection was identified as approximately equal to the shear modulus of a homogeneous cross-section equivalent to the actual five-layer CLT cross-section, indicating complete shear transfer through the connection.

The detailed 3D FE models are not suitable for routine engineering calculations, nor for the uncertainty analyses presented later in Chapters 6 and 9. Therefore, a 2D FE model of the three-panel floor was developed and shown to provide accuracy comparable to the 3D model at a substantially lower computational cost. Finally, since this dissertation includes analyses of both LFF and HFF, a corresponding 2D model of the HFF was developed as well.

6 Uncertainty analysis of modal properties of CLT floors

This chapter studies the uncertainty in natural frequencies and modal masses of CLT floors arising from variability in structural properties, i.e. timber material properties and parameters of the equivalent elastic strip representation of inter-panel connections. UQ and Sobol' indices-based SA for both LFF and HFF are carried out using PCE metamodels validated via SFEM, resulting in identification of a small set of influential parameters that govern the total variability of considered modal properties. Accordingly, reduced metamodels are developed and they provide a reliable basis for further uncertainty analysis of floor vibration response under pedestrian load. A part of the study elaborated in this chapter has been published in *Milojević M. et al. (2025) Uncertainty analysis of CLT floor vibrations due to inherent variability in structural properties. Journal of Building Engineering, 97, pp.110682*[161].

The level of uncertainty assigned to the timber material properties was defined based on findings reported in the literature, in order to ensure that the predicted output variability closely reflects the reality (Section 6.1). The influence of uncertainties in timber material and inter-panel connections on the natural frequencies and modal masses of both LFF and HFF was then investigated in Sections 6.2 and 6.3, respectively. Modes up to 100Hz were considered to assess whether the variability of input parameters affects these modal properties at both lower and higher frequencies in a similar manner. For both floor types, UQ was performed using two independent approaches: (i) SFEM based on 10,000 MC simulations and (ii) replacing the FE model with the PCE metamodel introduced in Section 3.3. In this way, the metamodel-based UQ results were validated against the SFEM. SA based on Sobol' indices method was subsequently carried out using the PCE metamodel and Eq. (3.27) to identify parameters with negligible influence on the output variability. Based on these findings, model reduction was carried out, resulting in the refined PCE metamodels that retain only the influential parameters (Sections 6.2.4 and 6.3.4) and are further used for the uncertainty analysis of the vibration response in Chapter 9. Key finding of this chapter are summarised in Section 6.4.

6.1 Characterisation of uncertainties

Each FE representation of the three-panel floor developed in previous chapter initially comprised 14 modelling parameters, including ten timber material properties, the width of the elastic strip and three material properties of the strip. However, these parameters do not

contribute equally to the floor's modal properties. A global SA based on the Spearman rank correlation coefficient (Section 5.3.1) showed that four timber material properties, i.e. elastic modulus E_R, Poisson's ratios ν_{LR} and ν_{RT} and shear modulus G_{LR}, exhibited negligible monotonic relationships with the natural frequencies and mode shapes. Therefore, these four parameters were considered non-influential and were further treated as deterministic, using the values listed in Table 5.1. The remaining ten parameters were considered uncertain. Their spatial variability due to local variations and imperfections such as knots was not considered in this study. Therefore, all uncertain parameters were modelled as random variables following normal distributions, which is the common practice in PCE metamodeling [111].

Uncertainties in the timber material parameters reported in the literature, whether obtained from experimental testing, recommended values, or adopted from previous studies, are summarised in Table 6.1. The corresponding mean values and COV adopted in this study are listed in Table 6.2. A COV of 10% was assumed for timber density ρ, which is in line with the values reported in the literature. Although longitudinal elasticity modulus E_L has been reported with COVs as high as 23% (Table 6.1), a value of 15% was adopted, as it is closer to the median of the published data. The same COV was assumed for E_L, ν_{LT} and G_{LT}, due to the lack of reliable and consistent information on their variability. Furthermore, for the most uncertain timber material parameter, i.e. rolling shear G_{RT}, a 20% COV was assumed.

Table 6.1: Literature review on uncertain timber material properties.

Source	**Property**	**COV** [%]	**Remarks**
Forest Products Laboratory [162]	ρ	10	Testing results from approximately 50 species of green wood.
	E_L	22	
Kasal and Anthony [163]	ρ	$5-13$	Reported range.
	E_L	$9-23$	
Joint Committee on Structural Safety [164]	ρ	10	Recommended value.
	E_L	13	
Lim et al. [165]	E_L	22.14	Based on tested 113 samples of untreated lumber.
	G_{RT}	20.36	
Wang et al. [166]	G_{RT}	$9-25$	Tested 5 groups of CLT samples, 10 samples per group.
Yin et al. [167]	ρ	12.24	Based on tested 600 samples of fast-growing Chinese fir lumbers.
	E_L	15.59	
Lim et al. [111]	ρ	9.10	Used in UQ analysis of timber joist floor, based on testing done in [109].
	E_L	13.38	
	G_{LT}, G_{RT}	12.59	
Faculty of Civil Engineering, University of Belgrade	ρ	10.50	CLT sample tests done according to EN 408 [168], ISO 13061-2 [169].
	E_L	14.80	

Knowledge regarding the four modelling parameters describing the equivalent elastic strip is limited, primarily due to the lack of extensive experimental data. Hence, a high level of uncertainty was assumed for each of these parameters, and a COV of 20% was assigned to each parameter (Table 6.2). Damping ratio ζ of any structure is highly uncertain modal property [170], and CLT floors are no exception [75, 79]. Experimental modal analysis of 24 identical

CLT beam-like substructures showed variations of up to ±45% around the median damping value [171]. However, unlike other modal properties, damping ratio cannot be calculated numerically. Therefore, it was described in this study as an independent variable which affects vibration response only (Chapter 9), while the analysed modal properties were assumed equal to those of the corresponding undamped system, which is common practice for lightly damped structures such as CLT floors. A 20% COV was assumed to represent its uncertainty (Table 6.2). Although mode-dependent damping ratios were measured (Table 4.1), a value of 1.04% corresponding to the first mode was adopted as the mean damping ratio for all modes in the vibration response analysis in Chapter 9.

Table 6.2: Properties of uncertain modelling parameters of CLT floor.

Modelling parameter	**Distribution type**	**Mean value**	**COV** [%]
C24 timber material			
ρ	Normal	424 kg/m^3	10
E_L	Normal	11084.34 MPa	15
E_T	Normal	464.45 MPa	15
ν_{LT}	Normal	0.407	15
G_{LT}	Normal	630.72 MPa	15
G_{RT}	Normal	66.56 MPa	20
Elastic strip			
a_{conn}	Normal	40 mm	20
E_{conn}	Normal	0.34 MPa	20
ν_{conn}	Normal	0.37	20
G_{conn}	Normal	306.53 MPa	20
Damping			
ζ	Normal	1.04 %	20

6.2 Low-frequency floor

Assuming zero correlation among the uncertain parameters, the Sobol sequence sampling technique [172] was utilised to generate datasets of varying sizes for PCE metamodel training. Sobol sequences are known to provide a more uniform and space-filling coverage of the input space compared to commonly used LHS [157]. However, for the validation via SFEM, a dataset of 10,000 points was generated using the LHS technique to make the difference [111, 172].

6.2.1 Training and validation of PCE metamodel

Two key parameters govern the development of a PCE metamodel: the polynomial order (p) and the size of training dataset (n). The former determines the total number of polynomial terms in the truncated expansion (Eq. (3.25)), while the latter specifies the number of samples required for training the metamodel. In this study, second- ($p = 2$) and third-order ($p = 3$) metamodels were considered, while the first-order ($p = 1$) metamodel was omitted as it cannot represent interactions between the input parameters. Training datasets comprising 32, 64, 128, 256, 512 and 1024 samples were generated. It should be noted that the Sobol sequence, as a

quadrature rule technique, preserves its space-filling properties when the sample size is a power of two. A root mean square relative error (RMSRE) defined as:

$$\text{RMSRE} = \sqrt{\frac{\varepsilon_\mu^2 + \varepsilon_{\text{COV}}^2}{2}} \cdot 100[\%] \tag{6.1}$$

was used to evaluate the UQ performance of PCE metamodels. In Eq.(6.1), ε_μ and ε_{COV} represent the relative errors between the mean value (μ) and COV, respectively, derived from PCE metamodel (Eq. (3.26)) and those calculated by SFEM, from 10,000 MC simulations:

$$\varepsilon_\mu = \frac{\mu_{\text{PCE}} - \mu_{\text{SFEM}}}{\mu_{\text{SFEM}}}, \quad \varepsilon_{\text{COV}} = \frac{\text{COV}_{\text{PCE}} - \text{COV}_{\text{SFEM}}}{\text{COV}_{\text{SFEM}}}. \tag{6.2}$$

The RMSREs of the natural frequencies and modal masses were calculated separately for each mode, with the results presented in Figures 6.1 and 6.2. Note that dataset comprising 32 training points is excluded from Figure 6.2 as it was insufficient to ensure convergence in the calculation of third-order PCE coefficients. The accuracy of the PCE metamodel increases with larger training sample sizes, eventually reaching a plateau beyond a certain threshold. In this study, the RMRSE for both natural frequencies and modal masses became stable at 128 training sample for second-order metamodel. The third-order metamodel required 512 training samples to achieve stable results across all natural frequencies and modal masses. Furthermore, Figures 6.1 and 6.2 reveal that the RMSRE values for both natural frequencies and modal masses are significantly higher for the 9th and 10th modes, particularly when smaller training dataset is used. This implies a higher degree of nonlinearity in the evaluation of these modal properties compared to the other modes, thereby underscoring the necessity of larger training sample sizes to obtain reliable and accurate predictions.

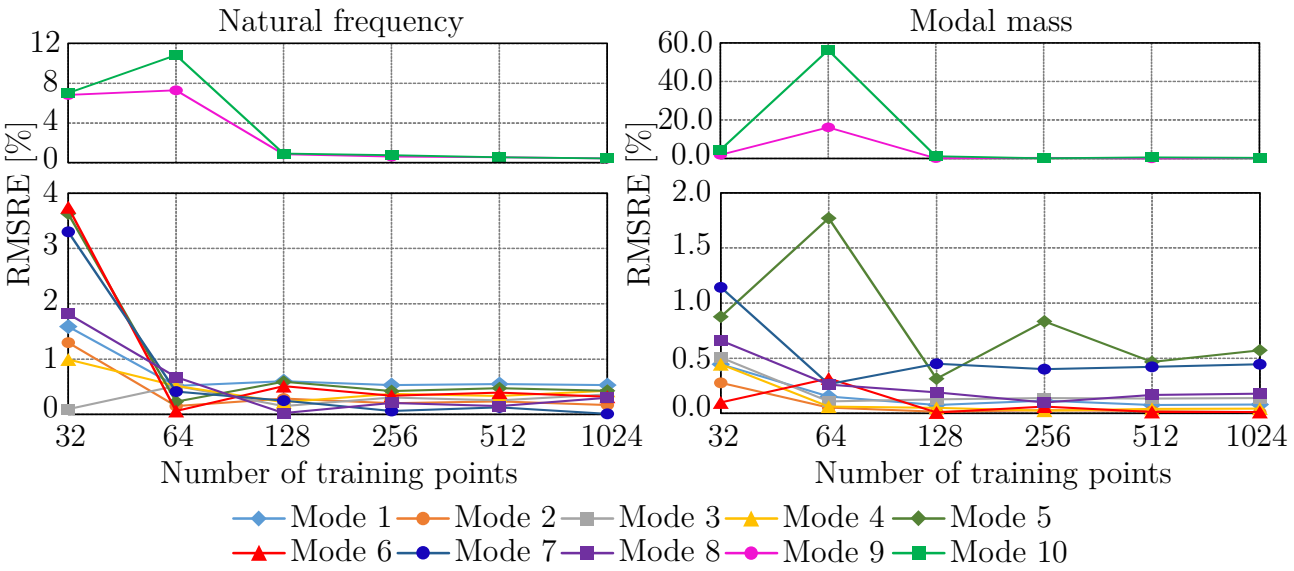

Figure 6.1: Evaluating minimal training sample size for second-order PCE metamodel.

The second-order PCE constructed with 128 training points yields average RMSRE values of 0.44% for ten natural frequencies and 0.25% for the corresponding modal masses. In comparison, the third-order PCE trained with 512 training points achieves slightly lower average RMSRE value of 0.32% for natural frequencies and 0.26% for modal masses. Given that a third-order PCE with ten uncertain variables comprises 286 polynomial terms, whereas a second-order formulation consists of only 66 terms, the latter offers more efficient metamodeling strategy and is therefore adopted for further analysis.

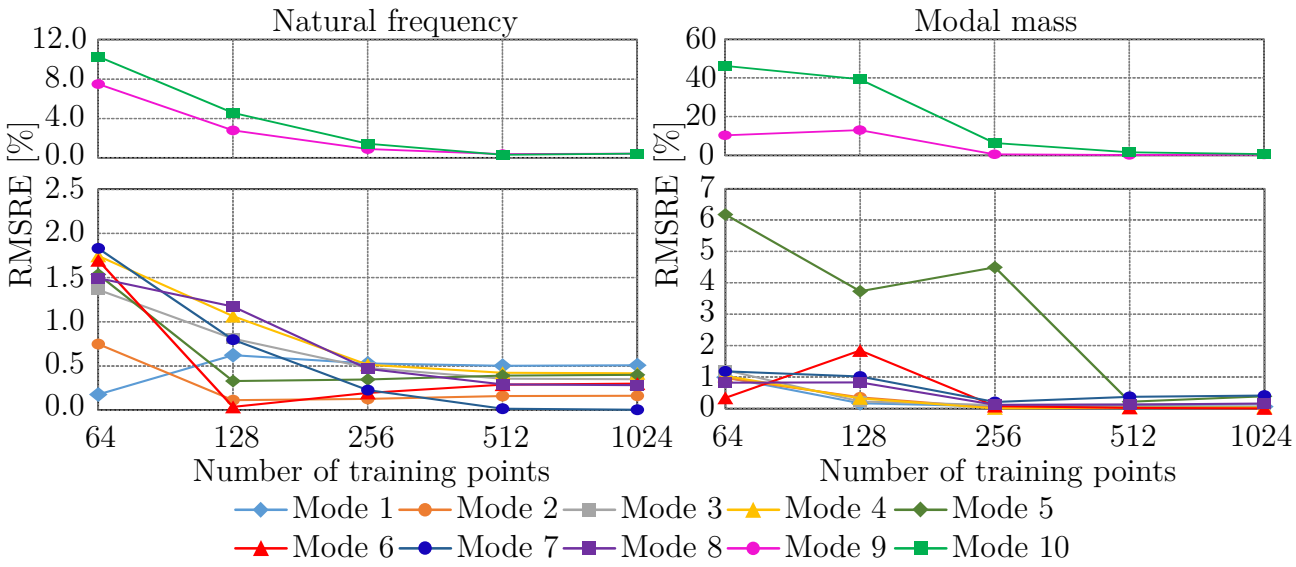

Figure 6.2: Evaluating minimal training sample size for third-order PCE metamodel.

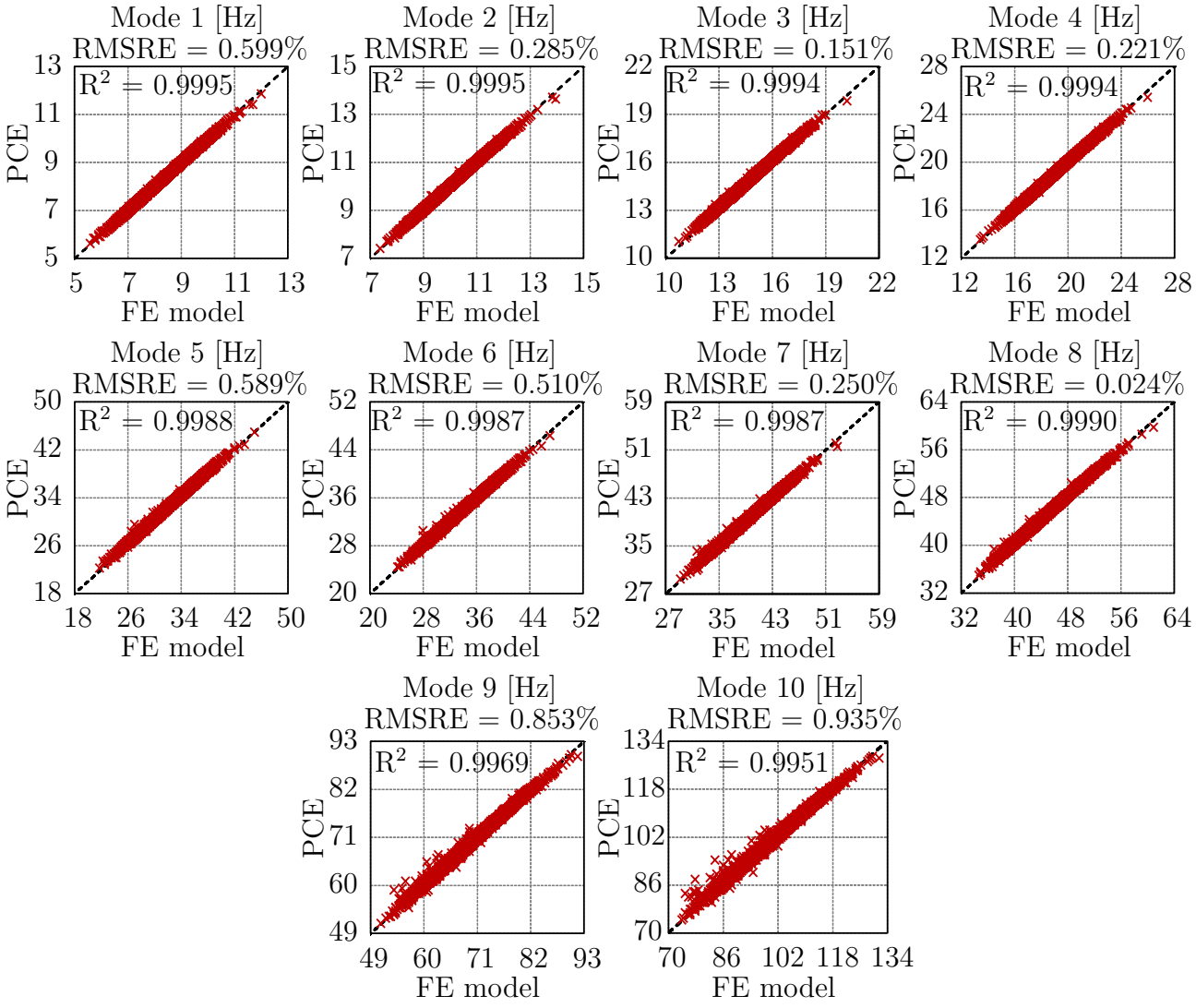

Figure 6.3: Comparison of natural frequencies predicted by the second-order PCE metamodel (n=128) and the FE model.

To further assess the PCE metamodel performance, the same 10,000 input samples employed for SFEM were applied to the developed second-order PCE trained with 128 points. The resulting natural frequencies and modal masses for all ten modes are presented in Figures 6.3 and 6.4, alongside the corresponding values obtained from the FE model. The associated RMSRE and R^2 values are also reported, where $R^2 = 1$ indicates exact replication of the FE model by the metamodel. Exceptionally high R^2 are achieved, exceeding 0.99 for all ten natural frequencies and for eight out of ten modal masses. Slightly lower values of 0.9898 and 0.9747 are obtained for the 5th and 10th modal masses, respectively. Nevertheless, these results generally demonstrate that the PCE metamodel provides an excellent approximation of the FE model.

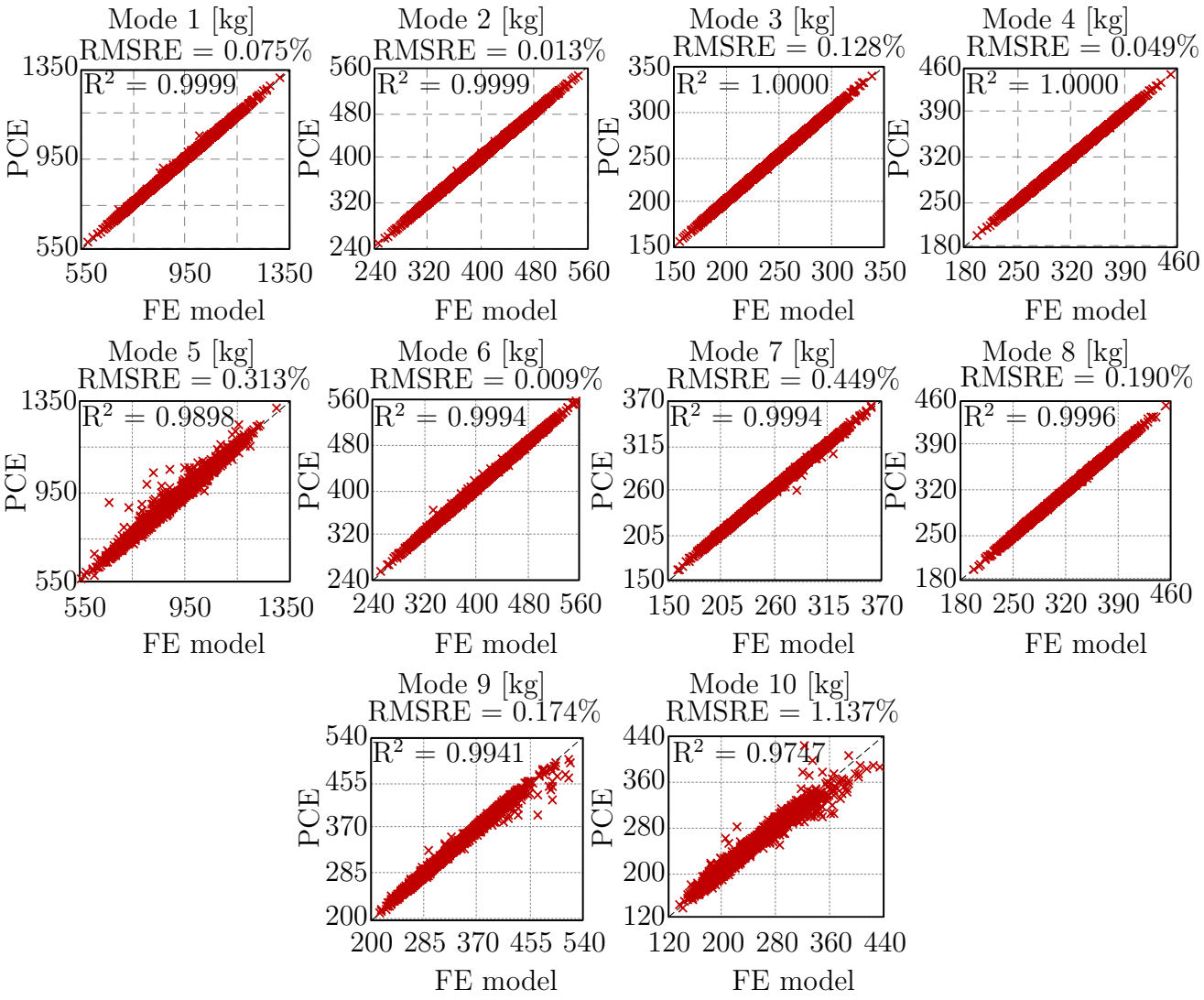

Figure 6.4: Comparison of modal masses predicted by the second-order PCE metamodel (n=128) and the FE model.

6.2.2 Uncertainty analysis of natural frequencies

The UQ results pertinent to the natural frequencies, including mean values, COVs, PDFs and cumulative distribution functions (CDFs) obtained using both PCE and SFEM, are presented in Figures 6.5, 6.6 and 6.7, respectively. The comparison demonstrates that PCE and SFEM provided nearly identical results. Differences in the COVs are below 1% for the first eight vibration modes and below 1.5% for the 9th and 10th modes. Both methods produced COVs within

a narrow range from 6.9 to 8.9%. The highest COV was observed in the natural frequencies of the 1st and 5th vibration modes, both characterised as bending modes.

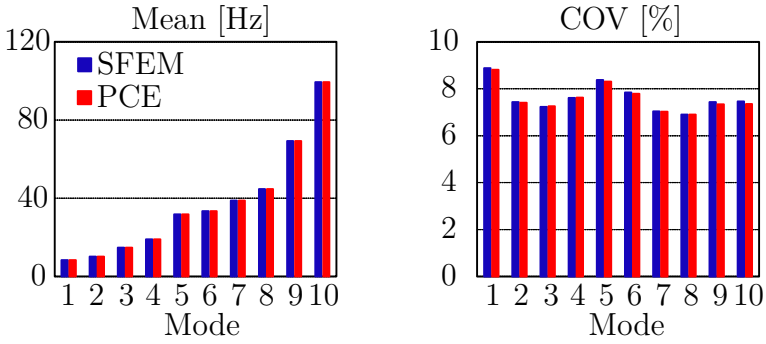

Figure 6.5: Mean values and COVs of natural frequencies obtained using PCE and SFEM.

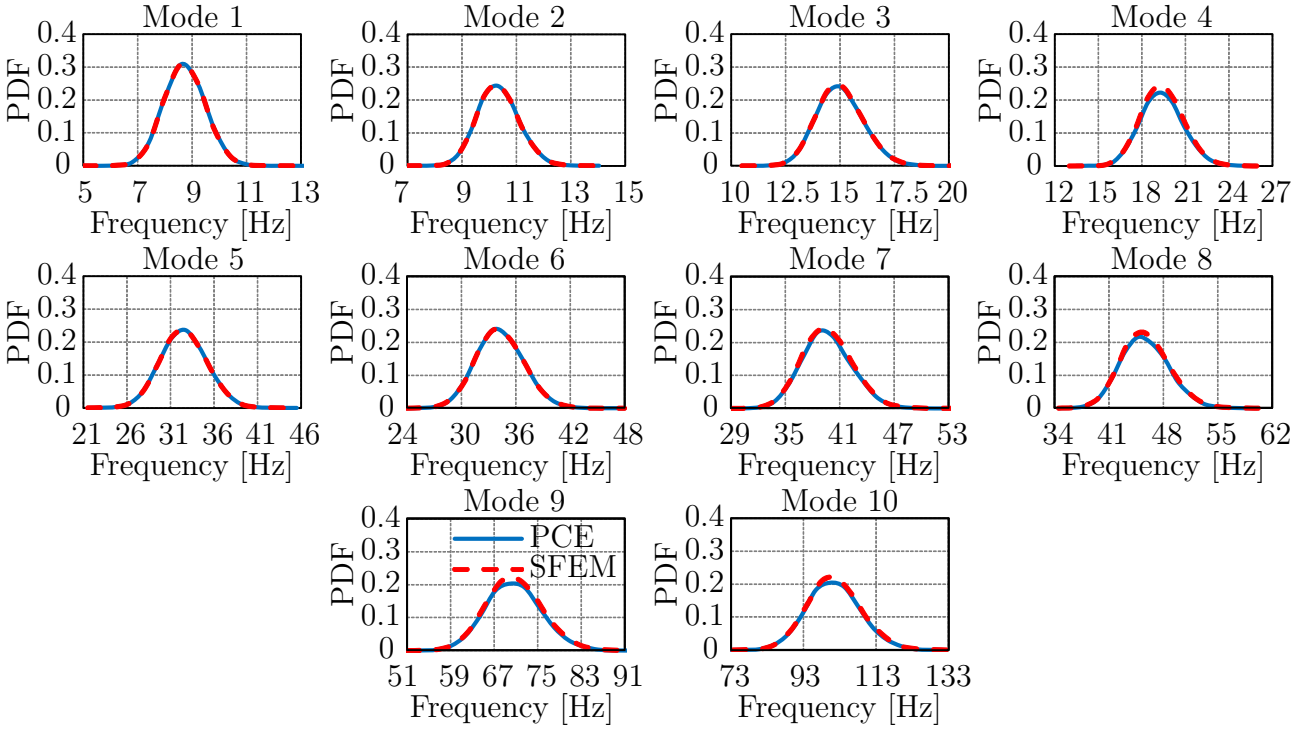

Figure 6.6: PDFs of natural frequencies obtained using PCE and SFEM.

The output of the global SA for natural frequencies are presented in Figure 6.8. The existing literature indicates the absence of universally accepted threshold criteria for Sobol indices. A classification of input parameters based on the values of S_i and S_{T_i} suggested by Cannavo [173] is given in Table 6.3. This classification adopts a relatively strict criterion, in which parameters contributing less that 50% of the total output variance are considered unimportant. On the other hand, Tang et al. [174], Coppitters et al. [175] and Hsieh et al. [176] adopted considerably lower cutoff values for S_i - 0.01, 0.02 and 0.05, respectively. Furthermore, Wei et al. [104] classified an input parameter as influential when S_{T_i} exceeded 0.07, while Zhang et al. [177] and Chan et al. [178] employed threshold values for S_{T_i} of 0.05 and 0.3, respectively. From an engineering standpoint, the present study adopts a pragmatic criterion, neglecting parameters whose contribution to the total variance is below 15% (i.e. $S_{T_i} < 0.15$).

The first and total order indices shown in Figure 6.8 are almost identical for each uncertain parameter across all considered natural frequencies. This behaviour indicates an absence of interaction among the parameters. Moreover, five parameters (E_T, ν_{LT}, E_{conn}, ν_{conn} and G_{conn})

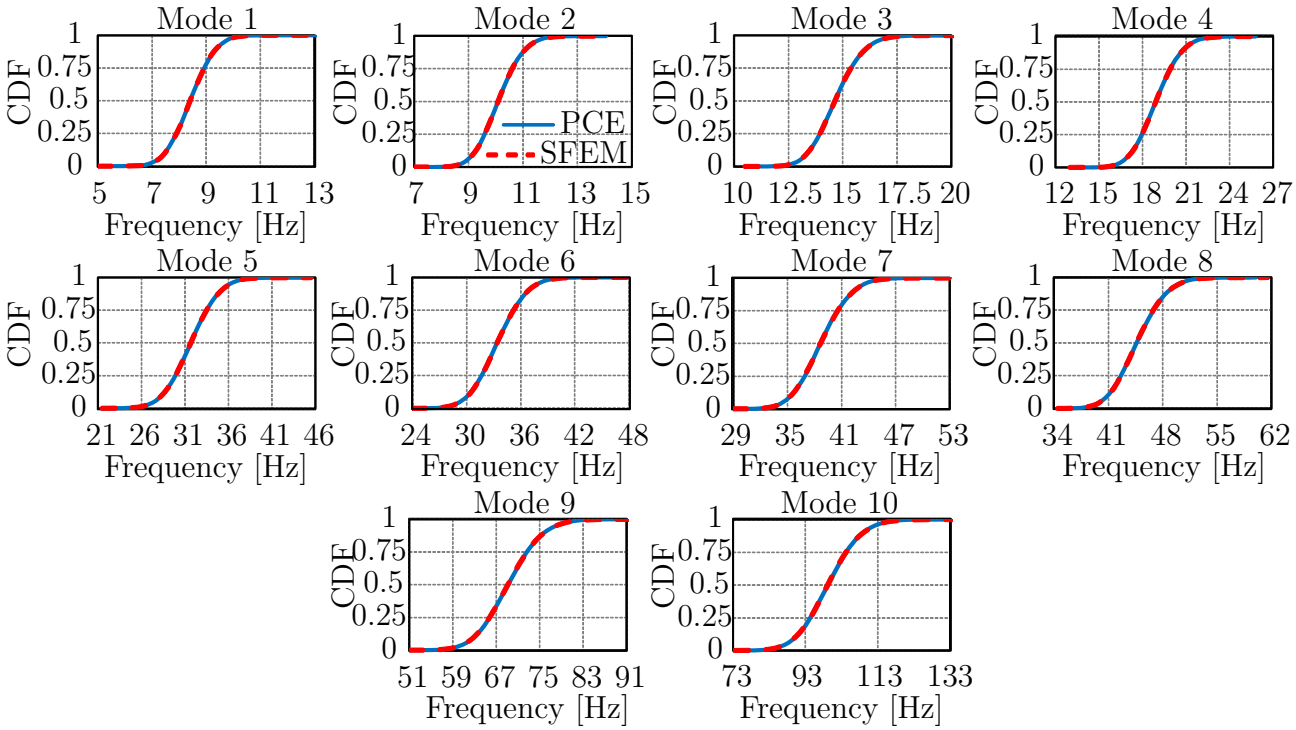

Figure 6.7: CDFs of natural frequencies obtained using PCE and SFEM.

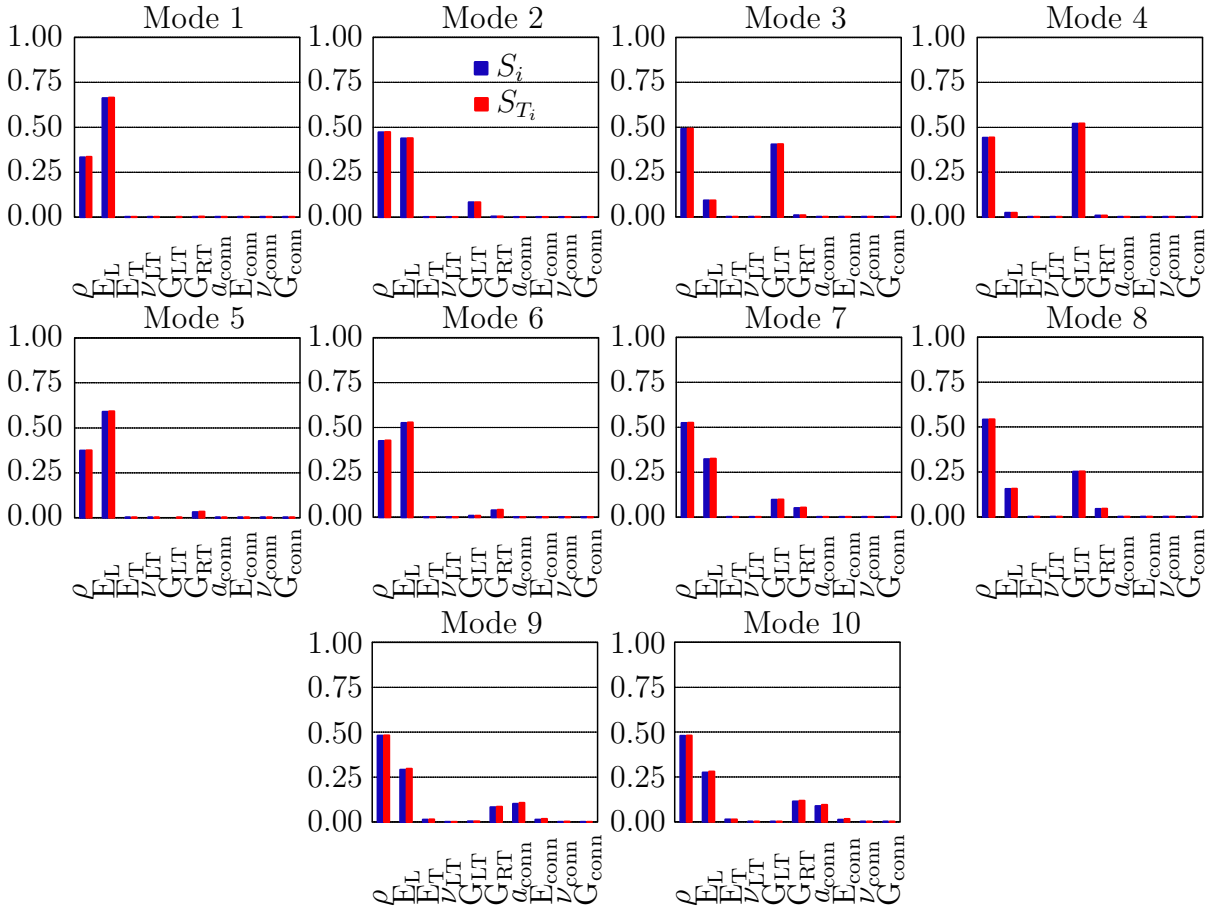

Figure 6.8: First order and total order Sobol' indices for natural frequencies.

Table 6.3: Relevance of an uncertain parameter based on Sobol' indices value [173].

Very important	$0.8 < S_i < S_{T_i} < 1.0$
Important	$0.5 < S_i < S_{T_i} < 0.8$
Unimportant	$0.3 < S_i < S_{T_i} < 0.5$
Irrelevant	$0.0 < S_i < S_{T_i} < 0.3$

exhibited values S_i and S_{T_i} close to zero, demonstrating that their variability has no appreciable influence on the variability of natural frequencies. With S_i and S_{T_i} around 0.1, the width of the elastic strip shows only a minor influence on natural frequencies of 9th and 10th modes. Similarly, the largest S_{T_i} value 0.12 of G_{RT} is observed for the 10th natural frequency. Therefore, both a_{conn} and G_{RT} are classified as non influential parameters for floor's natural frequencies. Finally, only three parameters, i.e. ρ, E_L and G_{LT}, exceeded the threshold value of 0.15. With sensitivity indices ranging from 0.33 to 0.53, timber density shows a substantial influence on the variability of all natural frequencies. The effect of E_L is most pronounced in the bending (the 1st and 5th) modes, for which the corresponding indices reach 0.66 and 0.59, respectively. This observation explains a slightly higher COV values previously noted for these modes. In addition, E_L considerably effects natural frequencies of the 2nd and 6th modes, with indices values reaching 0.44 and 0.53, respectively. Furthermore, the shear modulus G_{LT} has a significant impact on the natural frequencies of the 3rd and 4th modes, both characterised as torsional.

6.2.3 Uncertainty analysis of modal masses

The UQ results for the modal masses, including the mean values, COVs, PDFs and CDFs, are illustrated in Figures 6.9, 6.10, and 6.11, respectively.

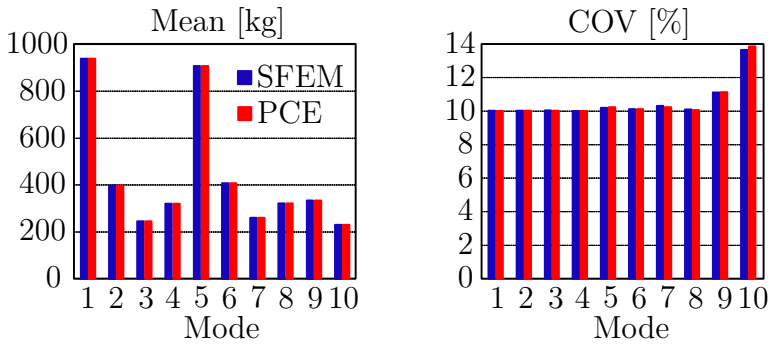

Figure 6.9: Mean values and COVs of modal masses obtained using PCE and SFEM.

Consistent with the findings for natural frequencies, the PCE metamodel reproduces SFEM results with excellent agreement. The only notable difference occurs for the 10th mode, where the COVs obtained by these two methods differ by approximately 1.6%. For the first eight modes, the COVs of the modal masses remained at approximately 10%, consistent with previous numerical findings [113], while higher COVs of 11.14% and 13.87% were obtained for the 9th and 10th modes, respectively. The global SA results presented in Figure 6.12 provide a clear interpretation of these observed COVs. For the first eight modes, ρ is the only influential parameter, indicating that total variability of modal masses in these modes arises solely from variability in timber density. For the 9th and 10th modes, the significant contribution to modal mass variability originates from the modelling parameters of the inter-panel connections, particularly the width of the elastic strip. Since a modal mass is defined as the structural mass

scaled by the corresponding mode shape, the first eight mode shapes of the analysed CLT floor may be regarded as deterministic modal properties. If subsequent analyses were to involve the 9th and 10th modes, the elastic strip width would need to be treated as an uncertain, rendering the associated mode shapes non-deterministic. However, this is not the case in presented study, as the 9th and 10th natural frequencies around 70Hz and 100Hz, respectively, are far too high to be relevant for pedestrian-induced vibrations.

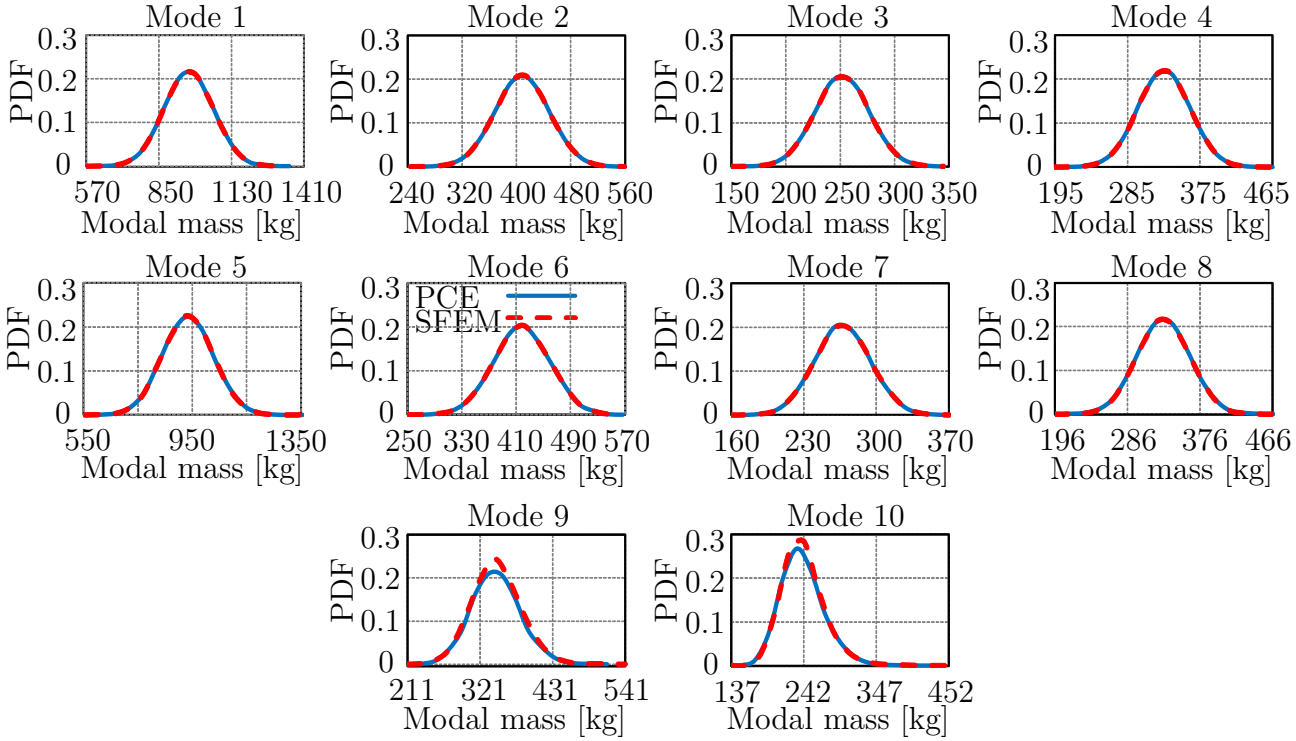

Figure 6.10: PDFs of modal masses obtained using PCE and SFEM.

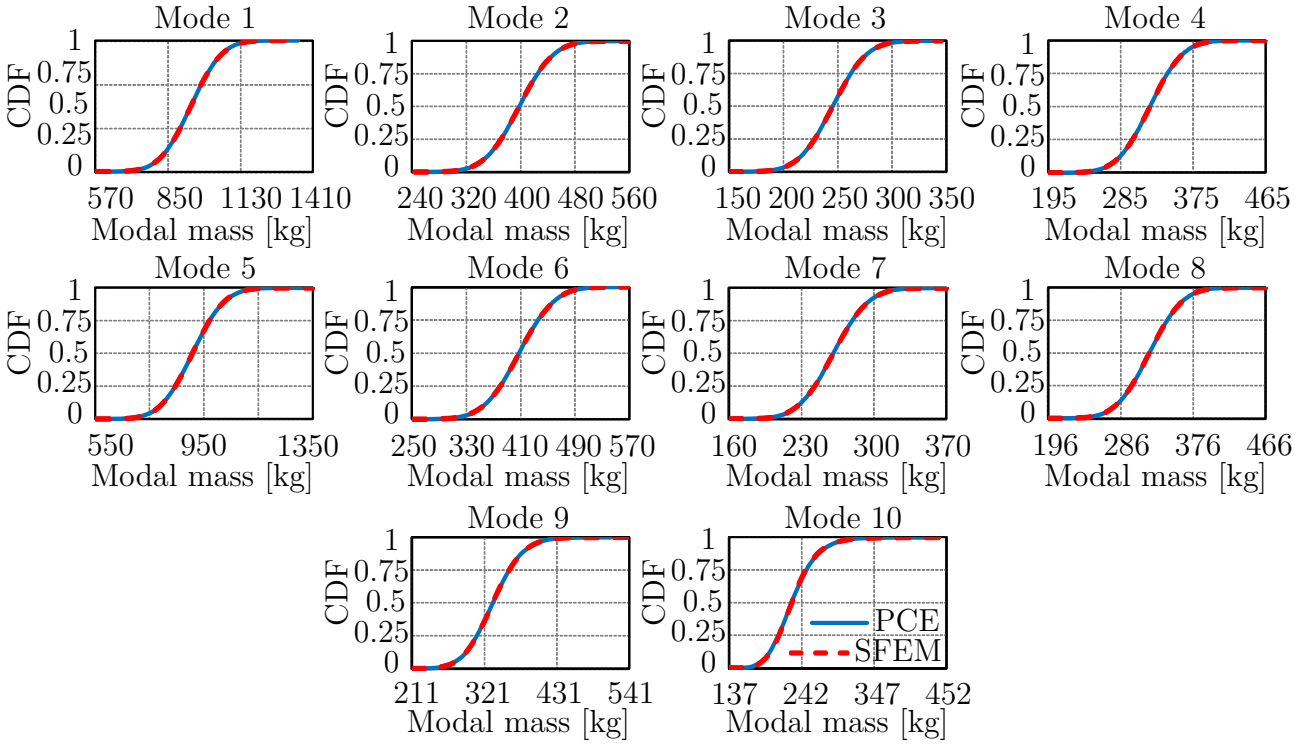

Figure 6.11: CDFs of modal masses obtained using PCE and SFEM.

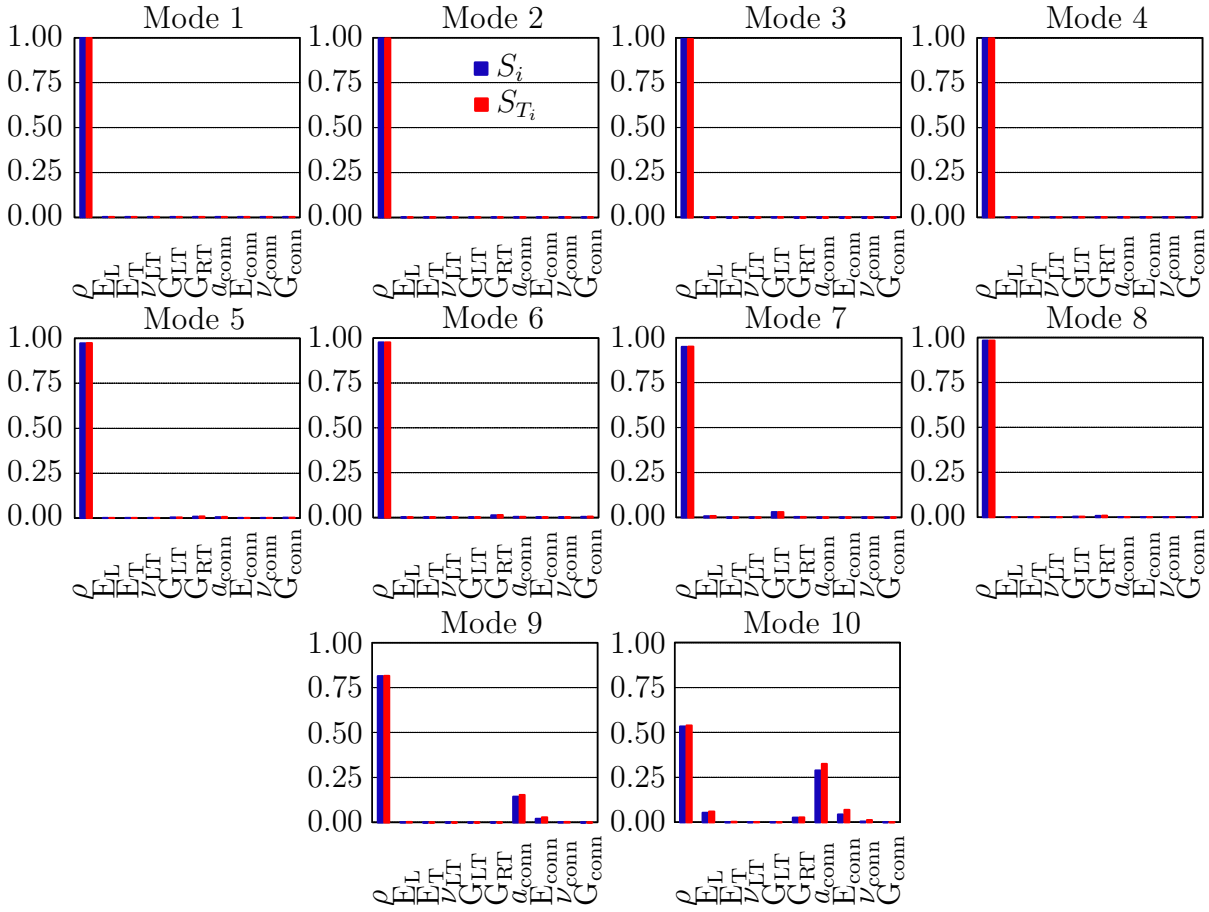

Figure 6.12: First order and total order Sobol' indices for modal masses.

6.2.4 Model reduction: uncertainty analysis considering three uncertain parameters

Variability in the natural frequencies and modal masses of the first eight modes of the considered low-frequency CLT floor is governed by only three out of ten uncertain parameters, i.e. ρ, E_L and G_{LT}. Accordingly, model reduction [117] was carried out and a new refined metamodel was developed, trained and validated for use in subsequent uncertainty analysis of the floor response presented in Chapter 9. This refinement was done only for the first three modes, as these are the only relevant to pedestrian-induced vibrations [41] for the considered LFF.

For the development of the PCE metamodel with three input variables, the same second-order formulation as in the case with ten variables was retained. Training datasets comprising 16, 32, 64, and 128 samples were generated using the Sobol' sequence sampling technique. Given that 128 training samples were sufficient to train a reliable metamodel with ten input variables, it is reasonable to expect that no larger dataset would be required to train a metamodel involving only three input variables. The validation dataset remained unchanged and consisted of 10,000 MC simulations performed on the FE model with ten input variables. As indicated by the RMSRE values for both natural frequencies and modal masses shown in Figure 6.13, a training set comprising 128 samples proved to be the optimal choice. Consequently, a second-order PCE metamodel trained with 128 samples was adopted as a surrogate for the FE model.

UQ and SA for the natural frequencies and modal masses of the first three vibration modes was repeated and validated against the corresponding SFEM analyses performed with ten uncertain

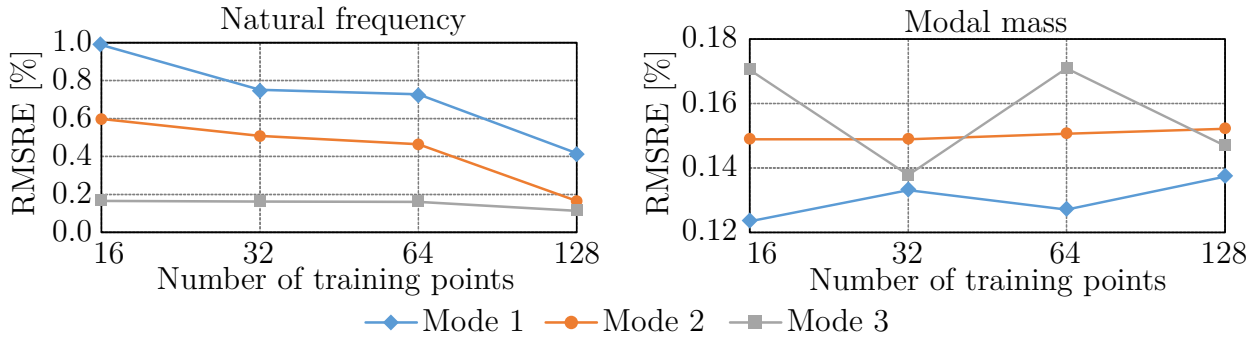

Figure 6.13: Evaluating minimal training sample size for second-order PCE metamodel with three variables.

input parameters (Figure 6.14). The relative error in the mean natural frequencies between the reduced (three parameters) and the full model (ten parameters) is below 0.13%, whereas the relative error between the corresponding COVs does not exceed 0.6%. Similarly, the relative errors in the mean values and COVs of the model masses are limited to 0.07% and 0.21%, respectively. The SA results exhibit a similar overall trend, with maximum error in the Sobol' indices for both natural frequencies and modal masses below 1.5%. These consistently low errors demonstrate that the overall uncertainty in the modal parameters associated with the first three vibration modes can be reliably represented using a reduced numerical model with only three uncertain parameters - ρ, E_L, and G_{LT}.

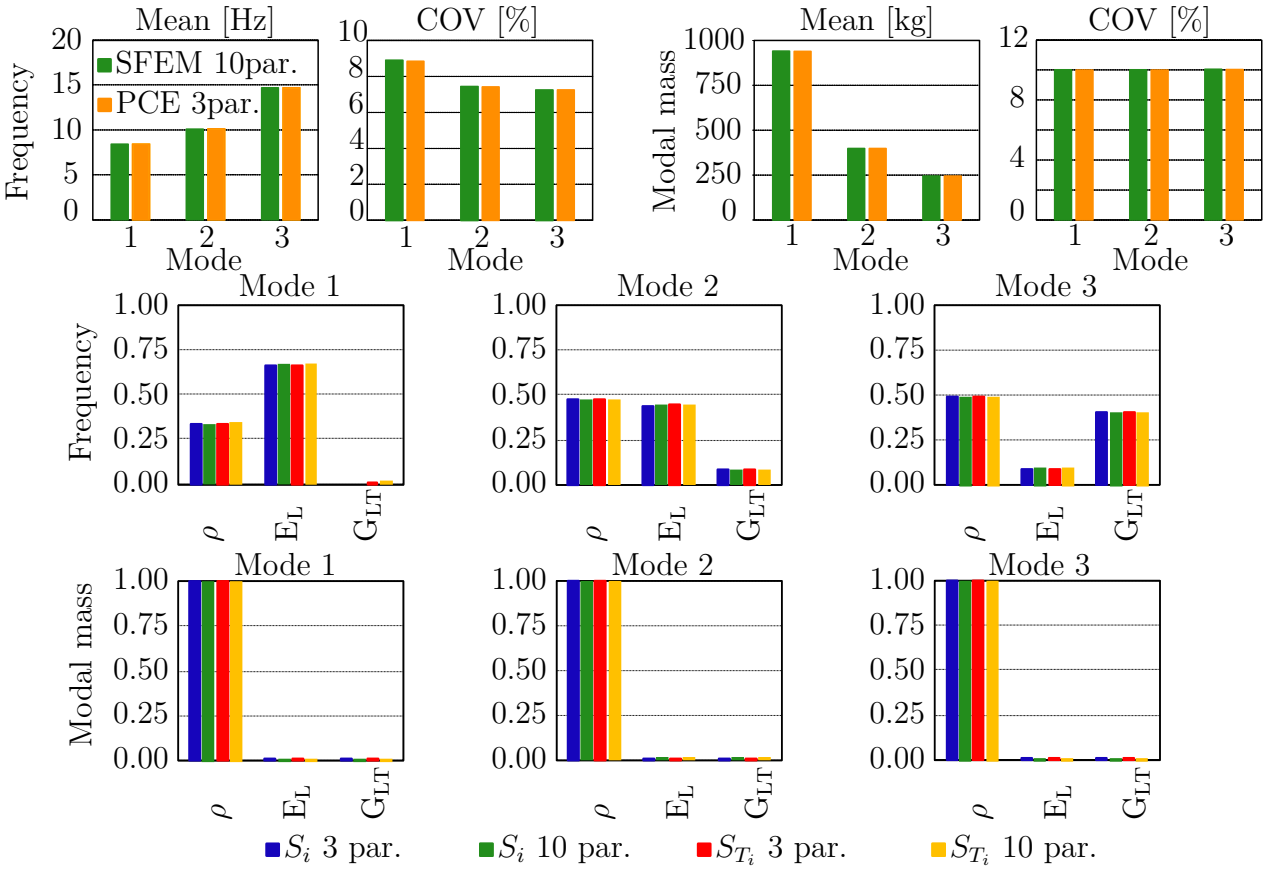

Figure 6.14: Comparison of UQ and SA for the first three modes, considering three and ten uncertain parameters

6.3 High-frequency floor

The same training dataset sizes, ranging from 32 to 1024 samples, as those adopted for the LFF were used for the development of the PCE metamodel of the HFF. In addition, set of 10,000 samples was employed for validation of the metamodel through SFEM.

6.3.1 Training and validation of PCE metamodel

Similarly to the LFF case, both second- and third-order PCE metamodels were studied. The RMSREs of the natural frequencies and modal masses obtained using the second-order PCE metamodel are presented in Figure 6.15, whereas the corresponding results for the third-order PCE metamodel are shown in Figure 6.16.

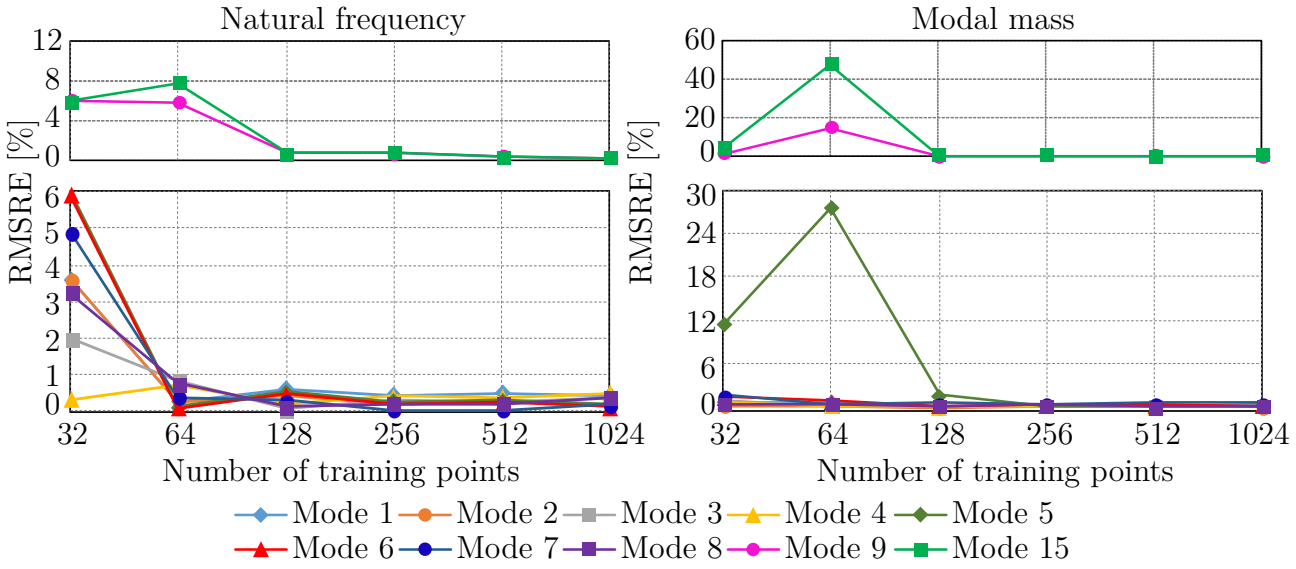

Figure 6.15: Evaluating minimal training sample size for second-order PCE metamodel.

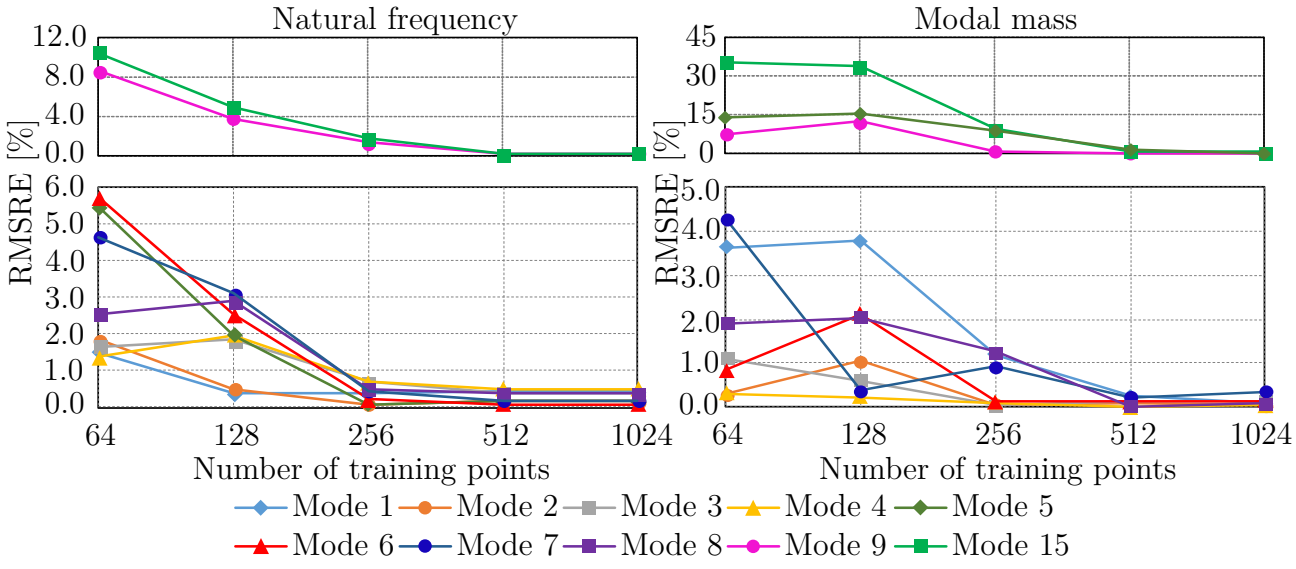

Figure 6.16: Evaluating minimal training sample size for third-order PCE metamodel.

The observed trends are consistent with those obtained in the previous analysis of the LFF. For the second-order PCE metamodel, the RMSREs of both natural frequencies and modal masses stabilise at a training dataset size of 128 samples. In contrast, the third-order PCE metamodel requires a larger dataset, with stable RMSREs for all natural frequencies and modal masses achieved when 512 training samples are used. In addition to the 9th and 15th modes, the 5th mode of the HFF exhibits a higher degree of nonlinearity, requiring a larger training dataset to achieve sufficiently accurate predictions. A second-order PCE with 128 training samples yields average RMSREs of 0.37% for the ten natural frequencies and 0.34% for the corresponding modal masses. By comparison, a third-order PCE trained on 512 samples achieves slightly lower average RMSREs of 0.22% and 0.32%, respectively. However, due to its higher computational efficiency, resulting from a smaller number of polynomial terms, the second-order PCE metamodel trained with 128 samples is adopted for the subsequent analysis.

Additional validation was carried out by applying the same set of 10,000 input samples used in the SFEM to the developed second-order metamodel trained on 128 samples (Figures 6.17 and 6.18). Again, exceptionally high R^2 are achieved, exceeding 0.99 for all ten natural frequencies and eight out of ten modal masses. Lower values of 0.9758 and 0.9722 are obtained for the 5th

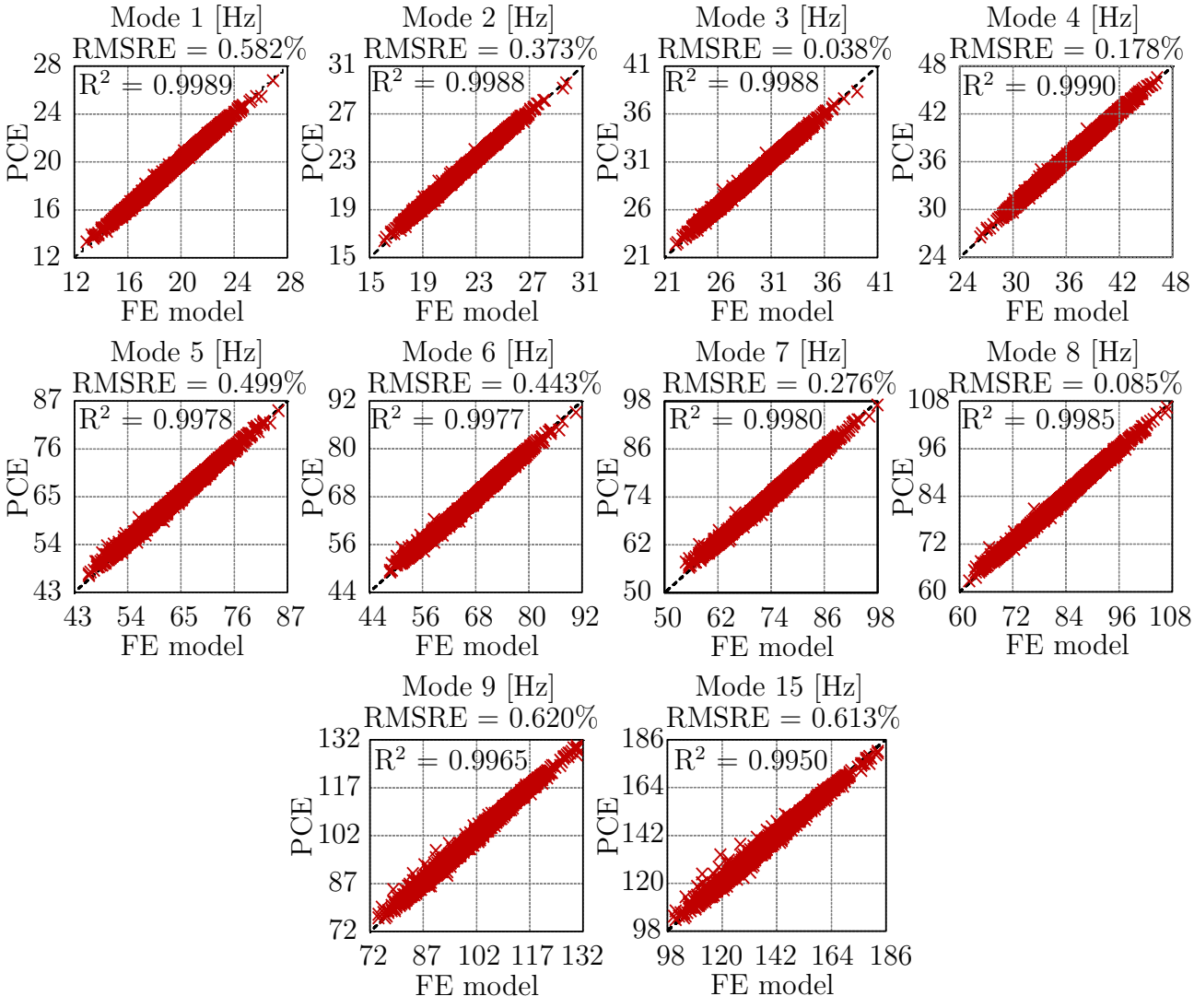

Figure 6.17: Comparison of natural frequencies predicted by the second-order PCE metamodel (n=128) and the FE model.

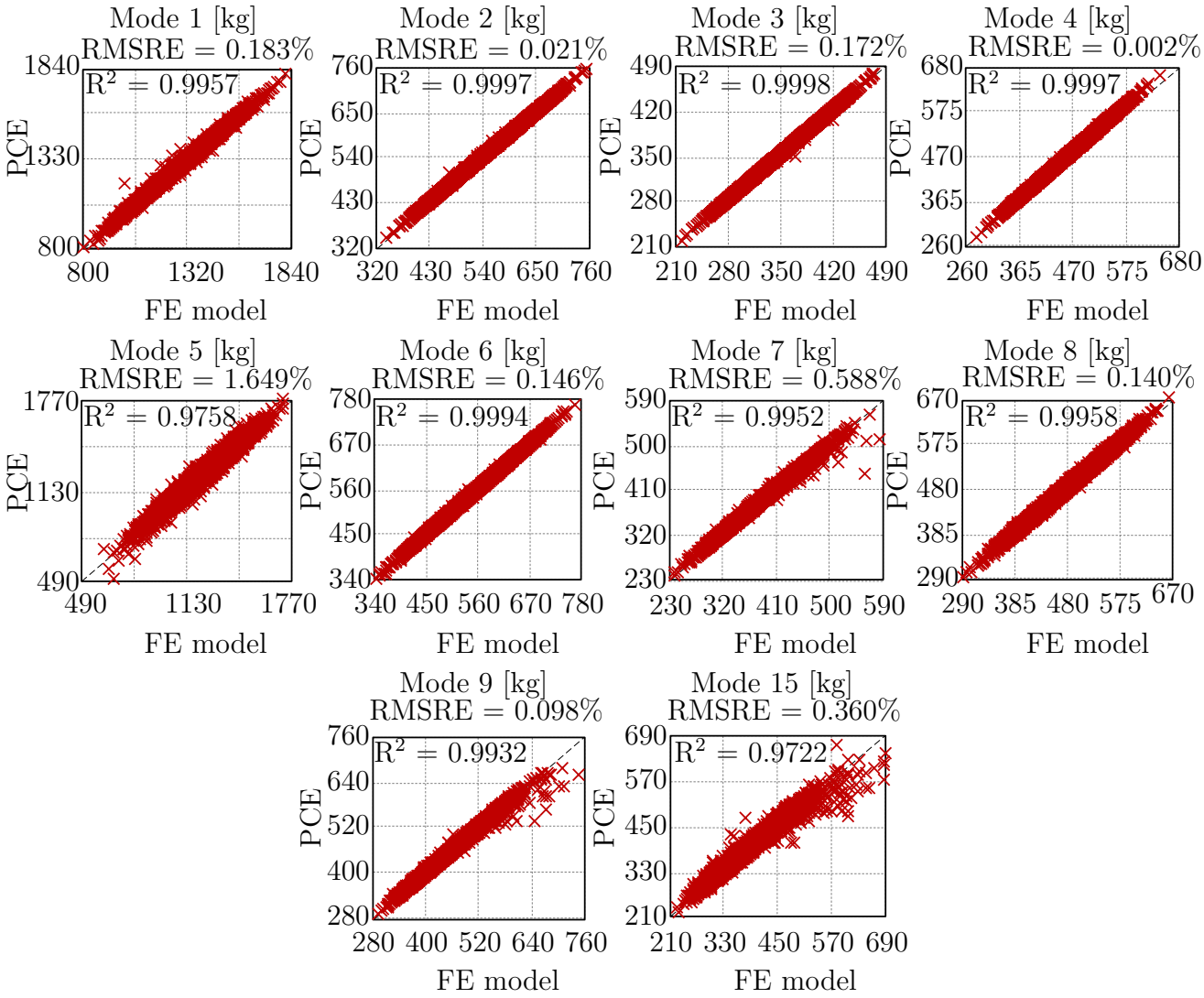

Figure 6.18: Comparison of modal masses predicted by the second-order PCE metamodel (n=128) and the FE model.

and 15th modal masses, respectively. Overall, these results confirm that the PCE metamodel provides an excellent approximation of the underlying FE model.

6.3.2 Uncertainty analysis of natural frequencies

The mean values, COVs, PDFs, CDFs of the natural frequencies obtained using both the PCE and SFEM approaches are presented in Figures 6.19, 6.20 and 6.21, respectively. The comparison shows that the PCE predictions closely match those of the SFEM, with differences in the mean values below 0.014%. Differences in the COVs remain below 0.7% for all ten vibration modes. Both methods yield COVs in the range of $6.9 - 8.4\%$, consistent with those obtained for the LFF. The largest COVs are observed for the bending-mode natural frequencies, namely the 1st and 5th modes.

The close agreement between the first-order and total-order Sobol indices for all parameters and across all modes (Figure 6.22) indicates a negligible level of interaction among the modelling parameters. Consistent with the sensitivity analysis results for the LFF, the same five modelling parameters (E_T, ν_{LT}, E_{conn}, ν_{conn}, and G_{conn}) exhibit no influence on the variability of the

natural frequencies of HFF. In addition, parameter a_{conn} show negligible effect on all considered natural frequencies. The main difference compared with the LFF is observed for G_{RT}, which has a small influence on the natural frequencies of the first four modes (S_{T_i} in range from 0.03 to 0.07) and more pronounced influence on higher modes with S_{T_i} ranging from 0.26 for mode 5 to 0.37 for mode 15. This effect is most likely associated with the increased layer thickness. However, for modes relevant for human-induced vibrations, this parameter is still below the threshold to be considered influential. Consequently, only ρ, E_L and G_{LT} exceed the adopted sensitivity threshold of 0.15, identically as for the LFF. Timber density remains the dominant source of variability across all natural frequencies with Sobol' indices ranging from 0.37 to 0.54, while E_L significantly affects the variability of the 1st, 2nd, 5th and 6th natural frequencies with corresponding indices of 0.6, 0.42, 0.33 and 0.28, respectively/ In addition, G_{LT} plays a key role in variability of torsional modes ($S_{T_i} = 0.28$ for the 3rd and $S_{T_i} = 0.41$ for the 4th natural frequency), confirming the consistency of the governing mechanisms identified for the LFF.

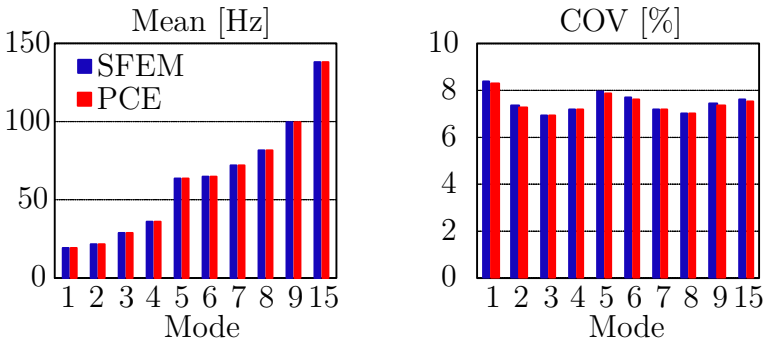

Figure 6.19: Mean values and COVs of natural frequencies obtained using PCE and SFEM.

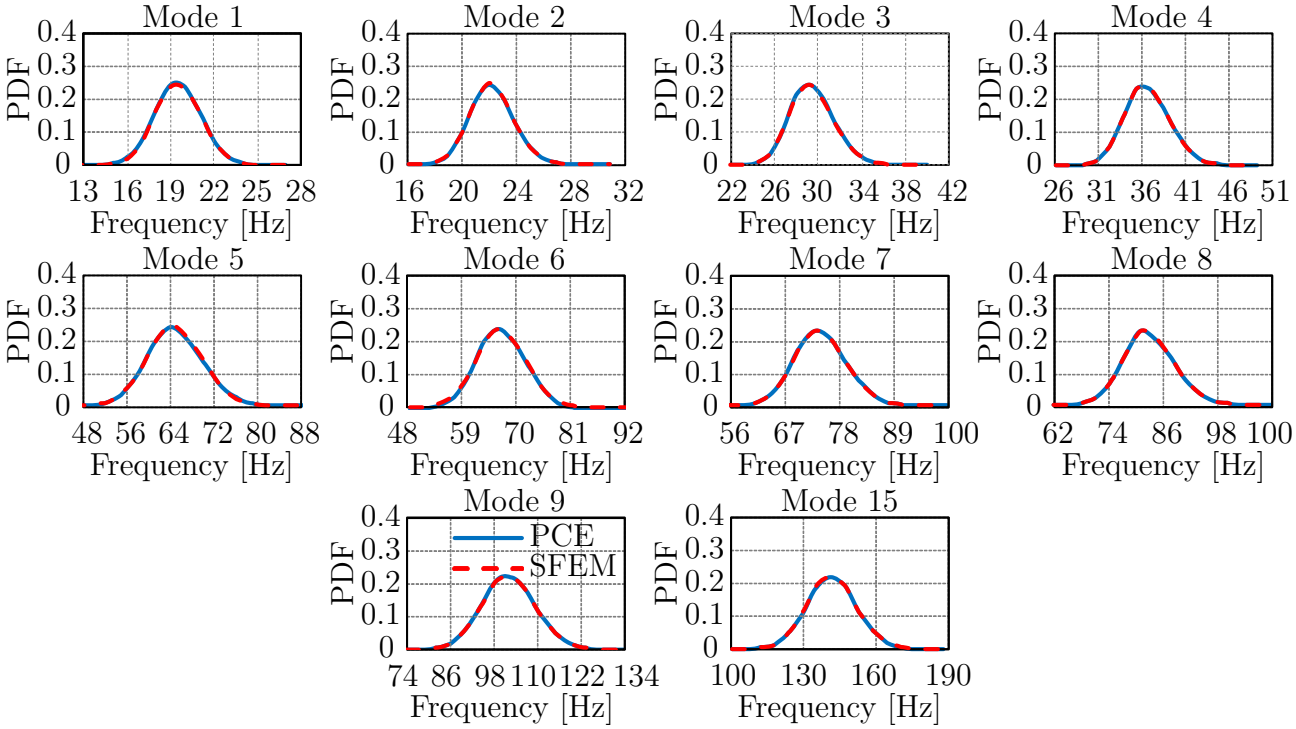

Figure 6.20: PDFs of natural frequencies obtained using PCE and SFEM.

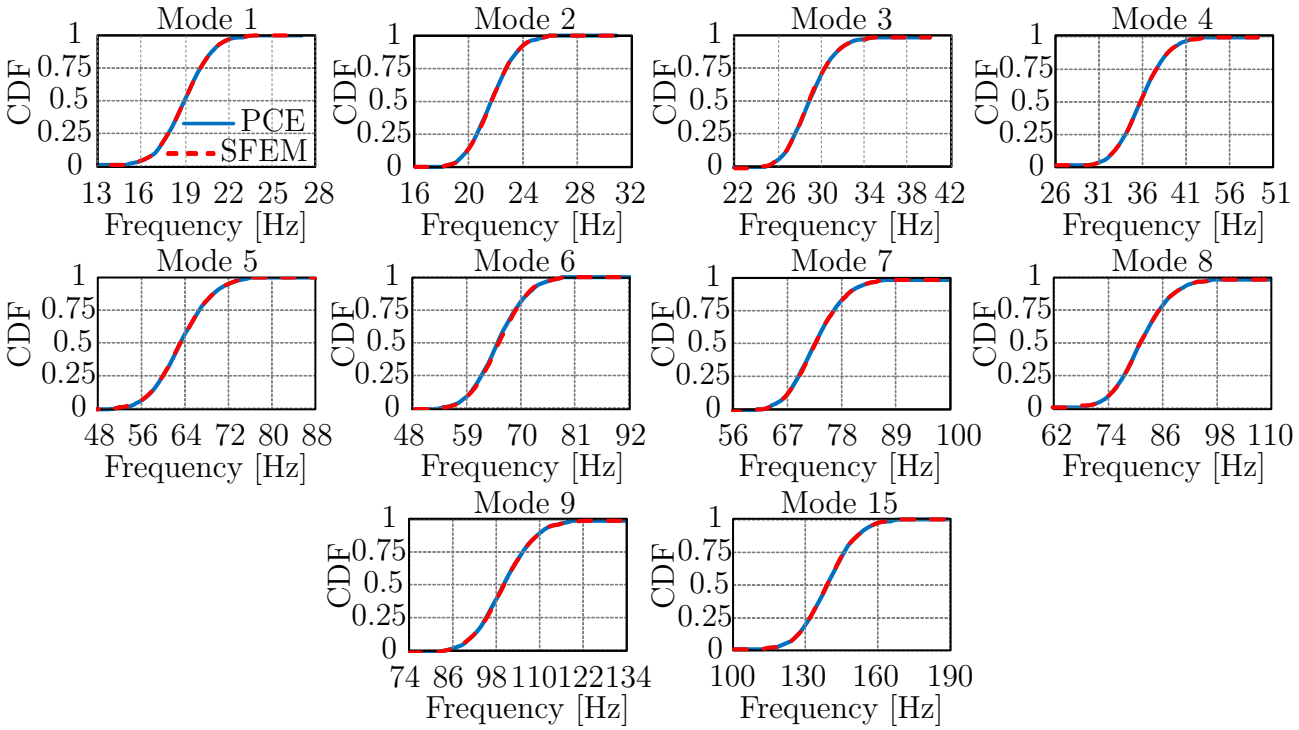

Figure 6.21: CDFs of natural frequencies obtained using PCE and SFEM.

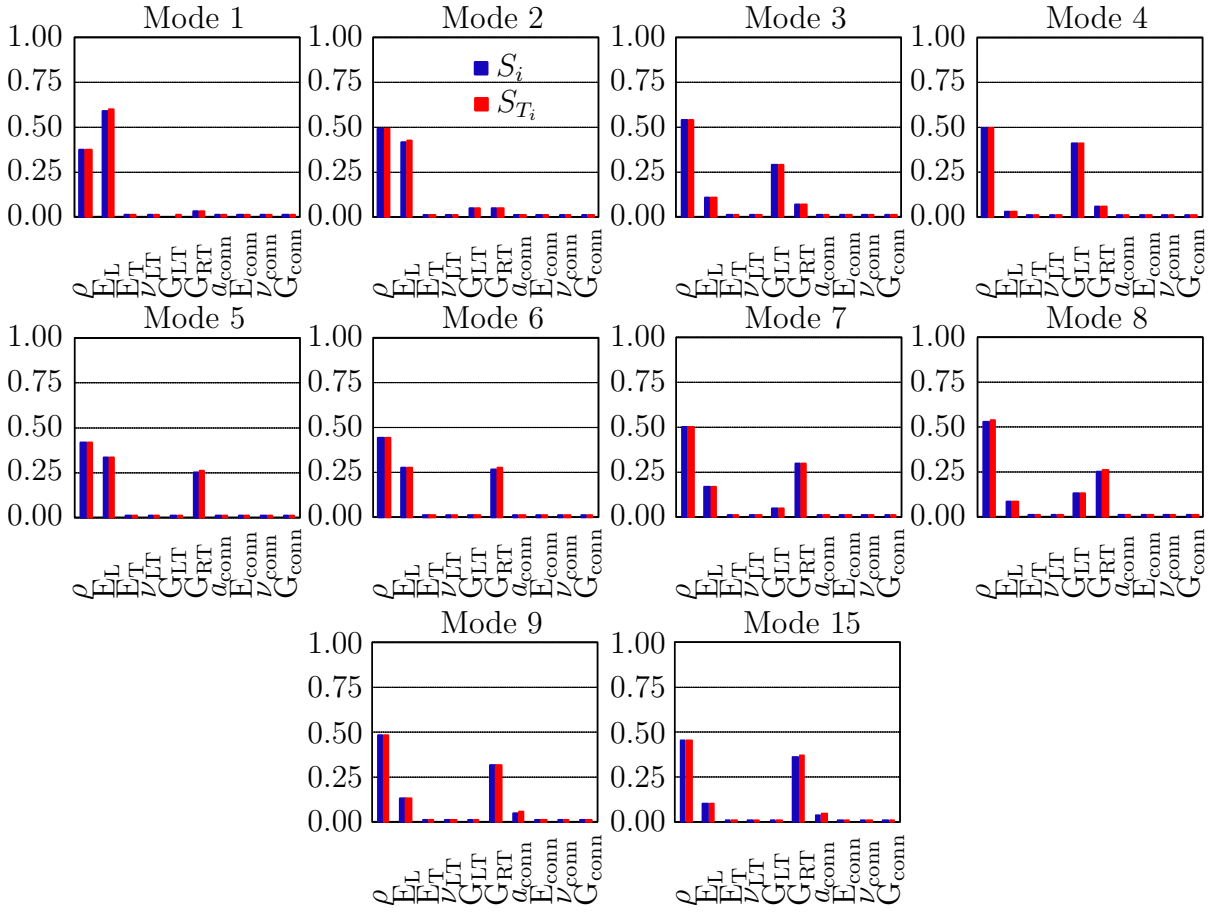

Figure 6.22: First order and total order Sobol' indices for natural frequencies.

6.3.3 Uncertainty analysis of modal masses

The UQ results for the modal masses, including mean values, COVs, PDFs and CDFs, are presented in Figures 6.23, 6.24 and 6.25, respectively. The only noticeable discrepancy between the PCE- and SFEM-based COVs occurs for the 5th mode, for which the difference is approximately 2.3%. For the first four modes, the modal mass COVs remain close to 10%, in agreement with the LFF results. For modes 6-9, COVs lie between 10% and 11%, whereas higher COVs of 11.41% and 13.31% are observed for the 5th and 15th modes. The SA results for the HFF modal masses (Figure 6.26) are analogous to those obtained for the LFF for 9 out of the 10 considered modes. For modes $1-4$ and $6-8$, ρ remains the sole parameter governing the variability of the modal masses, indicating that their uncertainty is entirely mass-driven. Furthermore, for the 9th and 15th modes, a non-negligible contribution arises from the inter-panel connection width. In contrast, only the 5th mode differs from the results obtained for the LFF. For this modal mass, a non-negligible influence arises from the variability in G_{RT}, with a resulting S_{T_i} of 0.18. However, as in the LFF case, the lower-order HFF mode shapes relevant to pedestrian-induced vibrations can be treated as deterministic.

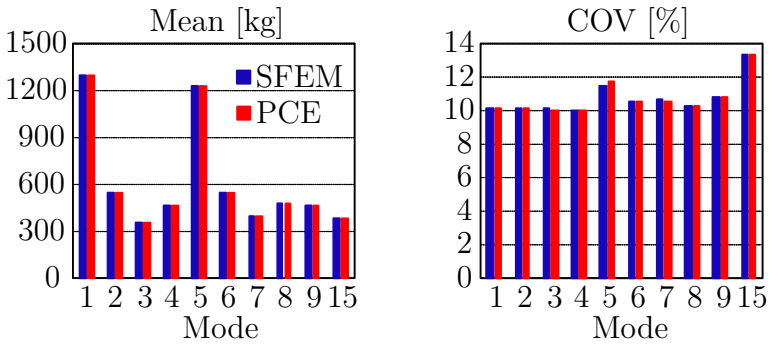

Figure 6.23: Mean values and COVs of modal masses obtained using PCE and SFEM.

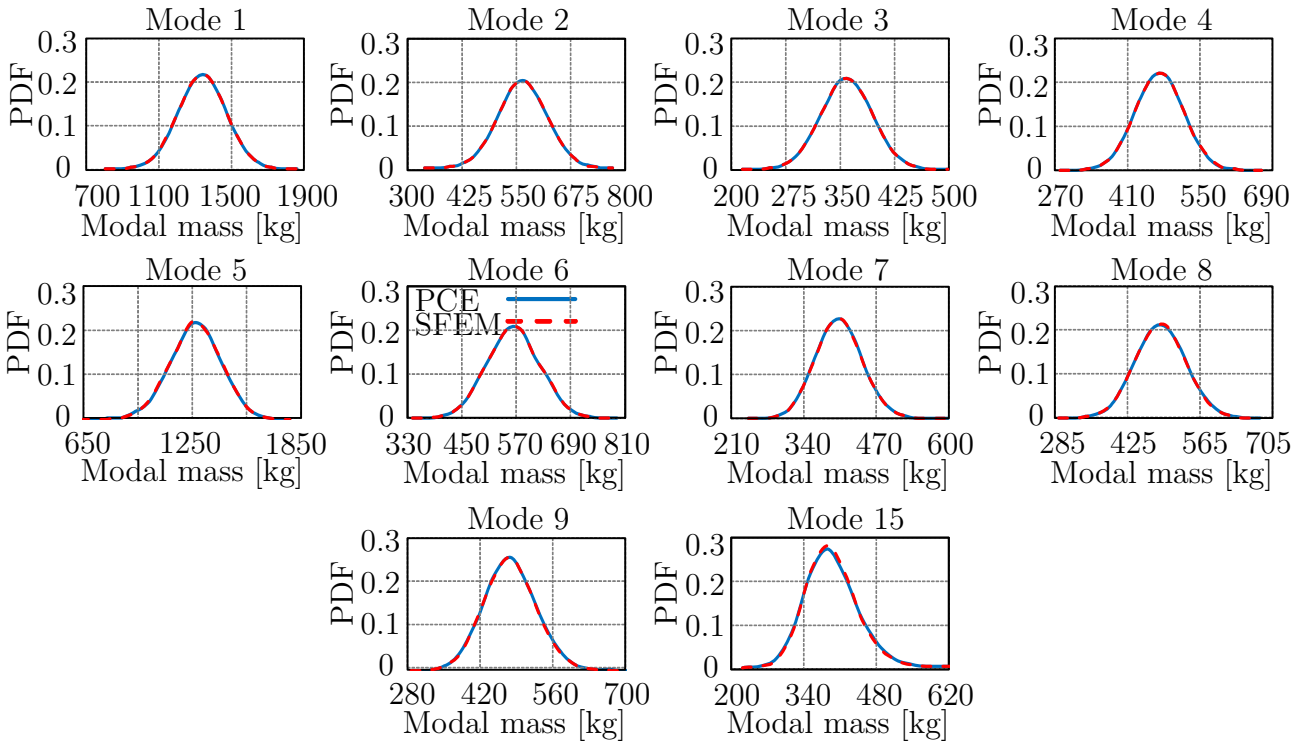

Figure 6.24: PDFs of modal masses obtained using PCE and SFEM.

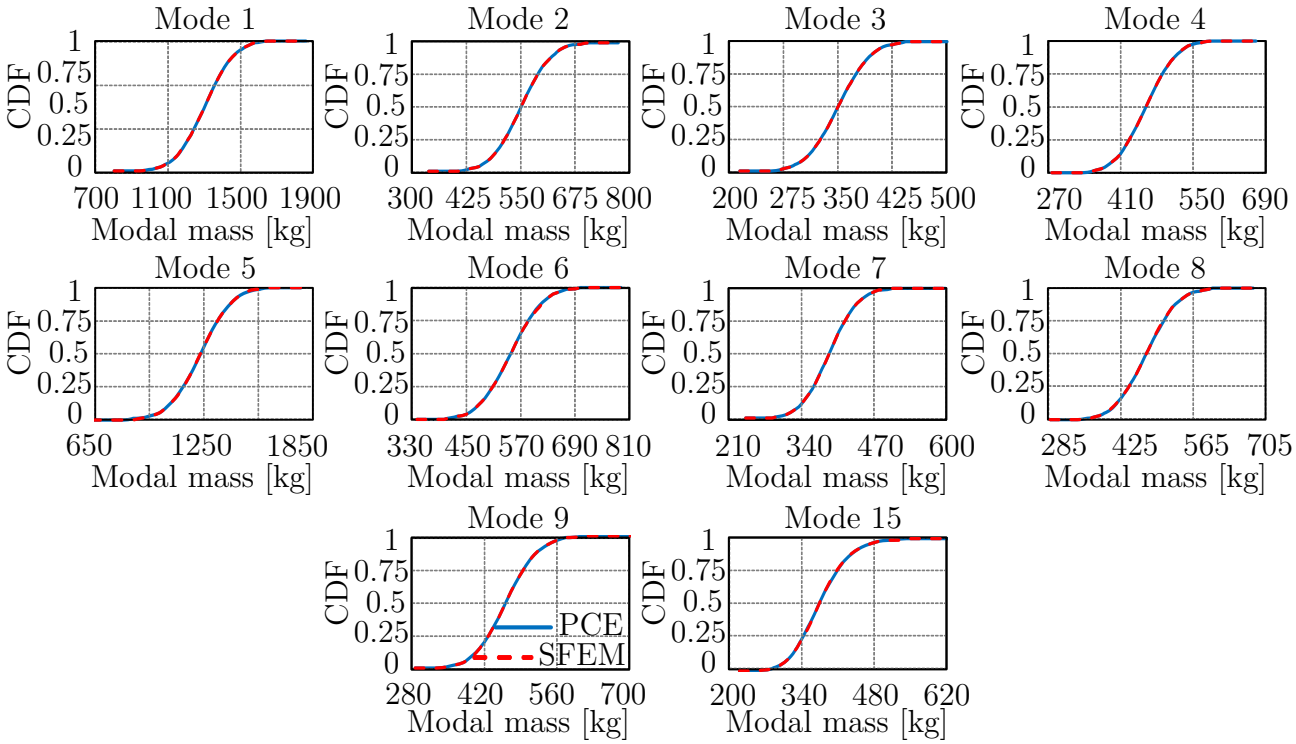

Figure 6.25: CDFs of modal masses obtained using PCE and SFEM.

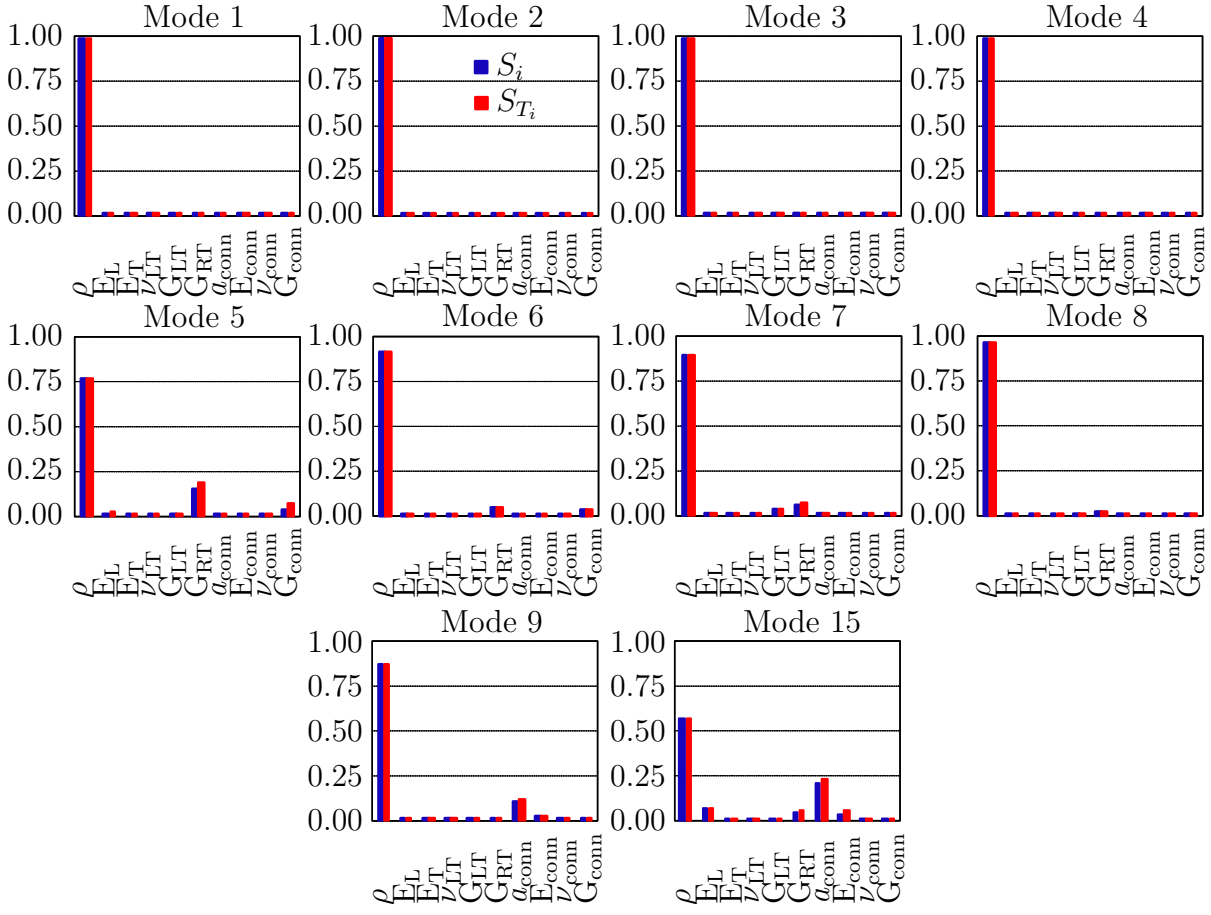

Figure 6.26: First order and total order Sobol' indices for modal masses.

6.3.4 Model reduction: uncertainty analysis considering three uncertain parameters

As in case of LFF, a reduced-order model [117] was developed, trained, and validated for the subsequent uncertainty analysis of the floor response in Chapter 9. This refinement was restricted to the first four modes, as these are the only modes relevant to pedestrian-induced vibrations for the considered HFF [41]. Only three uncertain parameters, ρ, E_L, and G_{LT}, dominate the variability of the natural frequencies and modal masses for these four modes of the considered high-frequency CLT floor.

The training datasets comprising 16, 32, 64, and 128 samples generated using the Sobol' sequence sampling technique were used to develop the second-order PCE metamodel with three input variables. The validation dataset remained unchanged and consisted of 10,000 MC simulations performed on the FE model with ten input variables. The RMSREs of the modal masses shown in Figure 6.27 remain constant with increasing training sample size. In contrast, the RMSREs of the natural frequencies decrease with increasing the sample size, and a training dataset of 128 samples is adopted for the three-parameter surrogate of the FE model.

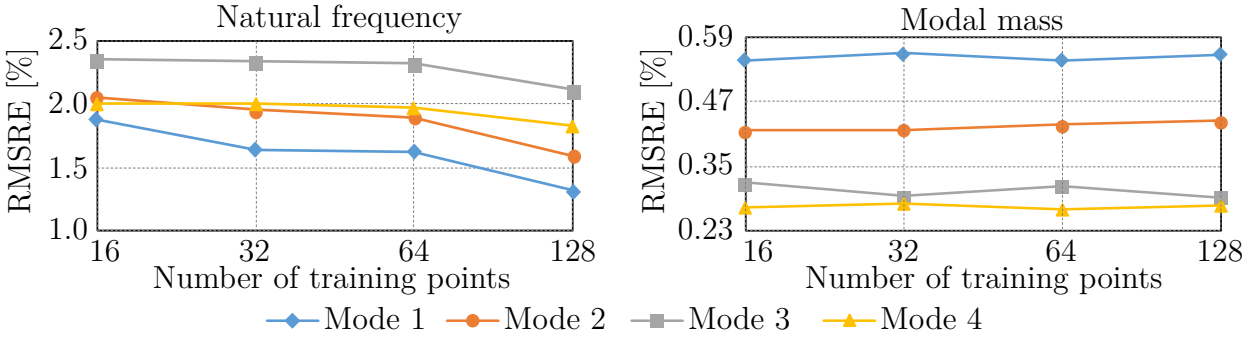

Figure 6.27: Evaluating minimal training sample size for second-order PCE metamodel with three variables.

UQ of the natural frequencies and modal masses of the first four vibration modes was repeated using the reduced three-parameter metamodel and validated against the corresponding SFEM results obtained with all ten uncertain parameters (Figure 6.28). The relative errors in the mean natural frequencies between the reduced and full models remain below 0.3%, while the errors in the mean modal masses do not exceed 0.5%. Similarly, the relative errors in the COVs of the modal masses are limited to 0.6%. However, the reduced model underestimates the COVs of the natural frequencies by up to 3%, as the variability in G_{RT}, which has a minor influence on the first four natural frequencies, was neglected.

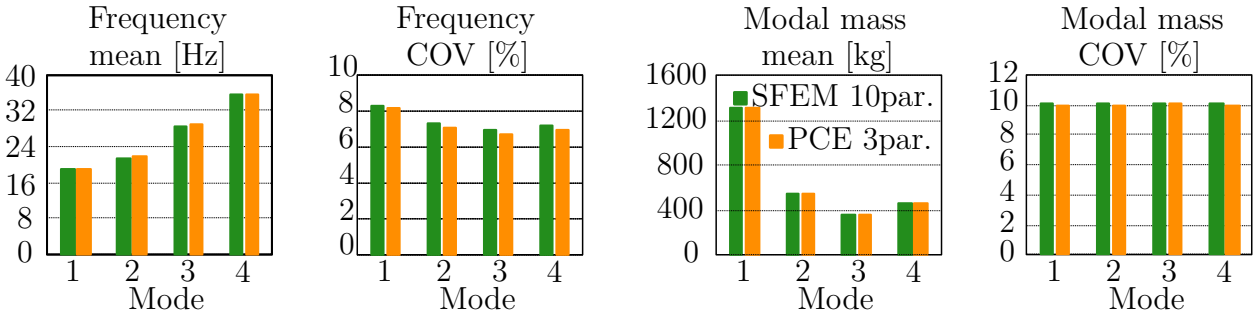

Figure 6.28: Comparison of UQ for the first four modes, considering three and ten uncertain parameters

The SA results shown in Figure 6.29 exhibit the same overall trends as the UQ. The maximum differences in the Sobol' indices for the modal masses remain below 1%, whereas larger differences, of up to 7%, are observed for the natural frequencies. Again, this is a consequence of neglecting part of the variability associated with G_{RT}. Overall, these results confirm that the uncertainty in the natural frequencies and modal masses of the first four HFF vibration modes is effectively captured by a reduced metamodel involving only ρ, E_L, and G_{LT}.

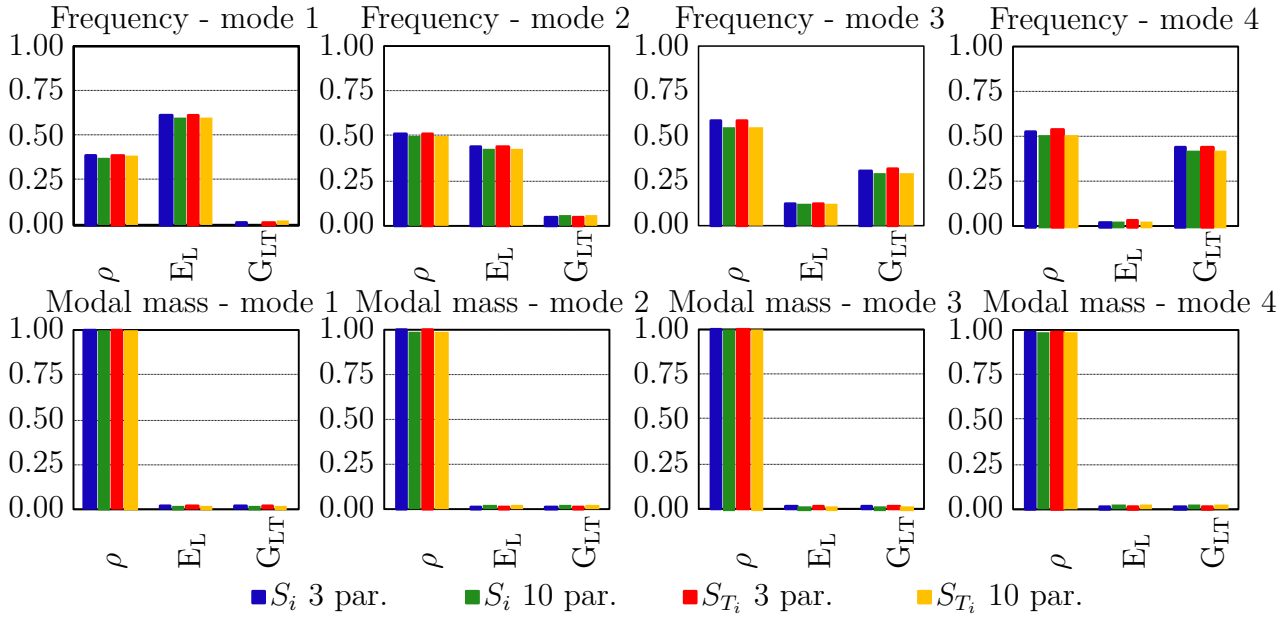

Figure 6.29: Comparison of SA for the first four modes, considering three and ten uncertain parameters

6.4 Chapter summary

In this chapter, a probabilistic uncertainty analysis of the natural frequencies and modal masses of a three-panel CLT floor was performed, accounting for variability in timber material properties and the modelling parameters of the inter-panel connections. Both the LFF and HFF configurations developed in Section 5.4 were considered. Uncertainty in the modelling parameters was defined based on the literature review to ensure that the resulting variability of the considered modal properties is representative of realistic conditions.

To reduce the computational cost, a second-order PCE metamodels with ten uncertain input parameters were developed as an efficient surrogate for the FE models in the evaluation of their natural frequencies and modal masses. Each metamodel required only 128 training samples to complete the full UQ and SA, compared to 10,000 MC simulations used in the SFEM-based analysis.

Overall, both floor configurations exhibited similar trends. The COVs of the natural frequencies and modal masses were found to fall within relatively narrow ranges of approximately $7-9\%$ and $10-14\%$, respectively. Among the ten uncertain parameters, timber density ρ, longitudinal modulus of elasticity E_L and shear modulus G_{LT} were identified as the dominant contributors to the variability of the modal properties relevant to pedestrian-induced vibrations. In particular, the variability of the first eight modal masses was governed almost entirely by ρ, while the width of the elastic strip affected only the modal masses of higher-order modes. This suggests

that the mode shapes associated with the vibration-relevant modes can be treated as effectively deterministic. Finally, reduced metamodels retaining only the three influential parameters were derived, providing a reliable and computationally efficient basis for the subsequent uncertainty analysis of floor vibration response under pedestrian excitation presented in Chapter 9.

7 Modelling dynamic force

This chapter extends the CCIP-016 harmonic and effective-impulse load models to account explicitly for both inter-subject variability between walking sessions and intra-subject variability between successive steps within an individual walking session. The harmonic model is expanded from four to six harmonics and reformulated using step-specific walking frequencies and force amplitudes. The effective-impulse model is extended by introducing a step-specific impulse expressed as a function of pacing rate, structural frequency and damping ratio. The governing parameters of both load models are defined using an extensive database of continuously measured walking forces. The database enables the statistical properties of these parameters and their mutual dependencies to be quantified, allowing them to be represented as correlated random variables. In addition to probabilistic load models, simplified deterministic formulations are proposed to provide user-friendly tools for routine design calculations. These formulations retain the main characteristics of the developed load models while avoiding the complexity of a full probabilistic analysis.

Unified force models capable of representing the full frequency content of walking excitation, although explored in research, have not yet been adopted in current design guidelines. This is because they are generally too complex for routine engineering practice. Consequently, this dissertation follows the conventional modelling framework adopted in existing guidelines, employing a harmonic force model for floors susceptible to resonant response (LFFs) and a series of effective impulses to represent the transient response of HFFs.

The database of continuously measured walking forces [40] used to estimate the modelling parameters for both load models is briefly introduced in Section 7.1. The recorded force signals are then processed on a step-by-step basis to extend the existing CCIP-016 [41] load models, elaborated in Section 2.3, for LFFs (Section 7.2) and HFFs (Section 7.3). Owing to the large number of available walking records, the statistical properties and mutual correlations of all modelling parameters can be evaluated, allowing both intra- and inter-subject variability to be represented. Intra-subject variability is characterised through step-by-step analysis within a single walking record, while aggregating results across all recorded signals provides an assessment of inter-subject variability. The CCIP-016 harmonic model is enhanced by increasing the number of harmonics from four to six and allowing the walking frequency and force amplitudes to vary from step to step. The effective-impulse model is improved by evaluating the impulse for each step and establishing its dependence on structural natural frequency and damping ratio and the pedestrian walking frequency.

7.1 Database description

The database consists of 852 continuously measured vertical walking force time histories obtained from 80 volunteers (55 males and 25 females; body mass 76.1 ± 15.3kg, height 174.8 ± 8.1cm, age 29.7 ± 9.3 years). Each record corresponds to a single individual walking session on an instrumented treadmill equipped with two independent force-measuring units, allowing separate identification of left and right footfalls. The dataset comprises walking speeds from 2km/h to the maximum comfortable speed for each participant, increased in increments of 0.5km/h, with a maximum recorded speed of 10km/h. Pacing rates were not imposed and were subsequently extracted from the force signals during post-processing. All force time histories were sampled at 200Hz and stored together with the corresponding participant and walking-condition metadata. Out of 852 recorded signals, some were excluded for the following reasons:

- signals corresponding to a walking speed of 2km/h, as this speed was considered too low and the resulting data were found to be unreliable;
- signals recorded at walking speeds of 8.5, 9.0, 9.5, and 10.0km/h, since motion at these speeds corresponds more closely to running than walking;
- signals containing less than 60 steps, as this number of steps was considered insufficient for evaluating the intra-subject variability;
- signals affected by measurement inaccuracies.

As a result, a total of 744 walking force signals were retained for further analysis. Although the database contains force measurements recorded separately for the left and right foot, these signals were summed to obtain the total vertical walking force (see Figure 2.1), which was subsequently analysed. Consequently, potential differences between the forces generated by the left and right foot were not considered in the present study.

7.2 Harmonic load model

A widely adopted harmonic force model for simulating resonant pedestrian-induced vibration response is given by Eq. (2.1), in which the number of included harmonics varies among proposed formulations [27, 48, 49, 51]. The CCIP-016 design guide [41], currently regarded as the most comprehensive reference for VSA, adopts a harmonic force model comprising four harmonics. However, Mohammed et al. [34] demonstrated that resonant responses may occur in structures with fundamental frequencies up to 14Hz. This suggests that a four-harmonic representation is insufficient to capture the relevant excitation content for structures with fundamental frequencies approaching 14Hz. Furthermore, the perfectly periodic harmonic load model cannot capture step-to-step variations in walking parameters (walking frequency and DLFs), i.e. cannot account for intra-subject variability of the human walk. These step-to-step variations spread the excitation energy around the nominal harmonic frequencies (see Figure 2.1*b*), affecting resonance build-up and the resulting response amplitude. Neglecting these variations may lead to inaccurate predictions of both the floor response and its variability.

The harmonic load model introduced in Subsection 7.2.1 represents an improvement over the CCIP-016 formulation in two key aspects: (i) it includes six harmonics instead of four, consistent with the proposed 14Hz cut-off frequency separating LFFs and HFFs [34], and (ii) it is formulated as a quasi-periodic model to describe intra-subject variability of the walking

force. All parameters characterising this load model are defined based on the processing of walking force database in Subsection 7.2.2. Subsection 7.2.3 presents a verification study in which the measured force signals are reconstructed and response of a single-degree-of-freedom (SDOF) oscillator is computed under both measured and reconstructed signals. Subsequently, the representation of the model parameters as correlated random variables is described in Subsection 7.2.4. Their implementation into the proposed quasi-periodic load model results in the probabilistic force model that takes into account both intra- and inter-subject variability. The procedure for generating representative probabilistic force time histories is provided in Subsection 7.2.5. However, this fully probabilistic formulation is not convenient for routine design calculations. Accordingly, a simplified harmonic load model is proposed in Subsection 7.2.6. The simplified model retains the six-harmonic representation and is intended for deterministic vibration response calculations, while still accounting for inter-subject variability through a user-defined probability of force-amplitude (DLFs) exceedance. For reference, the CCIP-016 force amplitudes correspond to a fixed 25% probability of exceedance.

7.2.1 Model formulation

The force within each individual step is assumed to be composed of six harmonics and characterised by the step-specific walking frequency $f_{p,\text{step}}$ and Fourier amplitudes $\text{DLF}_{h,\text{step}}$:

$$F_{p,\text{step}}(t) = \text{G}\left(1 + \sum_{h=1}^{6} \text{DLF}_{h,\text{step}} \sin\Big(2\pi h f_{p,\text{step}} t\Big)\right), \quad \text{step} = 1, 2, ..., N_{\text{step}}, \tag{7.1}$$

where N_{step} denotes the number of steps in the walking session. Walking frequency and DLFs are allowed to vary between consecutive steps, taking new values $f_{p,\text{step+1}}$ and $\text{DLF}_{h,\text{step+1}}$ for the subsequent step. This variation is not purely random but is modelled using an autoregressive (AR) model [179]. Generally speaking, AR models are stochastic processes commonly used to describe time-varying activities. In the first-order AR(1) model, utilised in this study, the parameter value at a given point in time (step) linearly depends on the value at the preceding step with the addition of a random component. Therefore, a correlation between successive steps is introduced, allowing for gradual variations between steps, rather than abrupt changes. The AR(1) formulation adopted in this study is expressed as:

$$\begin{aligned} f_{p,\text{step+1}} &= \mu_{f_p} + \rho_{f_p} \cdot \Big(f_{p,\text{step}} - \mu_{f_p}\Big) + \sigma_{f_p} \cdot \sqrt{(1-\rho_{f_p}^2)} \cdot \varepsilon_t, \\ \text{DLF}_{h,\text{step+1}} &= \mu_{\text{DLF}_h} + \rho_{\text{DLF}_h} \cdot \Big(\text{DLF}_{h,\text{step}} - \mu_{\text{DLF}_h}\Big) + \sigma_{\text{DLF}_h} \cdot \sqrt{(1-\rho_{\text{DLF}_h}^2)} \cdot \varepsilon_t, \end{aligned} \tag{7.2}$$

where μ_{f_p} and μ_{DLF_h} are the mean values of walking frequency and DLF_h, respectively, while σ_{f_p} and σ_{DLF_h} are corresponding standard deviations during a single walking session, ε_t is a standard normal random variable and parameter ρ, where $|\rho| \leq 1$, is the AR coefficient that controls the strength of temporal correlation between successive steps. If $\rho \to 1$, parameters of the successive steps are strongly correlated and the deviations from the mean value decay slowly. In contrast, when $\rho \to 0$, the process exhibits a weak temporal dependence, with successive parameter values revert rapidly toward the mean value. Finally, when $\rho < 0$, the process shows alternating behaviour, with successive values tending to fluctuate around the mean value.

7.2.2 Extraction of model parameters from the database

Each of the 744 measured force signals was first normalised by dividing it by the pedestrians self-weight and the unity mean value was removed. The walking frequency and the six amplitudes DLF_h were then evaluated on a step-by-step basis. Based on these stepwise values of f_p and DLF_h, the AR coefficients ρ_{f_p} and ρ_{DLF_h} were computed for each walking session.

Although not directly included in Eq.(7.1), step length is another parameter characterising walking load and can be estimated as the walking speed divided by the walking frequency. If walking speed was strictly constant and equal to the treadmill speed, all variability in step length would arise solely from variations in the walking frequency. However, pedestrians normally adjust their walking speed during walking session by moving forward and backward on the treadmill belt. Consequently, walking speed at each moment in time does not exactly coincide with the treadmill speed. Since the instantaneous walking speed was not measured, the variability in step length cannot be quantified from the available data. Nevertheless, variability in step length is indirectly accounted for through variations in walking frequency, assuming a constant walking speed.

7.2.2.1 Walking frequency

Frequency of the first harmonic represents a key property of the harmonic load model. To isolate the first harmonic, the normalised force signal was filtered using a low-pass filter with a cut-off frequency of 3Hz. To determine the frequency of the first harmonic individually for each step, the filtered force signal was segmented into individual periods $\mathrm{T}_{\mathrm{step},i}$. A single period was defined as the portion of the signal between every other zero crossing of the filtered signal (Figure 7.1), corresponding to two successive contacts of alternating feet (i.e. left to right or right to left). Note that the zero crossings of the filtered signal do not exactly coincide with the zero crossings of the original walking force (Figure 7.1), indicating that the frequency of the first harmonic determined on a step-by-step basis does not precisely match the frequency of each step. This discrepancy may arise from the biomechanical characteristics of human gait, measuring noise and/or the effects of signal filtering. However, due to the formulation of the harmonic load model, the parameter f_p in Eq.(7.1) corresponds to the frequency of the first harmonic and was therefore adopted as the representative walking frequency.

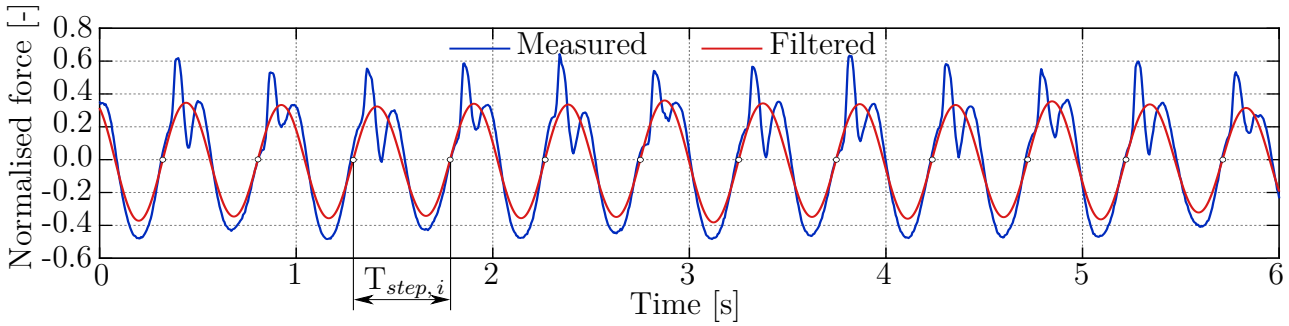

Figure 7.1: A portion of 35s-long measured normalised force [40], corresponding 3Hz filtered signal and defined period of a single step.

To minimise distortions at the beginning and the end of the signal in subsequent processing, both normalised and corresponding filtered force time histories were truncated by removing the first and last three steps. The truncation was applied so that signals start at zero with

an increasing trend and end while smoothly returning towards zero. The walking frequency of each step during walking session i, $f_{p,\text{step},i}$ was then determined as the reciprocal of the step period $\text{T}_{\text{step},i}$ extracted from the filtered force time history of the session i.

After identifying walking frequencies of each step, their mean value $\mu_{f_{p,i}}$, standard deviation $\sigma_{f_{p,i}}$ and $\text{COV}_{f_{p,i}}$ were calculated for each walking session i. Figure 7.2 illustrates the variation of walking frequency during a single 64-step walk (walking session $i = 446$), with mean value of 2.04Hz and standard deviation of 0.025Hz. A COV of 1.22% indicates low intra-subject variability of walking frequency for this walking session.

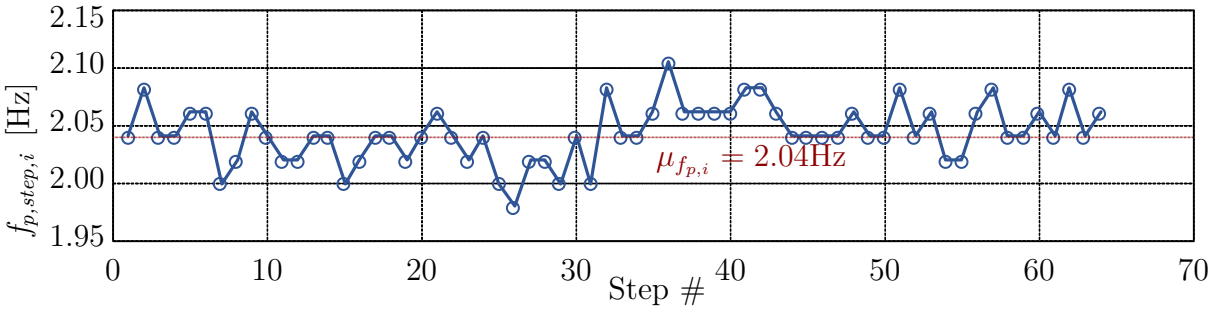

Figure 7.2: Variability of walking frequency during a single walk.

Identified $\text{COV}_{f_{p,i}}$ obtained from all 744 processed signals are plotted against the corresponding mean walking frequencies $\mu_{f_{p,i}}$ in Figure 7.3. The lowest COVs are observed for walking with mean frequencies in the range of $1.9 - 2.2$Hz, where the dispersion of these COV values remains within a narrow interval of approximately $1 - 3\%$. Walking at frequencies above 2.2Hz is relatively uncommon. The sessions recorded in this range exhibit slightly higher COVs, typically between 1.5 and 5%. In contrast, walking sessions with mean frequencies below 1.9Hz show substantially higher COVs, typically bellow 7.5%, but in some sessions reaching values of up to 10%. This higher COVs are accompanied by a pronounced scatter, which indicates that intra-subject variability in walking frequency is more pronounced at lower pacing rates, whereas pedestrians are better able to maintain a steady pace at higher walking frequencies. Lower pacing rates are associated with longer step periods, providing greater scope for step-to-step variations in timing. The narrow spread of COVs within the $1.9 - 2.2$Hz frequency range suggests that different pedestrians exhibit similar levels of intra-subject variability at these walking frequencies, while the large dispersion observed below 1.9Hz reflects a higher variations in intra-subject variability across individuals. These results and conclusions are consistent with the findings reported by Dang [93] for pedestrians walking on a rigid surface.

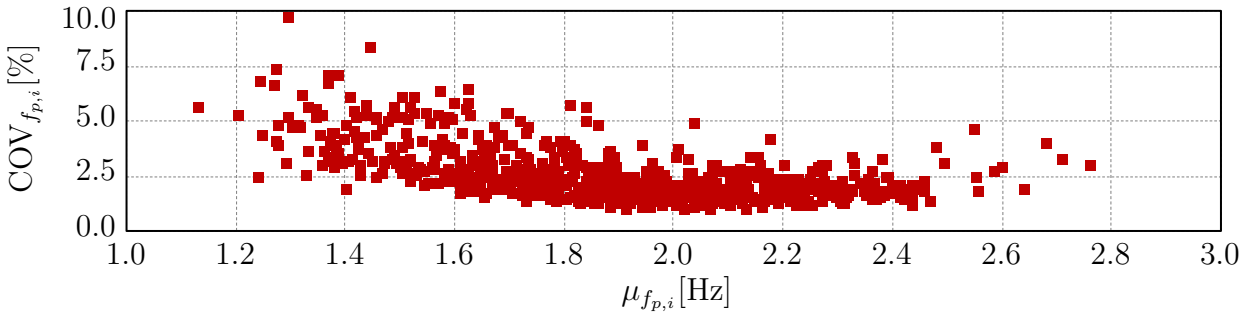

Figure 7.3: COVs with corresponding mean walking frequencies.

7.2.2.2 Dynamic load factors

To evaluate the DLFs on a step-by-step basis, each normalised force record was first segmented into previously identified N_{step} individual steps. Each step segment of signal i was then approximated by a truncated harmonic series of the form

$$F_{i,\text{step}}(t) \approx \sum_{h=1}^{6} \Big(A_{h,\text{step},i} \sin\Big(2\pi h f_{p,\text{step}} t\Big) + B_{h,\text{step},i} \cos\Big(2\pi h f_{p,\text{step}} t\Big)\Big), \tag{7.3}$$

where $A_{h,\text{step},i}$ and $B_{h,\text{step},i}$ are coefficients obtained by a least-squares fit to the measured step segment. This representation is equivalent to a single sine term with a phase shift:

$$\text{DLF}_{h,\text{step},i} \sin\Big(2\pi h f_{p,\text{step}} t + \varphi_{h,\text{step},i}\Big), \tag{7.4}$$

from which the DLF and phase angle of the hth harmonic follow as

$$\begin{aligned} \text{DLF}_{h,\text{step},i} &= \sqrt{A_{h,\text{step},i}^2 + B_{h,\text{step},i}^2}, \\ \varphi_{h,\text{step},i} &= \text{atan}\left(-\frac{B_{h,\text{step},i}}{A_{h,\text{step},i}}\right). \end{aligned} \tag{7.5}$$

It should be noted that the proposed harmonic force model defined by Eq. (7.1) does not include phase angles. They are evaluated here primarily to ensure best possible estimation of the DLFs and to enable reconstruction of the measured force time histories for the validation presented in Subsection 7.2.3. In Chapters 8 and 9, the CCIP-016-based procedure is adopted for calculating the vibration response. Since the relative phases of the harmonic components are not retained in the CCIP-016 load model, the corresponding response components cannot be directly superimposed. Instead, the total vibration response is calculated by combining magnitudes associated with the individual harmonics using the square-root-of-the-sum-of-squares (SRSS) method (see Section 2.3). Consequently, the relative phase angles between the harmonic components are not required for the purposes of this dissertation and are not considered further.

For each walking session i, the mean values $\mu_{\text{DLF}_{h,i}}$, standard deviations $\sigma_{\text{DLF}_{h,i}}$ and $\text{COV}_{\text{DLF}_{h,i}}$ were calculated. An example of variation in DLFs during walking session $i = 446$ is illustrated in Figure 7.4. A walking session characterised by a low coefficient of variation of 1.22% in walking frequency (Figure 7.2) nevertheless resulted in substantially higher COVs of the DLFs, ranging from 6.04% for DLF_1 to 29.38% for DLF_2. Such considerably higher variability in the DLFs than in walking frequency was typical across the analysed walking sessions.

Identified DLF mean values $\mu_{\text{DLF}_{h,i}}$ obtained from all processed signals are plotted against the corresponding mean walking frequencies $\mu_{f_{p,i}}$ in Figure 7.5. Consistent with the findings of Kerr [49] and Dang [93], a clear increasing trend of the mean DLF_1 with increasing mean walking frequency is observed. Much weaker, yet noticeable positive correlations are observed for $\mu_{\text{DLF2},i}$ and $\mu_{\text{DLF4},i} - \mu_{\text{DLF6},i}$, whereas $\mu_{\text{DLF3},i}$ shows no observable correlation with $\mu_{f_{p,i}}$. Furthermore, the COV of all DLFs for the 744 processed signals $\text{COV}_{\text{DLF}_{h,i}}$ are plotted against

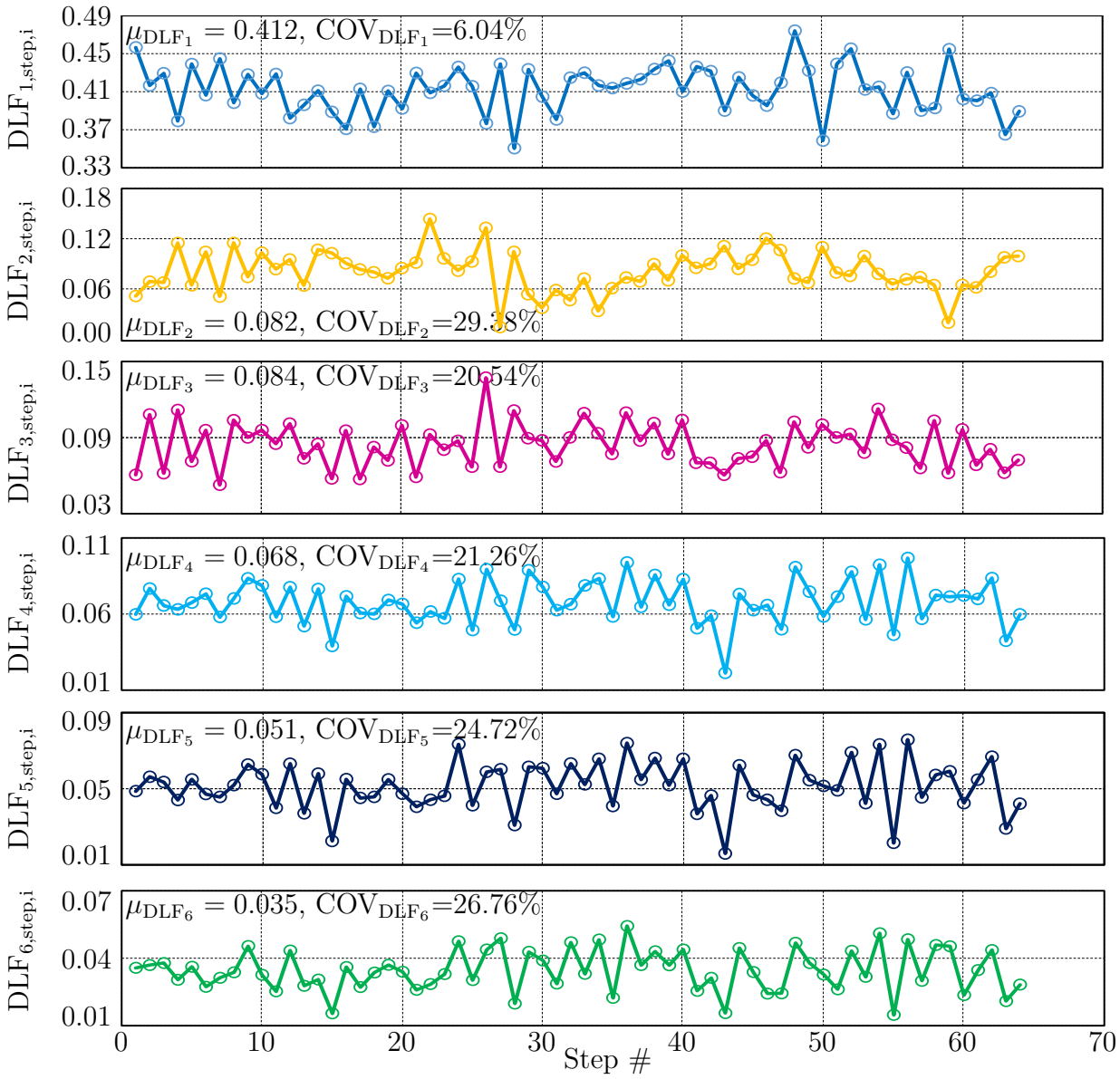

Figure 7.4: Variability of DLFs during a single walk.

the corresponding mean walking frequencies $\mu_{f_{p,i}}$ in Figure 7.6. The lowest step-by-step variability is observed for the DLF of the first harmonic. The maximum corresponding $COV_{DLF_{1,i}}$ reaches 24%, exhibiting a clear decreasing trend with μ_{f_p}. This indicates that pedestrians are better able to maintain a steady force when walking at higher pacing rates. A similar trend is documented by Dang [93]. In contrast, the highest variability is observed for the second and the sixth DLFs, with $COV_{DLF_{2,i}}$ reaching 80%, while the COVs for $DLF_{3,i}$-$DLF_{5,i}$ remain below 60%. Moreover, a pronounced scatter is evident for $DLF_{2,i}$-$DLF_{6,i}$, with no clear correlation observed with the mean walking frequency.

Figure 7.7 shows a matrix of pairwise scatter plots in which the mean values of the six DLFs are plotted against one another to illustrate their mutual correlation. The scatter plot matrix indicates that the mean DLFs are not statistically independent. Strong linear correlations are observed primarily among the higher harmonics ($\mu_{DLF_{4,i}}$-$\mu_{DLF_{6,i}}$), indicating that their amplitudes tend to increase and decrease together. In contrast, amplitudes $\mu_{DLF_{1,i}}$-$\mu_{DLF_{3,i}}$ exhibit weaker and less consistent correlations with the remaining harmonics. This is particularly pronounced for the amplitude of the third harmonic.

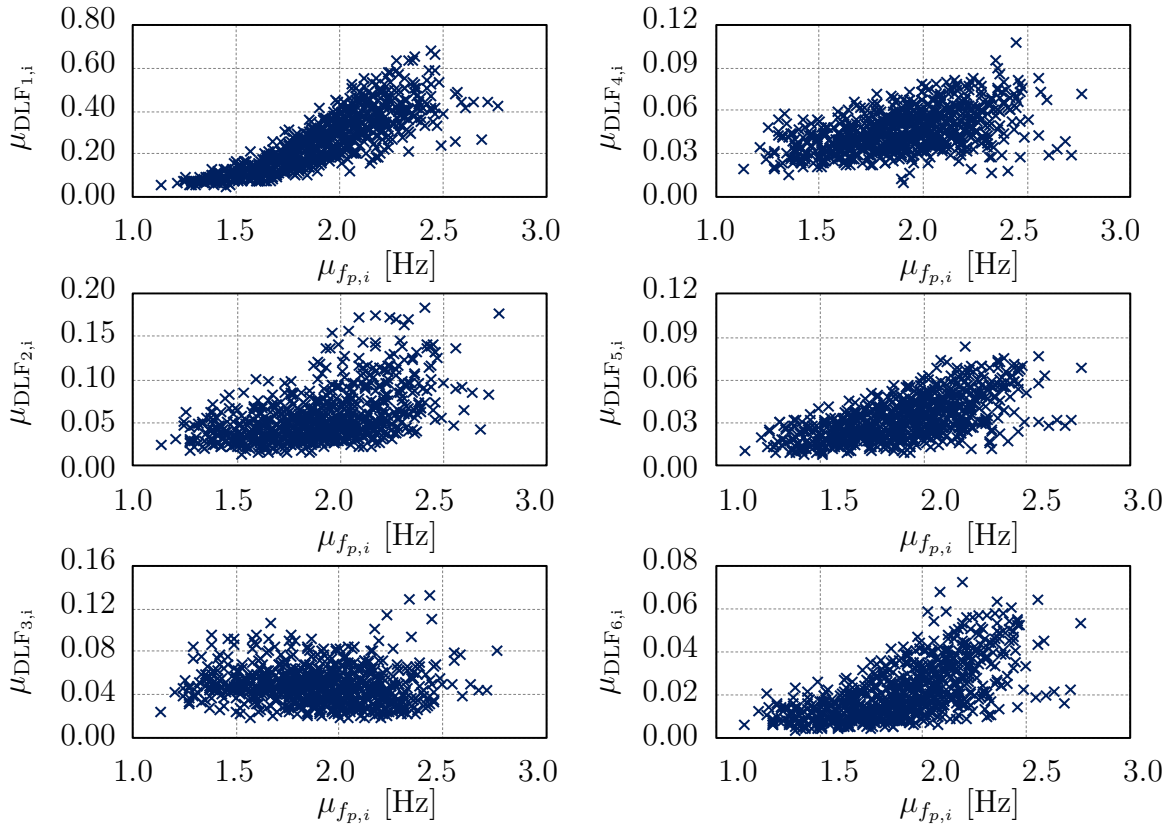

Figure 7.5: Mean values of DLFs with corresponding walking frequencies.

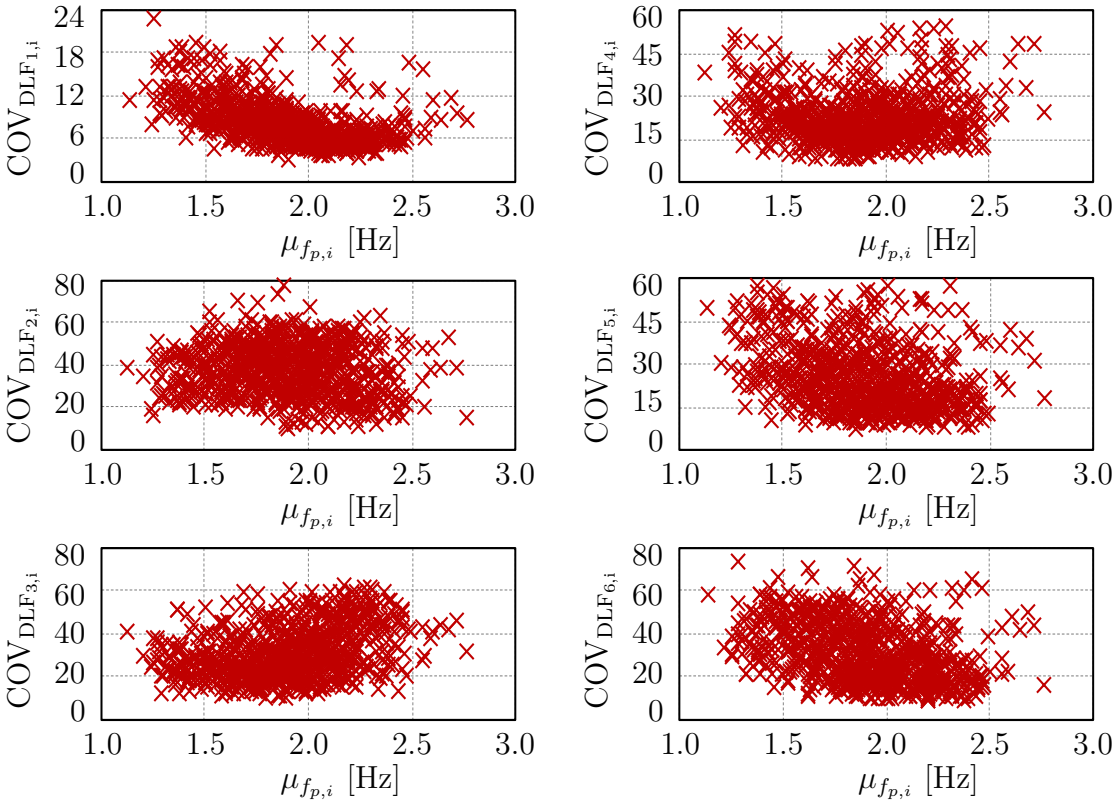

Figure 7.6: COVs of DLFs with corresponding walking frequencies.

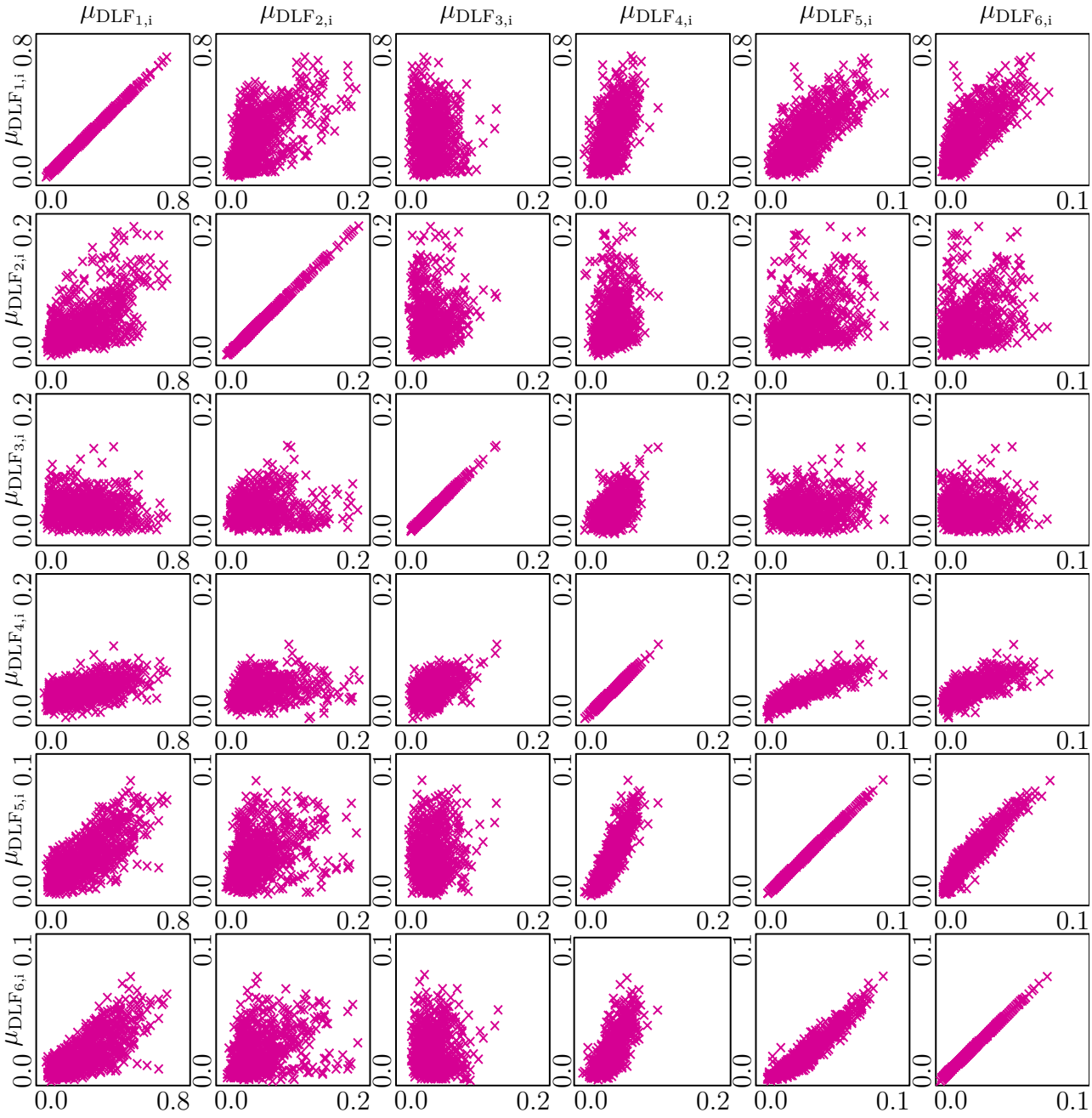

Figure 7.7: Correlation between DLF mean values for six harmonics.

7.2.2.3 Autoregressive coefficients

The AR coefficients ρ_{f_p} and ρ_{DLF_h} were estimated directly from the obtained step-by-step f_p and DLF_h series, respectively, using a least-squares approach. For each walking session and each parameter, the series was centred by removing its mean and the coefficient was computed as the ratio of the covariance between consecutive values and the variance of the previous values. Figures 7.8 and 7.9 show the estimated AR coefficients ρ_{f_p} and ρ_{DLF_h} plotted against the corresponding mean walking frequencies and mean DLF_h values, respectively. A substantial scatter is observed for all coefficients, indicating that the strength and even the sign of step-to-step dependence varies significantly between walking sessions and participants. Most values of ρ_{f_p} are negative, which suggests an alternating pattern in step-by-step walking frequency, i.e. values higher than mean tend to be followed by values lower than mean and vice versa.

A similar tendency is observed for $\rho_{\mathrm{DLF}_3} - \rho_{\mathrm{DLF}_6}$, whereas ρ_{DLF_1} and ρ_{DLF_2} are more evenly distributed around zero, implying no consistent behaviour for these harmonics.

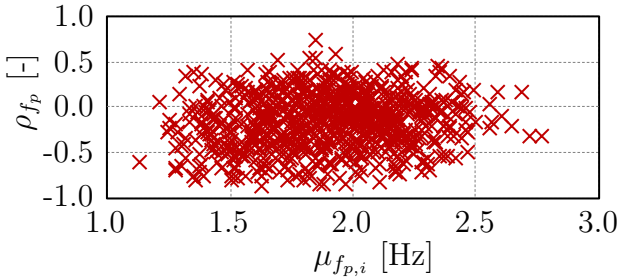

Figure 7.8: The AR coefficients ρ_{f_p} with corresponding mean walking frequencies.

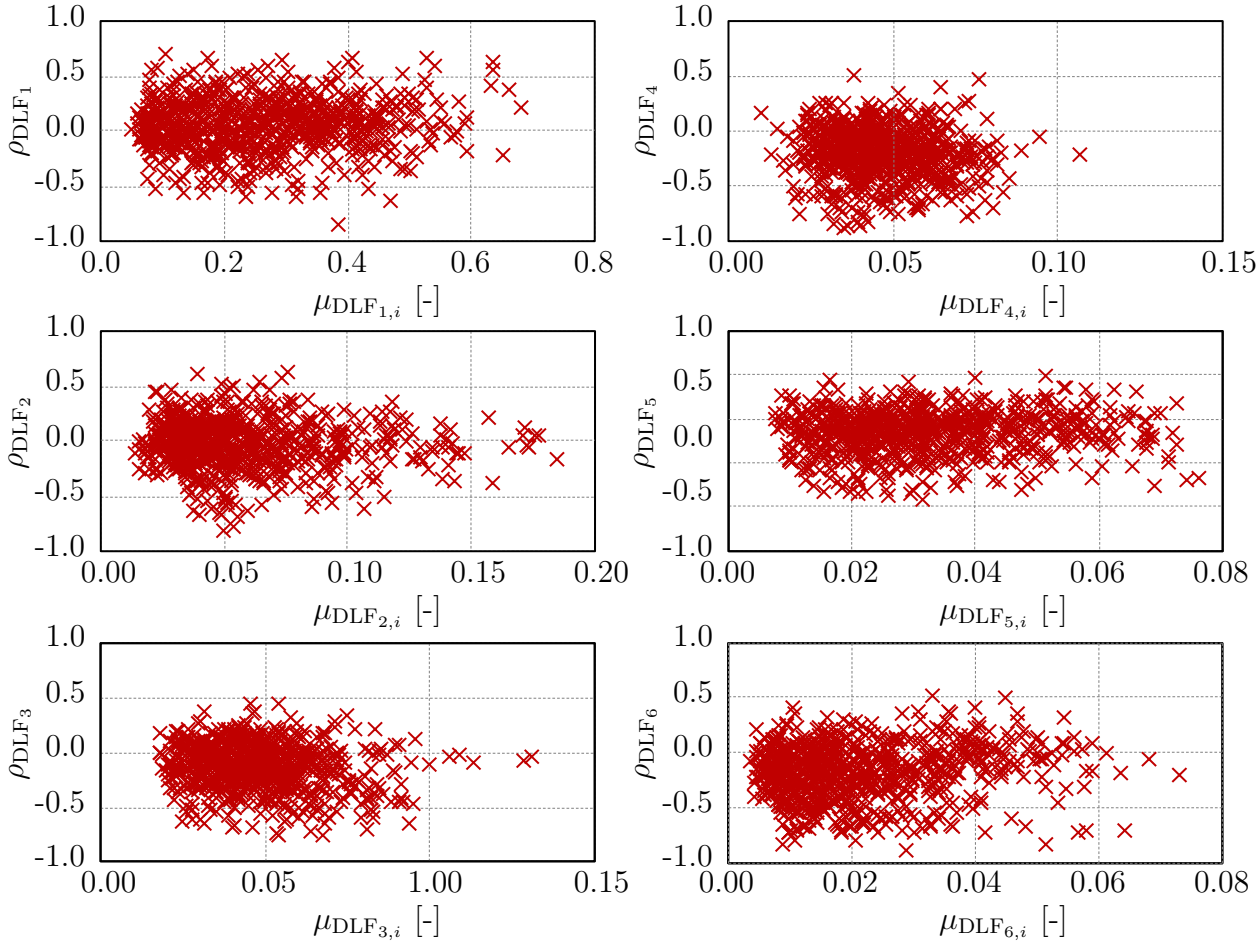

Figure 7.9: The AR coefficients ρ_{DLF_h} with corresponding mean DLFs.

7.2.3 Verification through force reconstruction and SDOF response calculation

Processing each of the 744 normalised force records produced, for every step in a walking session, walking frequency, six DLFs and the corresponding six phase angles. These parameters were then substituted into

$$F_{p,\mathrm{step}}(t) = 1 + \sum_{h=1}^{6} \mathrm{DLF}_{h,\mathrm{step}} \sin\Big(2\pi h f_{p,\mathrm{step}} t + \varphi_{h,\mathrm{step}}\Big), \tag{7.6}$$

to reconstruct the force time history for each step, resulting in 744 reconstructed signals with N_{step} step segments. One representative example of measured and reconstructed force signal is shown in Figure 7.10. Differences between the measured and reconstructed signals are confined to frequency components above the sixth harmonic in the amplitude spectrum (Figure 7.10b), and appear in the time domain only as slightly higher peak values (Figure 7.10a).

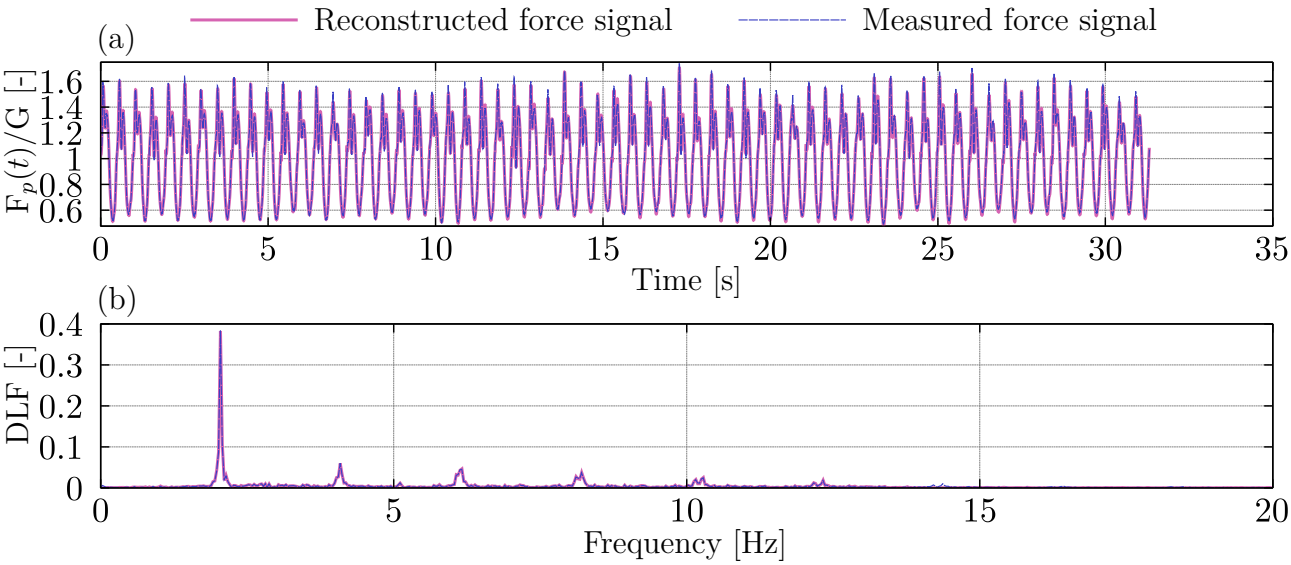

Figure 7.10: Measured and reconstructed force time histories (a) and corresponding Fourier amplitude spectra (b) for walking session $i = 446$.

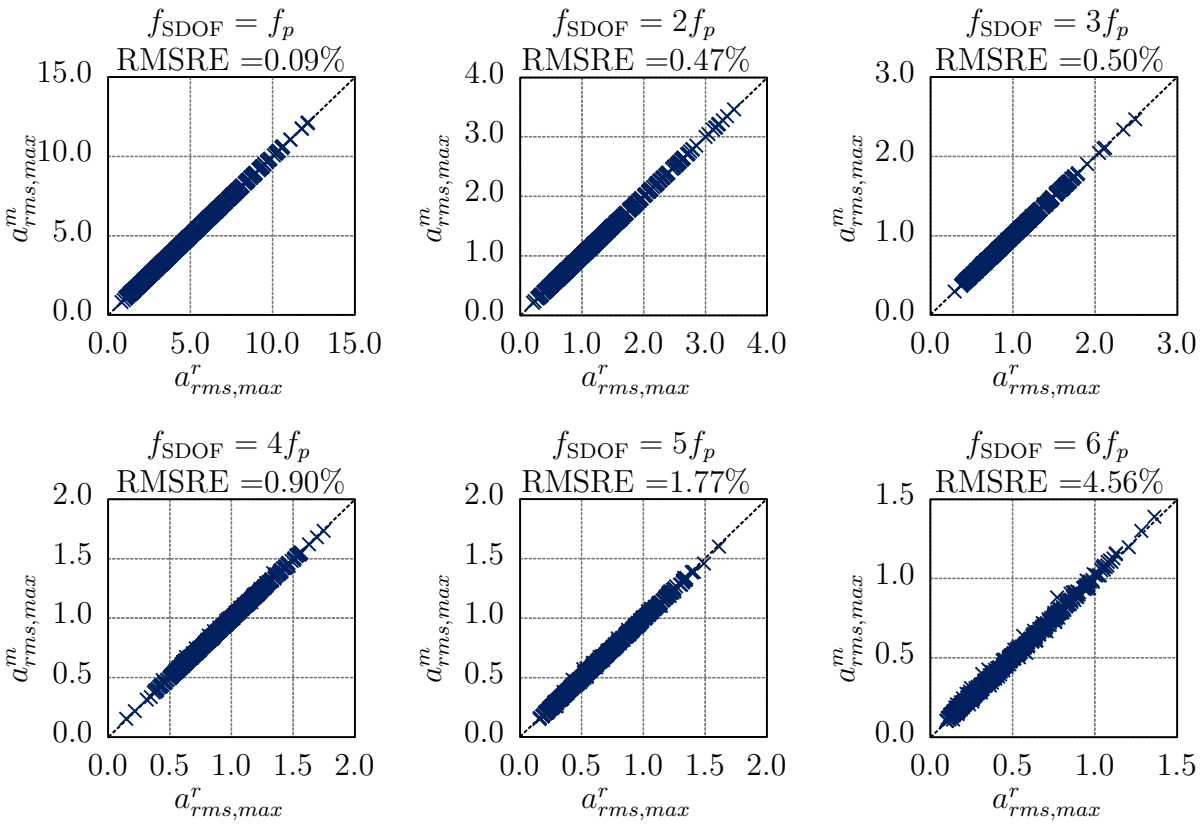

Figure 7.11: Acceleration response of the SDOF oscillators [mm/s^2] induced by all 744 measured ($a^m_{rms,max}$) and reconstructed ($a^r_{rms,max}$) force signals.

Furthermore, verification of the reconstructed force signal was performed by computing the acceleration response of a SDOF oscillator subjected to each of the 744 measured load signals and its corresponding reconstructed counterpart. The SDOF was assigned a modal mass of 1000kg and a damping ratio of 2%. Its natural frequency was successively set to f_p, $2f_p$,...,$6f_p$, so that the responses for all six harmonics could be compared directly. For each simulation, the maximum value of the 1-s moving root-mean-square (RMS) acceleration $a_{rms,max}$ was evaluated for both the measured (m) and reconstructed (r) forces. The resulting comparison is presented in Figure 7.11, while illustrative acceleration time histories are shown in Figures 7.12 and 7.13.

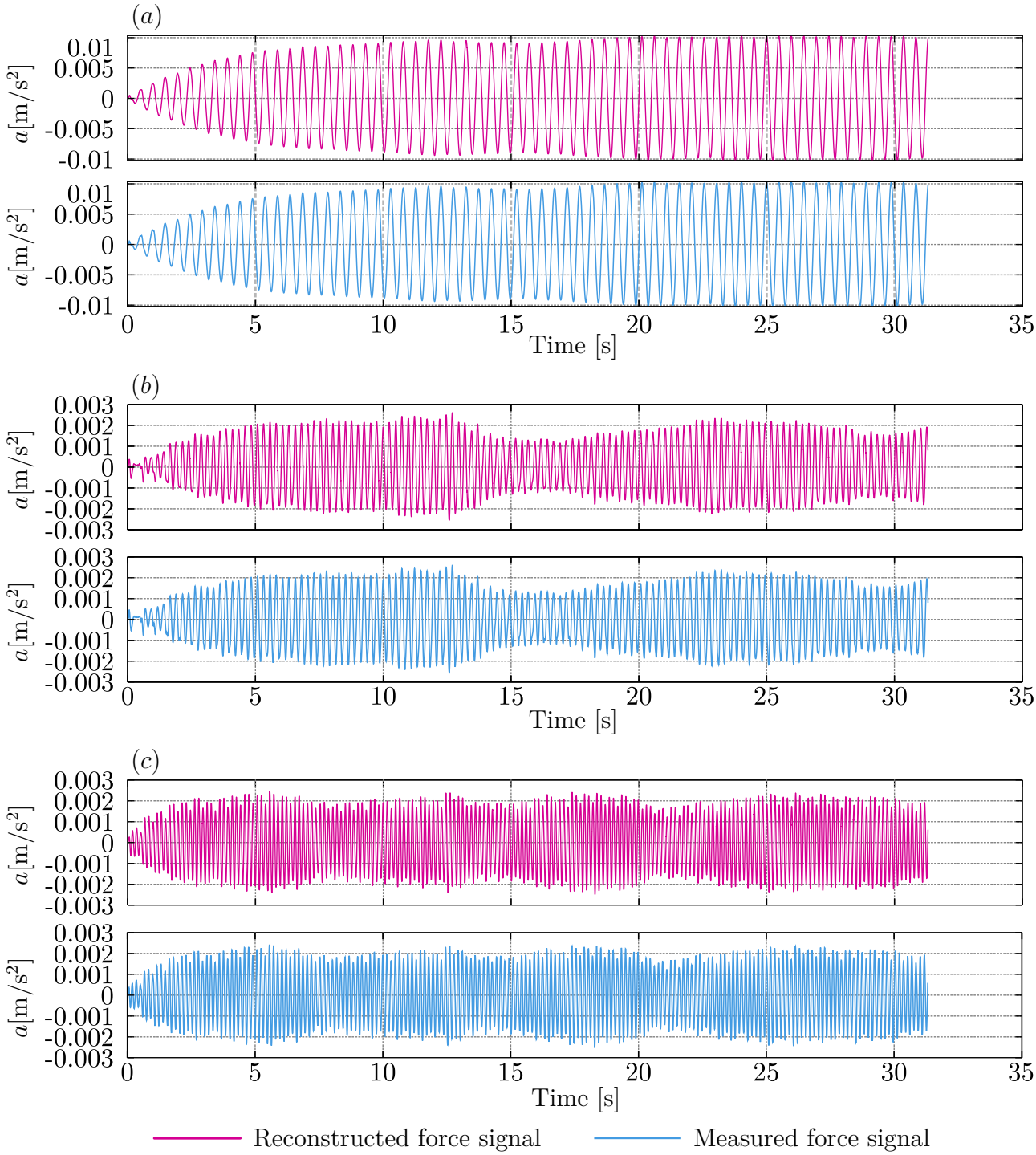

Figure 7.12: Acceleration response of the SDOF oscillators with frequency $f = f_p$ (a), $f = 2f_p$ (b) and $f = 3f_p$ (c) induced by measured and corresponding reconstructed force signal (walking session $i = 446$).

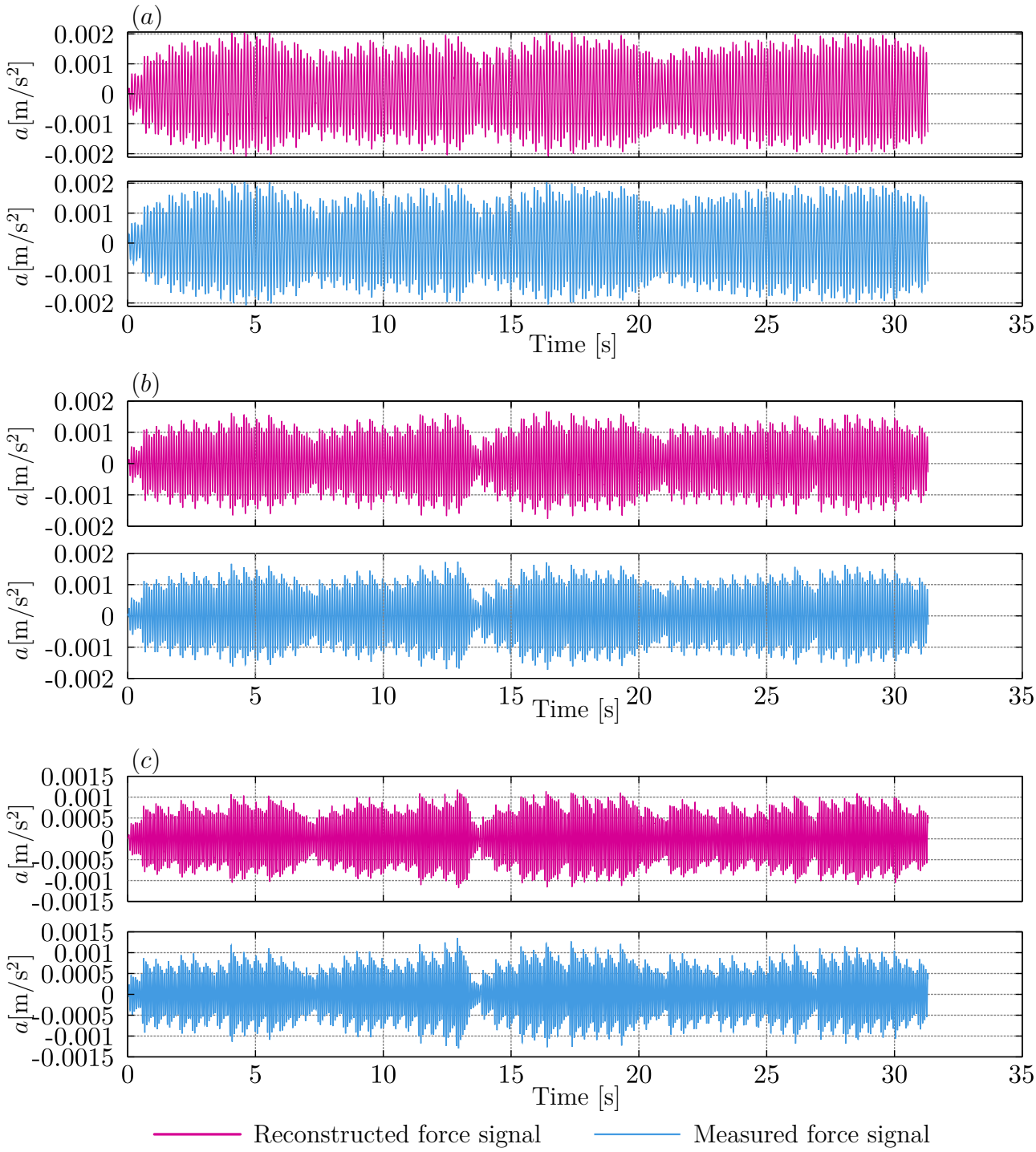

Figure 7.13: Acceleration response of the SDOF oscillators with frequency $f = 4f_p$ (a), $f = 5f_p$ (b) and $f = 6f_p$ (c) induced by measured and corresponding reconstructed force signal (walking session $i = 446$).

For each of the six SDOF oscillators, the RMSRE was computed as

$$\text{RMSRE} = \sqrt{\frac{1}{744}\sum_{i=1}^{744}\left(\frac{a^r_{rms,max} - a^m_{rms,max}}{a^m_{rms,max}}\right)^2} \tag{7.7}$$

and the resulting values are reported in Figure 7.11. With RMSRE values below 1%, the reconstructed forces reproduce the acceleration response associated with the first four harmonics with excellent accuracy. A modest increase in error is observed for the fifth harmonic, while

the largest discrepancy, 4.56%, occurs for the sixth harmonic. This increase is expected and remains acceptable, as the measured force spectrum contains very limited and more dispersed energy at higher harmonics. Consequently, their amplitudes are inherently more difficult to estimate and reconstruct reliably.

7.2.4 Probabilistic description of model parameters

The harmonic force model introduced in Subsection 7.2.1 and defined by Eqs. (7.1) and (7.2) is governed by 22 parameters: 15 force parameters (pedestrian's weight, walking frequency mean and standard deviation, mean and standard deviation for six DLFs) and 7 AR coefficients (one corresponding to walking frequency and six for each of DLFs). However, these two groups of parameters play different roles. Force parameters determine the magnitude and variability of the walking load and therefore constitute the primary sources of both inter- and intra-subject uncertainty. In contrast, the AR coefficients describe the temporal dependence between successive step values. Although they are also represented as random variables, they are treated as secondary parameters used to reproduce realistic step-to-step sequences rather than as principal drivers of load uncertainty. Consequently, the uncertainty analyses presented in Chapter 9 consider only the 15 force parameters, while the AR coefficients are retained solely to represent the temporal structure of the load.

The 15 force parameters were modelled as random variables by fitting probability distributions to the previously extracted statistics (Subsection 7.2.4.1). Five candidate distributions (normal, lognormal, gamma, Weibull, and beta) were examined and the most suitable distribution in each case was selected using the Kolmogorov-Smirnov (K-S) goodness-of-fit test [180]. Dependencies between the force parameters were accounted for in two ways (Subsection 7.2.4.2). First, statistical dependence between force parameters was represented using linear correlation coefficients estimated from the database. Second, temporal dependence within a walking session was defined through the already mentioned AR coefficients ρ_{f_p} and ρ_{DLF_h}.

7.2.4.1 Random-variable modelling of force parameters

Since body weight is constant for a given individual, it characterises only inter-subject variability of pedestrian-induced load. The histogram of body weight of all 80 volunteers presented in Figure 7.14 demonstrates that variability of pedestrian body weight was well represented by a normal distribution with a mean value of 757N, standard deviation of 151.55N and COV of 20%, which was adopted in the subsequent analyses.

For each walking session i, the step-by-step walking frequencies were represented by their mean value $\mu_{f_p,i}$ and standard deviation $\sigma_{f_p,i}$. The mean $\mu_{f_p,i}$ defines the average pacing rate maintained during session i, whereas $\sigma_{f_p,i}$ measures the fluctuation od the individual step frequencies around this session mean. Histograms of $\mu_{f_p,i}$ and $\sigma_{f_p,i}$ across the complete database are presented in Figure 7.15. By fitting appropriate distributions to these histograms, two random variables are defined: the mean walking frequency μ_{f_p} and the within-session standard deviation of walking frequency σ_{f_p}. Variability of μ_{f_p} represents differences in average pacing rates among walking sessions (inter-subject variability), while σ_{f_p} quantifies the magnitude of step-to-step variability within each session (intra-subject variability). The mean walking frequency is well approximated by a normal distribution with the mean value of 1.9Hz and standard deviation of 0.266Hz, corresponding to a COV of 14%. This mean value is consistent

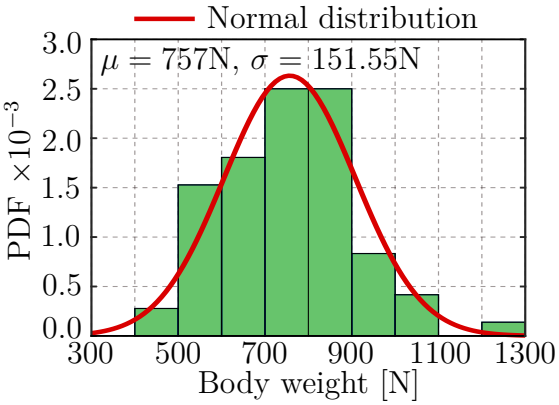

Figure 7.14: Histogram of pedestrian body weight and corresponding normal distribution.

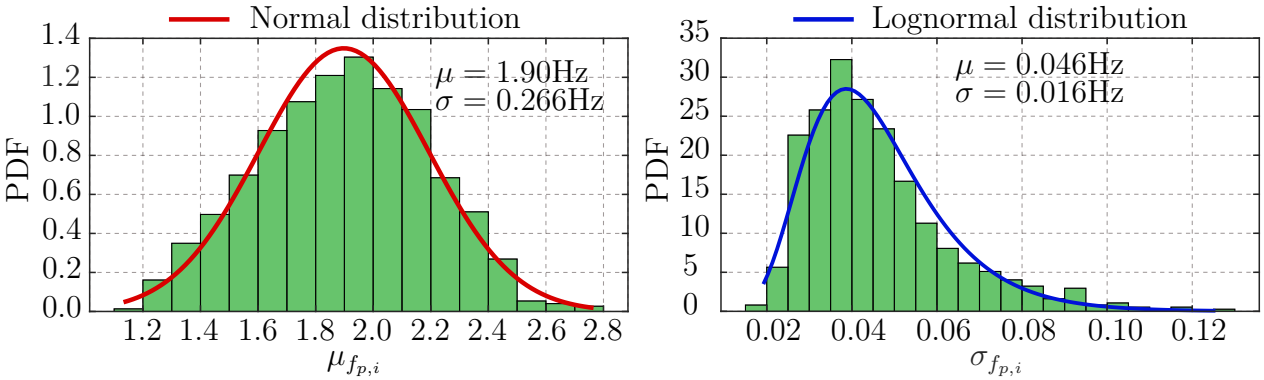

Figure 7.15: Histograms of walking frequency mean value $\mu_{f_{p,i}}$ and standard deviation $\sigma_{f_{p,i}}$, with distributions utilised to approximate μ_{f_p} and σ_{f_p}.

with previous studies listed in Table 2.1, while the associated standard deviation is found to be moderately higher. A lognormal distribution provides a good fit to the values of σ_{f_p}, with a mean of 0.046Hz and a standard deviation of 0.016Hz, corresponding to a COV of 35% (Figure 7.15). A comparison of the COVs of μ_{f_p} and σ_{f_p} indicates that a pedestrians ability to maintain a constant pacing rate exhibits greater variability than the walking frequency itself.

Analogously to the walking frequency, the variability of the DLFs for each of the six harmonics was characterised using two random variables. The mean value μ_{DLF_h} captures differences in mean force amplitude between walking sessions (inter-subject variability), whereas the standard deviation, σ_{DLF_h}, quantifies step-to-step amplitude variations within a single session (intra-subject variability). The probability distributions of μ_{DLF_h} were fitted to the histograms of the session-wise mean values $\mu_{\mathrm{DLF}_{h,i}}$ and are shown in Figure 7.16, while σ_{DLF_h} were fitted to the histograms of the session-wise standard deviations $\sigma_{\mathrm{DLF}_{h,i}}$ and are presented in Figure 7.17. The resulting fitted distributions and the corresponding parameter values for all 15 force parameters are summarised in Table 7.1.

The fitted distributions in Figure 7.16 demonstrate that three mean DLF values (μ_{DLF_2}, μ_{DLF_4}, μ_{DLF_6}) are best represented by lognormal, two (μ_{DLF_1}, μ_{DLF_5}) by beta, and one (μ_{DLF_3}) by a gamma distribution. As expected, μ_{DLF_1} attains the largest mean value, while μ_{DLF_2} is approximately 4.5 times smaller, and the mean values continue to decrease towards μ_{DLF_6}. The highest variability, with COV of 68%, is observed for μ_{DLF_6}. Furthermore, high variability is observed for μ_{DLF_1}, μ_{DLF_2} and μ_{DLF_5}, with COVs of 50, 52.6 and 46.9%, respectively. Finally, μ_{DLF_3} and μ_{DLF_4} exhibit lower variability, with COVs of 34.6 and 30.4%, respectively.

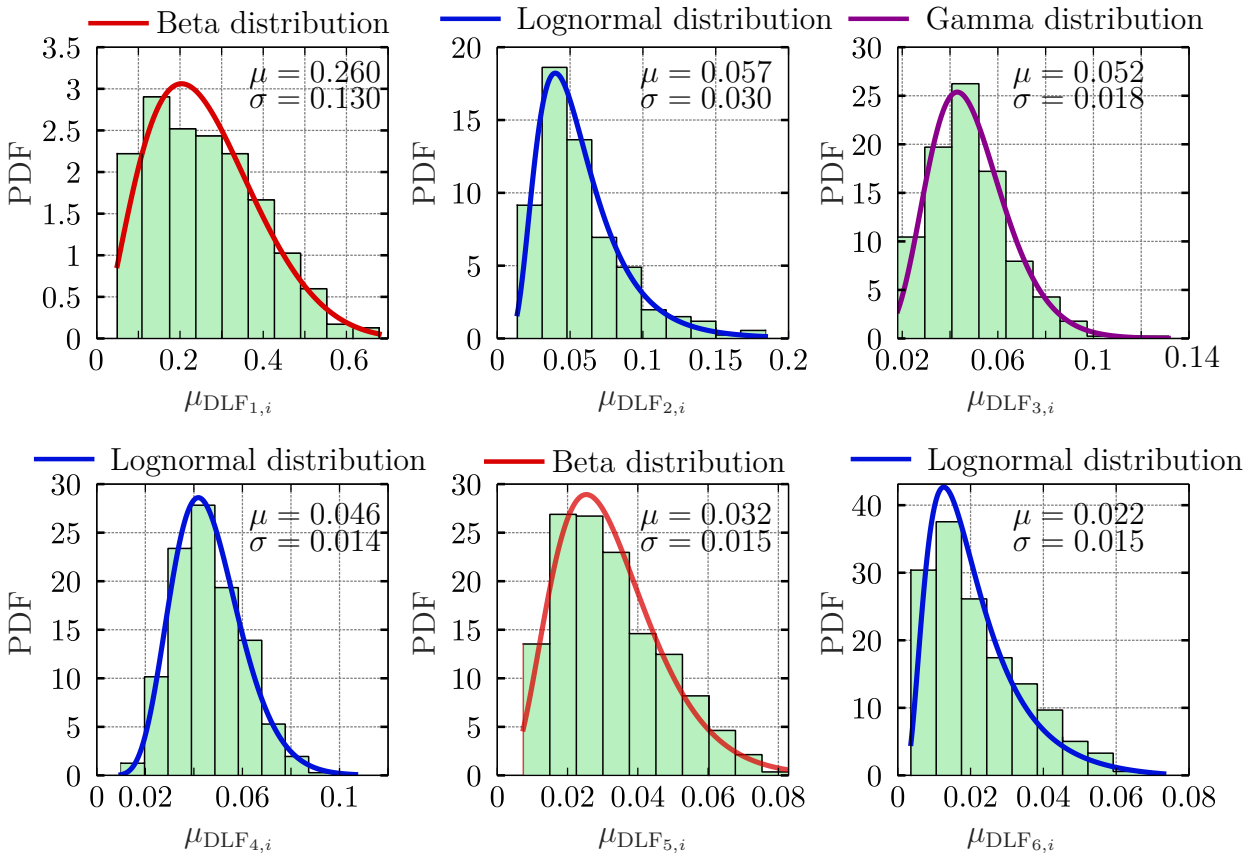

Figure 7.16: Histograms of DLF mean values $\mu_{\mathrm{DLF}_{h,i}}$ with distributions utilised to approximate μ_{DLF_h}.

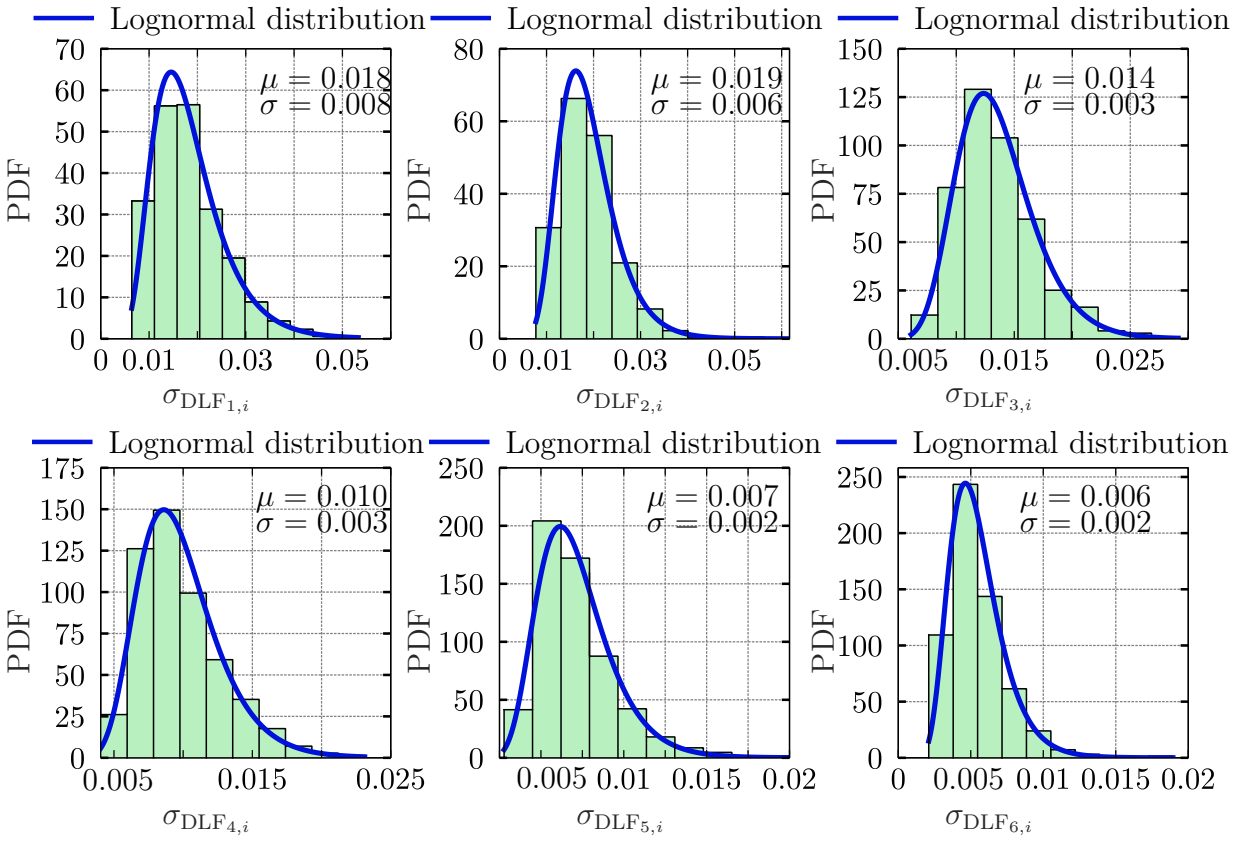

Figure 7.17: Histograms of DLF standard deviations $\sigma_{\mathrm{DLF}_{h,i}}$ with distributions utilised to approximate σ_{DLF_h}.

The standard deviations of all six DLFs are best described by lognormal distributions. The highest mean values of σ_{DLF_h} are obtained for DLF_1 and DLF_2, indicating that these harmonic amplitudes exhibit the largest step-to-step fluctuations. Moreover, σ_{DLF_1} shows the greatest relative variability within different walking sessions with COV of 44.4%, while σ_{DLF_3} demonstrates the lowest relative variability with COV of 21.4%. For the remaining σ_{DLF_h}, the COVs fall within a narrower range of approximately 28.5% to 33.3%.

Table 7.1: Fitted distributions of force parameters.

		Distribution properties		
Force parameter	**Label**	**Type**	**Parameter 1**	**Parameter 2**
Body weight	G	Normal	757	151.55
Mean f_p	μ_{f_p}	Normal	1.900	0.266
St. deviation f_p	σ_{f_p}	Lognormal	−3.137	0.341
Mean DLF_1	μ_{DLF_1}	Beta	2.720	7.725
St. deviation DLF_1	σ_{DLF_1}	Lognormal	−4.074	0.394
Mean DLF_2	μ_{DLF_2}	Lognormal	−2.981	0.497
St. deviation DLF_2	σ_{DLF_2}	Lognormal	−4.021	0.316
Mean DLF_3	μ_{DLF_3}	Gamma	8.650	0.006
St. deviation DLF_3	σ_{DLF_3}	Lognormal	−4.333	0.247
Mean DLF_4	μ_{DLF_4}	Beta	9.704	200.368
St. deviation DLF_4	σ_{DLF_4}	Lognormal	−4.668	0.297
Mean DLF_5	μ_{DLF_5}	Beta	4.404	131.927
St. deviation DLF_5	σ_{DLF_5}	Lognormal	−4.992	0.309
Mean DLF_6	μ_{DLF_6}	Lognormal	−4.001	0.608
St. deviation DLF_6	σ_{DLF_6}	Lognormal	−5.264	0.334

7.2.4.2 Dependence modelling

As noted earlier, dependencies among the force parameters were represented in two complementary ways: (i) statistical dependence, quantified via linear correlation coefficients, and (ii) temporal dependence within a walking session, captured using AR coefficients.

The matrix of linear correlation coefficients is shown in Figure 7.18. Coefficients with magnitudes close to 1 indicate a strong linear association between two parameters. A value of +1 corresponds to a perfect positive (increasing) linear relationship, whereas −1 denotes a perfect negative (decreasing) linear relationship. Overall, the matrix is dominated by positive correlations, indicating that many force parameters tend to vary in the same direction across the dataset. The only exception is σ_{f_p}, which exhibited several negative correlation coefficients. The most pronounced were −0.395 with μ_{DLF_1} and −0.250 with μ_{f_p}, μ_{DLF_5} and μ_{DLF_6}. The negative correlation with μ_{f_p} is consistent with the trend observed in Figure 7.3, where COV decreases as the mean walking frequency increases. Strong correlations are observed between mean walking frequency μ_{f_p} and the both DLF_1 parameters, with coefficients of 0.833 for μ_{DLF_1} and 0.711 for σ_{DLF_1}. In addition, μ_{f_p} shows moderate to high correlation with the most remaining DLF parameters, with coefficients ranging from 0.352 to 0.632. The only notable exception is μ_{DLF_3}, for which the correlation with μ_{f_p} is negligible. Furthermore, strong dependencies are

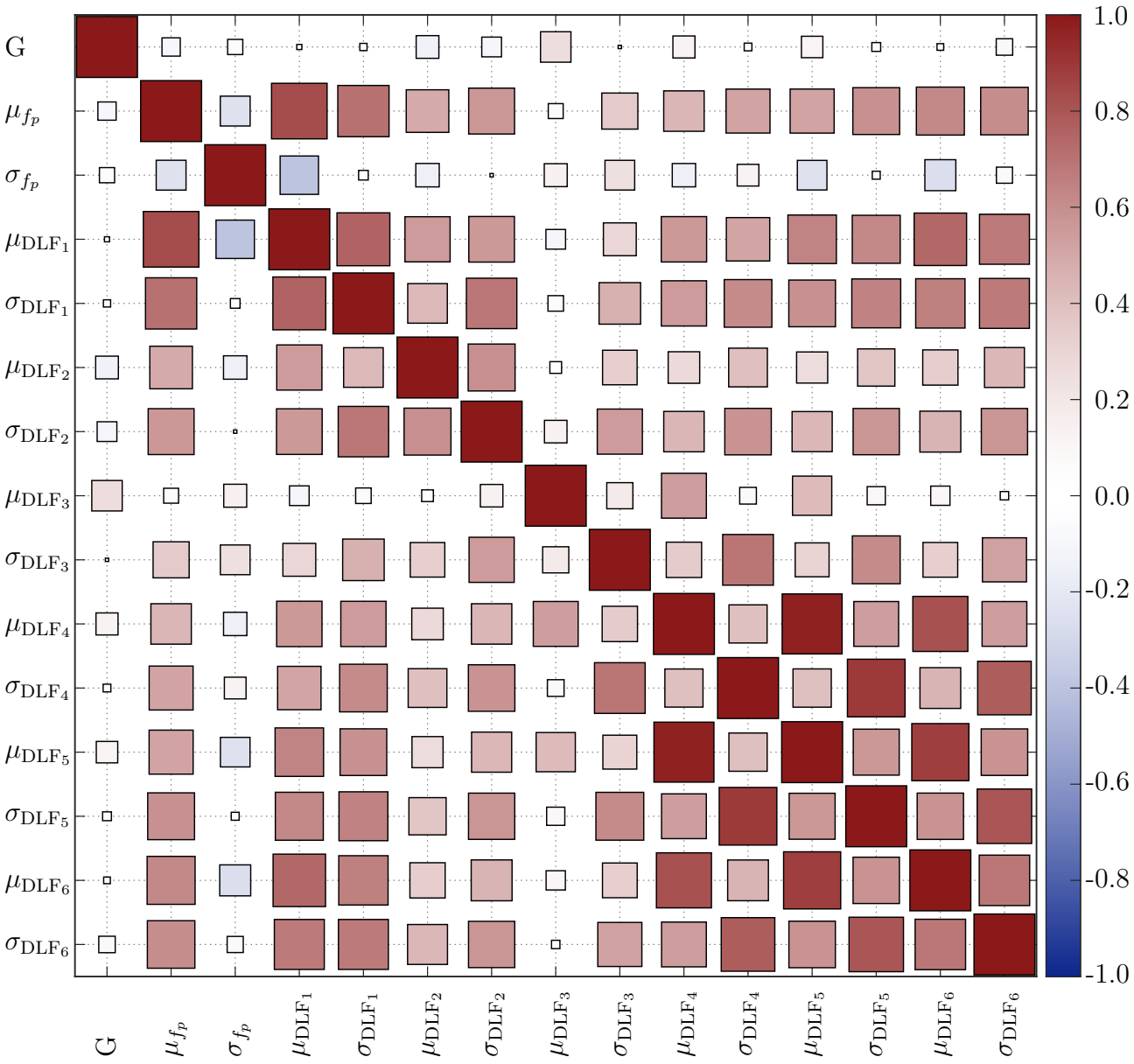

Figure 7.18: Matrix of linear correlation coefficients for 15 force parameters.

evident among the DLF-related parameters, forming two distinct correlation clusters separated by μ_{DLF_3}. The first cluster involves the first two harmonics, with the largest coefficient (0.754) observed between μ_{DLF_1} and σ_{DLF_1}. The second cluster is located in the bottom-right region of the matrix and corresponds to the higher harmonics. In this cluster, correlations are generally stronger between mean values across different harmonics ($0.740 - 0.950$) and, similarly, between standard deviations across different harmonics ($0.671 - 0.850$). In contrast, correlations between the corresponding mean and standard deviation within the same harmonic as well as across different harmonics are comparatively weaker ($0.342 - 0.609$). Finally, the body weight G shows predominantly weak correlations with the all remaining parameters.

Each of seven AR coefficients are bounded within $[-1, 1]$ and truncated normal distribution was adopted for their representation. Mean values and standard deviations for these seven coefficients are listed in Table 7.2. Distribution for modelling ρ_{f_p} with corresponding histogram is illustrated in Figure 7.19. Negative mean value of ρ_{f_p} confirms the predominantly alternating behaviour of the step frequency within a walking session, as discussed in Subsection 7.2.2. The corresponding standard deviation of 0.296 indicates a very high uncertainty in this parameter.

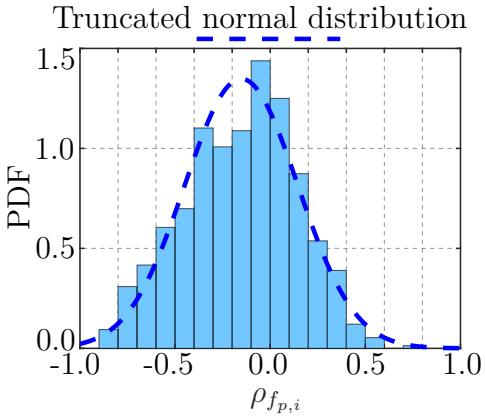

Figure 7.19: Histogram of AR coefficient for walking frequency $\rho_{f_{p,i}}$ with distribution utilised to approximate ρ_{f_p}.

Distribution parameters of AR coefficients ρ_{DLF_h}, listed in Table 7.2, indicate comparable standard deviations across all harmonics, ranging narrowly between 0.209 and 0.249, while the mean values vary from -0.198 to 0.048. To avoid introducing six separate random variables, these coefficients are modelled using a unified formulation. Accordingly, each ρ_{DLF_h} is expressed as:

$$\rho_{\mathrm{DLF}_h} = \mu_{\rho_{\mathrm{DLF}_h}} + \sigma_{\rho_{\mathrm{DLF}}} \cdot Z \tag{7.8}$$

where $\mu_{\rho_{\mathrm{DLF}_h}}$ denotes the mean value of ρ_{DLF_h} (Table 7.2), $\sigma_{\rho_{\mathrm{DLF}}} = 0.231$ is the average standard deviations of all ρ_{DLF_h}, and Z is a truncated normal random variable ($[-1, 1]$) with zero mean and unit standard deviation. Corresponding distributions are presented in Figure 7.20.

Table 7.2: Distribution parameters of AR coefficient.

Coefficient	**Mean value**	**Standard deviation**
ρ_{f_p}	-0.154	0.296
ρ_{DLF_1}	0.048	0.236
ρ_{DLF_2}	-0.041	0.218
ρ_{DLF_3}	-0.132	0.209
ρ_{DLF_4}	-0.198	0.225
ρ_{DLF_5}	-0.164	0.247
ρ_{DLF_6}	-0.164	0.249

7.2.5 Implementation and generation of probabilistic harmonic load

A procedure to generate a single realisation of the harmonic force is described in Algorithm 4. A sample of the 15 input force variables $\mathbf{X}_{\mathcal{F}}$ is first drawn from their joint distribution $\mathbf{G}_{\mathcal{F}}$ defined by the marginal distributions in Table 7.1 and the correlation matrix $\mathbf{C}_{\mathcal{F}}$ (Figure 7.18). The AR coefficient ρ_{f_p} is then sampled independently according to its distribution (Table 7.2), together with the auxiliary random variable Z. The remaining AR coefficients ρ_{DLF_h} are subsequently evaluated using Eq. (7.8). Next, the step-wise walking frequency and the six DLF values are generated from the AR(1) formulation in Eq. (7.2), with the initial-step values prescribed as the corresponding mean values. The harmonic force contribution for each step is then computed using Eq. (7.1). Finally, the complete force time history is obtained by concatenating the step-wise force segments into a single continuous signal.

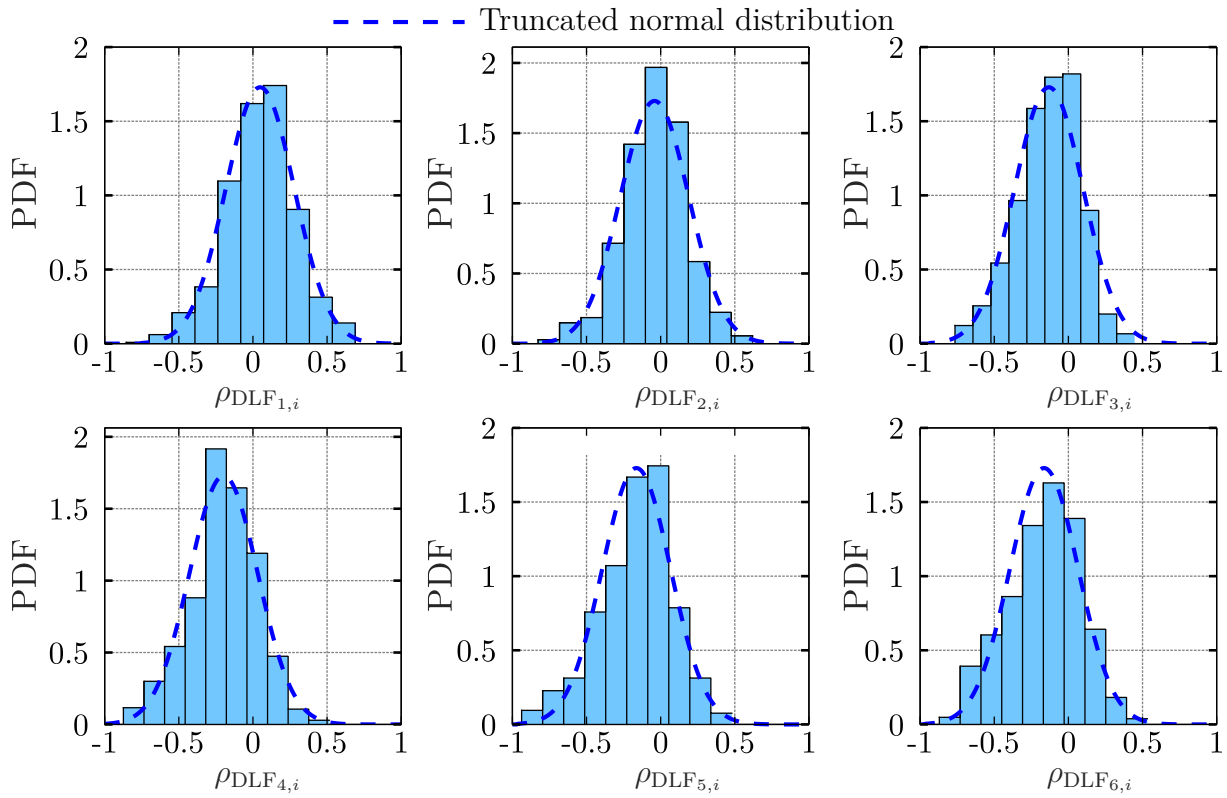

Figure 7.20: Histograms of AR coefficient for DLFs $\rho_{\mathrm{DLF}_{h,i}}$ with distribution utilised to approximate ρ_{DLF_h}.

Algorithm 4 Algorithm to generate a single probabilistic harmonic load

Choose N_{step}
Sample $\mathbf{X}_{\mathcal{F}} \sim \mathbf{G}_{\mathcal{F}}, \mathbf{C}_{\mathcal{F}}$
Sample ρ_{f_p} and Z
for $h = 1$ to 6 **do**
    $\rho_{\mathrm{DLF}_h} = \mu_{\rho_{\mathrm{DLF}_h}} + \sigma_{\rho_{\mathrm{DLF}}} \cdot Z$
end for
Set $f_{p,1} = \mu_{f_p}$
for $h = 1$ to 6 **do**
    Set $\mathrm{DLF}_{h,1}$=μ_{DLF_h}
end for
for step $= 1$ to $N_{\text{step}} - 1$ **do**
    $f_{p,\text{step}+1} = \mu_{f_p} + \rho_{f_p} \cdot \left(f_{p,\text{step}} - \mu_{f_p}\right) + \sigma_{f_p} \cdot \varepsilon_t$
    for $h = 1$ to 6 **do**
        $\mathrm{DLF}_{h,\text{step}+1} = \mu_{\mathrm{DLF}_h} + \rho_{\mathrm{DLF}_h} \cdot \left(\mathrm{DLF}_{h,\text{step}} - \mu_{\mathrm{DLF}_h}\right) + \sigma_{\mathrm{DLF}_h} \cdot \varepsilon_t$
    end for
    $F_{p,\text{step}}(t) = \mathrm{G}\left(1 + \sum_{h=1}^{6} \mathrm{DLF}_{h,\text{step}} \sin\left(2\pi h f_{p,\text{step}} t\right)\right)$
end for
Concatenate $F_{p,\text{step}}(t)$

Figure 7.21 illustrates the Fourier amplitude spectra of 200 generated force-samples with the mean walking frequency $\mu_{f_p} = 2.04$Hz, together with the Fourier spectrum of the experimentally measured force signal with the same mean f_p.

The probabilistic harmonic load model is applied to the numerical model of the low-frequency CLT floor defined in Section 5.4.1, with a full uncertainty analysis of calculated vibration response presented in Chapter 9.

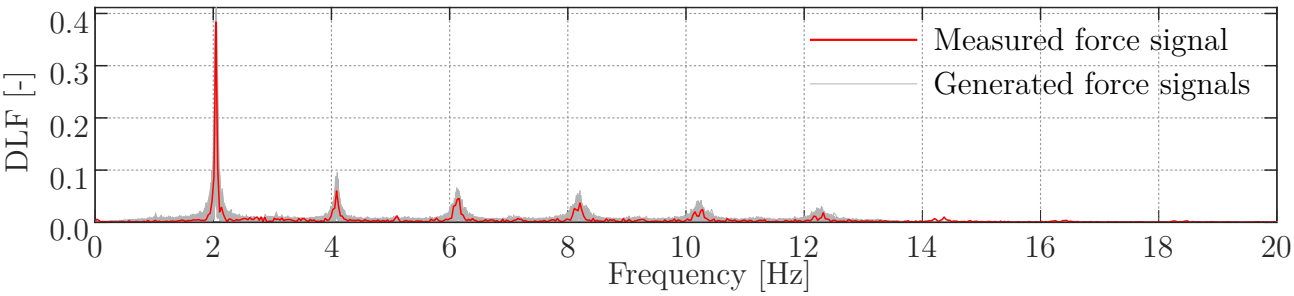

Figure 7.21: Fourier amplitude spectrum of the measured force (walking session $i = 446$, $f_p = 2.04$Hz) with spectra of 200 generated walking-forces with the same mean f_p.

7.2.6 Simplified harmonic load model for deterministic calculations

The simplified harmonic load model proposed here is intended to provide a practical and user-friendly tool for routine deterministic design calculations, in contrast to the fully probabilistic formulation, which explicitly accounts for both inter- and intra-subject variability and is therefore less practical for everyday use. The simplified model represents walking excitation as a perfectly periodic sinusoidal force presented by Eq. (2.1), comprising six harmonics, with constant walking frequency and constant DLFs throughout a single walking event. In other words, step-to-step variability is not modelled.

As in the CCIP-016 approach, the DLFs are expressed as functions of the walking frequency. However, in the present model, the DLFs additionally depend on a selected CDF level, which allows the designer to specify the desired probability of exceedance. For instance, a value corresponding to CDF = 0.4 has a 60% probability of exceedance. The dependence of mean DLF values on walking frequency is illustrated in Figure 7.5, wheres the CDFs for each DLF_h are plotted in Figure 7.22. The relationship between each DLF_h and f_p was approximated as linear, while the dependence on the CDF level was represented using a third-degree polynomial:

$$\mathrm{DLF}_h = p_{00} + p_{10} f_p + p_{01}\mathrm{CDF} + p_{11} f_p \mathrm{CDF} + p_{02}\mathrm{CDF}^2 + p_{12} f_p \mathrm{CDF}^2 + p_{03}\mathrm{CDF}^3 \qquad (7.9)$$

where $p_{00} - p_{03}$ are regression (hereafter referred to as p) coefficients. These p coefficients were obtained by fitting Eq. (7.9) to the mean DLF values extracted from the measured walking records (Section 7.2.2), together with associated mean walking frequencies and the corresponding empirical CDF values. To avoid unstable estimates associated with the distribution tails, the CDF level bellow 0.1 and higher than 0.9 were not considered. (Figure 7.22). Consequently, the proposed model accounts for probability of DLF exceedance between 10 and 90%. The resulting dataset was randomly split into two subsets. The 80% of the data was used for estimating the p coefficients by the least-squares method, which are listed in Table 7.3. The remaining 20% was reserved for validation by comparing the DLF values predicted by using Eq. (7.9) against those computed directly from the measured signals (Section 7.2.2).

Relative error between predicted $\mathrm{DLF}_{h,p}$ and corresponding measured $\mathrm{DLF}_{h,m}$ is calculated as:

$$\varepsilon = \frac{\mathrm{DLF}_{h,p} - \mathrm{DLF}_{h,m}}{\mathrm{DLF}_{h,m}} \cdot 100 \quad [\%] \qquad (7.10)$$

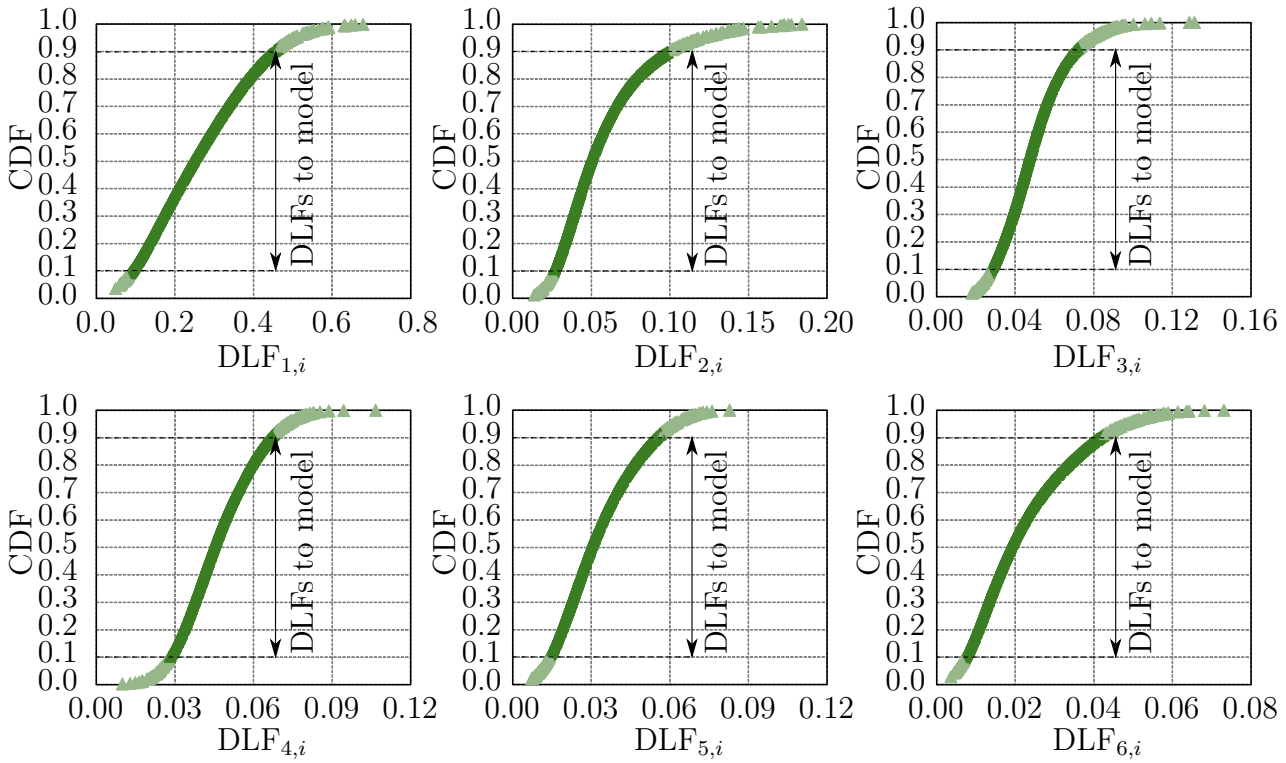

Figure 7.22: Mean DLFs and corresponding CDFs, with the selected subset for simplified force modelling.

Table 7.3: Values of p-coefficients for calculating DLFs of simplified harmonic force model.

Harm.	$\boldsymbol{p_{00}}$ $[10^{-3}]$	$\boldsymbol{p_{10}}$ $[10^{-3}]$	$\boldsymbol{p_{01}}$ $[10^{-3}]$	$\boldsymbol{p_{11}}$ $[10^{-3}]$	$\boldsymbol{p_{02}}$ $[10^{-3}]$	$\boldsymbol{p_{12}}$ $[10^{-3}]$	$\boldsymbol{p_{03}}$ $[10^{-3}]$
DLF_1	−313.40	239.49	−138.93	246.19	−354.34	29.975	210.78
DLF_2	−20.481	14.985	45.045	50.629	−237.68	28.959	154.372
DLF_3	35.671	−12.699	115.18	1.5891	−187.00	18.239	112.39
DLF_4	0.8361	8.8490	28.775	32.400	−97.748	−4.3282	73.625
DLF_5	−16.734	12.916	−18.003	48.612	−45.884	−20.032	59.551
DLF_6	−11.454	7.9466	−41.588	47.577	−21.727	−15.259	40.787

and is plotted in Figure 7.23 for all six DLFs. The smallest relative errors in DLF prediction are obtained for DLF_4-DLF_6, with relative errors confined to ±4%. The corresponding RMSRE values are 1.337%, 1.491% and 1.612%2 Slightly larger discrepancies are observed for DLF_3, with relative errors in the range from −5 to 3% and an RMSRE of 3.361%. In contrast, the largest deviations occur for DLF_1 and DLF_2, where the relative errors reach approximately 9%, yielding RMSRE values of 5.642% and 4.569%, respectively. Furthermore, Figure 7.23 indicates that, for these two harmonics, the simplified model tends to overestimate the corresponding measured DLF values. The only exception is DLF_2 for CDF>0.7. Since the model is intended for design applications, this systematic overestimation is conservative and therefore on the safe side. In contrast, DLF_3-DLF_6 are often slightly lower than the corresponding measured values. Nevertheless, the associated relative errors remain within approximately 2% in magnitude for most of the cases, and this underestimation is therefore considered acceptable.

The proposed simplified harmonic load model is applied to the numerical model of the low-frequency CLT floor defined in Section 5.4.1. The resulting response is compared with that obtained using the CCIP-016 load model in Chapter 8. Additionally, in Chapter 8, responses

predicted using the simplified model are compared with those obtained from the probabilistic force model to assess whether the additional complexity of a probabilistic analysis is justified for routine design calculations.

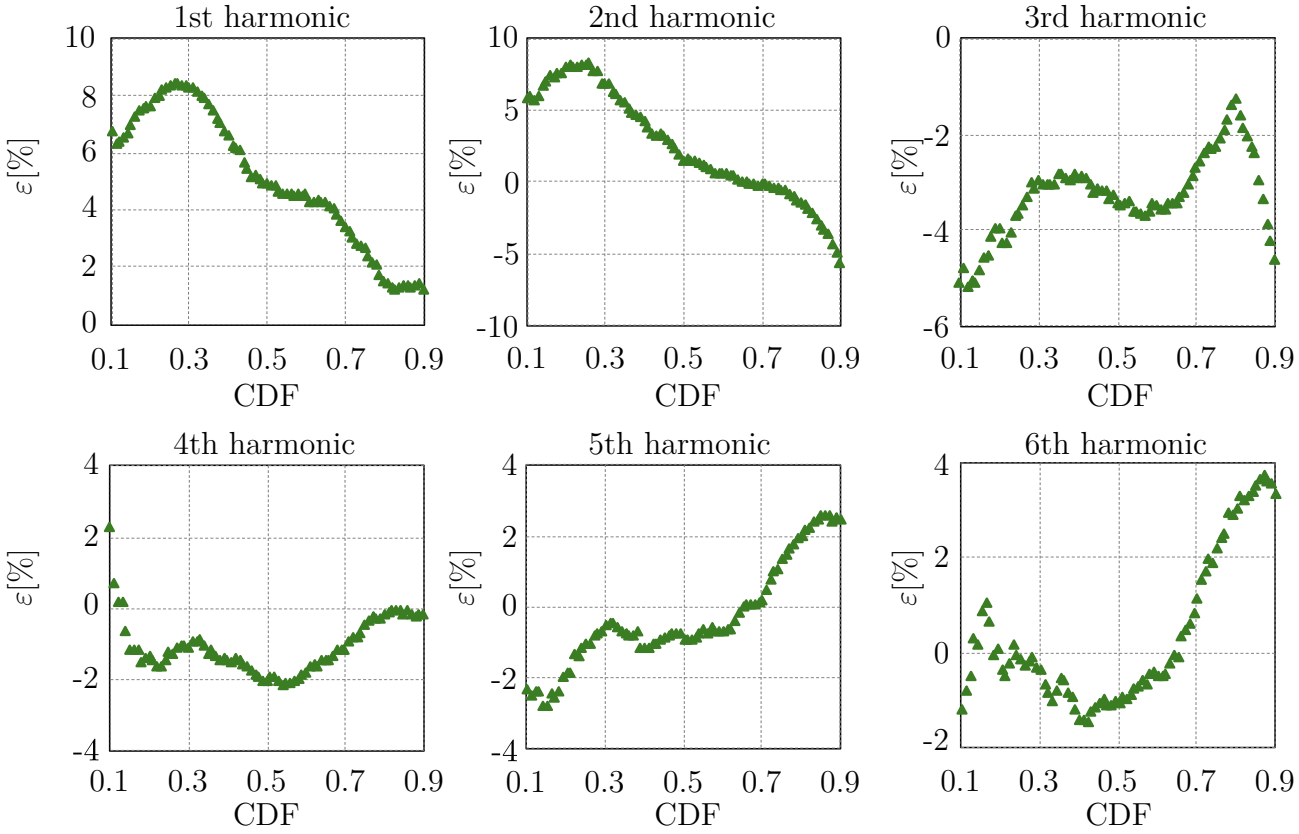

Figure 7.23: Relative errors between DLFs predicted by simplified force model and corresponding measured DLFs.

7.3 Impulse load model

As discussed previously, the transient response of HFF due to walking consists of a sequence of velocity peaks associated with individual heel strikes, each followed by a decaying free-vibration response before the next footfall occurs (Figure 2.2). From a theoretical point of view, such a response can be idealised as a succession of peak responses generated by individual footfalls, together with the corresponding exponentially decaying vibration between them (Figure 7.24).

This concept forms the basis of the effective impulse approach adopted in CCIP-016. Instead of using the complete force-time history of a footfall, the dynamic effect of each footfall is represented by a single equivalent impulse. To obtain this impulse, each measured footfall force from the database reported by Kerr [49] was applied to a set of SDOF oscillators with natural frequencies in the range $10 - 40$Hz. For each oscillator, only the maximum velocity response was extracted. The modal mass of the SDOF oscillator was taken as 1kg. Therefore, the extracted peak velocity is numerically equal to the impulse that would produce the same velocity response of the oscillator. This equivalent value is referred to as the effective impulse, I_{eff}. Based on the database of extracted effective impulse values, obtained for different SDOF

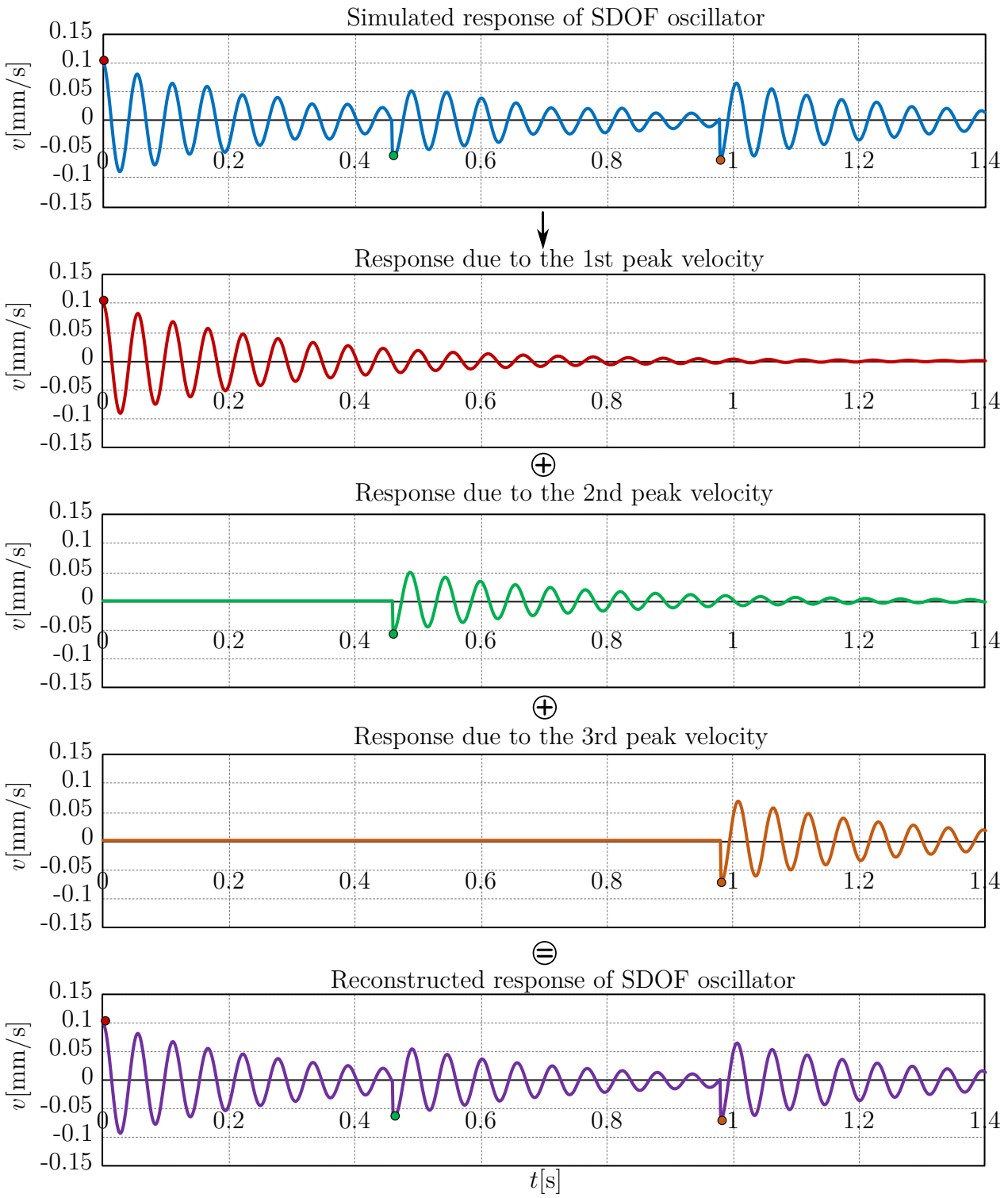

Figure 7.24: Reconstruction of a typical transient vibration response using effective impulses.

natural frequencies and walking frequencies, the following empirical expression was proposed:

$$I_{\text{eff}} = A \cdot \frac{f_p^a}{f_n^b} \tag{7.11}$$

where I_{eff} is the effective impulse, f_p is the pedestrian walking frequency, f_n is the natural frequency of the floor, and A, a, and b are empirical coefficients obtained by fitting the expression to the extracted peak velocity, i.e. effective impulse. This design model is mainly intended for practical deterministic calculations. The design coefficient $A = 54$ corresponds to effective

impulse values with a 25% probability of exceedance, meaning that inter-subject variability is considered to some extent. However, the model does not explicitly describe the step-to-step variability that occurs during a continuous walk.

An improved stochastic impulse model was proposed by Mohammed et al. [34], in which this variability was considered in more detail. Instead of using isolated footfall records, they used continuously measured treadmill force records containing 50 successive footfalls to extract the peak velocity responses of SDOF oscillators. Furthermore, the considered range of oscillator natural frequencies was $14 - 40$Hz, consistent with the 14Hz cut-off frequency between LFFs and HFFs. However, the resulting formulation is relatively complex for direct implementation in routine engineering practice.

For this reason, an impulse load model is developed in this dissertation with the aim of retaining the practical advantages of the effective impulse approach, while enabling a probabilistic description of continuous walking. In contrast to the original CCIP-016 formulation, the proposed model is derived from a database of continuously measured walking force records rather than from isolated footfall signals. The intra-subject variability of the impulse load parameters is represented by a first-order autoregressive AR(1) model, so that the correlation between successive steps can be included. Although this makes the proposed formulation somewhat more complex than the original CCIP-016, model it remains considerably less complex than the one developed by Mohammed et al. [34].

The remainder of this section is organised as follows. First, the formulation of the impulse load model is introduced (Subsection 7.3.1), where each step is represented by a single effective impulse. The procedure used for extracting the model parameters from the measured walking force records is then described in Subsection 7.3.2, and their values are subsequently verified through response calculations of SDOF systems (Subsection 7.3.3). Finally, the probabilistic description of the model parameters and their dependence structure is presented in Subsection 7.3.4, followed by the implementation procedure for generating probabilistic impulse loads (Subsection 7.3.5). A simplified deterministic version of the impulse model is presented in Subsection 7.3.6, while the influence of floor damping is analysed in Subsection 7.3.7.

7.3.1 Model formulation

Consistent with the effective impulse approach, each step is replaced by a single effective impulse. The impulse is applied at the time and position of the corresponding footfall and is assumed to produce the same relevant dynamic effect on the floor as the measured force generated during that step. As already mentioned, the intra-subject variability of the effective impulse, i.e. its variation from one step to the next, is modelled using the AR(1) formulation:

$$I_{\text{eff, step+1}} = \mu_{I_{\text{eff}}} + \rho_{I_{\text{eff}}} \cdot \left(I_{\text{eff, step}} - \mu_{I_{\text{eff}}}\right) + \sigma_{I_{\text{eff}}} \cdot \sqrt{(1 - \rho_{I_{\text{eff}}}^2)} \cdot \varepsilon_t \tag{7.12}$$

where $\mu_{I_{\text{eff}}}$ and $\sigma_{I_{\text{eff}}}$ are the mean value and standard deviation of the effective impulse within the single walk session, parameter $\rho_{I_{\text{eff}}}$ is the AR coefficient controlling the strength of temporal correlation between successive steps and ε_t is a standard normal random variable.

The step-by-step variability of the walking frequency f_p is described using the same AR(1) representation as that adopted for the harmonic load model:

$$f_{p,\text{step+1}} = \mu_{f_p} + \rho_{f_p} \cdot \left(f_{p,\text{step}} - \mu_{f_p}\right) + \sigma_{f_p} \cdot \sqrt{(1 - \rho_{f_p}^2)} \cdot \varepsilon_t \tag{7.13}$$

However, the definition of f_p is not identical in the two models. In the harmonic load model, f_p was determined as the frequency of the first harmonic of the measured walking force signal (Figure 7.1). In the impulse model, f_p is evaluated from the actual time interval between successive footfalls as illustrated in Figure 7.25. Therefore, the parameters μ_{f_p}, σ_{f_p}, and ρ_{f_p} are not taken from Section 7.2.2, but are re-evaluated in the following section.

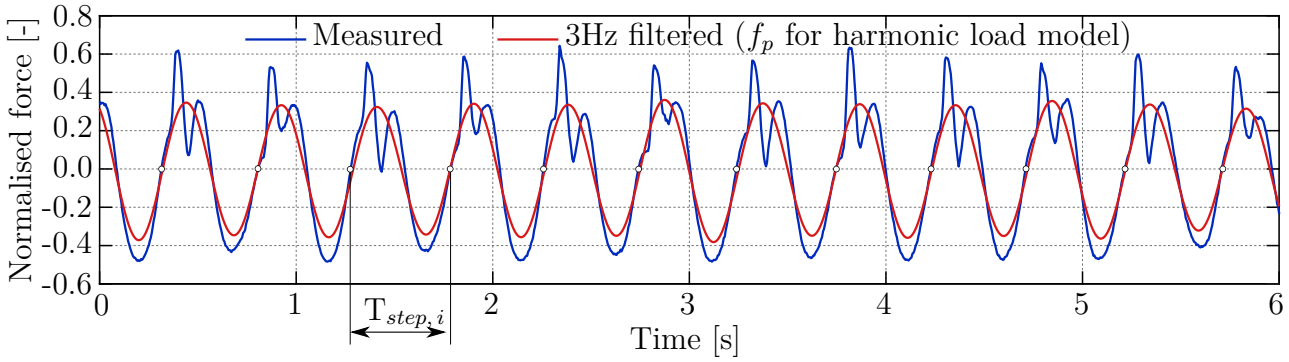

Figure 7.25: A portion of 35s-long measured normalised force [40], corresponding 3Hz filtered signal and defined period of a single step for f_p calculation.

7.3.2 Extraction of model parameters

Similarly as in Subsection 7.2.2, each of the 744 measured force signals was normalised by dividing it by the pedestrians self-weight and the unity mean value was removed. The walking frequency and the effective impulses were then evaluated on a step-by-step basis. Based on these stepwise values of f_p and I_{eff}, the AR coefficients ρ_{f_p} and $\rho_{I_{\text{eff}}}$ were computed for each walking session.

7.3.2.1 Walking frequency

Each of the 744 normalised walking force records was segmented into individual steps. To avoid possible irregularities associated with the beginning and end of the walking test, the first and last three steps were removed from each record. The walking frequency was then defined as the reciprocal of the single-step period $\text{T}_{\text{step},i}$, determined from the segment between every other zero crossing of the measured force signal, as illustrated in Figure 7.25.

After the walking frequencies was identified for each individual step, the corresponding mean value $\mu_{f_{p,i}}$, standard deviation $\sigma_{f_{p,i}}$ and $\text{COV}_{f_{p,i}}$ were calculated for each walking session i. Figure 7.26 shows the step-by-step variation of the walking frequency during one 64-step walk (walking session $i = 446$). For this record, the mean value is 2.04Hz, while the standard deviation and COV are 0.06Hz and 2.91%, respectively. Note that the same mean value was obtained when the walking frequency was determined from the first harmonic of the complete force signal (Figure 7.2). However, the standard deviation of the first-harmonic frequency is only 0.025Hz. Consequently, both standard deviation and the resulting COV are 2.4 times lower than those obtained from the step-by-step definition of f_p used in the impulse load.

Furthermore, the $\text{COV}_{f_{p,i}}$ obtained from all 744 processed signals are plotted against the corresponding mean walking frequencies $\mu_{f_{p,i}}$ in Figure 7.27. Compared with the values obtained

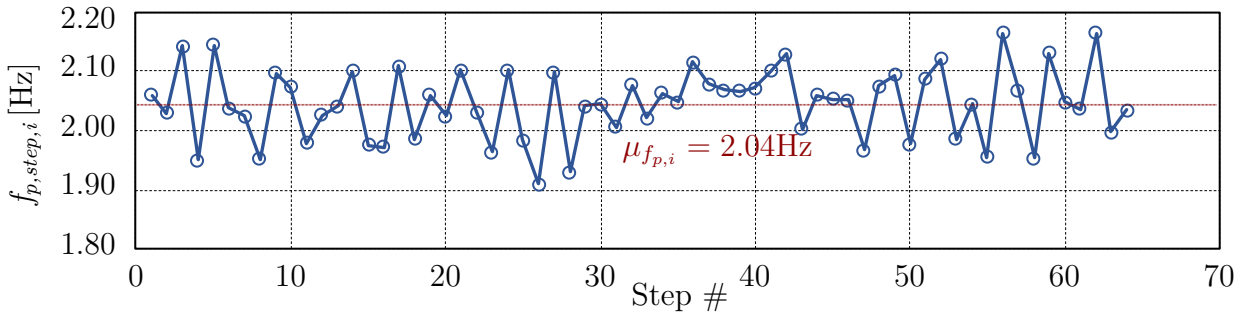

Figure 7.26: Variability of walking frequency during a single walk.

from the first-harmonic-based definition of f_p, the step-based COVs are generally higher, ranging approximately from 1 to 13.5%. The scatter is relatively large over the entire frequency range, and no clear functional relationship between COV and $\mu_{f_{p,i}}$ can be identified.

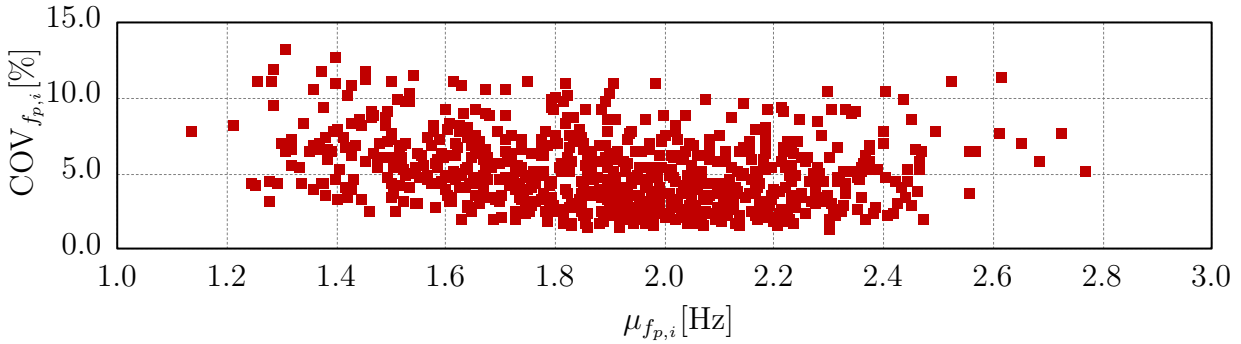

Figure 7.27: COVs with corresponding mean walking frequencies.

Finally, the mean values and corresponding COV of the step-based walking frequency, f_p, and the first-harmonic-based walking frequency, $f_{h=1}$, are compared in Figure 7.28. The mean values obtained from the two definitions are practically identical. However, as previously observed, the step-based definition leads to noticeably higher COV, with values twice as large on average. This difference can be attributed to the influence of higher harmonic components of the walking force. Since higher harmonic components are inherently more variable, their influence results in larger estimated COVs for the step-based walking frequency.

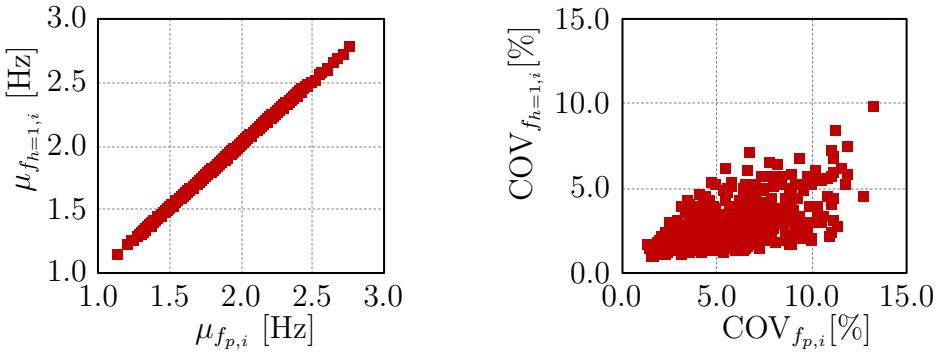

Figure 7.28: Comparison of step-based and first-harmonic-based definition of walking frequency.

7.3.2.2 Effective impulse

Following the procedure described by Mohammed et al. [34], which is based on the CCIP-016 effective impulse formulation, the calculation of I_{eff} was performed as follows:

- The natural frequencies of the SDOF oscillators were varied from 14Hz to 40Hz, with an increment of 0.1Hz, resulting in 261 different oscillators.
- The SDOF damping ratio was assumed to be 3%. The influence of the damping ratio on the effective impulse values will be discussed in Section 7.3.7.
- Each of the 744 normalised walking records was applied to all 261 SDOF oscillators, and the corresponding velocity response time histories were calculated.
- For each walking record and each oscillator frequency, the velocity response was processed step by step to identify the peak velocity, i.e. effective impulse associated with each footfall.

Since the walking force was normalised by the pedestrian body weight, the obtained peak velocity represents the effective impulse per unit body weight, which is expressed in [Ns/N]. The corresponding physical impulse is obtained by multiplying the normalised effective impulse by the pedestrian body weight.

An example of the step-by-step variation of the effective impulse during walking record $i = 446$ is shown in Figure 7.29 for four selected SDOF oscillator frequencies, $f_n = 14$, 20, 30, and 40Hz. With COVs in range $15 - 21\%$, variation in step-to-step effective impulses is notably higher than corresponding variation in walking frequency. Figure 7.30 further presents the mean values $\mu_{I_{\text{eff,i}}}$ and COVs of the effective impulse $\text{COV}_{I_{\text{eff,i}}}$ for the same walking record, evaluated over all 261 considered SDOF oscillator frequencies.

The mean effective impulse generally decreases with increasing SDOF natural frequency f_n. Distinct local maxima are also observed at frequencies close to integer multiples of the walking frequency ($f_p = 2.04$Hz) which is consistent with the observations reported by Mohammed et al. [34]. In contrast, the COV exhibits an oscillatory pattern, with local minima occurring approximately at the same integer multiples of f_p. Therefore, the effective impulse tends to be less variable at oscillator frequencies corresponding to harmonics of the walking frequency. The mean effective impulses and corresponding COV obtained for the 744 walking records were averaged for each SDOF natural frequency f_n and are presented in Figure 7.31. The averaged mean effective impulse decreases continuously as f_n increases, from approximately 0.004Ns/N at 14Hz to about 0.0006Ns/N at 40Hz. In contrast, the averaged COV follows a non-monotonic trend. It is lowest, at approximately 25%, for $f_n = 14$Hz, then gradually increases to a maximum of about 35% at $f_n \approx 27$Hz. Beyond this frequency, it decreases steadily, reaching approximately 30% at 40Hz.

7.3.2.3 Autoregressive coefficients

As in Subsection 7.2.2, the AR coefficients ρ_{f_p} and $\rho_{I_{\text{eff}}}$ were estimated from the corresponding step-by-step sequences of f_p and I_{eff}, respectively, using a least square approach. Figure 7.32 presents the obtained values of ρ_{f_p} as a function of the corresponding mean walking frequency. Similar to the results obtained for the first-harmonic-based definition of f_p considerable scatter is observed. However, in the present case, nearly all values of ρ_{f_p} are negative, indicating that successive deviations from the mean walking frequency tend to alternate in sign. In other

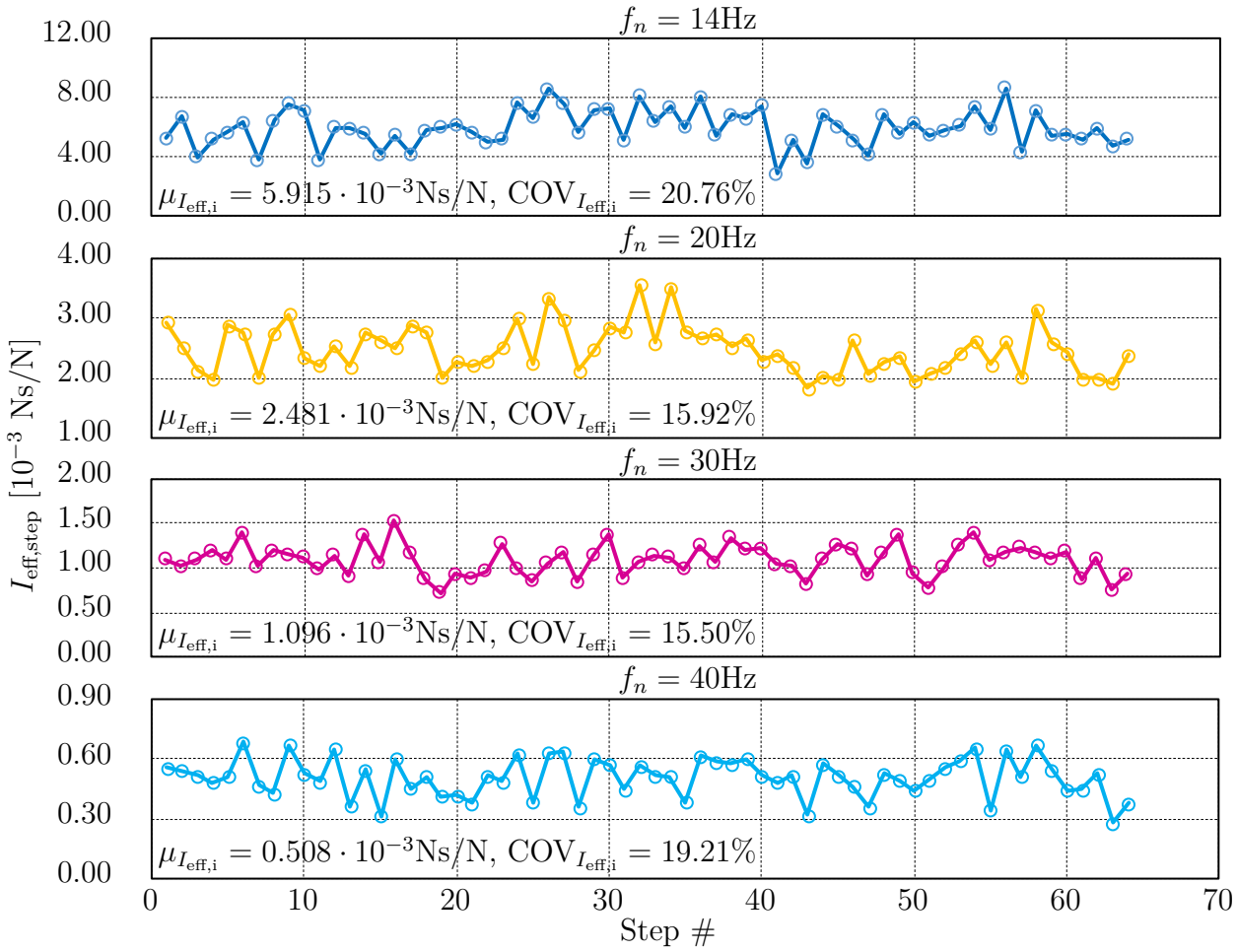

Figure 7.29: Variability of I_{eff} during the walking session $i = 446$ for SDOF oscillators with different frequencies.

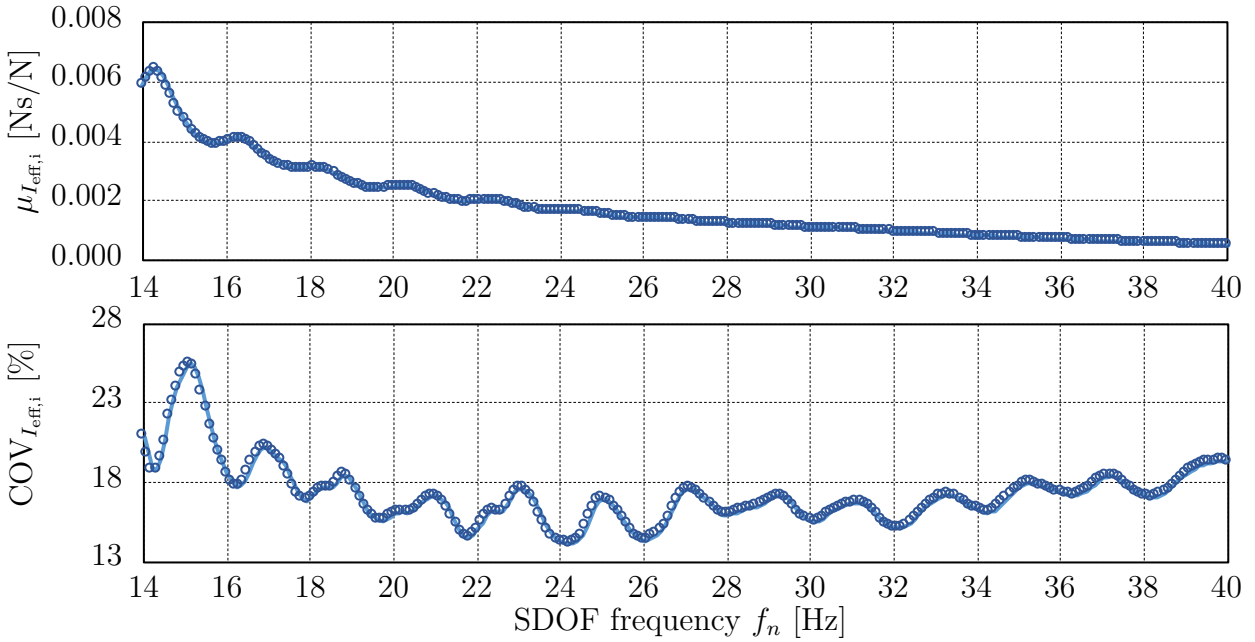

Figure 7.30: Mean value and COV of I_{eff} during walking session $i = 446$ for SDOF oscillators with different frequencies.

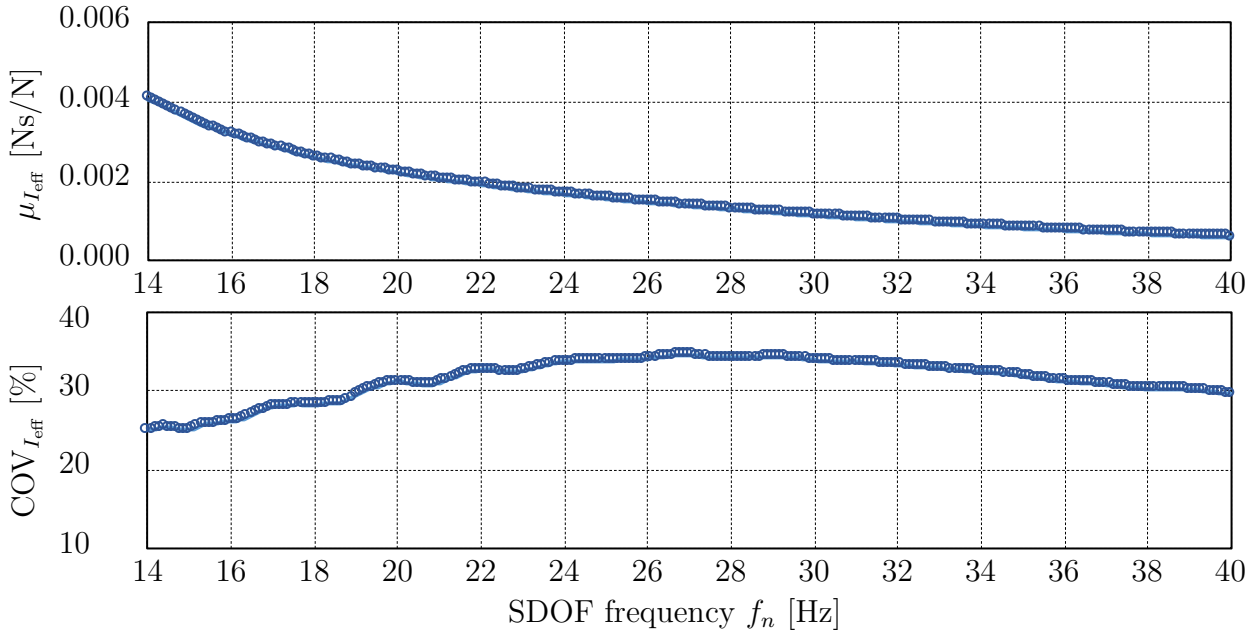

Figure 7.31: Averaged $\mu_{I_{\text{eff,i}}}$ and $\text{COV}_{I_{\text{eff,i}}}$ over 744 walking sessions for SDOF oscillators with different frequencies.

words, a step with a higher-than-average frequency is more likely to be followed by a step with a lower-than-average frequency, and vice versa.

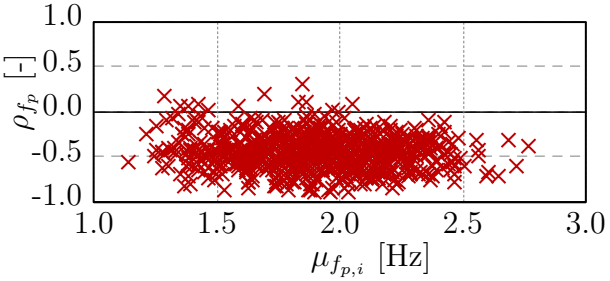

Figure 7.32: The AR coefficients ρ_{f_p} with corresponding mean walking frequencies.

The AR coefficients $\rho_{I_{\text{eff}}}$ were evaluated for each of the 744 walking records and all 261 SDOF oscillator natural frequencies. The values obtained for four selected frequencies ($f_n = 14, 20, 30$ and 40Hz) are plotted against the corresponding mean walking frequencies in Figure 7.33. A similar pattern is observed for all four oscillator frequencies. The results exhibit considerable scatter and are distributed approximately symmetrically around zero, with most values lying between -0.5 and 0.5.

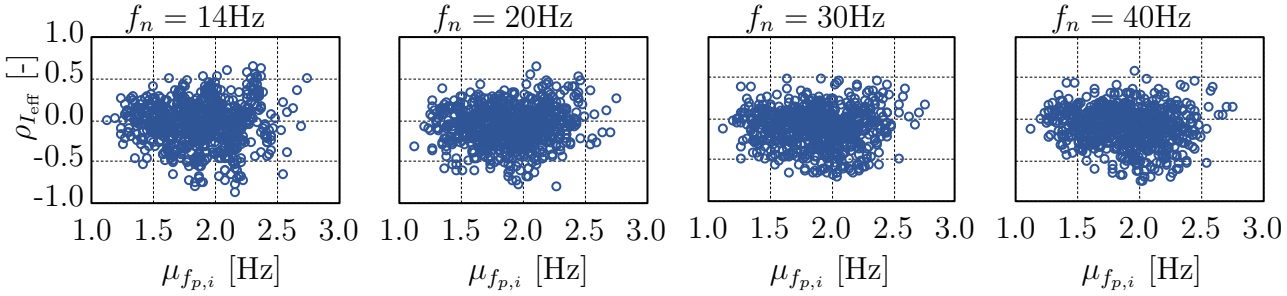

Figure 7.33: The AR coefficients $\rho_{I_{\text{eff}}}$ for SDOF oscillators with different natural frequencies, with corresponding mean walking frequencies.

For each SDOF natural frequency, the mean and standard deviation of $\rho_{I_{\text{eff}}}$ across all walking records were subsequently calculated and are presented in Figure 7.34. Both quantities vary only within relatively narrow ranges over the considered frequency interval. The mean values range from -0.146 to -0.051, while the corresponding standard deviations lie between 0.216 and 0.267. These relatively small variations suggest that, on average, temporal dependence between successive effective impulses is not strongly affected by the natural frequency of the SDOF oscillator.

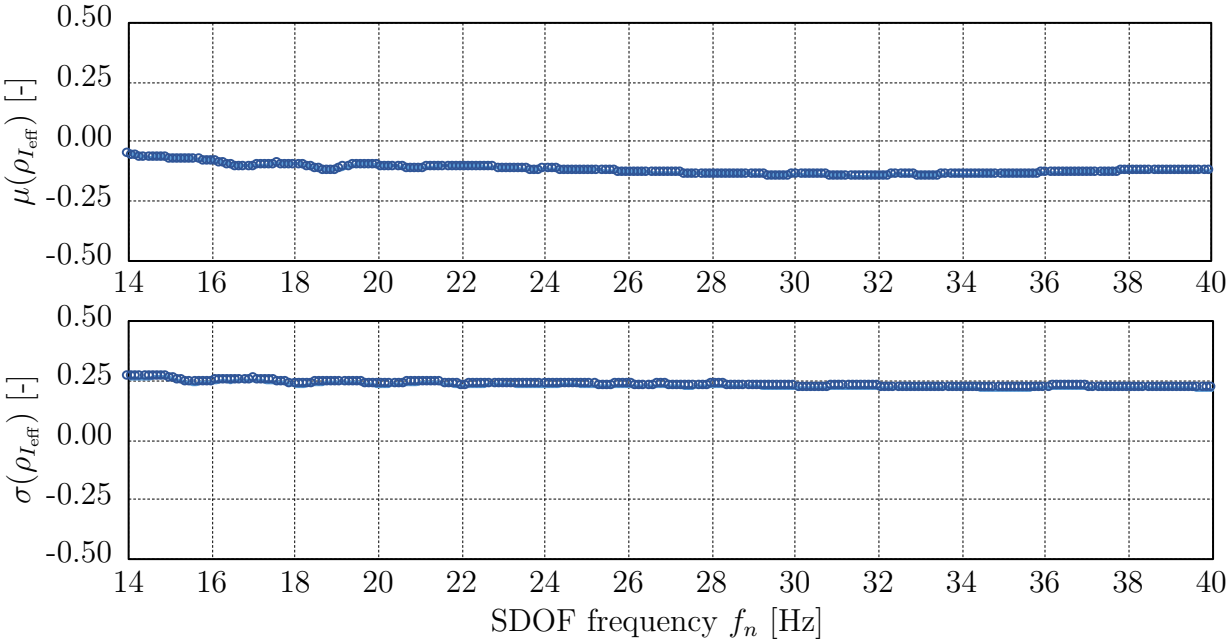

Figure 7.34: Mean value and standard deviation of the AR coefficients $\rho_{I_{\text{eff}}}$ for all walking sessions with corresponding SDOF oscillator natural frequencies.

7.3.3 Verification through SDOF response calculation

Applying the 744 normalised walking force records to 261 SDOF oscillators resulted in 194,184 step-by-step effective impulse sequences. Since each walking record contained on average 68 steps, the complete dataset comprised more than 13.2 million individual effective impulse values.

To verify the identified parameters, the velocity response of SDOF oscillators with a mass of $m =$ 1kg, a damping ratio of $\zeta = 3\%$ and natural frequencies ranging from 14 to 40Hz was calculated under both the measured normalised force records and the corresponding reconstructed impulse loads (194,184 simulations in total). A representative example for a 64-step walking record, corresponding to walking session $i = 446$, is shown in Figure 7.35, while Figure 7.36 presents a detailed view of the same response. Visual comparison indicates very good agreement between the velocity responses obtained from the measured and reconstructed loads.

Furthermore, for each of the 194,184 simulations, the peak velocity v_{peak} and the maximum value of the 1-s moving RMS velocity $v_{rms,max}$ were evaluated for both the measured force record (m) and the corresponding reconstructed impulse load (r). The results are compared in Figure 7.37. As the effective impulses were identified directly from the peak velocity response, the measured and reconstructed values of v_{peak} coincide exactly, resulting in a RMRSE of 0.00%. The agreement is also very good for $v_{rms,max}$, particularly at lower response levels. At higher values, the reconstructed impulse load shows a slight tendency to underestimate

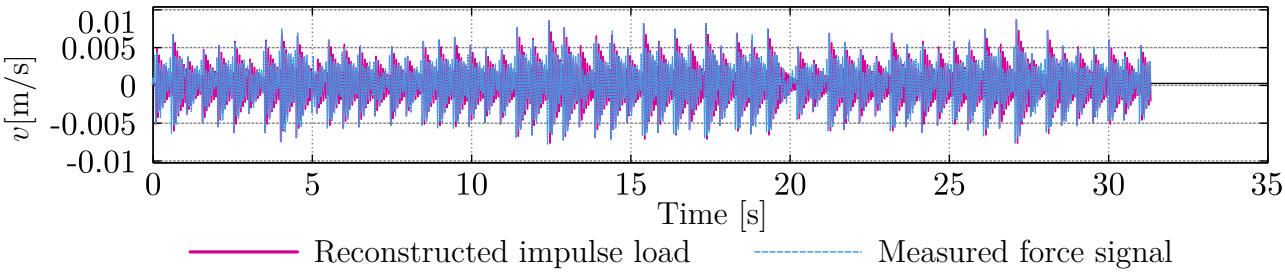

Figure 7.35: Velocity response of SDOF oscillator with frequency $f_n = 14$Hz induced by measured force signal and corresponding reconstructed impulse load.

the response, as indicated by the increasing deviation below the equality line. Nevertheless, the overall RMSRE of 11.18% demonstrates acceptable agreement between the measured and reconstructed responses.

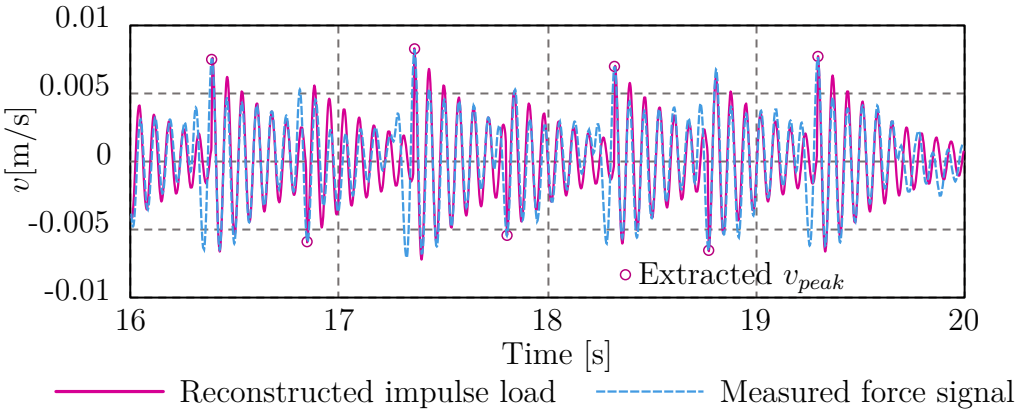

Figure 7.36: Velocity response of SDOF oscillator with frequency $f_n = 14$Hz induced by measured force signal and corresponding reconstructed impulse load - a detailed view.

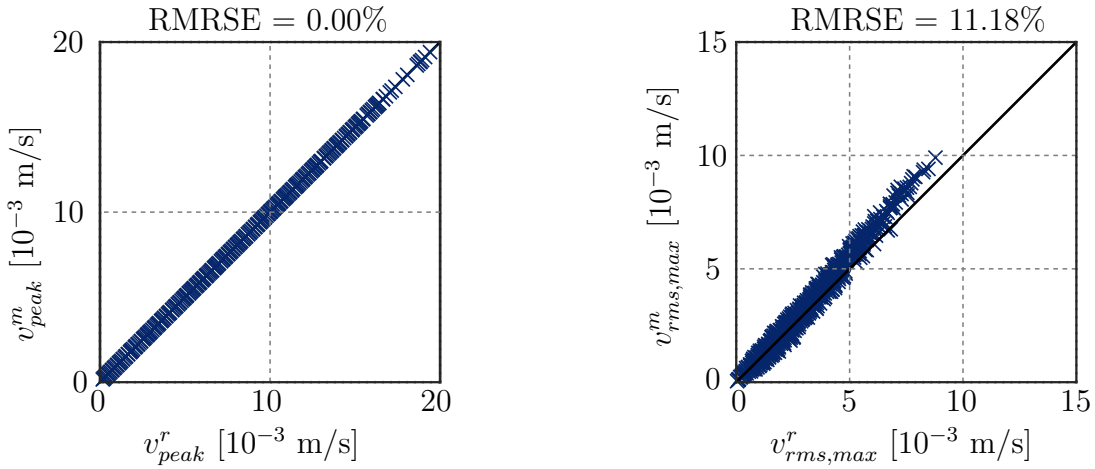

Figure 7.37: Peak velocity and maximum rms value for moving average (T=1s) of all 261 SDOF oscillators induced by all 744 measured (v^m_{peak}, $v^m_{rms,max}$) and reconstructed (v^r_{peak}, $v^r_{rms,max}$) force signals.

7.3.4 Probabilistic description of model parameters

The impulse load model introduced in Subsection 7.3.1 and defined by Eq. (7.12) is governed by seven parameters. Five of these are the load parameters: pedestrian weight, the mean and stan-

dard deviation of the walking frequency, and the mean and standard deviation of the effective impulse. The remaining two parameters are the AR coefficients associated with the walking frequency and the effective impulse. As in the harmonic load model, the load parameters account for both intra- and inter-subject variability and therefore represent the primary sources of uncertainty. On the other hand, the AR coefficients describe only the temporal dependence between successive steps and are consequently treated as secondary random variables.

The impulse load parameters were modelled as random variables by fitting appropriate probability distributions to the statistics extracted previously, as described in Subsection 7.3.4.1. As in the harmonic load model, the dependence between the load parameters was represented in two ways (Subsection 7.3.4.2). Statistical dependence between the force parameters was described using linear correlation coefficients estimated from the database, whereas the temporal dependence between successive steps within a walking record was represented through the AR coefficients ρ_{f_p} and $\rho_{I_{\text{eff}}}$.

7.3.4.1 Random-variable modelling of impulse load parameters

The overall variability of the walking frequency was described, as in the harmonic load model, using its mean value μ_{f_p} and standard deviation σ_{f_p}. The former represents the variation in pacing rate between different walking records, whereas the latter quantifies the step-to-step variability within an individual record. The corresponding histograms and fitted probability distributions are presented in Figure 7.38. Since the mean walking frequency obtained from the step-based definition is identical to that determined from the first harmonic of the force signal, the resulting distributions of μ_{f_p} also coincide. Accordingly, μ_{f_p} is best represented by a normal distribution with a mean value of 1.9Hz and a standard deviation of 0.266Hz. In contrast, the step-based definition of σ_{f_p} produces a more widely dispersed set of values. This parameter is now best described by a beta distribution with a mean value of 0.096Hz and a standard deviation of 0.042Hz. The mean is more than twice that obtained using the first-harmonic-based definition. In addition, the resulting COV of 44% is noticeably higher than the corresponding value of 35% obtained from the first-harmonic-based approach.

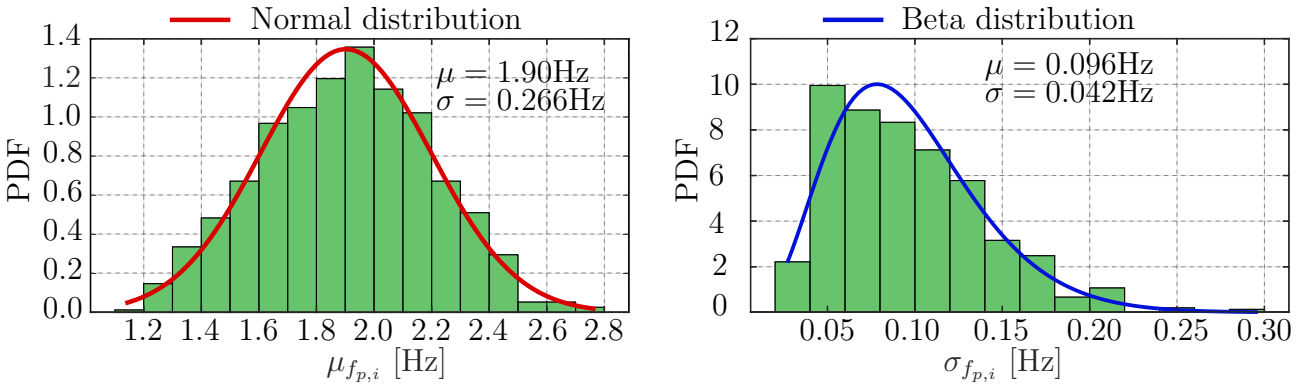

Figure 7.38: Histograms of step-based walking frequency mean value $\mu_{f_{p,i}}$ and standard deviation $\sigma_{f_{p,i}}$ with distributions utilised to approximate μ_{f_p} and σ_{f_p}.

The total variability of the effective impulse was likewise described using its mean value $\mu_{I_{\text{eff}}}$ and standard deviation $\sigma_{I_{\text{eff}}}$. For each SDOF oscillator natural frequency, the statistical properties of $\mu_{I_{\text{eff}}}$ were determined from the individual mean values $\mu_{I_{\text{eff},i}}$ obtained for all walking sessions. Analogously, the statistical properties of $\sigma_{I_{\text{eff}}}$ were derived from the corresponding individual standard deviations $\sigma_{I_{\text{eff},i}}$. The resulting histograms of $\mu_{I_{\text{eff},i}}$ and $\sigma_{I_{\text{eff},i}}$ for four selected SDOF

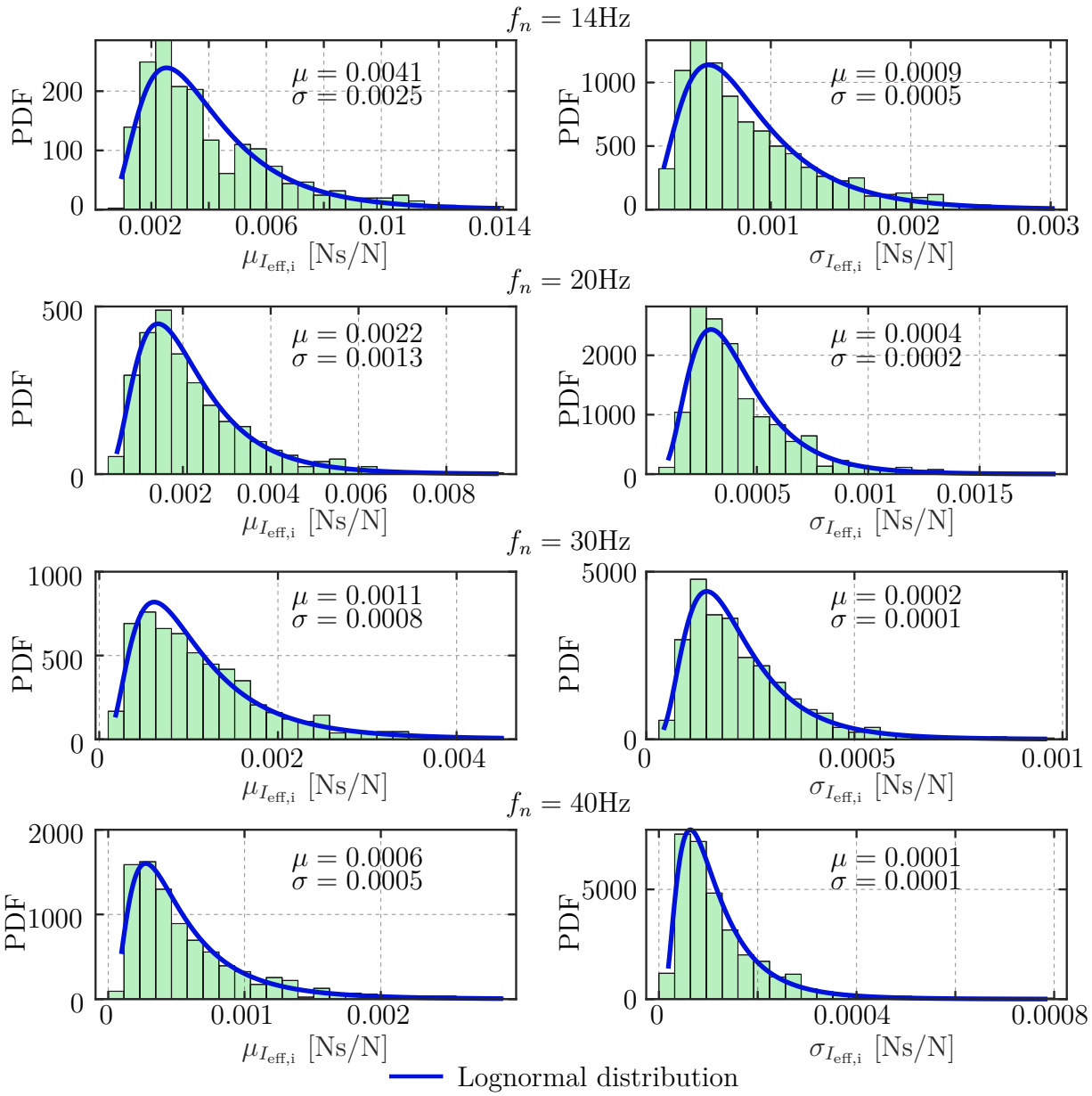

Figure 7.39: Histograms of mean value $\mu_{I_{\text{eff,i}}}$ and standard deviation $\sigma_{I_{\text{eff,i}}}$ of effective impulse with distributions utilised to approximate $\mu_{I_{\text{eff}}}$ and $\sigma_{I_{\text{eff}}}$, for four different SDOF oscillator frequencies.

oscillator frequencies (f_n = 14, 20, 30, and 40Hz) are presented in Figure 7.39. It is evident that the statistical properties of both $\mu_{I_{\text{eff}}}$ and $\sigma_{I_{\text{eff}}}$ vary with the oscillator natural frequency f_n. Accordingly, both parameters were modelled using lognormal distributions. The corresponding lognormal distribution parameters, $\mu_{\ln}$ and $\sigma_{\ln}$, were evaluated separately for each SDOF oscillator natural frequency and are plotted in Figure 7.40. To enable their continuous representation over the considered frequency range, best-fit expressions were subsequently derived. A linear function was adopted for $\mu_{\ln}$, whereas $\sigma_{\ln}$ was represented by a third-degree polynomial. The resulting expressions are summarised in Table 7.4.

Finally, the fitted probability distributions and corresponding parameters for all five impulse load parameters are summarised in Table 7.5. The pedestrian body weight is independent of the parameters of both the harmonic and impulse load models and is therefore represented by the same probability distribution in both formulations.

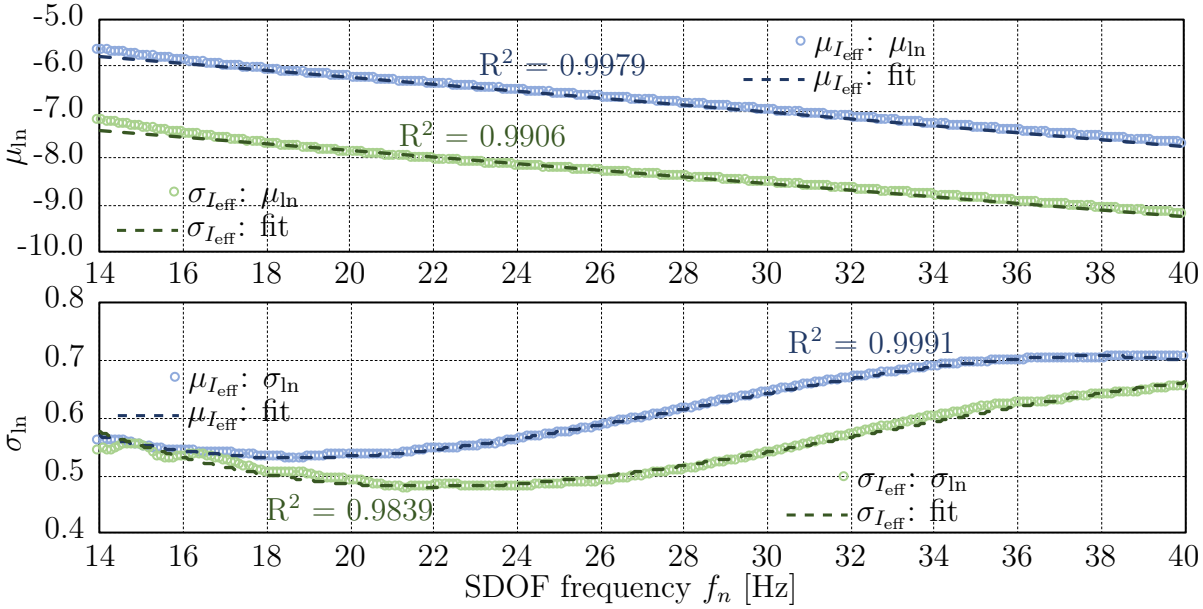

Figure 7.40: Lognormal distribution parameters $\mu_{\ln}$ and $\sigma_{\ln}$ for $\mu_{I_{\text{eff}}}$ and $\sigma_{I_{\text{eff}}}$ as functions of the SDOF oscillator frequency, with the corresponding fitted trend lines.

Table 7.4: Best-fit equations for the parameters of the lognormal distributions fitted to $\mu_{I_{\text{eff}}}$ and $\sigma_{I_{\text{eff}}}$.

Variable	**Parameter**	**Equation**
$\mu_{I_{\text{eff}}}$	$\mu_{\ln}$	$-0.0749 \cdot f_n - 4.7314$
	$\sigma_{\ln}$	$-5 \cdot 10^{-5} \cdot f_n^3 + 0.0042 \cdot f_n^2 - 0.1060 \cdot f_n + 1.3607$
$\sigma_{I_{\text{eff}}}$	$\mu_{\ln}$	$-0.0719 \cdot f_n - 6.3929$
	$\sigma_{\ln}$	$-4 \cdot 10^{-5} \cdot f_n^3 + 0.0036 \cdot f_n^2 - 0.1061 \cdot f_n + 1.4513$

Table 7.5: Fitted distributions of impulse load parameters.

		Distribution properties		
Force parameter	**Label**	**Type**	**Parameter 1**	**Parameter 2**
Body weight	G	Normal	757	151.55
Mean f_p	μ_{f_p}	Normal	1.900	0.266
St. deviation f_p	σ_{f_p}	Beta	4.567	42.993
Mean I_{eff}	$\mu_{I_{\text{eff}}}$	Lognormal	Table 7.4	Table 7.4
St. deviation I_{eff}	$\sigma_{I_{\text{eff}}}$	Lognormal	Table 7.4	Table 7.4

7.3.4.2 Dependence modelling

The linear correlation coefficients r between μ_{f_p} and $\mu_{I_{\text{eff}}}$, μ_{f_p} and $\sigma_{I_{\text{eff}}}$, σ_{f_p} and $\mu_{I_{\text{eff}}}$, σ_{f_p} and $\sigma_{I_{\text{eff}}}$, as well as between $\mu_{I_{\text{eff}}}$ and $\sigma_{I_{\text{eff}}}$, were calculated separately for each SDOF oscillator natural frequency. The resulting coefficients plotted in Figure 7.41 indicate considerable linear dependence between several impulse load parameters. The strongest correlation is observed between $\mu_{I_{\text{eff}}}$ and $\sigma_{I_{\text{eff}}}$, with r ranging from 0.80 to 0.91. Relatively high correlations are also obtained between μ_{f_p} and $\mu_{I_{\text{eff}}}$, and between μ_{f_p} and $\sigma_{I_{\text{eff}}}$, with coefficients ranging from 0.76 to 0.80 and from 0.66 to 0.76, respectively. In contrast, σ_{f_p} exhibits substantially weaker

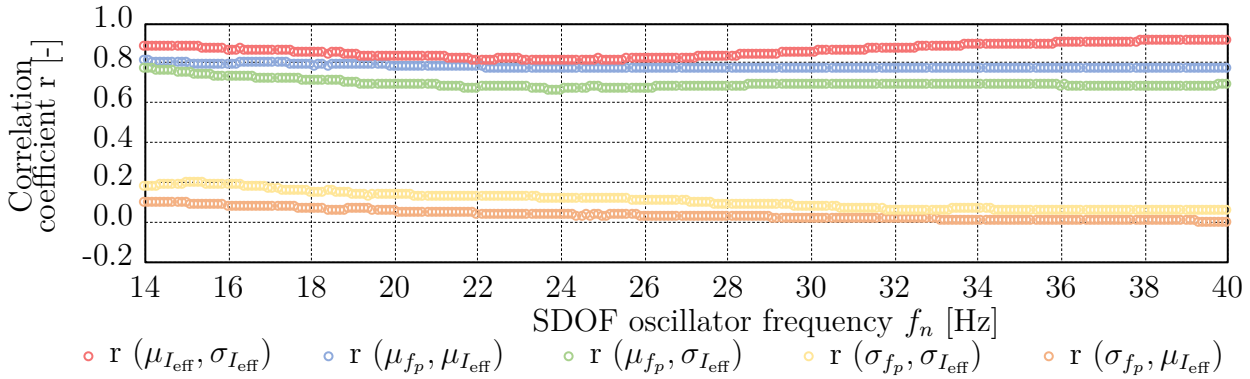

Figure 7.41: Correlation coefficients between four impulse load parameters for different SDOF oscillator natural frequencies.

correlation with the effective impulse parameters. The correlation coefficient between σ_{f_p} and $\sigma_{I_{\text{eff}}}$ ranges from 0.05 to 0.19, while that between σ_{f_p} and $\mu_{I_{\text{eff}}}$ varies from -0.01 to 0.09. None of the considered correlation coefficients varies substantially with the SDOF oscillator natural frequency f_n. Therefore, the correlations were assumed to remain constant over the considered frequency range and were represented by their mean values in Figure 7.42. In addition, Figure 7.42 indicates a weak linear correlation, with $r = 0.16$, between μ_{f_p} and σ_{f_p}. Since this coefficient is independent of f_n, it is not included in Figure 7.41.

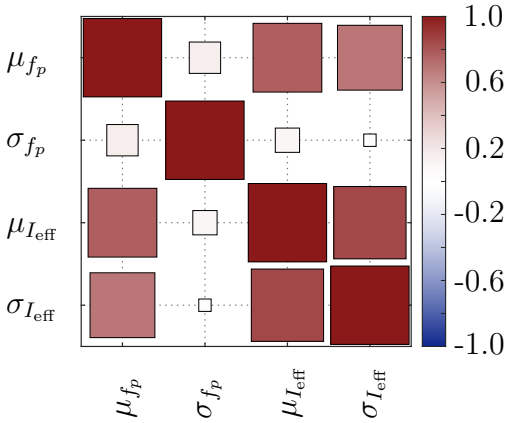

Figure 7.42: Matrix of linear correlation coefficients for four impulse load parameters.

The AR coefficients ρ_{f_p} and $\rho_{I_{\text{eff}}}$ were modelled using truncated normal distributions (Figure 7.43). The distributions were truncated to the interval $[-1, 1]$, corresponding to the admissible range of AR coefficients. A single distribution was adopted for ρ_{f_p}, based on the coefficients estimated from all 744 walking records. The results presented in Subsection 7.3.2 showed that the statistical properties of $\rho_{I_{\text{eff}}}$ varied only slightly with the SDOF oscillator natural frequency f_n. This indicates that the temporal dependence between successive effective impulses is not affected by the frequency of the oscillator used for their identification. Therefore, the values obtained for all walking records and all considered SDOF frequencies were combined, and a single truncated normal distribution of $\rho_{I_{\text{eff}}}$ was adopted over the entire frequency range.

7.3.5 Implementation and generation of probabilistic impulse load

The procedure for generating a single realisation of the effective impulse sequence is summarised in Algorithm 5. For the natural frequency of the considered structure f_n the parameters of the

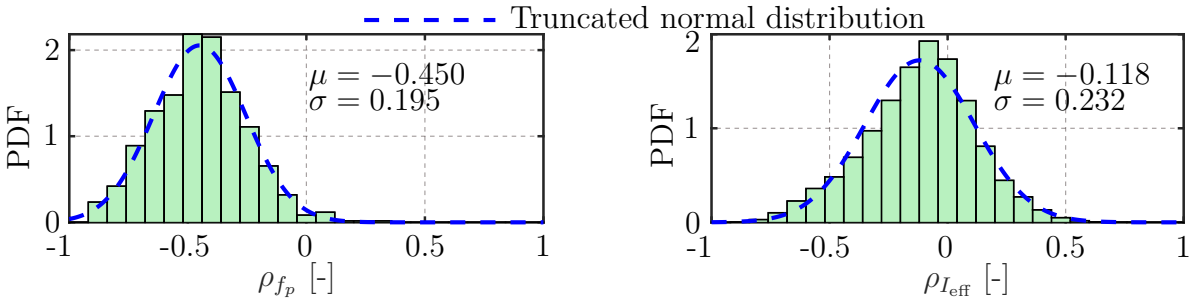

Figure 7.43: Histograms of AR coefficients for f_p and I_{eff} with distributions to approximate ρ_{f_p} and $\rho_{I_{\text{eff}}}$.

marginal distributions of $\mu_{I_{\text{eff}}}$ and $\sigma_{I_{\text{eff}}}$ are first evaluated based on the expressions given in Table 7.4. A sample of the five force-related input variables, $\mathbf{X}_{\mathcal{F}}$, is then drawn from their joint distribution, $\mathbf{G}_{\mathcal{F}}$, defined by the marginal distributions listed in Table 7.5 and the correlation matrix $\mathbf{C}_{\mathcal{F}}$ shown in Figure 7.42. The AR coefficients ρ_{f_p} and $\rho_{I_{\text{eff}}}$ are subsequently sampled independently from the fitted distributions presented in Figure 7.43. The step-by-step values of the walking frequency and effective impulse are then generated using the AR(1) formulation given in Eq. (7.12) and Eq. (7.2), with the values at the first step set equal to the corresponding sampled mean values. Finally, the generated effective impulses are multiplied by pedestrian's weight and applied successively to the structure at the times and positions of the corresponding footfalls. The location of each impulse along the walking path is determined from the generated step frequency $f_{p,\text{step}}$ and the adopted constant walking speed v.

The probabilistic impulse load model is applied to the numerical model of high-frequency CLT floor described in Section 5.4.2, and a full uncertainty analysis of calculated vibration response is presented in Chapter 9.

Algorithm 5 Algorithm for generating a single realisation of the probabilistic effective impulse sequence.

Choose N_{step}, f_n
Calculate distribution parameters of $\mu_{I_{\text{eff}}}$:
$\mu_{\ln} = -0.0749 \cdot f_n - 4.7314$
$\sigma_{\ln} = -10^{-5} \cdot f_n^3 + 0.0042 \cdot f_n^2 - 0.1060 \cdot f_n + 1.3607$
Calculate distribution parameters of $\sigma_{I_{\text{eff}}}$:
$\mu_{\ln} = -0.0719 \cdot f_n - 6.3929$
$\sigma_{\ln} = -4 \cdot 10^{-5} \cdot f_n^3 + 0.0036 \cdot f_n^2 - 0.1061 \cdot f_n + 1.4513$
Sample $\mathbf{X}_{\mathcal{F}} \sim \mathbf{G}_{\mathcal{F}}, \mathbf{C}_{\mathcal{F}}$
Sample ρ_{f_p} and $\rho_{I\text{eff}}$
Set $f_{p,1} = \mu_{f_p}$
Set $I_{\text{eff},1} = \mu_{I_{\text{eff}}}$
for step $= 1$ to $N_{\text{step}} - 1$ **do**
    $f_{p,\text{step}+1} = \mu_{f_p} + \rho_{f_p} \cdot \left(f_{p,\text{step}} - \mu_{f_p}\right) + \sigma_{f_p} \cdot \sqrt{(1 - \rho_{f_p}^2)} \cdot \varepsilon_t$
    $I_{\text{eff},\text{step}+1} = \mu_{I_{\text{eff}}} + \rho_{I_{\text{eff}}} \cdot \left(I_{\text{eff},\text{step}} - \mu_{I_{\text{eff}}}\right) + \sigma_{I_{\text{eff}}} \cdot \sqrt{(1 - \rho_{I_{\text{eff}}}^2)} \cdot \varepsilon_t$
    Apply $G \cdot I_{\text{eff},\text{step}}$ at point defined by $L_{\text{step}} = v / f_{p,\text{step}}$.
end for

7.3.6 Simplified deterministic effective impulse model

A simplified effective impulse model, suitable for routine design calculations, is proposed as a function of the walking frequency f_p and the structural natural frequency f_n:

$$I_{\text{eff,CDF}}(f_p, f_n) = A_{\text{CDF}}(f_n) \left(\frac{f_p}{f_{p,0}} \right)^{a(f_n)} \tag{7.14}$$

where CDF denotes the selected cumulative probability level, $A_{\text{CDF}}(f_n)$ is the corresponding effective impulse amplitude and $a(f_n)$ describes the influence of the walking frequency. The reference walking frequency is taken as $f_{p,0} = 1.9$Hz corresponding to the mean walking frequency obtained from the experimental database. Once f_p, f_n, and CDF are specified, Eq. (7.14) provides a single deterministic value of the effective impulse. For example, the I_{eff} corresponding to CDF = 0.90 is expected to exceed approximately 90% of the database values obtained for the corresponding combinations of f_p and f_n. The analysis of the experimental database (Subsection 7.3.2) provided a mean walking frequency f_p for each walking session and a corresponding mean effective impulse I_{eff} for each of the 261 considered SDOF oscillator natural frequencies. Consequently, the database comprises 744 × 261 = 194,184 pairs of $\left(f_p, I_{\text{eff}}\right)$. The subsets corresponding to four selected structural natural frequencies, f_n = 14, 20, 30, and 40Hz, are presented in Figure 7.44.

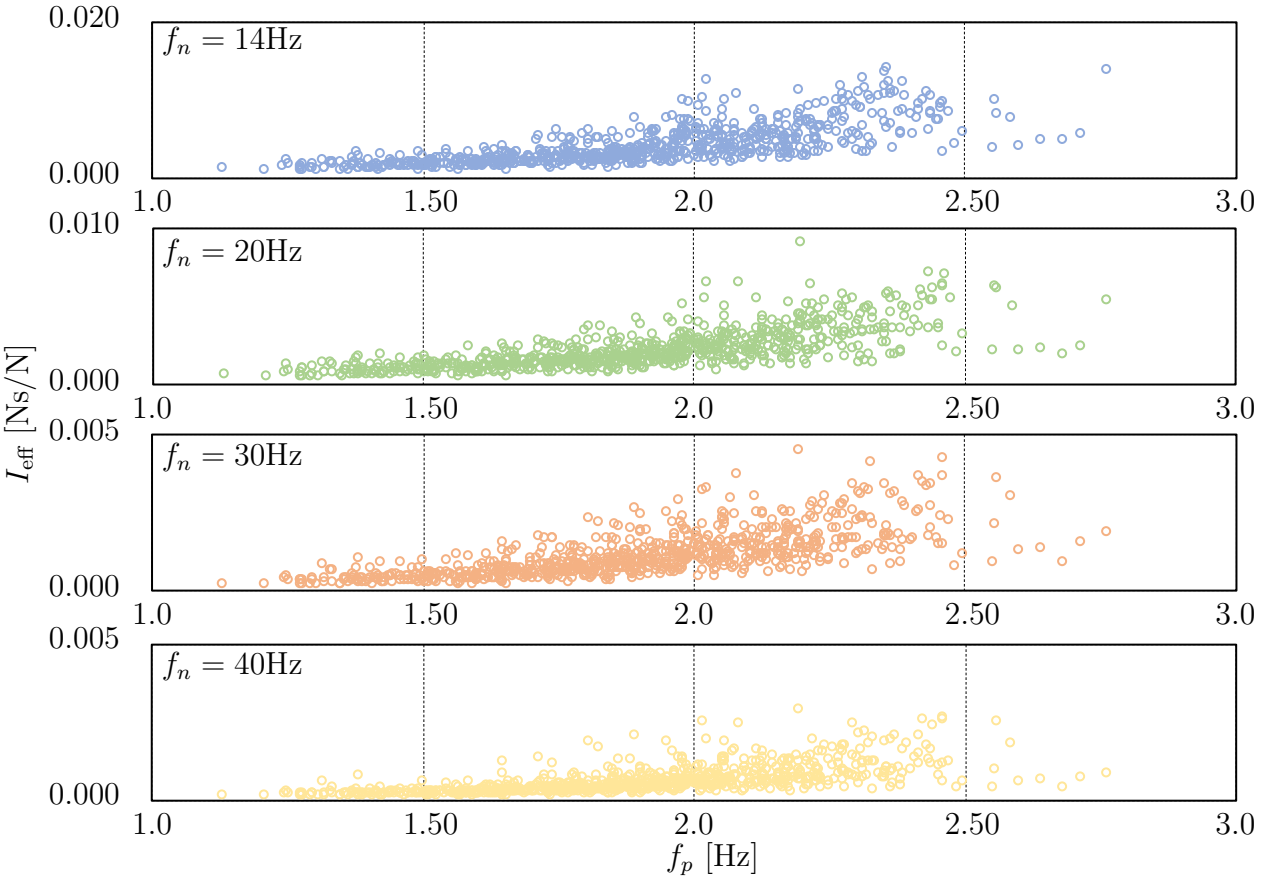

Figure 7.44: Scatter plots of mean I_{eff} versus walking frequency f_p for four different f_n.

The relationship between I_{eff} and f_p was examined separately for each considered value of f_n. For a fixed f_n, a power-law relationship was assumed between the effective impulse and the walking frequency:

$$I_{\text{eff}} = A(f_n) \left(\frac{f_p}{f_{p,0}} \right)^{a(f_n)} \cdot e^{\varepsilon}, \tag{7.15}$$

where $A(f_n)$ represents the fitted effective impulse amplitude at the reference walking frequency, $a(f_n)$ controls the dependence on f_p, and ε represents the deviation of an individual database value from the fitted relationship. For parameter estimation, Eq. (7.15) was expressed in logarithmic form:

$$\ln I_{\text{eff}} = \ln A(f_n) + a(f_n) \ln\left(\frac{f_p}{f_{p,0}}\right) + \varepsilon. \tag{7.16}$$

For each value of f_n, Eq. (7.16) represents a linear relationship between $\ln I_{\text{eff}}$ and $\ln\left(\frac{f_p}{f_{p,0}}\right)$. The intercept of this relationship is equal to $\ln A(f_n)$, while its slope is equal to $a(f_n)$. The two parameters were determined separately for each f_n using ordinary least-squares regression. The logarithmic deviation associated with database observation i was calculated as

$$\varepsilon_i = \ln I_{\text{eff},i} - \left[\ln A(f_n) + a(f_n) \ln\left(\frac{f_{p,i}}{f_{p,0}}\right)\right]. \tag{7.17}$$

A preliminary fit of Eq. (7.16) was first performed using all 194,184 database observations. For each f_n, the resulting logarithmic deviations were arranged in ascending order and assigned CDF values between zero and one. Observations located between the CDF levels of 0.10 and 0.90 were retained for the final fitting procedure. Thus, the lowest and highest 10% of the deviations were excluded when determining the main dependence between I_{eff} and f_p. This step was introduced to prevent a relatively small number of extreme observations from having a disproportionate influence on the fitted values of $A(f_n)$ and $a(f_n)$.

The retained observations were randomly divided into two subsets: 80% for parameter estimation and 20% for model validation. The final values of $A(f_n)$ and $a(f_n)$ were obtained from the first subset by re-fitting Eq. (7.16) separately for each f_n.

The variation of the resulting exponent $a(f_n)$ over the considered frequency range is presented in Figure 7.45. For each f_n and selected CDF level, $A_{\text{CDF}}(f_n)$ was determined from $A(f_n)$ by accounting for the corresponding level of scatter around the fitted relationship. Therefore, $A_{\text{CDF}}(f_n)$ represents the effective impulse amplitude associated with the selected CDF level. Its variation with the SDOF frequency for nine CDF levels, ranging from 0.1 to 0.9, is illustrated in Figure 7.46.

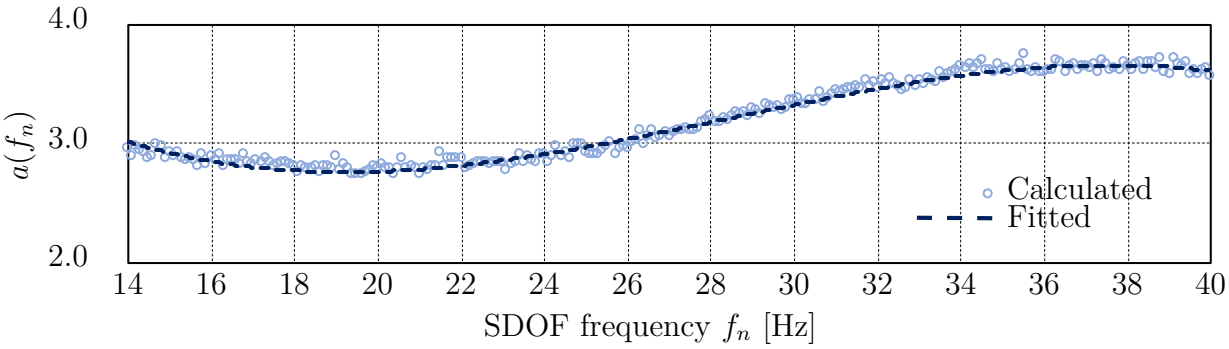

Figure 7.45: Variation of coefficient $a(f_n)$ over f_n.

To provide expressions suitable for routine calculations, $a(f_n)$ and $A_{\text{CDF}}(f_n)$ values were approximated by third-order polynomial functions. The obtained expression for $a(f_n)$ is as follows:

$$a(f_n) = 7.7535 - 8.7782 \cdot \left(\frac{f_n}{f_{n,0}}\right) + 4.8348 \cdot \left(\frac{f_n}{f_{n,0}}\right)^2 - 0.7945 \cdot \left(\frac{f_n}{f_{n,0}}\right)^3 \tag{7.18}$$

where $f_{n,0} = 14\text{Hz}$ was chosen.

For each selected probability level, the following expression for $A_{\text{CDF}}(f_n)$ was fitted:

$$A_{\text{CDF}}(f_n) = p_0(\text{CDF}) + p_1(\text{CDF})\left(\frac{f_n}{f_{n,0}}\right) + p_2(\text{CDF})\left(\frac{f_n}{f_{n,0}}\right)^2 + p_3(\text{CDF})\left(\frac{f_n}{f_{n,0}}\right)^3 \tag{7.19}$$

The coefficients $p_0(\text{CDF}) - p_3(\text{CDF})$ were determined separately for CDF levels from 0.10 to 0.90, with an increment of 0.10 and are listed in Table 7.6. For probability levels located between the tabulated values, the polynomial coefficients can be obtained by linear interpolation.

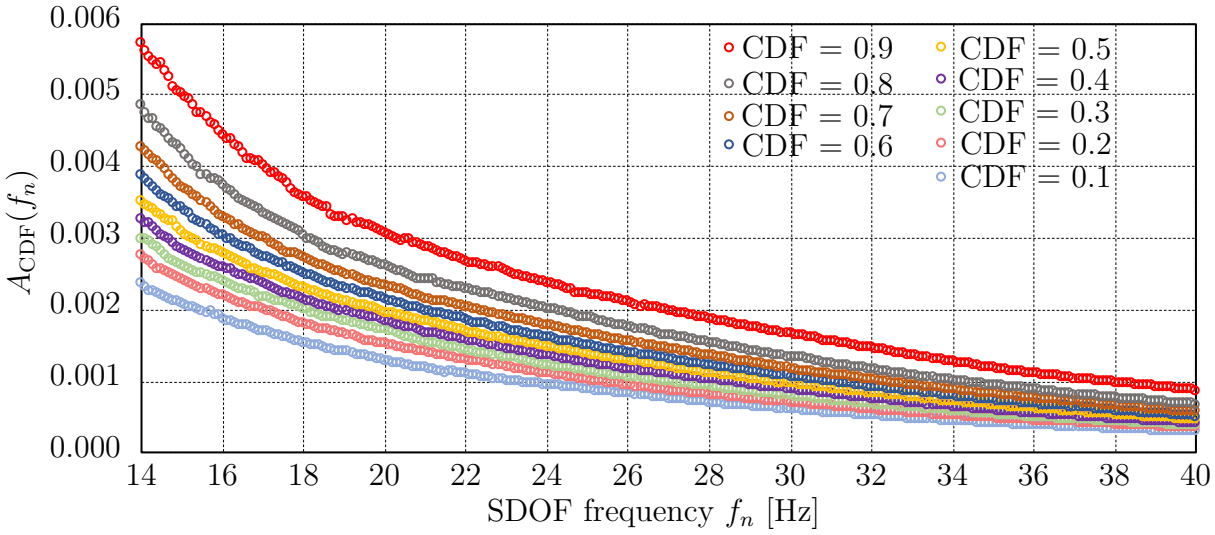

Figure 7.46: Variation of coefficient $A_{\text{CDF}}(f_n)$ over f_n for different CDF levels.

Table 7.6: Values of coefficients $p_0(\text{CDF}) - p_3(\text{CDF})$ for calculating $A_{\text{CDF}}(f_n)$ of simplified impulse load model.

CDF	**0.1**	**0.2**	**0.3**	**0.4**	**0.5**	**0.6**	**0.7**	**0.8**	**0.9**
$p_0[10^{-3}]$	8.055	8.506	9.026	9.674	10.34	11.42	12.38	13.64	15.56
$p_1[10^{-3}]$	−8.146	−8.489	−8.992	−9.750	−10.49	−11.81	−12.93	−14.41	−16.67
$p_2[10^{-3}]$	3.067	3.180	3.384	3.730	4.053	4.635	5.138	5.779	6.764
$p_3[10^{-3}]$	−0.408	−0.424	−0.456	−0.511	−0.560	−0.648	−0.726	−0.821	−0.969

Bearing all this in mind, effective impulse value is calculated in three steps. First, the exponent $a(f_n)$ is determined for the considered structural frequency f_n using Eq. 7.18. Second, $A_{\text{CDF}}(f_n)$ is calculated from Eq. (7.19) for the selected CDF level using coefficients from Table 7.6. Finally, the effective impulse is calculated from Eq. (7.14) for the specified walking frequency. This procedure is applied to the validation subset containing 20% of database realisations. The effective impulse values predicted by the simplified model, I^p_{eff}, are compared with the corresponding database values, I^d_{eff}, in Figure 7.47.

As shown in Figure 7.47(a), the predicted values are closely distributed around the line of equality, indicating very good overall agreement between the proposed expression and the experimental database. Figure 7.47(b) presents the RMRSE calculated separately for each SDOF oscillator natural frequency. For most of the considered frequency range, the RMRSE remains below approximately 5%, with a mean value of 3.59%. Somewhat larger errors are observed at the upper end of the frequency range, particularly near $f_n = 40\text{Hz}$, where the

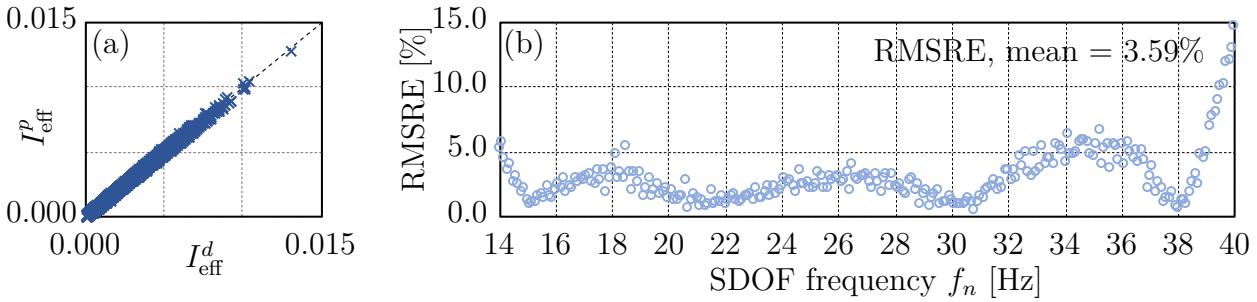

Figure 7.47: Predicted and database values of effective impulse (a) and calculated RMSRE for different f_n (b).

RMRSE reaches approximately 15%. Nevertheless, the generally low error levels confirm that the simplified model provides sufficiently accurate representation of the effective impulse over the considered range of structural natural frequencies.

The proposed simplified effective impulse model is applied to the numerical model of the high-frequency CLT floor described in Subsection 5.4.2, while its predicted response is compared with the one obtained using the CCIP-016 load model in Chapter 8. Additionally, the simplified effective-impulse formulation is compared against the probabilistic model in Chapter 8 to determine whether the latter provides sufficient benefit to warrant its use in routine design calculations.

7.3.7 Damping effect consideration

To account for SDOF damping ratios different from the reference value of $\zeta_{\text{ref}} = 3\%$, the effective impulse obtained for the reference damping ratio was multiplied by a correction factor:

$$I_{\text{eff}}(\zeta) = I_{\text{eff}}(\zeta_{\text{ref}})\, C(\zeta). \tag{7.20}$$

The influences of the SDOF natural frequency f_n and walking frequency f_p on the relative change in I_{eff} were found to be negligible. Therefore, the correction factor was expressed solely as a function of the damping ratio:

$$C(\zeta) = \exp\left(b_1 r + b_2 r^2\right), \qquad r = \ln\left(\frac{\zeta}{\zeta_{\text{ref}}}\right). \tag{7.21}$$

This formulation ensures that $C(\zeta_{\text{ref}}) = 1$.

The numerical simulations described in Subsection 7.3.2 for determining the effective impulse were repeated for SDOF damping ratios ranging from 0.5% to 6%, with an increment of 0.5%. The resulting dataset was divided into a calibration subset containing 80% of the results and a validation subset containing the remaining 20%. The calibration subset was used to determine the coefficients b_1 and b_2, yielding

$$b_1 = -0.1683, \qquad b_2 = 0.01357. \tag{7.22}$$

According to Eq. (7.21), the correction factor varies between 0.896 and 1.412. The lower limit corresponds to $\zeta = 6\%$, while the upper limit is obtained for $\zeta = 0.5\%$. Thus, increasing the damping ratio reduces the effective impulse relative to the reference value, whereas lower damping ratios lead to an increase in I_{eff}.

The remaining 20% of the results were used to validate the proposed correction factor, as presented in Figure 7.48. Excellent agreement is observed at lower effective impulse values, corresponding primarily to higher damping ratios. Somewhat greater scatter is present at higher impulse values, associated with lower damping ratios. Nevertheless, the overall mean RMSRE of 5.54% confirms that the influence of damping on the effective impulse is represented with satisfactory accuracy by the relatively simple expression given in Eq. (7.21).

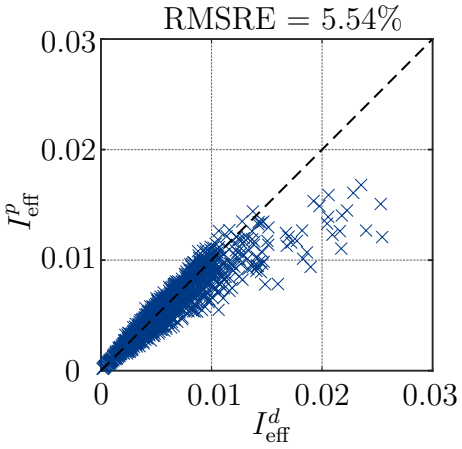

Figure 7.48: Predicted I^p_{eff} and database values I^d_{eff} of effective impulse taking into account different damping ratio

7.4 Chapter summary

This chapter extended the CCIP-016 harmonic and effective impulse representations of walking excitation using a database of 744 continuously measured vertical walking force records [40]. The main objective was to retain the physical basis and practical advantages of the established models while introducing probabilistic formulations capable of representing both inter-subject variability between different walking records and intra-subject variability between successive steps within an individual walk.

In contrast to the four harmonic load model adopted in CCIP-016, the LFF force model developed in this dissertation was represented by six harmonic components and formulated as a quasi-periodic process. Within each individual step, the six-harmonic sine sum was defined by step-specific values of walking frequency and the harmonic amplitudes. Across successive steps, these parameters were allowed to vary according to first-order autoregressive AR(1) processes. In this way, the model explicitly accounted for the step-to-step variability observed during continuous walk. The walking frequency and six dynamic load factors (DLFs) were extracted for each step from all force signals in the established database, and their statistical properties were evaluated. Across all walking records, the mean walking frequency was found to be 1.9Hz, with a COV of approximately 14%. Within individual walking records, the COV of the walking frequency generally ranged from 1 to 10%. The results indicated that pedestrians maintained the most regular pacing rates at mean walking frequencies between approximately 1.9 and 2.2Hz, whereas walking at lower frequencies was generally associated with greater step-to-step variability. The mean values of the DLFs, particularly DLF_1, exhibited a pronounced dependence on the mean walking frequency. In contrast, the corresponding COVs showed no clear relationship with the walking frequency. Considerable statistical dependence was also identified between the DLFs of different harmonic orders. The complete probabilistic harmonic load formulation

comprised 15 primary force parameters: pedestrian weight, the mean and standard deviation of the walking frequency, and the mean and standard deviation of each of the six DLFs. The variability of these parameters was represented through fitted marginal probability distributions, while their mutual statistical dependence was described using correlation coefficients obtained from the experimental database. The extracted harmonic load parameters were verified by reconstructing the measured walking force records and comparing the resulting responses of SDOF oscillators. Temporal dependence between successive steps was incorporated through the corresponding AR(1) coefficients. They were introduced as secondary random variables governing the temporal dependence of the step-by-step parameter sequences.

The impulse load model was formulated by replacing each footfall with a single effective impulse. Sequences of effective impulses were identified from the velocity responses of SDOF oscillators with a modal mass of 1kg, a damping ratio of 3% and natural frequencies between 14 and 40Hz, subjected to the continuously measured walking force records. This procedure enabled both the variation of the effective impulse between successive steps and its dependence on the SDOF natural frequency to be quantified. The walking frequency adopted in the impulse model was defined differently from that used in the harmonic model. In the harmonic formulation, it was determined from the first harmonic of the force signal, whereas in the impulse formulation it was calculated as the reciprocal of the time interval between successive footfalls. Although the two definitions produced practically identical mean values, they resulted in different estimates of intra-subject variability. On average, the step-based walking frequency exhibited COV approximately twice as large as those obtained from the first-harmonic-based definition. Across the complete database, the step-based coefficients of variation ranged from approximately 1% to 13.5%. The variability of the effective impulse was considerably greater. Depending on the natural frequency of the SDOF oscillator, its mean COV ranged from approximately 25% to 35%. The probabilistic impulse load model was defined by five primary force parameters: pedestrian weight, the mean and standard deviation of the walking frequency, and the mean and standard deviation of the effective impulse. Their marginal probability distributions and mutual correlations were determined from the experimental database, while the temporal dependence between successive walking frequencies and effective impulses was described through two additional AR(1) coefficients. The impulse identification and reconstruction procedures were verified by comparing the velocity responses obtained from the measured walking force records with those generated by the corresponding effective impulse sequences. In addition, a correction factor was introduced to account for damping ratios different from the reference value of 3% adopted during the effective impulse identification.

Finally, simplified deterministic formulations of both the harmonic and impulse load models were proposed for routine design calculations. These formulations preserve the principal dependence of the load parameters on the walking frequency and, in the case of the impulse model, on the structural natural frequency, while avoiding the computational complexity of a complete probabilistic simulation. The selected CDF level of DLFs and I_{eff} is included as an input parameter, allowing the user to choose the desired probability level used to define the design loading.

8 Verification of deterministic vibration response predictions

This chapter presents a deterministic approach to the VSA of floors based on the framework recommended in CCIP-016 and incorporating the simplified walking-load models developed in Chapter 7. The resulting VSA algorithm was implemented in Hindu, a Python-based software developed within the scope of this dissertation for calculating pedestrian-induced floor vibrations. An earlier version of Hindu was presented in the conference paper *Milojević M. et al. (2022) Software for calculation of pedestrian-induced vibration of floors. In: Proceedings of the 16th Congress hosted by Association of Structural Engineers of Serbia, Aranđelovac, Serbia* [42]. Furthermore, the chapter evaluates the performance of the proposed simplified load models by comparing the resulting vibration responses with those obtained using the original CCIP-016 walking forces, measured walking-force signals and the probabilistic load model developed in Chapter 7. This comparison is intended to assess whether the simplified deterministic models provide sufficiently reliable response predictions to support their use in routine engineering practice. Where available, the responses are also compared with experimental test results.

Both pedestrian-induced loading and the modal properties of a floor are inherently uncertain, so a fully probabilistic VSA would provide the most complete representation of the expected structural response. However, such analyses generally require considerable computational effort, making them unsuitable for routine engineering design, where quick and straightforward assessment procedures are typically required. In everyday practice, vibration serviceability is therefore normally assessed using deterministic procedures based on representative values of the structural and loading parameters. Among the available deterministic approaches, the methodology proposed in CCIP-016 [41], elaborated in Section 2.3, provides one of the most reliable frameworks for predicting pedestrian-induced floor vibrations. It is based on the principles of modal analysis and therefore enables the vibration response to be evaluated directly from the modal properties of the structure, without relying on simplified empirical criteria. Furthermore, the procedure can be readily combined with FE analysis, which may be used to determine the required modal properties. For these reasons, the CCIP-016 methodology is adopted in this dissertation as the basis for the deterministic VSA of CLT floors.

The CCIP-016 original walking load models are replaced by the harmonic and effective impulse models developed in Chapter 7, as described in Section 8.1, while the general structural response framework and serviceability criteria are retained. The resulting assessment procedures are implemented in Hindu, a software developed as part of this research and presented

in Section 8.2. The software facilitates definition of the input parameters (such as floor modal properties, walking path, walking frequency, receiver point etc.), calculation of the floor response and visualisation of the results. Finally, Section 8.3 presents the vibration responses of the LFF and HFF defined in Chapter 5, calculated using both the original CCIP-016 and proposed simplified walking load models. Calculated responses are evaluated against probabilistic responses obtained using measured walking-force signals and the probabilistic load models developed in Chapter 7. This comparison is used to assess whether the simplified models can provide sufficiently reliable response estimates to justify their use in routine engineering practice in place of more computationally demanding probabilistic analyses. For the LFF, the numerical predictions are additionally compared with experimentally measured responses, whereas for the HFF, the assessment is limited to comparisons based on numerical simulations.

8.1 Proposed simplified load models

As previously noted, the proposed formulation aims to preserve the simplicity of the CCIP-016 methodology while introducing several improvements defined in Chapter 7. First, the boundary between LFFs and HFFs is increased to 14Hz, consistent with the observation by Mohammed et al. [34] that resonant response may occur in floors with natural frequencies up to this value. Accordingly, the proposed harmonic load model (Section 7.2) includes six harmonics. For a maximum walking frequency of 2.5Hz, the highest excitation frequency is therefore 15Hz. Second, while the CCIP-016 load models were derived from more than 800 individual footfall records, the parameters of the proposed harmonic and effective impulse models were obtained from 744 continuous walking force records. Finally, both the harmonic and effective impulse models defined in Sections 7.2.6 and 7.3.6 allow the user to select the required load quantile through a prescribed CDF value, and thus to control the corresponding probability of exceedance.

8.1.1 Low-frequency floors

The procedure for evaluating the vibration serviceability of LFFs differs from CCIP-016 (see Algorithm 1 in Section 2.3) only in Steps #4 and #6. In Step #4, the number of harmonics is increased from four to six ($h = 1 - 6$), while Step #6 is modified to account for the proposed DLF formulation. Although the calculation of the DLFs for the simplified harmonic load model is described in Subsection 7.2.6, it is repeated here for completeness and ease of reference.

The CDF level may be selected within the range $0.1 - 0.9$, corresponding to probabilities of exceedance between 90% and 10%, respectively. Once the CDF level has been specified, the DLFs for the six harmonics are calculated as follows:

$$\mathrm{DLF}_h = p_{00} + p_{10} f_p + p_{01}\mathrm{CDF} + p_{11} f_p \mathrm{CDF} + p_{02}\mathrm{CDF}^2 + p_{12} f_p \mathrm{CDF}^2 + p_{03}\mathrm{CDF}^3 \tag{8.1}$$

with coefficients $p_{00} - p_{03}$ given in Table 8.1.

Figure 8.1 compares the DLFs calculated according to CCIP-016 (Table 2.2) with those obtained using the proposed harmonic model (Eq. (8.1) and Table 8.1) for walking frequencies ranging from 1.5 to 2.5Hz and a CDF level of 0.75. The corresponding empirical 75th-percentile values obtained directly from the database are also presented.

Table 8.1: Values of p-coefficients for calculating DLFs of simplified harmonic force model.

Harm.	$\boldsymbol{p_{00}}$ $[10^{-3}]$	$\boldsymbol{p_{10}}$ $[10^{-3}]$	$\boldsymbol{p_{01}}$ $[10^{-3}]$	$\boldsymbol{p_{11}}$ $[10^{-3}]$	$\boldsymbol{p_{02}}$ $[10^{-3}]$	$\boldsymbol{p_{12}}$ $[10^{-3}]$	$\boldsymbol{p_{03}}$ $[10^{-3}]$
DLF_1	−313.40	239.49	−138.93	246.19	−354.34	29.975	210.78
DLF_2	−20.481	14.985	45.045	50.629	−237.68	28.959	154.372
DLF_3	35.671	−12.699	115.18	1.5891	−187.00	18.239	112.39
DLF_4	0.8361	8.8490	28.775	32.400	−97.748	−4.3282	73.625
DLF_5	−16.734	12.916	−18.003	48.612	−45.884	−20.032	59.551
DLF_6	−11.454	7.9466	−41.588	47.577	−21.727	−15.259	40.787

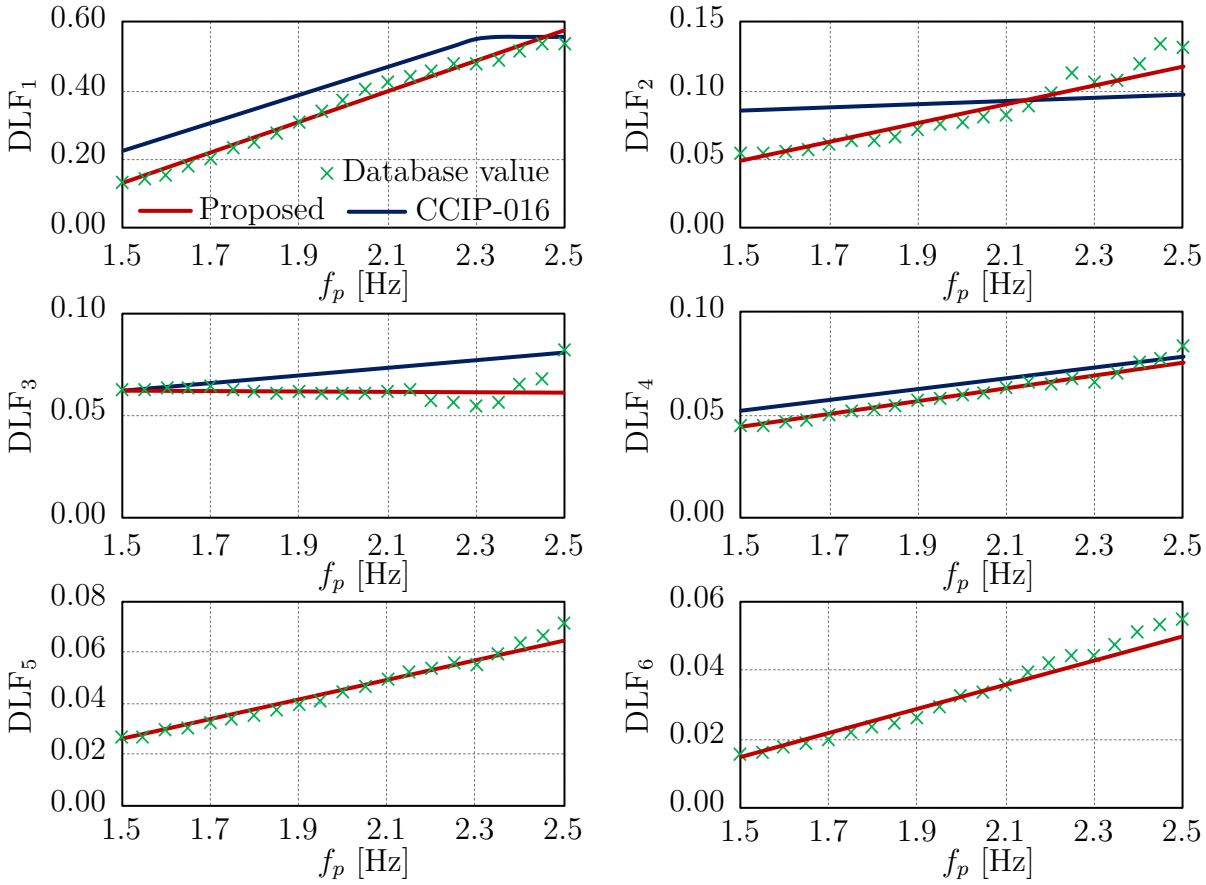

Figure 8.1: Comparison of DLFs according to CCIP-016, proposed formulation and database values for CDF= 0.75 (corresponding to CCIP-016).

The proposed formulation generally reproduces the database values well, which is expected given that it was derived from the same dataset. The exception is for the highest walking frequencies, where proposed model slightly underestimates the database values for DLF_3 and DLF_6. CCIP-016 gives consistently higher values for DLF_1 and DLF_3 than proposed model, while the differences for DLF_4 are comparatively small. A different trend is observed for DLF_2, where the CCIP-016 value remains almost constant, and both the proposed model and the database values increase with walking frequency. Consequently, the proposed DLF_2 exceeds the CCIP-016 value for walking frequencies above approximately 2.2Hz.

8.1.2 High-frequency floors

The procedure for evaluating the vibration serviceability of high-frequency floors differs from Algorithm 2 (Section 2.3) only in Step #5. Instead of calculating the design effective impulse using Eq. (2.8), the proposed formulation determines the effective impulse as

$$I_{\text{eff,CDF}}(f_p, f_n) = GC(\zeta)A_{\text{CDF}}(f_m)\left(\frac{f_p}{f_{p,0}}\right)^{a(f_m)} \tag{8.2}$$

where $f_{p,0} = 1.9\text{Hz}$. Note that the CCIP-016 expressions for I_{eff}, given by Eqs. (2.7) and (2.8), already account for the pedestrian weight. In contrast, the effective impulse obtained from the proposed model is normalised with respect to body weight and must therefore be multiplied by the pedestrian weight (G).

The frequency-dependent exponent $a(f_n)$ is calculated from the natural frequency f_n of the considered mode as

$$a(f_n) = 7.7535 - 8.7782 \cdot \left(\frac{f_n}{f_{n,0}}\right) + 4.8348 \cdot \left(\frac{f_n}{f_{n,0}}\right)^2 - 0.7945 \cdot \left(\frac{f_n}{f_{n,0}}\right)^3 \tag{8.3}$$

where $f_{n,0} = 14\text{Hz}$. The coefficient $A_{\text{CDF}}(f_n)$ is evaluated as

$$A_{\text{CDF}}(f_n) = p_0(\text{CDF}) + p_1(\text{CDF})\left(\frac{f_n}{f_{n,0}}\right) + p_2(\text{CDF})\left(\frac{f_n}{f_{n,0}}\right)^2 + p_3(\text{CDF})\left(\frac{f_n}{f_{n,0}}\right)^3 \tag{8.4}$$

where the coefficients $p_0 - p_3$ depend on the selected CDF level and are listed in Table 8.2. For the CDFs located between values presented in Table 8.2, the polynomial coefficients can be obtained by linear interpolation.

Table 8.2: Values of coefficients $p_0(\text{CDF}) - p_3(\text{CDF})$ for calculating $A_{\text{CDF}}(f_n)$ of simplified impulse load model.

CDF	**0.1**	**0.2**	**0.3**	**0.4**	**0.5**	**0.6**	**0.7**	**0.8**	**0.9**
$p_0[10^{-3}]$	8.055	8.506	9.026	9.674	10.34	11.42	12.38	13.64	15.56
$p_1[10^{-3}]$	−8.146	−8.489	−8.992	−9.750	−10.49	−11.81	−12.93	−14.41	−16.67
$p_2[10^{-3}]$	3.067	3.180	3.384	3.730	4.053	4.635	5.138	5.779	6.764
$p_3[10^{-3}]$	−0.408	−0.424	−0.456	−0.511	−0.560	−0.648	−0.726	−0.821	−0.969

The reference formulation corresponds to a damping ratio of $\zeta_{\text{ref}} = 3\%$. For other damping ratios, the correction factor $C(\zeta)$ is calculated as

$$C(\zeta) = \exp\left(-0.1683r + 0.01357r^2\right), \qquad r = \ln\left(\frac{\zeta}{\zeta_{\text{ref}}}\right). \tag{8.5}$$

Figure 8.2 compares the effective impulse values obtained using the CCIP-016 methodology and the proposed formulation with the corresponding database-derived values. The comparison is presented for natural frequencies of $f_n = 14, 20, 30$ and 40Hz, and walking frequencies in the range $1.5 - 2.5\text{Hz}$. To ensure consistency, the proposed and database-derived values correspond to a CDF level of 0.75, i.e. a 25% probability of exceedance, a pedestrian weight of $G = 750\text{N}$ and a damping ratio of $\zeta = 3\%$.

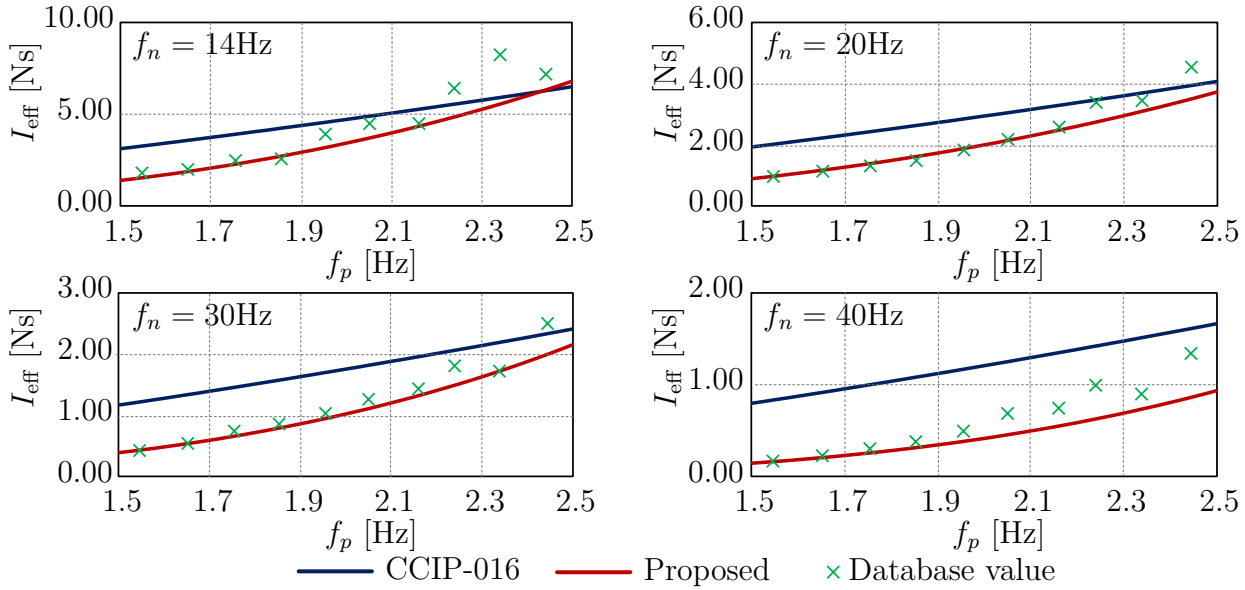

Figure 8.2: Comparison of I_{eff} according to CCIP-016, proposed formulation and database values for CDF= 0.75, $G = 750$N and $\zeta = 3\%$ (corresponding to CCIP-016).

At low and moderate walking frequencies, the CCIP-016 formulation generally predicts higher effective impulse values than both the proposed model and the database. This overestimation becomes more pronounced as the natural frequency increases and is particularly evident for $f_n = 40$Hz. However, for $f_n = 14$Hz, the CCIP-016 curve intersects the database trend at approximately $f_p = 2.1 - 2.2$Hz and underestimates the effective impulse at higher walking frequencies. A similar, although less pronounced, tendency is observed for $f_n = 20$Hz. On the other hand, the proposed formulation follows the database values more closely over the considered frequency range, particularly for walking frequencies up to approximately 2Hz. At higher walking frequencies, it tends to underestimate the effective impulse. This discrepancy is most pronounced for natural frequencies of 14Hz and 40Hz, whereas comparatively better agreement is obtained for $f_n = 20 - 30$Hz.

8.2 Hindu software for vibration response calculation

Hindu (shortened from **h**uman-**indu**ced vibrations) is a Python-based [141] software application developed within the scope of this dissertation for the prediction of floor vibration response induced by pedestrian walking. Its computational framework follows the conventional source-path-receiver concept, integrating the walking excitation, structural modal properties and response evaluation within a unified analysis environment. Although the software remains at an early stage of development, it demonstrates considerable potential, particularly through its intuitive graphical user interface (GUI), which facilitates the efficient definition of input data, execution of analyses and interpretation of results.

8.2.1 Computational framework and implementation

The response calculation consists of several stages, beginning with the definition of the structural transmission path through the modal properties of the floor. Hindu does not perform

modal analysis. Therefore, the natural frequencies, modal masses and mode shapes must be obtained externally and imported into the software. At present, Hindu supports the import of modal properties calculated in Abaqus/CAE. Experimentally identified modal properties may also be used. However, modal masses are generally not obtained directly from ambient-vibration tests and must therefore be specified separately in this case.

Several walking load models from design guidelines and the literature have been implemented in Hindu, including those proposed by Rainer et al. [48], Kerr and Bishop [56], Živanović and Pavić [27] and CCIP-016 [41], together with the simplified models elaborated in Section 8.1. Some of these models are intended exclusively for LFFs (Rainer et al. [48] and Kerr and Bishop [56]), whereas the model proposed by Živanović and Pavić [27] may be applied to both low- and high-frequency floors. For the CCIP-016 methodology and the models proposed in this dissertation, Hindu identifies the floor type from its fundamental natural frequency and automatically selects the corresponding load representation.

Most design guidelines, including CCIP-016, simplify the response calculation by assuming a stationary force applied at the most adverse point on the floor. However, Hindu allows the user to define a straight walking path along which the excitation moves, thereby providing a more realistic simulation of pedestrian walking. Since the spatial variation of the excitation is represented explicitly, the reduction factor ρ, defined by Eq. (2.4), does not need to be applied separately. In all other aspects, the vibration response is calculated according to the procedure described in Section 2.3, with modal superposition employed for both LFFs and HFFs.

The calculated results include displacement, velocity and acceleration time histories at any selected point on the floor. These responses may be displayed separately for each included mode or as the total superimposed response. One-second running RMS acceleration and velocity diagrams are also available. In addition, Hindu calculates the maximum absolute acceleration at each point of the floor and presents its spatial distribution as a two-dimensional response map. At the current stage of development, Hindu does not calculate the R factor or directly classify the vibration serviceability of the floor. This final evaluation is therefore left to the engineer, i.e. software user.

8.2.2 Graphical user interface

To improve accessibility and ease of use, Hindu was equipped with a GUI developed using PySide6, the Python bindings for the Qt application framework. The interface guides the user through the main stages of the analysis, including the import of structural modal properties, definition of the walking path, selection of the walking load model, specification of the analysis parameters, execution of the response calculation and visualisation of the results.

8.2.2.1 Main window

Running Hindu opens the main window, which is divided into five principal sections, as shown in Figure 8.3. The *Menu bar* contains six tabs (Figure 8.3*a*): File, Floor, Model, Response diagrams, Options and Help. These tabs provide access to the main functions required for vibration response analysis. The *Available modes* section (Figure 8.3*b*) enables the user to select the modes included in the response calculation based on modal superposition. The parameters required for the analysis are specified in the *Input parameters* section (Figure 8.3*c*). These

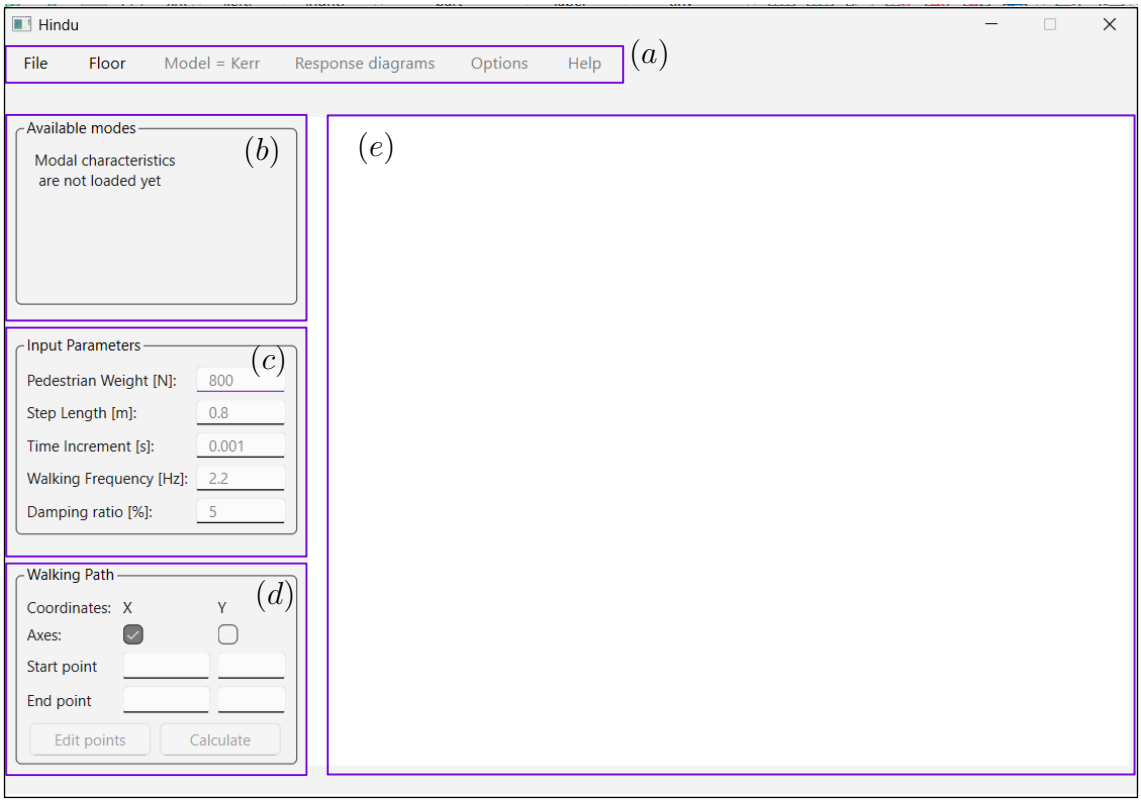

Figure 8.3: Hindu software main window and its components: Menu bar (a), Available modes (b), Input parameters (c), Walking path (d) and Canvas (e).

include the pedestrian weight, step length, walking frequency, modal damping ratio and time increment used in the numerical solution of the equation of motion for each mode. Note that default values are assigned to all input parameters. Therefore, if a parameter is not specified by the user, the corresponding predefined value is adopted in the analysis. In the *Walking path* section (Figure 8.3d), the user defines a straight walking trajectory by specifying its start and end points. The largest part of the main window is occupied by the *Canvas* (Figure 8.3e), which is used to display the imported mode shapes of the floor.

8.2.2.2 Floor modal properties and walking path

The *Floor* tab contains two options (Figure 8.4a): *Load geometry/modes* and *Define walking path*. The latter is initially disabled and becomes available only after the floor geometry and modal properties have been imported. Selecting *Load geometry/modes* opens a separate window (Figure 8.4b) in which the user may choose to import modal data either from Abaqus/CAE or from experimental testing. Once the modal properties have been loaded, they are displayed graphically on the *Canvas* (Figure 8.4c). The user may browse through the available mode shapes using the *Next mode* and *Previous mode* controls. All imported modes are also listed in the *Available modes* section, where individual modes can be selected for inclusion in the modal-superposition response calculation.

After the floor geometry and modal properties have been loaded, the *Define walking path* option becomes active. Selecting this option opens a separate window (Figure 8.5) in which the user defines a straight walking path by specifying its start and end points. The same window may

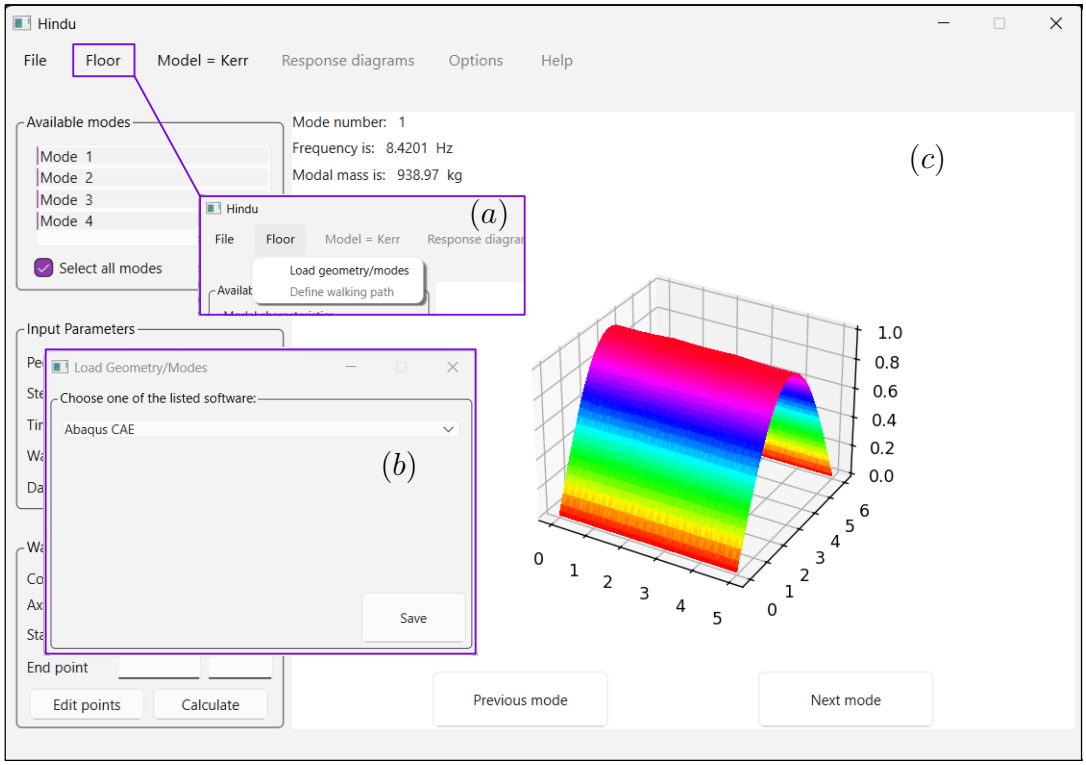

Figure 8.4: Floor tab - available options (a), choosing one of the listed FE software (b), displayed loaded modal properties (c).

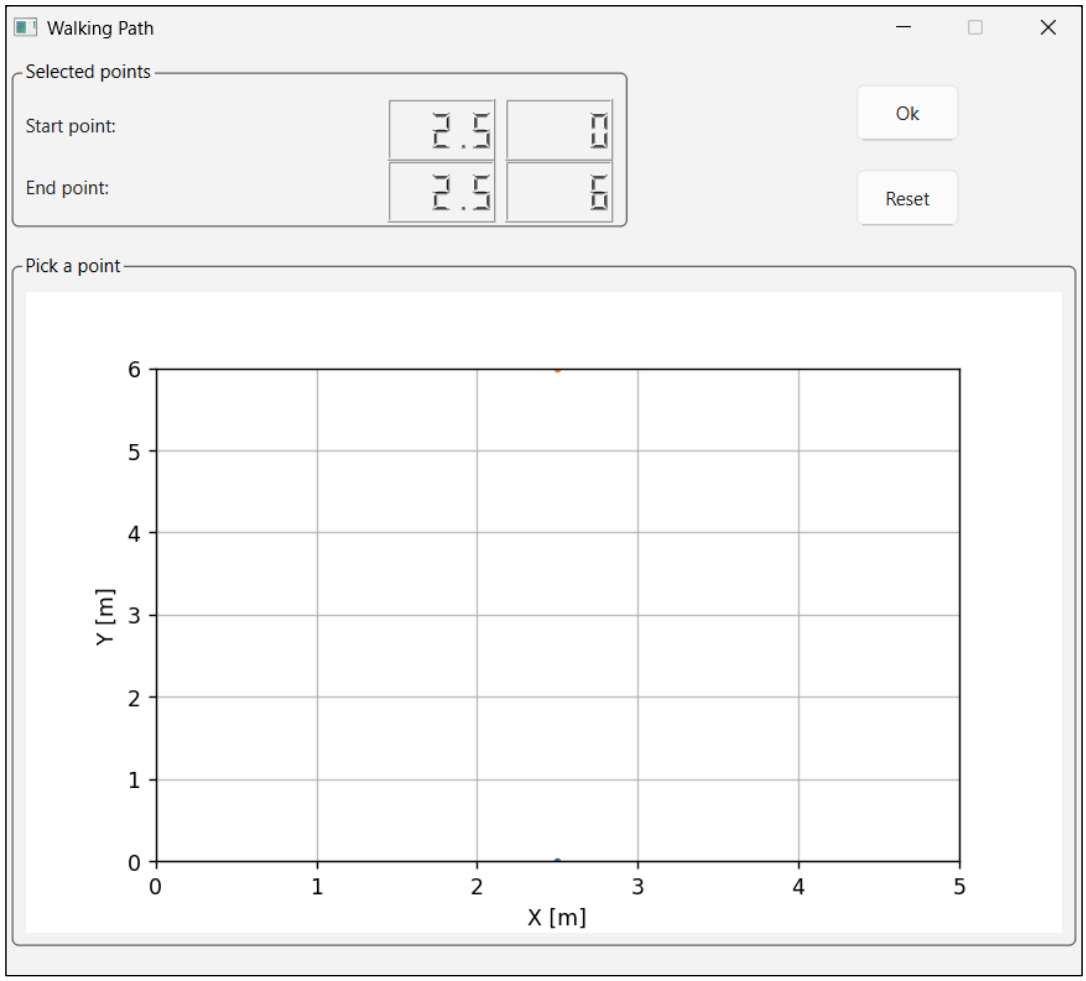

Figure 8.5: Walking path window.

also be accessed through the *Edit points* button in the *Walking path* section of the main window (Figure 8.3*d*), which is likewise activated after the floor modal properties have been imported.

8.2.2.3 Design guidelines and walking force models

The *Model* tab enables the user to select one of the available force models (Figure 8.6*a*). As previously noted, the models proposed by Rainer et al. [48] and Kerr and Bishop [56] are intended exclusively for LFFs, whereas the model proposed by Živanović and Pavić [27] may be applied to both LFFs and HFFs. For the CCIP-016 (denoted as Arup within the software), and for the models proposed in this dissertation, Hindu classifies the floor according to its fundamental natural frequency and automatically selects the appropriate load representation.

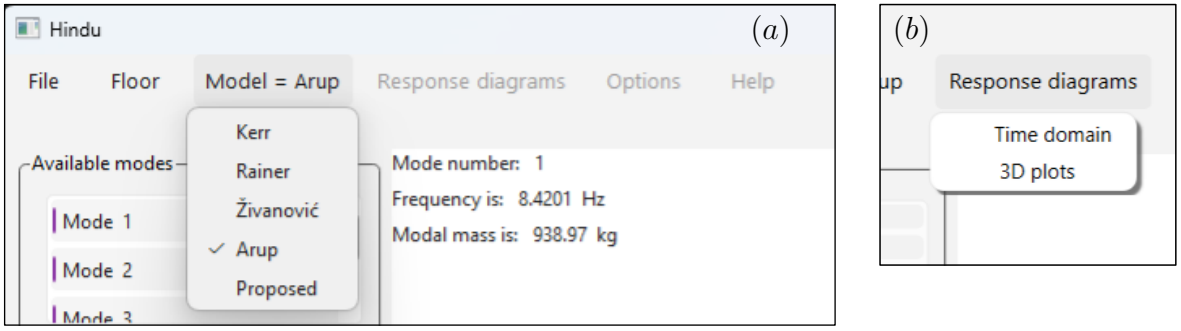

Figure 8.6: The *Model* tab with the implemented walking load models and assessment procedures (*a*), and the *Response diagrams* tab with the available visualisation options (*b*).

8.2.2.4 Results, visualisation and reports

Once all parameters have been defined in the *Input parameters* section, the floor response in modal coordinates is calculated by selecting the *Calculate* button located in the lower-left corner of the main window (Figure 8.3). Upon completion of the analysis, the options within the *Response diagrams* tab become available (Figure 8.6*b*). Selecting the *Time domain* option opens a separate window in which the response time histories at the specified receiver location may be displayed. Acceleration, velocity and displacement histories can be presented either separately for each included mode or as the total response obtained by modal superposition (Figure 8.7*a*). In addition, the corresponding one-second running RMS acceleration and velocity histories may be superimposed on the total response diagrams (Figure 8.7*b*).

The second option available within the *Response diagrams* tab is 3D *plots*. Selecting this option opens a separate window in which the spatial distribution of the maximum absolute response may be displayed over the floor surface (Figure 8.8). The available response quantities include acceleration, velocity, displacement and the maximum one-second running RMS values of both acceleration and velocity. When the *Plot Slider* option is activated, the user may additionally examine the spatial response distribution at each time step throughout the pedestrian crossing.

An approximate R factor may be estimated by dividing the maximum one-second running RMS acceleration by the reference value of 0.005m/s^2. This does not represent an exact calculation of the R factor, since the reference acceleration depends on the vibration frequency of the floor. Instead, it provides a conservative estimate, as the adopted value of 0.005m/s^2 corresponds to the frequency range of $4-8\text{Hz}$, within which human sensitivity to vertical vibration is greatest.

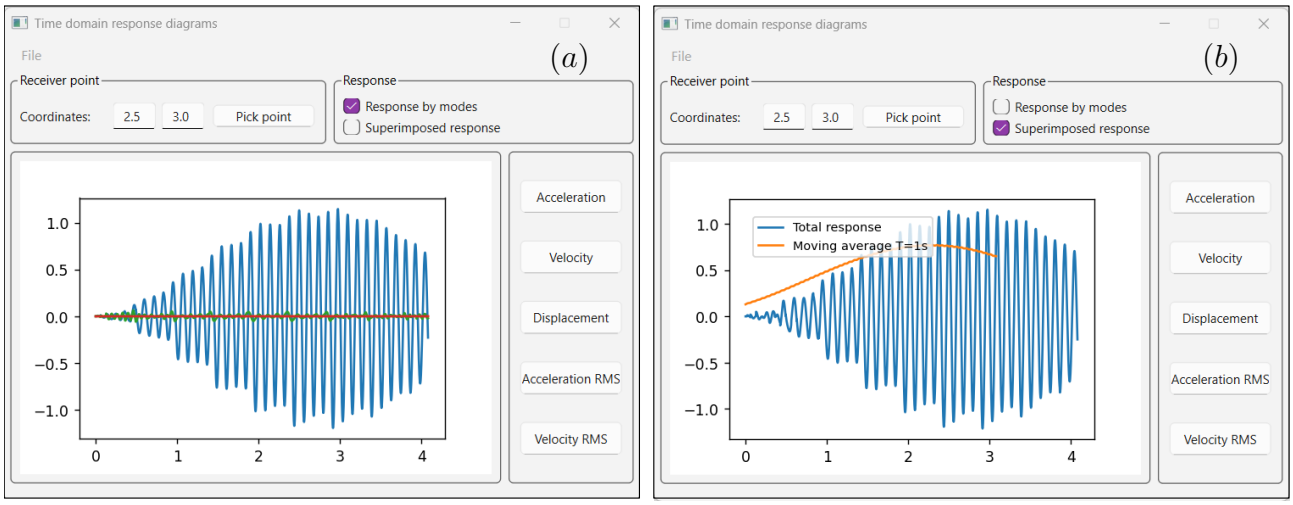

Figure 8.7: Time-domain response histories at the receiver point: contributions of individual modes (a) and the total response with the corresponding one-second running RMS history (b).

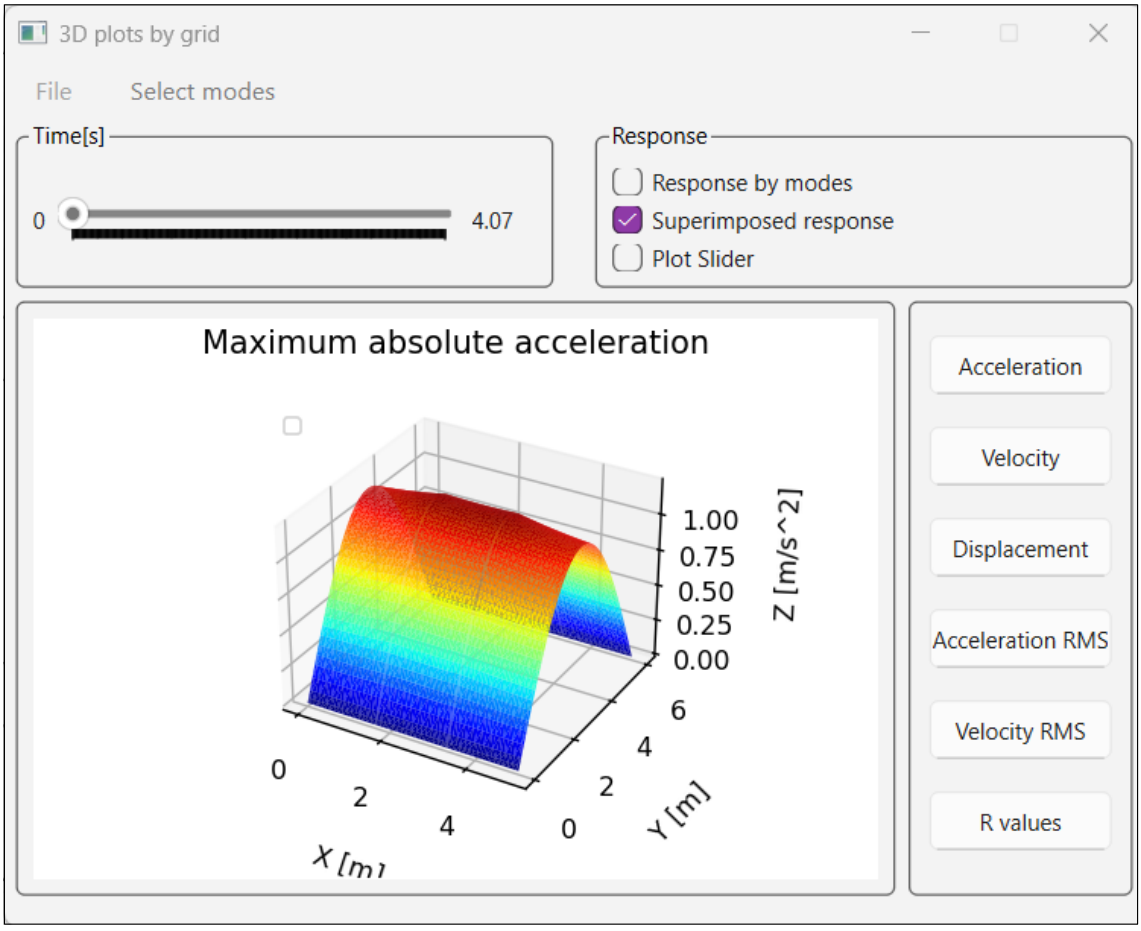

Figure 8.8: 3D visualisation of the spatial distribution of the floor vibration response.

8.3 Response verification and VSA using the CCIP-016 and proposed simplified load models

This section presents a verification of the deterministic vibration responses of the LFF and HFF models under pedestrian-induced loading. For both floors, responses are calculated using the original CCIP-016 and proposed simplified walking-load models for CDF=0.75. In accordance with CCIP-016, the first three vibration modes are included in the LFF response calculation, whereas the first four modes are considered for the HFF. Two walking paths (WPs) are considered and shown in Figure 8.9 with the corresponding receiver point. In contrast to the simplified CCIP-016 assumption of a stationary force acting at the most adverse point, the pedestrian excitation is explicitly moved along the prescribed WP, thereby accounting for the variation in the mode shape amplitudes at successive footfall locations.

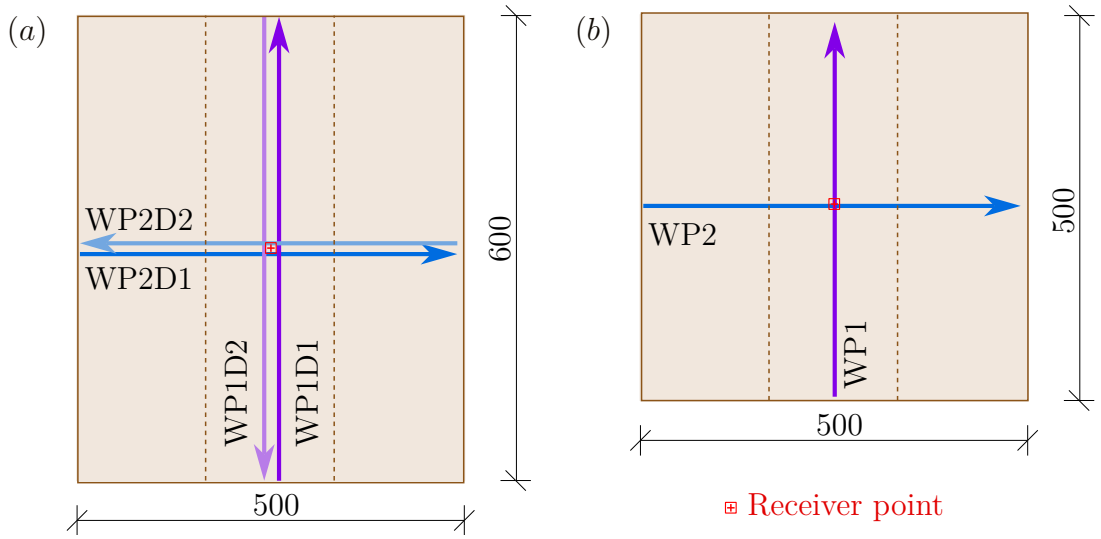

Figure 8.9: Walking paths and receiver point for LFF (a) and HFF (b).

Experimental response measurements are available for the LFF (Section 4.2) and are used to evaluate the numerical predictions. To ensure consistency with the experimental conditions, the initial analyses are performed using a walking frequency of $f_p = 2$Hz, a pedestrian (TS1) weight of $G = 480$N and a damping ratio of $\zeta = 1.04\%$. This case is hereafter referred to as the non-resonant response. Since the non-resonant response is not governing for VSA design, the resonant response is subsequently examined for $f_p = 2.1$Hz, for which the fourth harmonic of the walking force is equal to the fundamental frequency of the floor. In this case, pedestrian weight is set to 750N, a value commonly adopted in floor VSA. In this manner, the VSA obtained using the CCIP-016 and proposed formulations are directly compared.

Since no experimental response data are available for the HFF, the comparison is limited to the numerical predictions. A walking frequency of $f_p = 2.5$Hz is selected, corresponding to the maximum value recommended by CCIP-016 for corridors and other circulation areas. Furthermore, a damping ratio of $\zeta = 3\%$ is adopted, as this is the reference value used in the development of both effective impulse formulations, while the pedestrian weight is set to 750N.

The calculated responses of both the LFF and HFF are further verified against those obtained using the measured walking forces and the proposed probabilistic formulation. The modal properties of the floors are kept fixed, i.e. their variability is not considered, so that the comparison focuses exclusively on the walking load models. To ensure consistency among

the different sets of results, the probabilistic responses are evaluated for fixed mean walking frequencies. For the measured forces, signals with mean walking frequencies within ±2% of the corresponding target values are included in the LFF analysis. Due to the limited number of measured force records with mean walking frequencies around 2.5Hz, the HFF analysis includes signals within ±5% of this target frequency.

8.3.1 Low-frequency floors

As explained in Chapter 7, the proposed harmonic load model (as well as the one proposed by CCIP-016) does not specify the phase angle associated with each harmonic component. The individual harmonic contributions cannot therefore be combined through direct superposition and are instead combined using the SRSS method (Section 2.3). Although this procedure provides the magnitude of the total response, it eliminates information on the relative timing and signs of the harmonic components. Consequently, a unique physically meaningful acceleration time history cannot be reconstructed from either the proposed formulation or the corresponding CCIP-016 procedure. Exclusively, an acceleration time history may be represented when the response is dominated by a single harmonic, as occurs under resonant excitation. In that case, the contribution of the dominant harmonic governs the total response, while the influence of the remaining harmonics is comparatively small.

Consequently, for the trials in which TS1 walked at $f_p = 2$Hz, the comparison between the measured and non-resonant responses predicted using the CCIP-016 and proposed harmonic load models is limited to the peak acceleration and the maximum one-second running RMS acceleration. In contrast, the comparison of resonant responses evaluated using CCIP-016 and proposed load models includes the full time histories, as well as the corresponding peak and maximum one-second running RMS accelerations.

8.3.1.1 Verification of non-resonant response

Table 8.3 summarises and Figure 8.10 illustrates the peak acceleration and maximum one-second running RMS acceleration predicted using the proposed and CCIP-016 load models with the corresponding experimental responses for WP1 and WP2, respectively. As described in Section 4.2, TS1 walked along each of the WPs in two directions, D1 and D2 (Figure 8.9*a*), resulting in two measured responses for each path. For WP1, the CCIP-016 peak and maximum running RMS accelerations exceed the corresponding predictions of the proposed model by approximately 16.6% and 6%, respectively. For WP2, the CCIP-016 predicted 5% lower peak and 14.9% higher maximum running RMS accelerations. This confirms the generally more conservative character of the CCIP-016 load mentioned in Section 8.1.

Furthermore, the numerical results show generally better agreement with the measurements obtained in direction D1 than with those obtained in direction D2. For WP1D1, the proposed model underestimates the measured peak acceleration by 0.65%, while overestimating the maximum running RMS acceleration by 19.3%. The corresponding CCIP-016 predictions exceed the measured values by 15.9% and 26.5%, respectively. For WP2D1, the proposed model overestimates the measured peak acceleration by 14.9% and the maximum running RMS acceleration by 13.6%, whereas CCIP-016 overestimates these quantities by 9.1% and 30.5%, respectively. Thus, the proposed model provides the closer overall agreement with response level measured in direction D1, particularly for the maximum one-second running RMS acceleration.

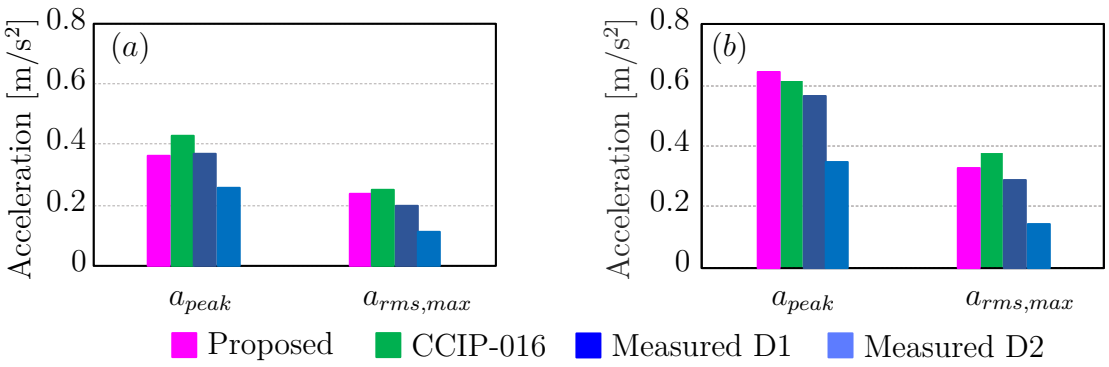

Figure 8.10: Comparison of the measured peak and maximum one-second running RMS acceleration with those predicted using the CCIP-016 and proposed load models for TS1 walking at $f_p = 2$Hz along WP1 (a) and WP2 (b).

Table 8.3: Comparison of peak and maximum one-second running RMS acceleration values obtained using the proposed model, CCIP-016 and experimental measurements for TS1 walking at $f_p = 2$Hz.

	WP1		**WP2**	
Response	a_{peak} [m/s^2]	$a_{rms,max}$ [m/s^2]	a_{peak} [m/s^2]	$a_{rms,max}$ [m/s^2]
Proposed model	0.3652	0.2383	0.6456	0.3273
CCIP-016	0.4260	0.2527	0.6130	0.3760
Measured – D1	0.3676	0.1997	0.5617	0.2882
Measured – D2	0.2576	0.1143	0.3502	0.1449

In contrast, the responses measured in direction D2 are substantially lower than both numerical predictions and responses measured in direction D1. For WP1D2, the proposed model exceeds the measured peak and maximum running RMS accelerations by approximately 41.8% and 108.5%, respectively, while the corresponding CCIP-016 overestimations are 65.4% and 121.1%. Even larger discrepancies are obtained for WP2D2, for which the proposed model exceeds the measured values by 84.4% and 125.9%, whereas CCIP-016 exceeds them by 75.0% and 159.5%.

Additional verification of the predicted responses is carried out using two sets of calculated responses obtained from: (i) 10,000 proposed probabilistic walking-force signals generated following Algorithm 4, with the mean walking frequency fixed at 2Hz, and (ii) 76 measured walking-force signals with mean walking frequencies within the range 2 ± 0.04Hz. Since the mean pedestrian weight in the database is 757N, the calculated probabilistic responses are scaled to the weight of TS1 (480N) to ensure comparability. For each response, the maximum one-second running RMS acceleration is evaluated, and the resulting cumulative distributions for both WPs are presented in Figure 8.11.

Note that a slight difference can be observed between the CDFs obtained using the measured forces and the proposed probabilistic model, where measured forces produced somewhat larger responses. This discrepancy is attributed to the contribution of the third mode, with a natural frequency of 14.67Hz. For the measured walking-force signals within the range 2 ± 0.04Hz, the seventh harmonic may fall close to this frequency, producing a third-mode response comparable to that of the first mode. On the other hand, the proposed harmonic model includes only the first six harmonics and therefore, for a walking frequency of 2Hz, cannot reproduce excitation in the vicinity of 14.67Hz.

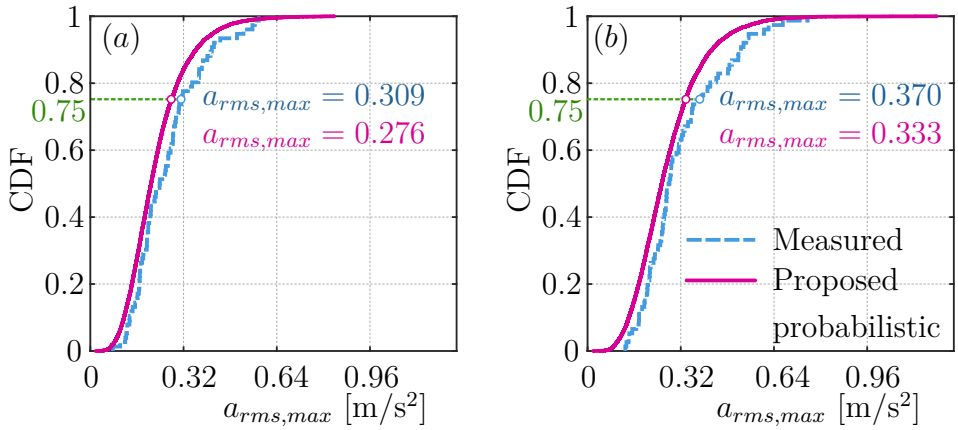

Figure 8.11: CDFs of the maximum one-second running RMS acceleration obtained using 76 measured walking-force signals and the proposed probabilistic formulation, for a pedestrian walking at $f_p = 2$Hz along WP1 (a) and WP2 (b).

In addition, Figure 8.11 highlights the $a_{rms,max}$ values corresponding to a CDF of 0.75, allowing direct comparison with the results presented in Table 8.3. For WP1, the proposed simplified model underestimates $a_{rms,max}$ due to measured-forces by 23.9% and due to the proposed probabilistic formulation by 13.7%. The corresponding underestimations obtained using CCIP-016 are 18.2% and 8.6%, respectively. For WP2, the proposed simplified model underestimates the measured-force and proposed probabilistic results by 11.5% and 1.7%, respectively. In contrast, CCIP-016 slightly overestimates the measured-force results by 1.6% and the proposed probabilistic results by 12.9%. Generally, the proposed simplified model consistently underestimates the reference responses. At first glance, CCIP-016 appears to show closer agreement with the responses obtained using the measured forces. However, it should be noted that CCIP-016 is also unable to capture the response contribution of the third mode due to its four-harmonic force representation, and its higher predicted responses therefore result primarily from the more conservative DLF values adopted in the model.

Finally, the measured responses obtained for a TS1 walking along the two WPs in directions D1 and D2 are located in the lower part of the corresponding CDFs. For WP1, the two measured responses correspond approximately to the 39th percentile for D1 and the 4th percentile for D2. Similarly, for WP2, they correspond to approximately the 58th percentile for D1 and the 5th percentile for D2. These percentile levels would be even lower if the difference between the TS's weight and the mean pedestrian weight adopted in the probabilistic analysis were taken into account. Overall, available experimental results, comprising only two WPs and one TS walking at a single pacing rate, are insufficient to provide a robust validation of the proposed model across a representative range of walking conditions. A more comprehensive validation is therefore required, based on an expanded database of measured structural responses that includes a larger number of TSs and a broader range of prescribed pacing rates. Such a dataset would allow the predictive capability and general applicability of the proposed model to be assessed more reliably.

8.3.1.2 Verification of resonant response and VSA of the floor

Figure 8.12 presents the resonant acceleration responses for WP1 and WP2 obtained using the proposed and CCIP-016 harmonic load models, while peak and maximum one-second running RMS accelerations are summarised in Table 8.4. For both WPs, CCIP-016 and proposed

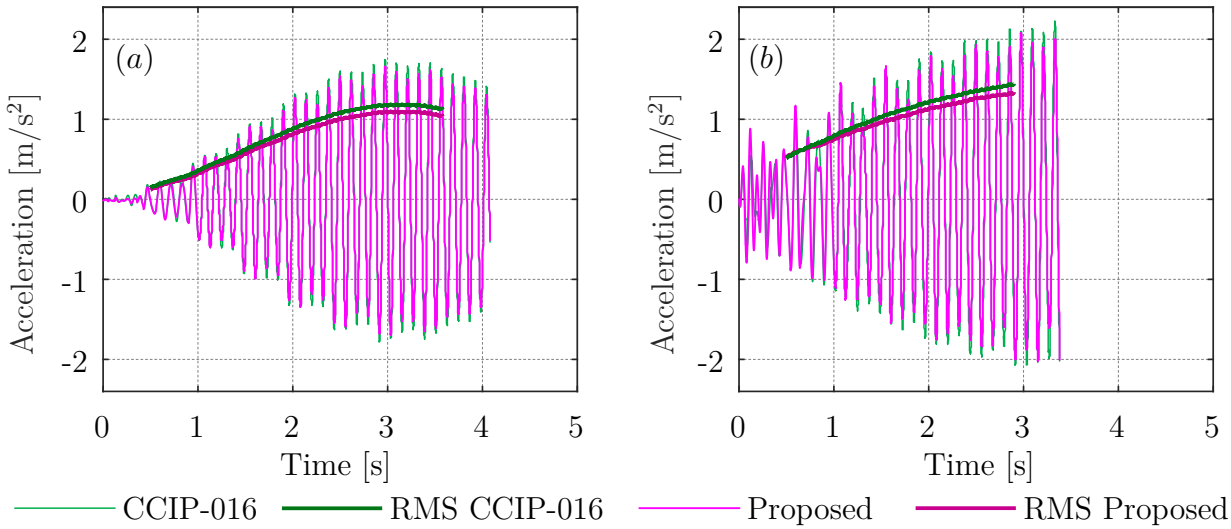

Figure 8.12: Comparison of the acceleration time histories with corresponding one-second running RMS obtained using the CCIP-016 and proposed load models for pedestrian walking at $f_p = 2.1$Hz along WP1 (a) and WP2 (b).

model predict similar resonant response levels. For WP1, the CCIP-016 a_{peak} and $a_{rms,max}$ are approximately 6.6% and 7.3% higher, respectively, than those obtained using the proposed model. Similar differences are observed for WP2, where the corresponding CCIP-016 predictions are approximately 7.2% and 7.8% higher. Both models predict a more severe response for WP2, where a_{peak} and $a_{rms,max}$ are approximately 25% and 22% higher than those obtained for WP1.

Table 8.4: Comparison of peak and maximum one-second running RMS acceleration values of resonant response obtained using the proposed model and CCIP-016.

	WP1		**WP2**	
Response	a_{peak} [m/s^2]	$a_{rms,max}$ [m/s^2]	a_{peak} [m/s^2]	$a_{rms,max}$ [m/s^2]
Proposed model	1.6698	1.1032	2.0758	1.3384
CCIP-016	1.7800	1.1842	2.2250	1.4429

Figure 8.13 illustrates the CDFs of the maximum one-second running RMS acceleration responses obtained from: (i) 10,000 probabilistic walking-force signals generated using the proposed model following Algorithm 4, with the mean walking frequency fixed at 2.1Hz, and (ii) 63 measured walking-force signals with mean walking frequencies within the range 2.1 ± 0.042Hz. Since the deterministic resonant response was previously calculated using a pedestrian weight of 750N, no additional scaling of the probabilistic response was required. As in the case of the non-resonant response, a difference is observed between the CDFs obtained using the measured forces and the proposed probabilistic model, attributed to the contribution of the third mode to the total response.

The proposed simplified model yields approximately 16.5% higher $a_{rms,max}$ values than the proposed probabilistic model at a CDF of 0.75 for both WPs. Compared to the responses obtained using measured forces, the simplified model gives a 0.8% lower value for WP1 and a 9.2% higher value for WP2. The discrepancies are larger for CCIP-016, which overestimates the proposed probabilistic results by approximately 25% for both WPs, and the measured-force results by 6.5% for WP1 and 17.7% for WP2. Overall, the comparison supports the use of the proposed simplified model for deterministic resonant response calculation in routine

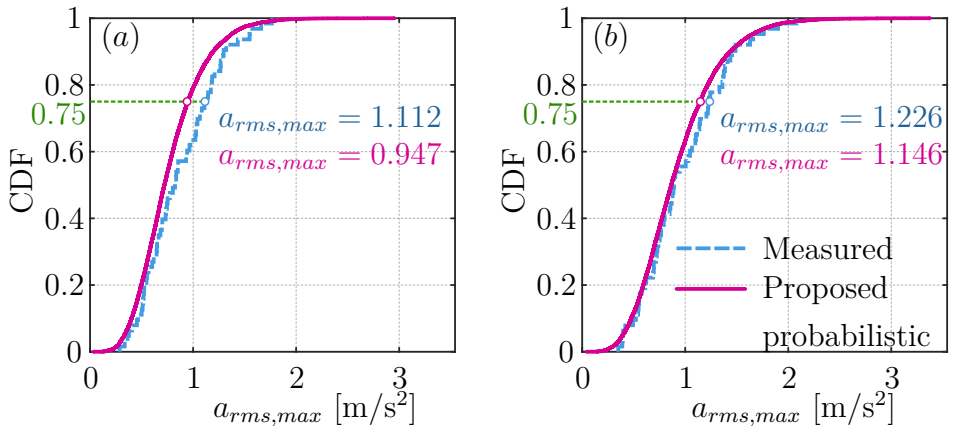

Figure 8.13: CDFs of the maximum one-second running RMS acceleration obtained using 76 measured walking-force signals and the proposed probabilistic formulation, for a pedestrian walking at $f_p = 2.1$Hz along WP1 (a) and WP2 (b).

engineering practice. Although some discrepancies relative to the probabilistic and measured-force responses remain, the simplified model generally reproduces the resonant response level with acceptable accuracy.

The corresponding R factors, calculated in accordance with CCIP-016 by assuming that the response is dominated by the fourth walking harmonic at 8.4Hz, are summarised in Table 8.5. The simplified proposed model yields R=224.4 for WP1 and R=278.9 for WP2, whereas CCIP-016 gives higher values of 239.2 and 299.0, respectively. These R factors are exceptionally high and indicate an unacceptable vibration response for the analysed bare CLT floor under the assumed resonant excitation. However, they should not be regarded as representative of a completed floor system. In practice, additional floor layers, finishes and other non-structural components increase the total and modal masses and damping, thereby inevitably reducing the resulting acceleration response. Although such non-structural components introduce additional uncertainty into the prediction of the vibration response, their effects are not considered in this dissertation. Accordingly, the interpretation of the results will focus on the influence of uncertainty on the predicted response (Chapter 9), rather than on evaluating the vibration serviceability of the floor for a specific occupancy or use.

Table 8.5: Comparison of resonant R factors obtained using the proposed model and CCIP-016.

R factor	**WP1**	**WP2**
Proposed model	224.4	278.9
CCIP-016	239.2	299.0

8.3.2 High-frequency floors

Figure 8.14 presents the velocity responses obtained for WP1 and WP2 using the proposed and CCIP-016 effective impulse models, while the corresponding peak velocities v_{peak} and the maximum one-second running RMS velocities $v_{\text{rms,max}}$ are summarised in Table 8.6. For each load model, values of v_{peak} and $v_{\text{rms,max}}$ obtained for the WP2 are around 9% higher than values obtained for WP1. For WP1, the maximum response occurs when the pedestrian steps near the centre of the floor, where the amplitude of the dominant mode shape reaches 1, as shown

in Figure 8.14*a*. In contrast, WP2 follows a region along which the mode-shape amplitude remains approximately equal to 1 over the entire path (Figure 5.22). Consequently, successive footfalls generate peaks of comparatively magnitude throughout the crossing, as illustrated in Figure 8.14*b*.

Table 8.6: Comparison of peak and maximum one-second running RMS velocity values of transient response obtained using the proposed model and CCIP-016.

	WP1		**WP2**	
Response	v_{peak} [m/s]	$v_{rms,max}$ [m/s]	v_{peak} [m/s]	$v_{rms,max}$ [m/s]
Proposed model	0.0042	0.0012	0.0046	0.0013
CCIP-016	0.0046	0.0013	0.0050	0.0014

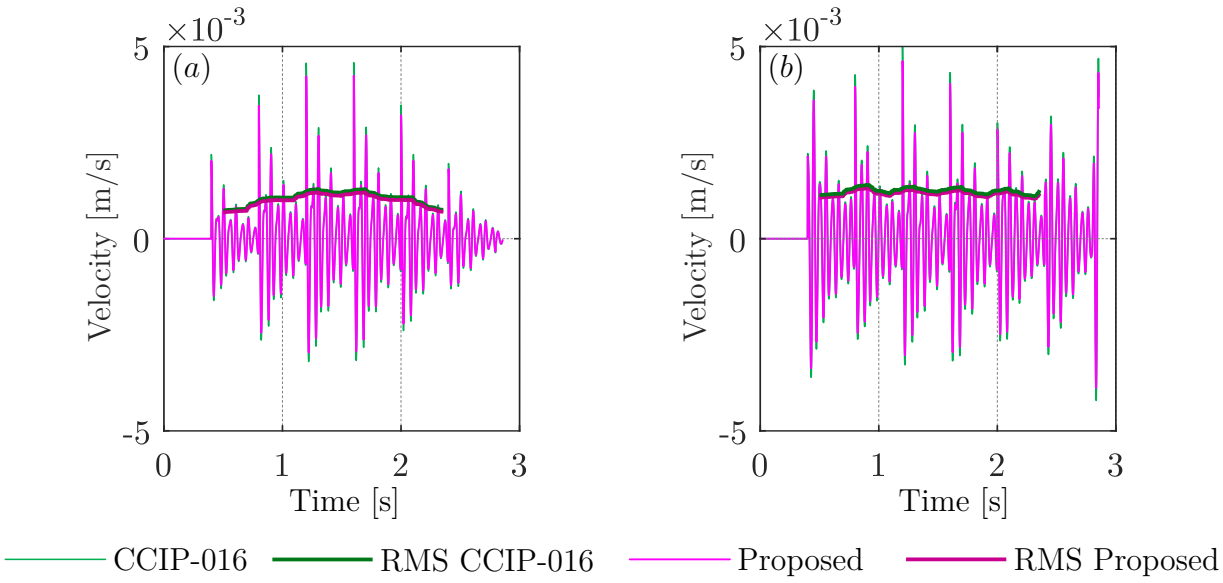

Figure 8.14: Comparison of the velocity time histories with corresponding one-second running RMS obtained using the CCIP-016 and proposed load models for pedestrian walking at $f_p = 2.1$Hz along WP1 (*a*) and WP2 (*b*).

As observed in Section 8.1, at higher walking frequencies and for a floor natural frequency of approximately 20Hz, the CCIP-016 and proposed formulations yield similar effective impulse values (Figure 8.2) and, consequently, similar response predictions. Specifically, the peak velocity predicted using CCIP-016 is approximately 9% higher, while the maximum one-second running RMS velocity is approximately 8% higher than the corresponding values obtained using the proposed effective impulse model.

Figure 8.15 illustrates the CDFs of the maximum one-second running RMS velocity responses obtained from: (i) 10,000 series of probabilistic effective impulses generated following Algorithm 5, with the mean walking frequency fixed at 2.5Hz, and (ii) 31 measured walking-force signals with mean walking frequencies within the range 2.5±0.125Hz. The CDFs obtained using the proposed probabilistic model and the measured forces agree closely. At the 75th percentile, the proposed probabilistic model yields approximately 5% and 6% higher values of $v_{rms,max}$ than the measured forces for WP1 and WP2, respectively. In contrast, both the proposed simplified model and CCIP-016 yield lower responses. For both WPs, the proposed simplified model gives approximately 23% lower $v_{rms,max}$ value than the measured-force value and 27% lower than the corresponding probabilistic-model value. The CCIP-016 value of 0.0013m/s is approximately 17% and 21% lower than the measured-force and probabilistic-model values, respectively, for

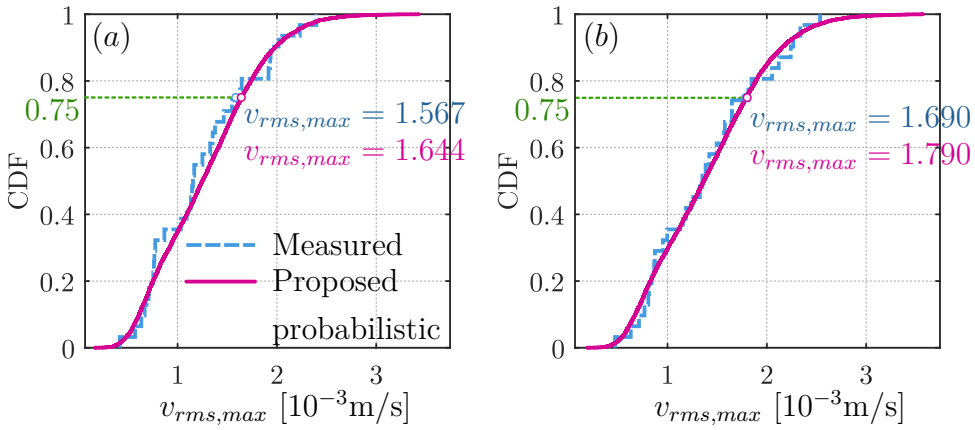

Figure 8.15: CDFs of the maximum one-second running RMS acceleration obtained using 31 measured walking-force signals and the proposed probabilistic formulation, for a pedestrian walking at $f_p = 2.5$Hz along WP1 (a) and WP2 (b).

both WPs. This trend is somewhat anticipated, as both the proposed simplified model and CCIP-016 were previously shown to underestimate the effective impulse values obtained from the measured-force database at higher walking frequencies, across the entire range of structural natural frequencies considered (see Figure 8.2).

The corresponding R factors, calculated in accordance with CCIP-016, are summarised in Table 8.7. The proposed model yields R=12.0 for WP1 and R=13.0 for WP2, whereas CCIP-016 predicts a higher values of R=13.0 and R=14.0 for WP1 and WP2, respectively. These values are substantially lower than those obtained previously for the LFF and lie considerably closer to the limiting value of R=8, specified for continuous vibrations in workshops [89]. Nevertheless, the calculated R factors should not be interpreted as representative of the vibration serviceability of a floor system, since the additional mass and possible damping contribution of non-structural components are not included in the analysis.

Table 8.7: Comparison of R factors obtained using the proposed model and CCIP-016.

R factor	**WP1**	**WP2**
Proposed model	12.0	13.0
CCIP-016	13.0	14.0

8.4 Chapter summary

This chapter presented the implementation of the simplified walking-load models developed in Chapter 7 within the deterministic VSA framework recommended in CCIP-016 for LFFs and HFFs subjected to pedestrian walking. The CCIP-016 procedure was adopted as the basis of the assessment because it provides a comprehensive modal-analysis-based framework that can be readily combined with numerical floor models. The proposed walking-load models were incorporated into this framework while preserving its main advantages and established analysis principles.

The complete procedure for response calculation was implemented in Hindu, a Python-based application with a user-friendly GUI. The software enables the import of numerical or experi-

mental modal properties, selection of vibration modes and load models, definition of walking paths (WPs) and receiver locations, calculation and visualisation of displacement, velocity and acceleration responses. Unlike the conventional stationary-force assumption, Hindu models the pedestrian moving along a prescribed WP, thereby accounting directly for the spatial variation of modal amplitudes and eliminating the need for the corresponding reduction factor. The available outputs include total response histories, one-second running RMS responses and spatial distributions of maximum response quantities. The current version of Hindu represents an initial stage of software development and provides considerable scope for further improvement and extension. Future developments may include the implementation of a module for calculating floor modal properties directly within the software, as well as support for importing modal data from a wider range of FE software packages. The existing deterministic VSA framework could also be extended by incorporating probabilistic analysis as well.

The verification of the deterministic vibration response predictions was carried out for the LFF and HFF developed in Section 5.4, using both the original CCIP-016 and the simplified load models proposed in Chapter 7. The resulting responses were compared with two sets of probabilistic responses calculated for the same floors while keeping the modal properties fixed, i.e. deterministic. The former was obtained from 10,000 realisations generated using the proposed probabilistic load models developed in Chapter 7, while the latter was obtained using measured walking-force signals. In both cases, the mean walking frequency was fixed at the same values as those used in the deterministic analyses: 2.0Hz and 2.1Hz for the non-resonant and resonant responses of the LFF, respectively, and 2.5Hz for the HFF. In addition, the non-resonant response of the LFF was compared with the available experimental measurements.

For the non-resonant LFF case, the proposed simplified model underestimated the maximum one-second running RMS acceleration ($a_{rms,max}$) obtained using the proposed probabilistic formulation at a CDF of 0.75 by 13.7% for WP1 and only 1.7% for WP2. The corresponding CCIP-016 predictions were 8.6% lower and 12.9% higher, respectively. Relative to the responses obtained using measured force signals, the proposed model underestimated $a_{rms,max}$ by 23.9% for WP1 and 11.5% for WP2, whereas CCIP-016 underestimated it by 18.2% for WP1 and slightly overestimated it by 1.6% for WP2. Comparison with the available experimental measurements showed generally reasonable agreement with one set of measured responses, while substantially overestimating the other.

For the resonant LFF case at $f_p = 2.1$Hz, the proposed and CCIP-016 models predict comparable response levels for both WPs. Relative to the proposed probabilistic formulation at a CDF of 0.75, the proposed simplified model overestimates $a_{rms,max}$ by approximately 16.5% for both WPs, while CCIP-016 overestimates it by about 25%. Compared with measured-force responses, the corresponding differences are -0.8% and $+9.2\%$ for the proposed model and $+6.5\%$ and $+17.7\%$ for CCIP-016. The resulting R factors are nevertheless exceptionally high, indicating unacceptable vibration levels for the analysed bare CLT floor, although these values are expected to decrease in a completed floor system due to the additional mass and damping provided by non-structural components.

For the HFF case, the proposed and CCIP-016 effective impulse models produced relatively close deterministic response levels, with CCIP-016 predicting approximately 8% higher maximum one-second running RMS velocities. However, comparison with the probabilistic and measured-force responses showed that both deterministic approaches underestimate $v_{rms,max}$ at the 75th percentile: the proposed simplified model by approximately 23% relative to the measured forces and 27% relative to the probabilistic model, and CCIP-016 by about 17% and 21%, respectively. The corresponding R factors are substantially lower than those obtained for the LFF, although

they should not be interpreted as representative of a completed floor system because the effects of non-structural mass and damping are not included.

Overall, for the floors considered in this study, the proposed simplified load models provided vibration response predictions of a similar order and accuracy to those obtained using CCIP-016. However, the proposed formulations offer greater flexibility and a broader range of applicability than the corresponding CCIP-016 load models. In particular, the harmonic load model enables resonant excitation to be represented for floor frequencies up to 15Hz, while the effective impulse model can account for a wider range of damping ratios. In addition, both models allow the load magnitude to be selected at different percentile levels of the corresponding probability distributions, providing flexibility in defining the load level used in the assessment. These features give the proposed models considerable potential to overcome some of the limitations of the CCIP-016 formulations while retaining the simplicity required for routine engineering application. Nevertheless, comprehensive experimental validation across a broader range of floor systems and response conditions is required to confirm these advantages and establish the reliability of the proposed models in practical applications.

9 Uncertainty analysis of vibration response of CLT floors

This chapter presents the final phase of the research conducted in this dissertation in which the vibration response of CLT floors due to pedestrian load is evaluated while accounting for uncertainties associated with both the structure and the walking load. While these two sources of uncertainty were investigated separately in the preceding chapters, they are integrated here to quantify their combined influence on the predicted vibration response of both LFF and HFF. For LFF, both non-resonant and resonant responses are considered. In the non-resonant case, the mean walking frequency is sampled according to its prescribed probability distribution, independently of the fundamental frequency of the floor. In the resonant case, the mean walking frequency is selected in each simulation such that resonance with the floor is achieved. For each considered response case, uncertainty quantification (UQ) and Shapley effect-based sensitivity analysis (SA) are performed for two representations of walking-load variability: one accounting for both intra- and inter-subject variability, and the other accounting only for inter-subject variability. Explicitly accounting for intra-subject variability is not practical in routine engineering applications and the comparison aims to determine the extent to which it affects the predicted vibration response and whether its consideration is necessary for practical VSA.

The uncertainty analysis of the floor modal properties presented in Chapter 6 demonstrated that their variability is governed predominantly by three structural parameters: timber density ρ, longitudinal modulus of elasticity E_L and shear modulus G_{LT}. Consequently, only these were retained in the reduced metamodel representation of the floor. Additionally, the modal damping ratio ζ represents the fourth uncertain structural parameter. Due to the limited availability of experimental data suitable for defining the joint probabilistic model of these four structural parameters, their marginal distributions and statistical properties were adopted from the literature. In the absence of sufficient information regarding their correlations, they were assumed to be statistically uncorrelated, meaning their correlation coefficients were set to zero.

The probabilistic walking-load models developed in Chapter 7 are used to represent the uncertainty associated with pedestrian excitation. The probabilistic harmonic load model is governed by 15 random parameters (Section 7.2.5), whereas the probabilistic effective impulse model is governed by five (Section 7.3.5). For both models, the probability distributions, statistical properties and mutual correlations of the load parameters were derived from the database of 744 continuously measured walking-force records [40]. The complete set of structural (Chapter 6, Table 6.2) and walking-load random variables (Chapter 7, Tables 7.1 and 7.5) considered in the present analysis is summarised in Tables 9.1 and 9.2.

Table 9.1: Distributions of parameters for vibration response analysis of LFF.

			Distribution properties	
Force parameter	**Label**	**Type**	**Parameter 1**	**Parameter 2**
CLT floor structure				
Timber density	ρ	Normal	424	42.40
Elasticity modulus	E_L	Normal	11084.34	1662.65
Shear modulus	G_{LT}	Normal	630.72	94.61
Damping	ζ	Normal	1.04	0.208
Harmonic load model				
Body weight	G	Normal	757	151.55
Mean f_p	μ_{f_p}	Normal	1.900	0.266
St. dev. f_p	σ_{f_p}	Lognormal	−3.137	0.341
Mean DLF_1	μ_{DLF_1}	Beta	2.720	7.725
St. dev. DLF_1	σ_{DLF_1}	Lognormal	−4.074	0.394
Mean DLF_2	μ_{DLF_2}	Lognormal	−2.981	0.497
St. dev. DLF_2	σ_{DLF_2}	Lognormal	−4.021	0.316
Mean DLF_3	μ_{DLF_3}	Gamma	8.650	0.006
St. dev. DLF_3	σ_{DLF_3}	Lognormal	−4.333	0.247
Mean DLF_4	μ_{DLF_4}	Beta	9.704	200.368
St. dev. DLF_4	σ_{DLF_4}	Lognormal	−4.668	0.297
Mean DLF_5	μ_{DLF_5}	Beta	4.404	131.927
St. dev. DLF_5	σ_{DLF_5}	Lognormal	−4.992	0.309
Mean DLF_6	μ_{DLF_6}	Lognormal	−4.001	0.608
St. dev. DLF_6	σ_{DLF_6}	Lognormal	−5.264	0.334

Table 9.2: Distributions of parameters for vibration response analysis of HFF.

			Distribution properties	
Force parameter	**Label**	**Type**	**Parameter 1**	**Parameter 2**
CLT floor structure				
Timber density	ρ	Normal	424	42.40
Elasticity modulus	E_L	Normal	11084.34	1662.65
Shear modulus	G_{LT}	Normal	630.72	94.61
Damping	ζ	Normal	3	0.6
Effective impulse load model				
Body weight	G	Normal	757	151.55
Mean f_p	μ_{f_p}	Normal	1.900	0.266
St. dev. f_p	σ_{f_p}	Beta	4.567	42.993
Mean I_{eff}	$\mu_{I_{\text{eff}}}$	Lognormal	Table 7.4	Table 7.4
St. dev. I_{eff}	$\sigma_{I_{\text{eff}}}$	Lognormal	Table 7.4	Table 7.4

The proposed load models involve an additional source of variability associated with the temporal correlation of load parameters between successive steps. This variability is introduced by the autoregressive (AR) coefficients for walking frequency and DLFs in the harmonic load model (Eq. (7.2)), and for walking frequency and effective impulse in the impulse load model (Eqs. (7.12) and (7.13)). Each AR(1) formulation also contains a random noise term, ε_t. As a result, the AR(1)-based load models are stochastic, meaning that repeated simulations performed with the same vector of input parameters would produce different load histories and, consequently, different structural responses. The load model therefore introduces an additional residual variance associated with its internal stochasticity, which must be considered in the uncertainty analysis.

Taking all these uncertainties into account, the vibration response caused by a pedestrian moving along the two WPs defined in Chapter 8 and illustrated in Figure 8.9 was evaluated. The natural frequencies and modal masses required for the response calculations were generated using the refined Polynomial Chaos Expansion metamodels developed in Sections 6.2.4 and 6.3.4, whereas the mode shapes were treated as deterministic. Uncertainty quantification (UQ) and sensitivity analysis (SA) were performed for both the LFF and HFF models developed in Section 5.4. UQ was conducted using 10,000 MC simulations, providing probabilistic descriptions of the resulting vibration responses. The relative contributions of the structural and walking-load parameters to the response variability were evaluated using the Shapley effects described in Subsection 3.2.2. Shapley effect calculation was performed following the Algorithm 3, which is governed by the parameters N_I, N_O and m. In accordance with the recommendations of Song et al. [126], $N_I = 3$ and $N_O = 1$ were adopted, while the number of random permutations m was selected to achieve satisfactory accuracy of the Shapley indices while minimising the computational cost.

Particular attention was devoted to distinguishing the contributions of intra-subject and inter-subject variability in pedestrian loading. The initial UQ and SA therefore included all uncertain load parameters. The analyses were subsequently repeated after excluding the parameters governing intra-subject, or step-to-step, variability. Comparison of the two sets of results enabled the contribution of intra-subject variability to the overall uncertainty in the vibration response to be evaluated. This distinction is particularly useful because intra-subject variability is considerably more difficult to characterise and model than inter-subject variability.

In the first section of this chapter (Section 9.1), the contribution of the internal stochastic variability of the AR(1) proposed load models to the response variance is evaluated. The chapter then presents convergence study aimed at determining the minimum value of m for which the estimated Shapley effects are sufficiently stable (Section 9.2). The UQ and SA results for the LFF and HFF are presented in Sections 9.3 and 9.4, respectively. The deterministic response predictions obtained using CCIP-016 and the proposed simplified load models in Section 8.3 are evaluated against the corresponding probabilistic responses for both floor types. Additionally, the available experimental results from the walking tests presented in Section 4.2 are compared with the probabilistic response predictions for the LFF.

9.1 Internal stochastic variability of AR(1) load models

The formulation of the Shapley effects assumes that the model output is fully determined once all input variables are fixed. Accordingly, the cost function $c(\mathcal{J})$, which quantifies the

contribution of a set of uncertain input variables $\mathcal{J}$ to the output variance, satisfies

$$c(\emptyset) = 0, \tag{9.1}$$

as discussed in Section 3.2.2. In other words, if none of the explicitly defined input variables is allowed to vary, no output variance remains.

This assumption is not directly applicable to the proposed harmonic and effective-impulse load models. Both models use an AR(1) formulation to represent step-to-step variations in the walking load. Therefore, even when all explicitly sampled structural and pedestrian parameters collected in the input vector $\mathbf{X}$ are kept fixed, repeated simulations do not produce exactly the same walking-load history and vibration response. This remaining variability is caused by the random quantities generated internally by the AR(1) model, namely the AR coefficients and the random terms ε_t.

To account for this additional source of variability, the initial Shapley cost was defined as

$$c(\emptyset) = \mathrm{E}_{\mathbf{X}}\left[\mathrm{Var}\left[Y \mid \mathbf{X}\right)\right], \tag{9.2}$$

where Y denotes the considered vibration-response quantity, such as $a_{rms,max}$ and $v_{rms,max}$. In other words, $c(\emptyset)$ represents the average response variance that remains when all explicitly considered input variables are fixed and only the internal random components of the AR(1) load model are allowed to vary. $c(\emptyset)$ was evaluated separately for each response case, including the LFF and HFF responses for both WPs, using a nested MC procedure.

First, $n_{\mathbf{X}_0}$ different samples of the input vector $\mathbf{X}$ were generated. Each sample, denoted by $\mathbf{X}_0$, represents one fixed combination of structural and load parameters. For each $\mathbf{X}_0$, the response analysis was then repeated $n_{\mathbf{X}_I}$ times. During these repeated calculations, all components of $\mathbf{X}_0$ remained unchanged, while only the internally generated AR(1) quantities were resampled. The variance of the $n_{\mathbf{X}_I}$ responses therefore represents the internal response variance associated with that particular input combination,

$$\mathrm{Var}\left[Y \mid \mathbf{X}_0\right]. \tag{9.3}$$

The same procedure was repeated for all $n_{\mathbf{X}_0}$ input combinations, and the resulting conditional variances were averaged to obtain $c(\emptyset)$.

Convergence was examined with respect to both levels of the nested simulation: the number of repeated AR(1) realisations for each fixed input vector $n_{\mathbf{X}_I}$ and the number of different input vectors $n_{\mathbf{X}_0}$. Increasing $n_{\mathbf{X}_I}$ from 100 to 1000 produced negligible changes in the estimated $c(\emptyset)$, indicating that $n_{\mathbf{X}_I} = 100$ was sufficient. A larger number of outer samples was required because the magnitude of the internal response variance varied considerably between different input combinations. Based on the convergence study, $n_{\mathbf{X}_0} = 2000$ was adopted for the final estimation of $c(\emptyset)$.

Finally, the values of $c(\emptyset)$, representing the internal stochastic variability of the AR(1) load models, are presented together with the remaining results of uncertainty analysis for the LFF and HFF responses in Sections 9.3 and 9.4, respectively.

9.2 Convergence study of Shapley effects

The computational cost of the adopted Shapley-effect estimator increases rapidly with the number of random perturbations m, requiring $mN_IN_O(d-1)$ model evaluations for each analysis, where $N_I = 3$, $N_O = 1$ and d represents the number of uncertain input parameters.

The convergence study was carried out for the LFF subjected to walking along WP1, as this case involves the largest number of uncertain inputs: four structural and 15 force parameters, giving a total of 19 random variables (Table 9.1). The value of m established through this analysis was subsequently adopted for the HFF SA, although the HFF response is governed by a considerably smaller set of nine random variables (Table 9.2).

Therefore, for the considered case with $d = 19$, the procedure requires $54 \cdot m$ model evaluations, corresponding to approximately $1.62 \cdot 10^6$ evaluations for $m = 30{,}000$. To examine convergence, m was varied from 1,000 to 50,000. After the initial values of 1,000 and 5,000, m was increased in increments of 5,000, i.e. 10,000, 15,000, and so on, up to 50,000. The normalised Shapley effects for the considered case obtained for each value of m are presented in Figure 9.1.

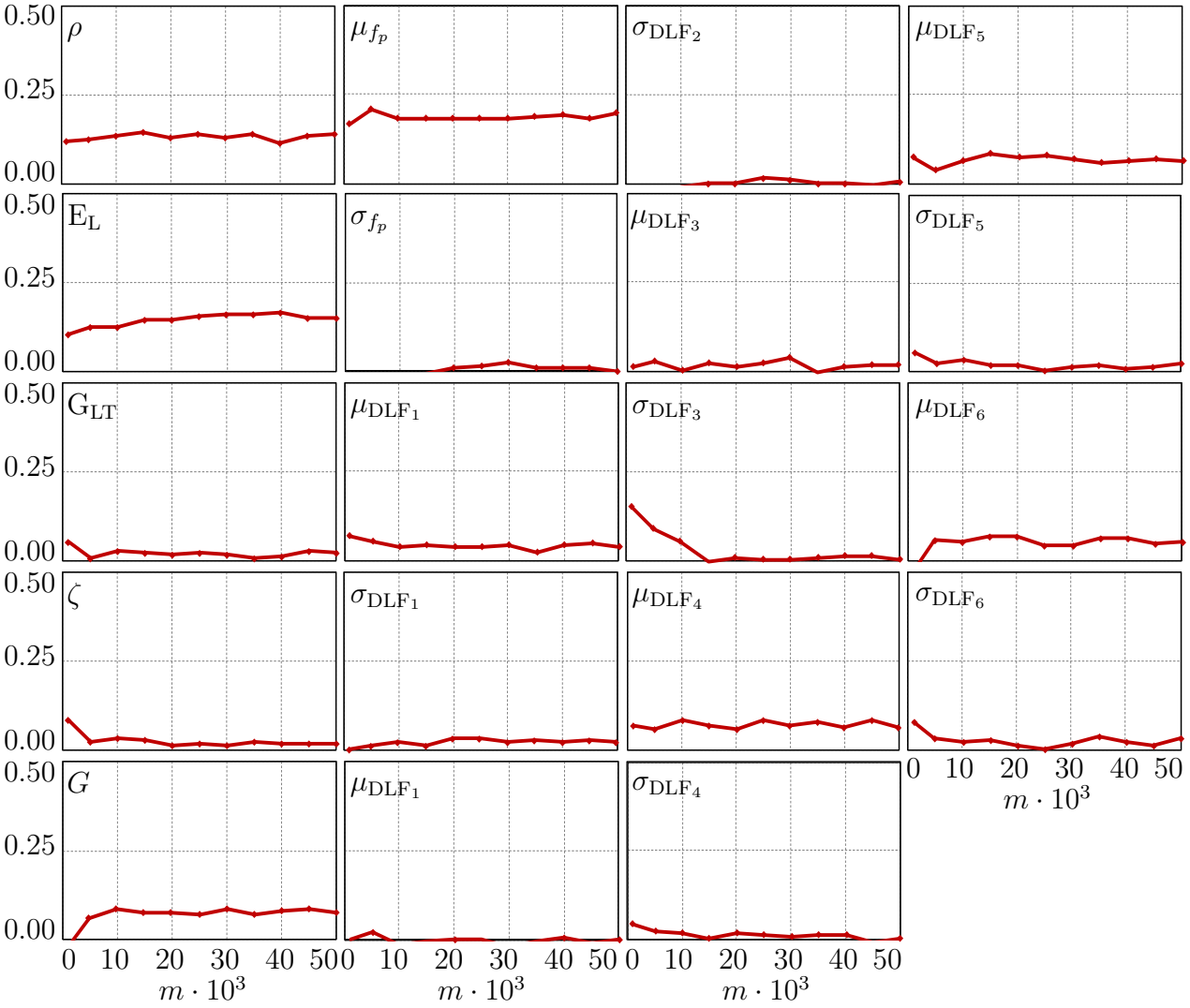

Figure 9.1: Normalised Shapley effects convergence with increasing number of permutations m

For sample sizes smaller than $m = 15{,}000$, the estimated normalised Shapley effects show relatively large point-to-point variations. As m increases, these variations become progressively

smaller, and from approximately $m = 25{,}000$ onward most estimates fluctuate within a comparatively narrow range. Some residual oscillations remain, particularly for parameters with low Shapley effects. Additionally, occasional slightly negative estimates are obtained. Since Shapley effects are theoretically non-negative, such negative values are attributed to MC sampling error. As increasing m beyond approximately $25{,}000 - 30{,}000$ provides only limited improvement in the overall stability of the estimates, $m = 30{,}000$ was adopted for the final analysis as a compromise between convergence and computational cost.

9.3 Low-frequency floor

For the uncertainty analysis of the LFF response, two sets of vibration-response simulations were performed, hereafter referred to as the non-resonant and resonant cases. In the non-resonant case, the walking frequency was treated as an uncertain input parameter and sampled from its corresponding probability distribution (Table 9.1). Consequently, resonance occurred occasionally and unintentionally for particular combinations of the timber material parameters and walking frequency. This case is intended to demonstrate that resonance has a relatively low probability of occurrence in reality. In the resonant case, by contrast, the mean walking frequency was not considered uncertain. It was adjusted in each simulation to induce resonance with an appropriate harmonic of the walking load. Depending on the fundamental frequency of the floor, the lowest harmonic order that resulted in a walking frequency within the realistic range of $1.5 - 2.5$Hz was selected. The aim of the resonant-response case was to analyse the uncertainty in the predicted resonant vibration amplitudes arising from variability in all input parameters except f_p.

The influence of intra-subject variability was examined separately. In this context, two sets of vibration response calculations were performed for both non-resonant and resonant cases. The first set included both intra- and inter-subject variability (i.e. total variability) of the harmonic force. In the second set, intra-subject variability was excluded by removing the parameters that define it, namely the standard deviations of the walking frequency and DLFs (σ_{f_p} and $\sigma_{\mathrm{DLF}_{1-6}}$).

Overall, these cases result in four different uncertainty analyses for LFF response, presented in the following subsections. The quantity of interest was defined as the maximum one-second running RMS acceleration $a_{rms,max}$, evaluated for both WPs in the receiver point (Figure 8.9). For all cases, four candidate probability distributions were fitted to the data (lognormal, Weibull, inverse Gaussian and exponential), and the best-fitting distribution was selected using the K-S goodness-of-the-fit test [180].

9.3.1 Uncertainty analysis of non-resonant response considering total load variability

The UQ results for the non-resonant response, considering the total variability of the walking load, are presented in Figure 9.2. The results include the empirical PDFs and CDFs obtained from 10,000 MC simulations for WP1 and WP2, together with the corresponding best-fit distributions. For both WPs, the non-resonant response is best represented by a lognormal distribution. Figure 9.2 also presents the mean values of $a_{rms,max}$ and their corresponding standard deviations. The mean response obtained for WP2 is approximately 20% higher than that for

WP1, accompanied by an approximately 14.5% increase in standard deviation. Nevertheless, the corresponding COV is slightly lower for WP2 (73.4%) than for WP1 (77.0%).

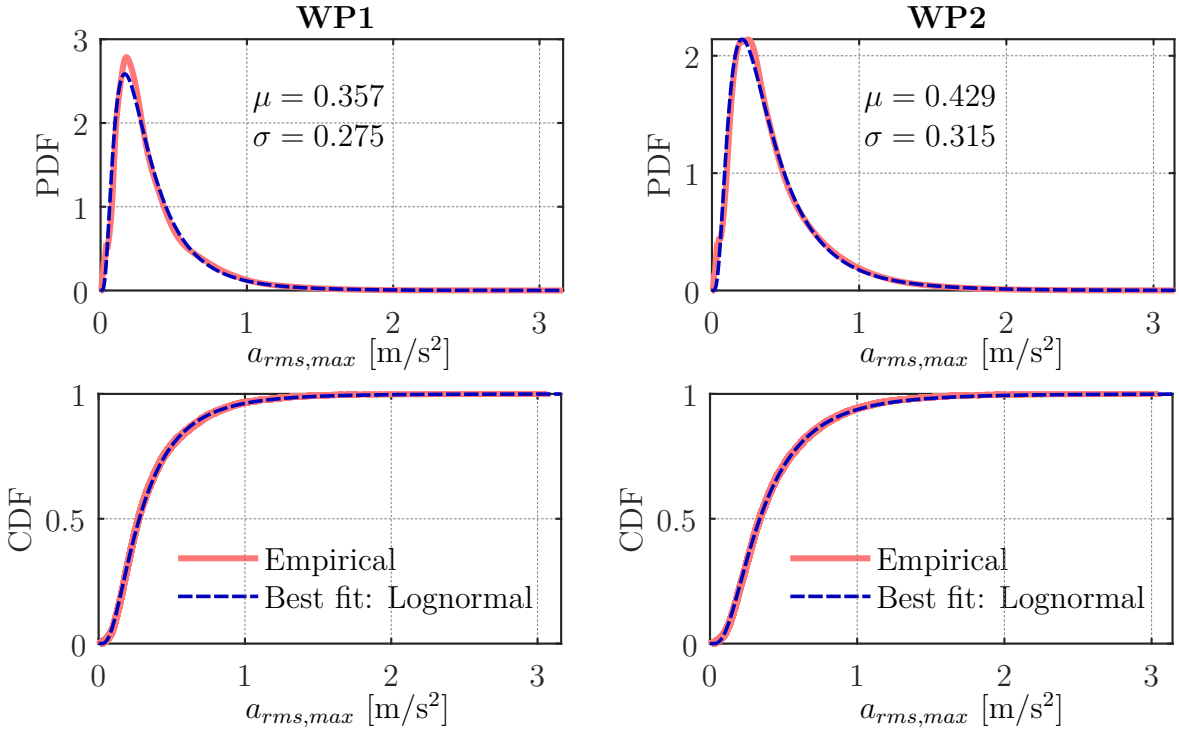

Figure 9.2: Empirical and best-fit distribution of non-resonant $a_{rms,max}$ considering total variability for WP1 and WP2.

Distributions for both WPs are characterised by a long right tail, indicating that a relatively small number of simulations produce vibration responses substantially higher than the corresponding mean values. These high-response realisations are associated with the occurrence of resonance, arising from particular combinations of the uncertain input parameters for which the natural frequency of the floor approaches one of the harmonics of the walking frequency.

As shown in Figure 9.3, the largest response amplitudes are concentrated within relatively narrow regions where the floor fundamental-to-walking frequency ratio f_1/f_p approaches an integer value, with the most pronounced peaks occurring around the fourth and fifth harmonics and a less pronounced peak around the sixth harmonic. Third-harmonic resonance also produces elevated responses, but is only sparsely represented in Figure 9.3, since the combination of structural and walking parameters required to obtain $f_1/f_p \approx 3$ is relatively rare. Only 83 out of 10,000 MC realisations (0.83%) fall within the range $2.9 \leq f_1/f_p \leq 3.1$, compared with 1008 realisations (10.1%) within $3.9 \leq f_1/f_p \leq 4.1$. Outside these resonance regions, the response amplitudes are generally considerably lower. However, a relatively broad scatter of elevated responses is observed between the third and fourth harmonics. For these realisations, the walking frequency is approximately 2.45Hz, placing its sixth harmonic at approximately 14.7Hz, within the frequency range of the third mode. Therefore, these responses are associated with resonance of the third mode rather than the first mode. Since the horizontal axis is expressed in terms of f_1/f_p, resonance involving the third mode does not occur at a fixed integer value on this axis and therefore appears as a broader scatter of elevated responses.

The near-resonant response can be defined to occur when the ratio f_1/f_p lies within ± 0.05 of an integer value corresponding to the third to sixth harmonics (i.e. 3, 4, 5, or 6) [161]. Of the 10,000 Monte Carlo simulations, 969 realisations (9.69%) satisfy this criterion. When responses

associated with resonance of the third vibration mode are also included, approximately 10% of all realisations may be classified as resonant or near-resonant.

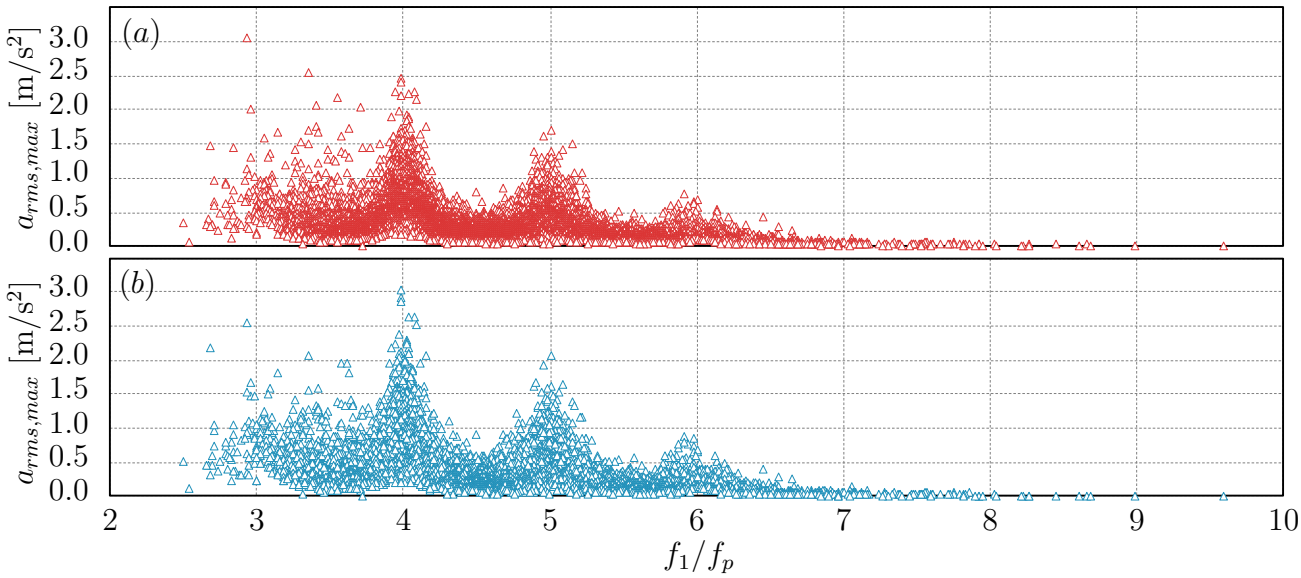

Figure 9.3: Calculated $a_{rms,max}$ as a function of the floor fundamental-to-walking frequency ratio f_1/f_p for WP1 (a) and WP2 (b).

Figure 9.4 illustrates the CDFs of the non-resonant responses obtained for the two WPs. Furthermore, the experimentally measured responses of the two TSs walking freely along both

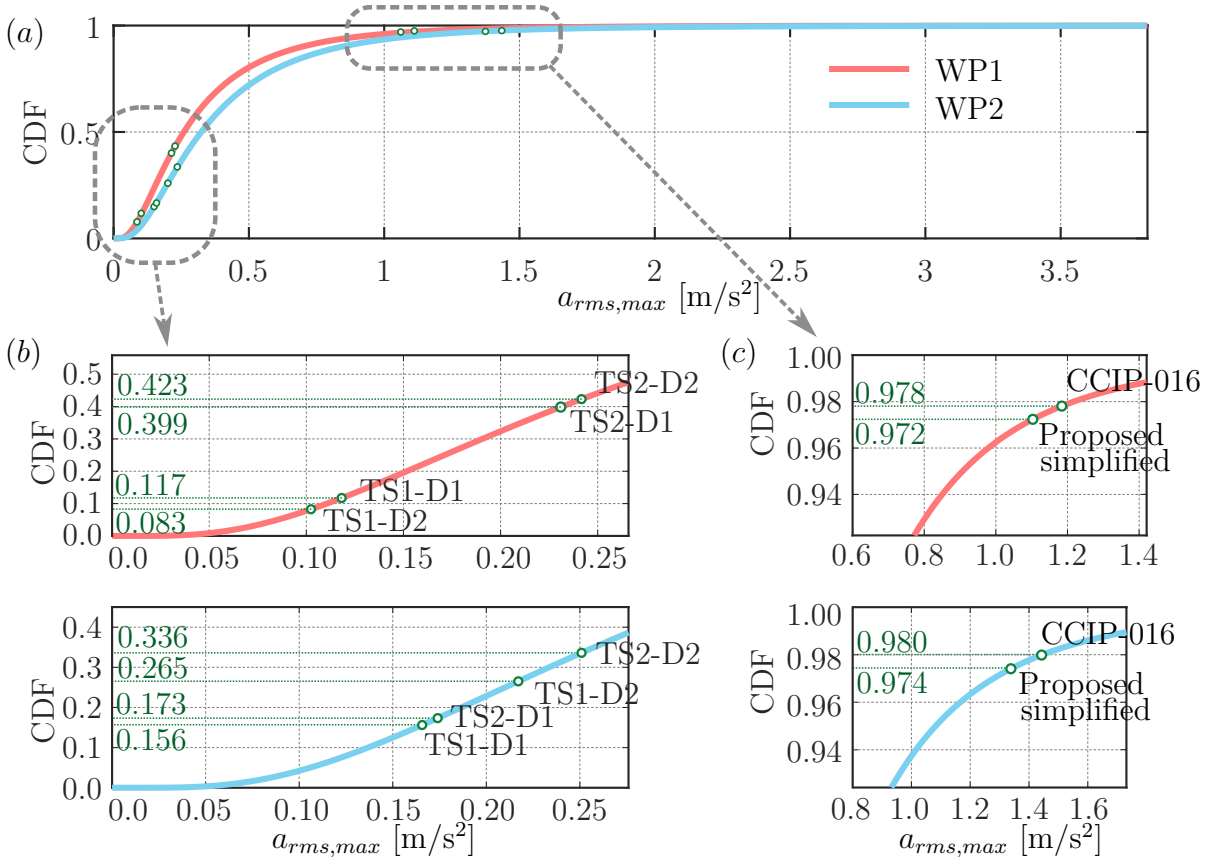

Figure 9.4: CDFs of non-resonant $a_{rms,max}$ considering total variability for WP1 and WP2 (a), with experimentally measured responses (b) and resonant responses obtained deterministically using CCIP-016 and the proposed simplified load model (c).

WPs (Table 4.3) are superimposed on the corresponding CDFs in Figure 9.4*b*. For both TSs, the measured values of $a_{rms,max}$ fall within the lower portion of the corresponding distributions. This is particularly evident for TS1 walking along WP1, for which the measured responses lie within the lowest 12% of the distribution. None of the walking tests produced a response exceeding the corresponding mean value. The measured response closest to the mean value was obtained for TS2 walking along WP1-D2, corresponding to a CDF value of 0.423. One possible explanation for the generally low measured responses is the relatively low body weight of both TSs compared with the average value adopted in the probabilistic model. Assuming a linear relationship between pedestrian weight and response amplitude, scaling the measured responses to the mean pedestrian weight of 757N would increase $a_{rms,max}$ by approximately 50%, shifting the measured values towards higher cumulative probabilities within the corresponding distributions.

In contrast, the deterministic responses obtained using CCIP-016 and the proposed simplified load model in Section 8.3 are located in the upper tails of the distributions (Figure 9.4*c*). The responses predicted by the proposed simplified model correspond to CDF values of approximately 0.972 and 0.974 for WP1 and WP2, respectively, while the CCIP-016 predictions correspond to approximately 0.978 and 0.980. Although 10% of all calculated responses can be cathegorised as resonant or near-resonant, both CCIP-016 and proposed simplified load models yield response levels within the highest 3% of the distribution.

The results of the SA, expressed in terms of normalised Shapley effects $\widehat{Sh}_i$ for the 19 uncertain input parameters together with the contribution of the internal stochasticity of the AR(1) load model, are presented in Figure 9.5. The contribution of the internal AR(1) variability amounts to approximately 8% for WP1 and 6.5% for WP2. Compared with WP2, WP1 exhibits a slightly greater contribution from the structural parameters and a slightly smaller contribution from the mean values and standard deviations of the higher-order harmonics. However, these differences remain relatively small, not exceeding 1.5 percentage points. Overall, the relative importance of the uncertain inputs is therefore consistent between the two WPs, indicating that the choice of WP has only a limited influence on the sensitivity ranking.

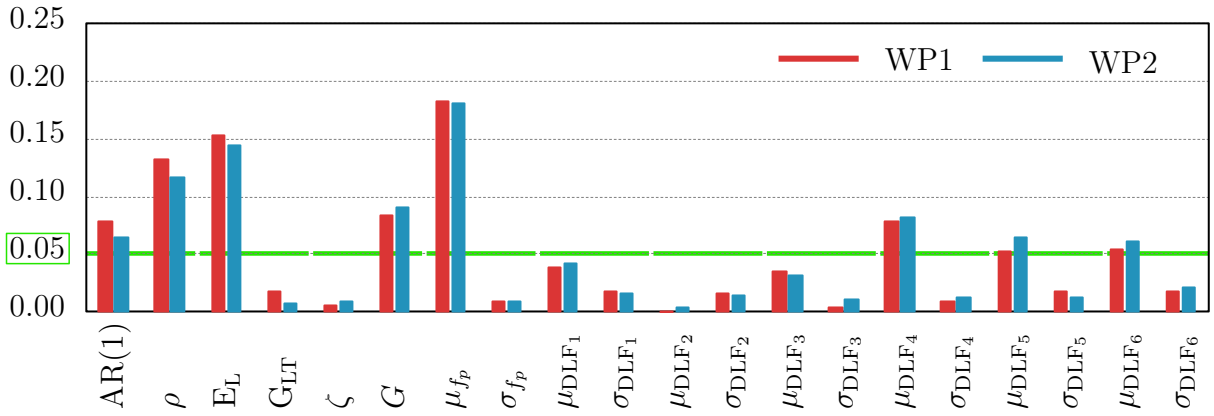

Figure 9.5: Internal AR(1) model variability and normalised Shapley effects of the 19 uncertain input parameters for the non-resonant responses along WP1 and WP2.

There is currently no general consensus regarding the ranking of Shapley effects or the threshold below which a normalised Shapley effect can be regarded as negligible. Following common practice in GSA [181], a heuristic threshold of 0.05 was therefore adopted to identify non-influential parameters.

Among the uncertain input parameters, the mean walking frequency μ_{f_p} has the largest influence on the total variance of the non-resonant $a_{rms,max}$ ($\widehat{Sh}_{f_p} = 0.18$), followed by the longitudinal modulus of elasticity E_L ($\widehat{Sh}_{E_L} = 0.15$) and timber density ρ ($\widehat{Sh}\rho = 0.13$). Particular combinations of these parameters can shift the natural frequencies of the floor such that the first or third mode approaches one of the harmonics of the walking load, thereby producing near-resonant conditions and, consequently, exceptionally high values of $a_{rms,max}$. In contrast, G_{LT} exhibits a negligible influence, with a normalised Shapley effect of 0.013. This can be attributed to the dominant contribution of the bending modes to the overall vibration response, as their natural frequencies are governed predominantly by E_L. A greater contribution of G_{LT} would be expected if a torsional mode played a more significant role in the response. Similarly, the damping ratio has a negligible influence on the non-resonant response [161].

Variability in pedestrian weight G represents another important source of response uncertainty, with $\widehat{Sh}_G = 0.09$. Among the DLF-related parameters, the significant contributions arise from variability in their mean values. The effects are most pronounced for the fourth, fifth, and sixth harmonics, with normalised Shapley effects of approximately 0.08, 0.05, and 0.06, respectively. This is consistent with the occurrence of occasional resonant or near-resonant responses associated with these harmonics, as observed in Figure 9.3. Contributions bellow the adopted threshold are obtained for μ_{DLF_3} and μ_{DLF_1}, with normalised Shapley effects of approximately 0.03 and 0.04, respectively. The relatively low influence of μ_{DLF_3} is consistent with the comparatively rare occurrence of the third-harmonic resonance (Figure 9.3). In contrast, the small contribution of μ_{DLF_1} is not associated with near-resonant amplification, but can be attributed to its correlation with other uncertain input parameters (Figure 7.18). Finally, none of the standard deviations of f_p or the DLFs has a normalised Shapley effect greater than 0.02, indicating that the individual parameters governing intra-subject variability make statistically no significant contribution to the overall variance of the vibration response.

9.3.2 Uncertainty analysis of non-resonant response considering only inter-subject load variability

The UQ analysis of the non-resonant $a_{rms,max}$ was repeated after removing all variables governing intra-subject variability, namely the standard deviations of f_p and of all six DLFs. Since intra-subject variability is no longer represented, the internal stochastic variability associated with the AR(1) load models is also eliminated. Consequently, the remaining response uncertainty arises solely from structure and inter-subject variability of the walking load. The results including the empirical and best-fit lognormal distribution PDFs and CDFs, mean values and standard deviations are presented in Figure 9.6. Pedestrian walking along WP2 resulted in a 26.4% higher mean $a_{rms,max}$ and a 13.9% lower standard deviation compared with WP1. Consequently, COV increased from 80.3% for WP1 to 89.1% for WP2.

The comparison of the mean values and standard deviations obtained when considering total walking-force variability and inter-subject variability only is presented in Figure 9.7. For WP1, excluding intra-subject variability reduced the mean response by 9.78% and increased the standard deviation by 4.66%. Consequently, the COV increased from 77.0% to 89.1%. For WP2, the mean response decreased by 5.09%, whereas the standard deviation increased by 3.61%, resulting in an increase in the COV from 73.5% to 80.3%. Overall, the exclusion of intra-subject variability therefore lead to lower mean values of non-resonant $a_{rms,max}$, but greater dispersion of the response about the mean.

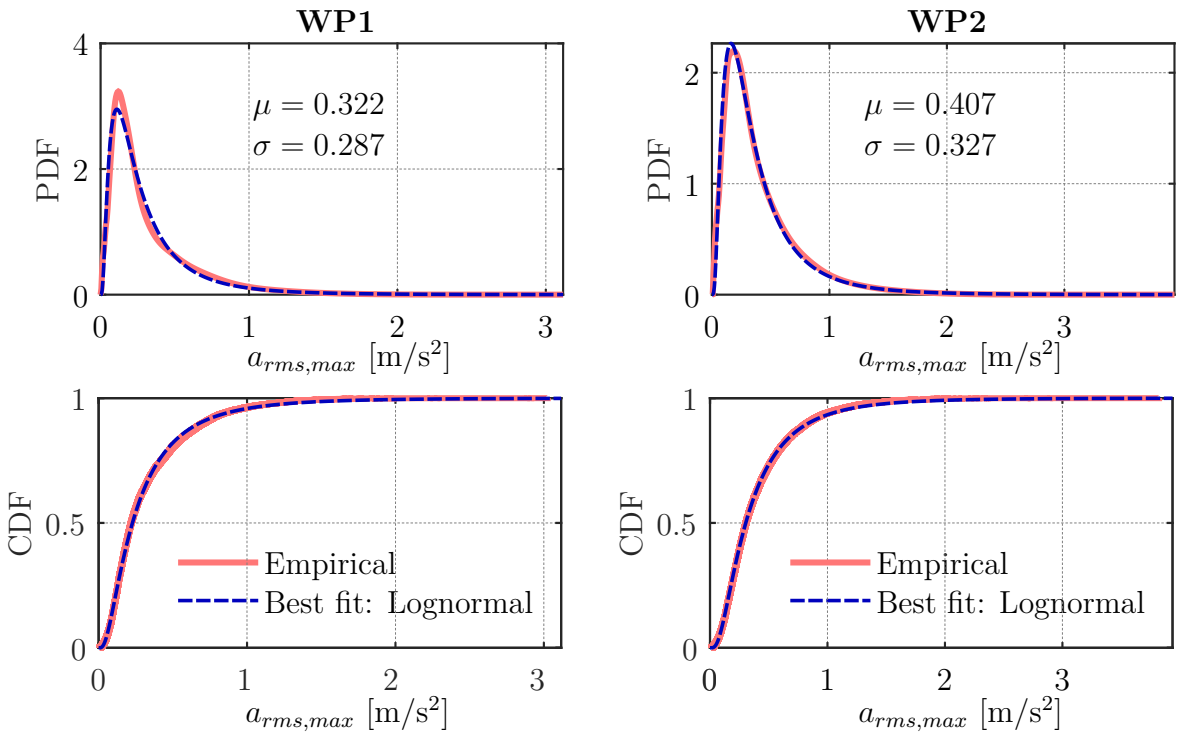

Figure 9.6: Empirical and best-fit distribution of non-resonant $a_{rms,max}$ considering only inter-subject variability for WP1 and WP2.

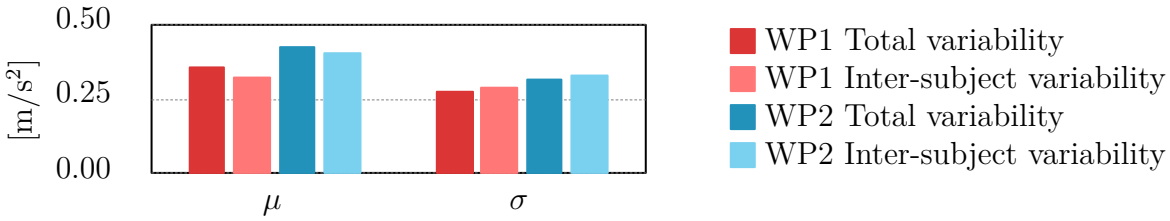

Figure 9.7: Mean values and standard deviation of non-resonant $a_{rms,max}$, considering total and inter-subject variability cases, for WP1 and WP2.

This behaviour can be attributed predominantly to the absence of step-to-step variations in walking frequency. Once the mean walking frequency is sampled, its combination with the structural parameters, and hence with the floor natural frequencies, determines whether resonant or near-resonant response occurs. If the sampled walking frequency does not produce resonant or near-resonant responses initially, the absence of intra-subject variability prevents shifts in walking frequency towards resonance, thereby limiting the mean response. Conversely, when the sampled walking frequency corresponds to resonant or near-resonant conditions, the frequency remains close to resonance throughout the walking session, without fluctuations that would move it away from the resonance and reduce the response. This produces a small number (i.e. 10%) of exceptionally high values of $a_{rms,max}$, which increase the overall dispersion and, consequently, the standard deviation of the response.

The SA was repeated after removing the standard deviations of f_p and the DLFs, leaving 12 uncertain parameters representing the structural properties and inter-subject variability of the walking load. The resulting normalised Shapley effects are presented in Figure 9.8. Overall, the trends observed for the total-variability case (Figure 9.5) are preserved. The structural parameters exhibit a slightly greater influence for WP1, whereas the parameters governing the walking-force amplitudes generally have a greater influence for WP2.

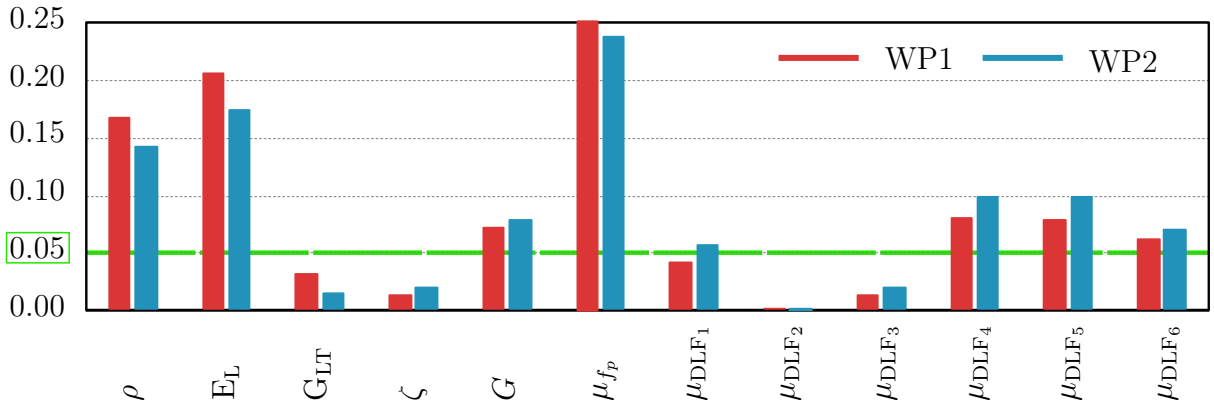

Figure 9.8: Normalised Shapley effects of the 12 uncertain input parameters for the non-resonant responses along WP1 and WP2, considering only inter-subject variability.

Since seven uncertain parameters together with the internal stochastic variability of the AR(1) models were removed, the total response variance is distributed among a smaller number of remaining inputs. Consequently, their normalised Shapley effects generally increase, with the increase being more pronounced for the parameters that were already identified as dominant in the total-variability case. For both WPs, the dominant parameters remain the mean walking frequency, timber density and longitudinal modulus of elasticity, followed by the mean DLFs associated with the fourth, fifth, and sixth harmonics. Pedestrian weight has a significant influence as well. In contrast, the mean value of DLF_1 exhibits a moderate influence, with a normalised Shapley effect of approximately 0.05, whereas G_{LT}, the damping ratio, and the mean values of DLF_2 and DLF_3 remain below the adopted threshold.

9.3.3 Uncertainty analysis of resonant response considering total load variability

The UQ results for the resonant response, considering the total variability of the walking load, are presented in Figure 9.9. The figure includes the empirical distributions obtained for both WPs together with the corresponding best-fit lognormal distributions, as well as the mean values of $a_{rms,max}$ and their standard deviations. The mean response for WP2 is approximately 20% higher than that for WP1, while the corresponding standard deviation is approximately 20.5% higher. As a result, the relative dispersion of the response remains essentially unchanged, with COVs of 44.8% for WP1 and 44.9% for WP2.

The mean resonant responses are more than twice those obtained for the non-resonant case, corresponding to an increase of approximately 119%. In contrast, the associated COVs are considerably lower, 42% for WP1 and 39% for WP2. This reduction in relative variability arises because resonant response is deliberately enforced in every simulation, thereby eliminating the variability associated with whether resonance occurs.

Figure 9.10 presents the CDFs of the resonant responses obtained for the two WPs, with the deterministic predictions based on CCIP-016 and the proposed simplified load model superimposed. Although both deterministic approaches use load amplitudes corresponding to the 75th percentile, the resulting responses are located at higher percentiles of the probabilistic response distributions. Specifically, the CCIP-016 predictions correspond to CDF values of 0.867 and 0.873 for WP1 and WP2, respectively, while the proposed simplified model yields corresponding

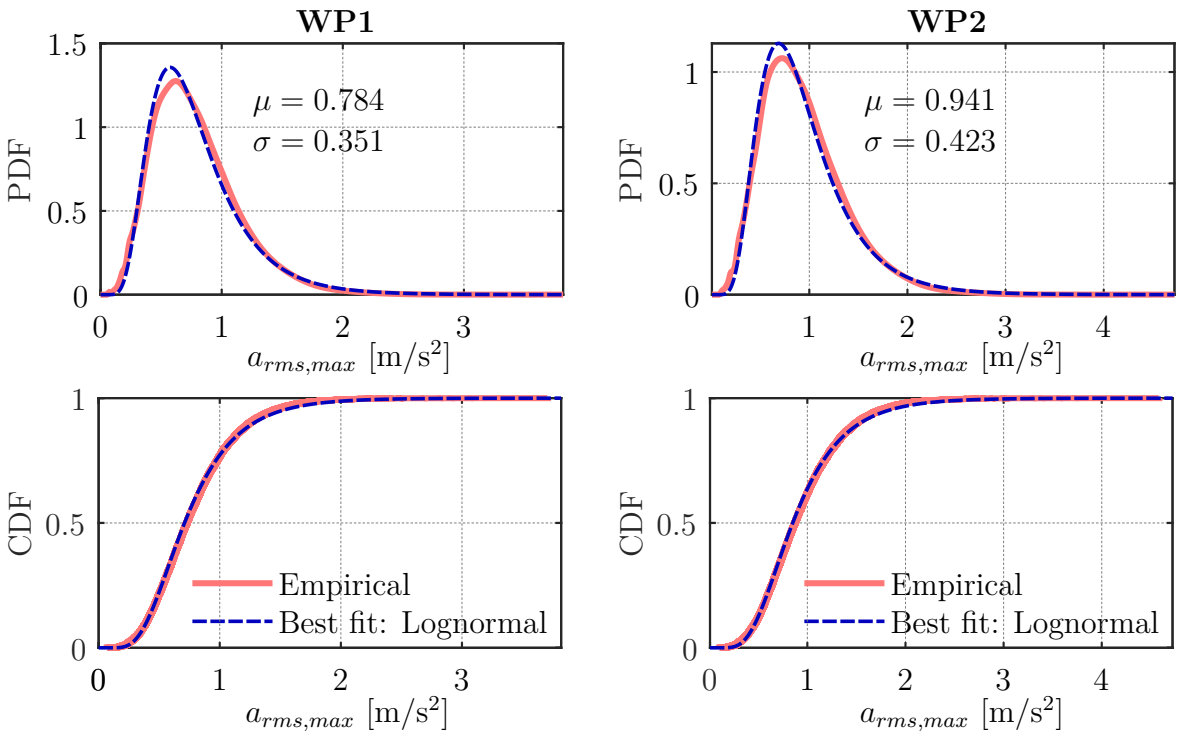

Figure 9.9: Empirical and best-fit distribution of resonant $a_{rms,max}$ considering total variability for WP1 and WP2.

values of 0.831 and 0.836. As demonstrated in Section 8.3, the deterministic responses obtained using the 75th-percentile loading already exceed the 75th percentile of the probabilistic response for the deterministic floor structure (0.9 for CCIP-016 and 0.86 for proposed simplified load model). When uncertainty in the floor properties is additionally considered, however, these predictions correspond to somewhat lower response percentiles. This means that some realisations of the structural properties lead to higher resonant responses than those obtained for the deterministic floor. This further demonstrates that the percentile assigned to the input load does not translate directly into the same percentile of the resulting vibration response.

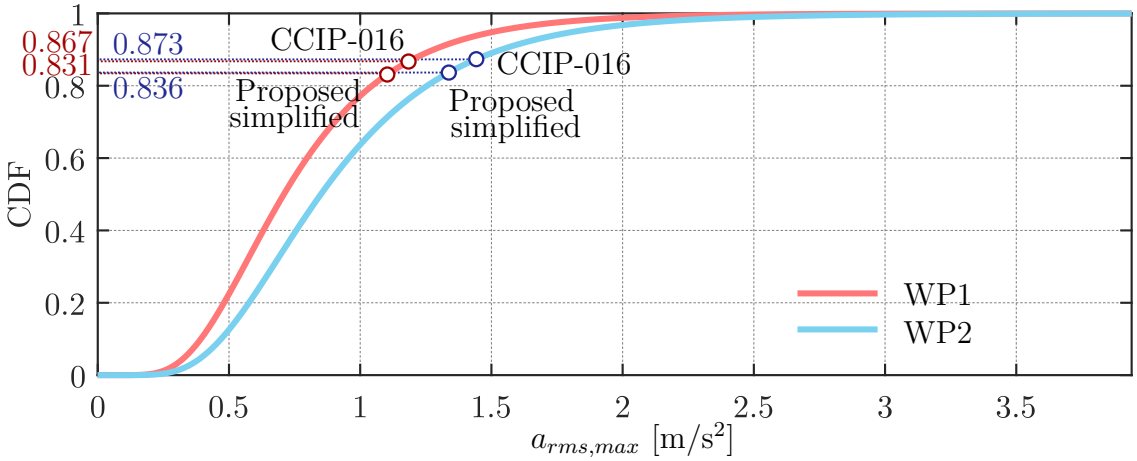

Figure 9.10: CDFs of resonant $a_{rms,max}$ considering total variability for WP1 and WP2 with resonant responses obtained deterministically using CCIP-016 and the proposed simplified load model.

The results of the SA, presented in Figure 9.11, indicate that the relative influence of the 18 uncertain input parameters is generally consistent for both WPs. The contribution of the

internal variability of the AR(1) load model is lower than that observed for the non-resonant response, accounting for approximately 6.4% and 4.4% of the total response variance for WP1 and WP2, respectively. For the resonant response, the largest contributions to the response variance arise from the parameters governing the walking-force amplitudes. Pedestrian weight is the most influential parameter, with $\widehat{Sh}_G = 0.22$, followed by the mean values of DLF_4, DLF_5, DLF_3, and DLF_6, with normalised Shapley effects of approximately 0.19, 0.11, 0.07 and 0.07, respectively. With normalised Shapley effects below 0.05, the remaining walking-load parameters exhibit a negligible influence on the response variance.

Bear in mind that the small Shapley effect of 0.025 for σ_{f_p} does not imply that step-to-step variability in pacing frequency is negligible, since the actual frequency sequence during a single walk is governed jointly by σ_{f_p}, the AR coefficient and the noise term. Rather, it indicates that uncertainty in the magnitude of σ_{f_p} itself has only a limited effect on the resonant response. Taken together, the contributions of σ_{f_p} and the internal variability of the AR(1) model indicate that step-to-step variability remains a non-negligible source of uncertainty in the resonant response.

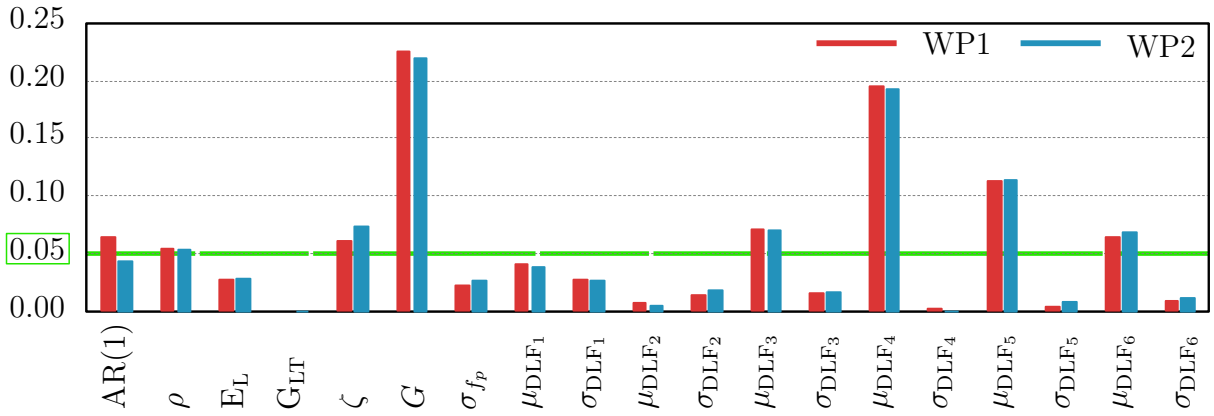

Figure 9.11: Internal AR(1) model variability and normalised Shapley effects of the 18 uncertain input parameters for the resonant responses along WP1 and WP2.

In contrast to the non-resonant response, the structural parameters have only moderate to no influence on the variability of the resonant response. Among them, the damping ratio is the most influential, with $\widehat{Sh}_\zeta = 0.07$, while the normalised Shapley effects associated with timber density and $\mathrm{E_L}$ are approximately 0.05 and 0.03, respectively.

The relatively small Shapley effect of timber density may initially appear unexpected, since the resonant acceleration is inversely proportional to the modal mass and, for the adopted deterministic mode shapes, the modal mass varies directly with timber density. Therefore, increasing the structural mass (together with increasing damping) represents one of the principal mechanisms for reducing the vibration amplitude under resonant excitation. However, the Shapley effect reflects the contribution of an uncertain input to the variability of the response, rather than its physical importance alone. The variability associated with timber density, and consequently with the modal mass, is comparatively small, with a COV of 10%. In contrast, the excitation amplitude is affected by substantially more variable parameters: pedestrian weight has a COV of approximately 15%, while the mean DLFs have COVs ranging from approximately 30% to 70%. The comparatively small contribution of timber density to the total response variance is therefore consistent with its lower relative uncertainty, despite its direct influence on the resonant response amplitude.

9.3.4 Uncertainty analysis of resonant response considering only inter-subject load variability

The UQ analysis of the resonant $a_{ms,max}$ was repeated after removing all variables governing intra-subject variability, namely the standard deviations of f_p and of all six DLFs. The resulting distributions are presented in Figure 9.6. For both WPs, the resonant $a_{rms,max}$ is best represented by a lognormal distribution. Both the mean response and the corresponding standard deviation for WP2 are approximately 21.3% higher than those obtained for WP1, resulting in the same COV of 43.6% for both WPs.

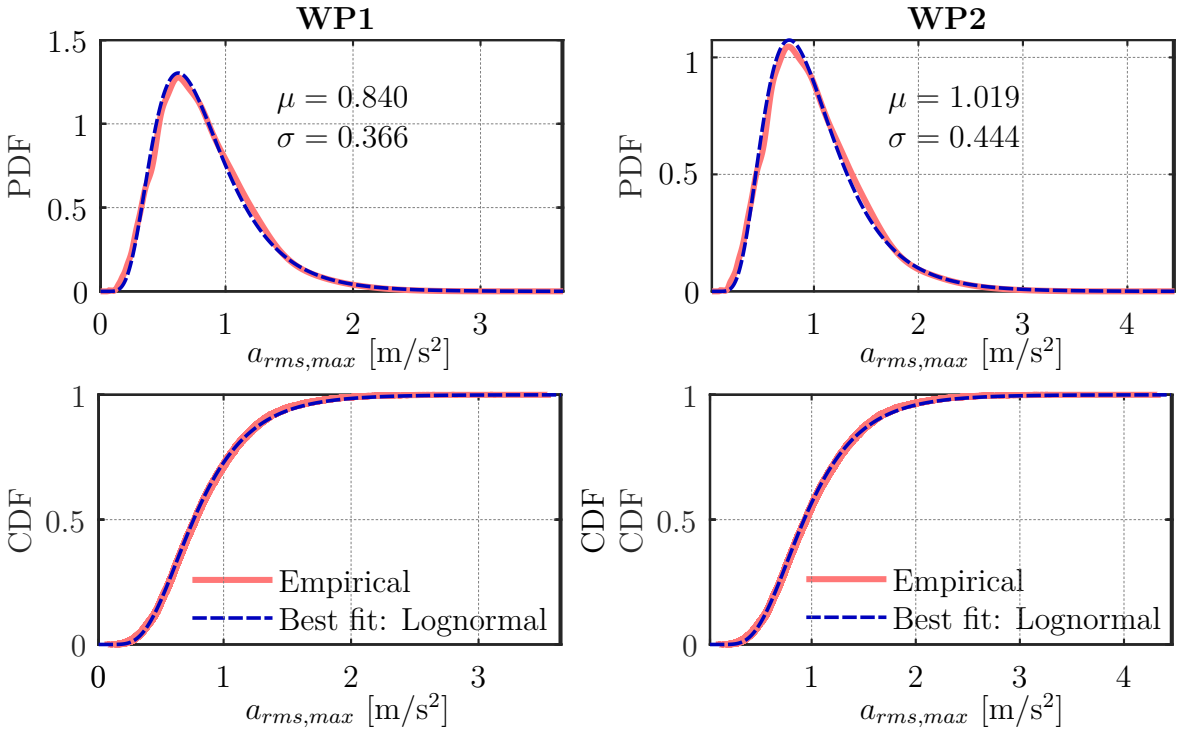

Figure 9.12: Empirical and best-fit distribution of resonant $a_{rms,max}$ considering only inter-subject variability for WP1 and WP2.

Removing the parameters governing intra-subject variability results in mean responses that are 7.12% and 8.26% higher for WP1 and WP2, respectively (Figure 9.13). The corresponding standard deviations increase by 4.41% and 5.03%, while the COVs decrease by approximately 3% relative to the total-variability case. This behaviour can be attributed primarily to the intra-subject variability of the walking frequency. When resonance is imposed, the mean walking frequency is selected to induce the resonant response. However, within-session fluctuations in f_p temporarily shift the excitation away from exact resonance, thereby reducing the resulting response. Once these fluctuations are removed, the walking frequency remains at the resonant

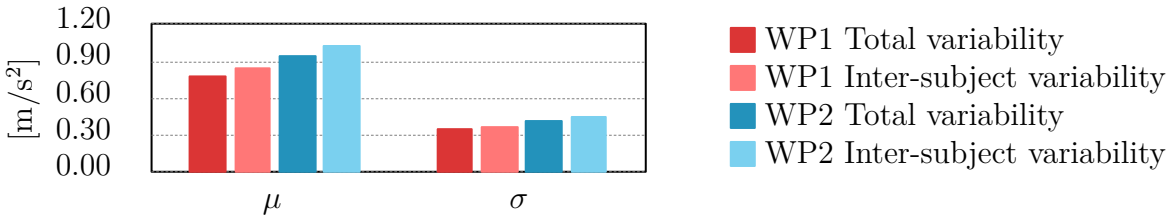

Figure 9.13: Mean values and standard deviation of resonant $a_{rms,max}$, considering total and inter-subject variability cases, for WP1 and WP2.

value throughout the simulation, leading to higher mean response amplitudes. At the same time, maintaining resonance throughout the walking session leads to greater differences between individual response realisations and, consequently, a higher standard deviation. Since the increase in the mean is greater than the increase in the standard deviation, the resulting COV is slightly lower.

Figures 9.14 and 9.15 illustrate the effect of excluding the parameters governing intra-subject variability on the PDFs and CDFs, respectively, for both the non-resonant and resonant responses. A small, but notable shift of the distributions is observed when only inter-subject variability is considered. For the non-resonant response, the distributions shift towards lower response amplitudes, reflecting the reduction in the mean value. In contrast, the resonant-response distributions shift towards higher amplitudes, consistent with the increase in the mean response. From the perspective of VSA, neglecting intra-subject variability is not conservative for the non-resonant response. However, the resonant response is relevant for the floor design, and in this case the exclusion of intra-subject variability results in more conservative response predictions and is therefore acceptable.

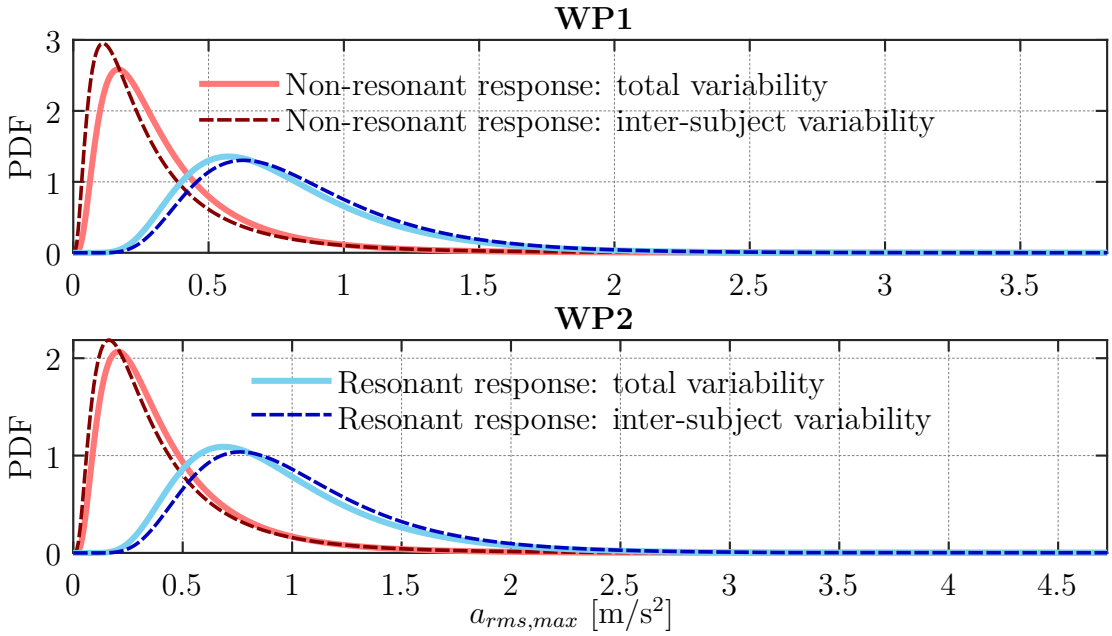

Figure 9.14: PDFs of non-resonant and resonant $a_{rms,max}$ considering total and inter-subject variability cases for WP1 and WP2.

Finally, the SA results for the resonant response considering only inter-subject variability (Figure 9.16) are fully consistent with those obtained when total load variability is considered (Figure 9.11). The relative importance and ranking of the uncertain parameters remain essentially unchanged, while the corresponding normalised Shapley effects are higher because the total response variance is distributed among a smaller number of uncertain inputs.

9.4 High-frequency floor

The uncertainty of the HFF transient response is governed by the nine uncertain parameters listed in Table 9.2. However, two of the walking-load parameters, namely the mean value and standard deviation of I_{eff}, require special treatment because their probability distributions

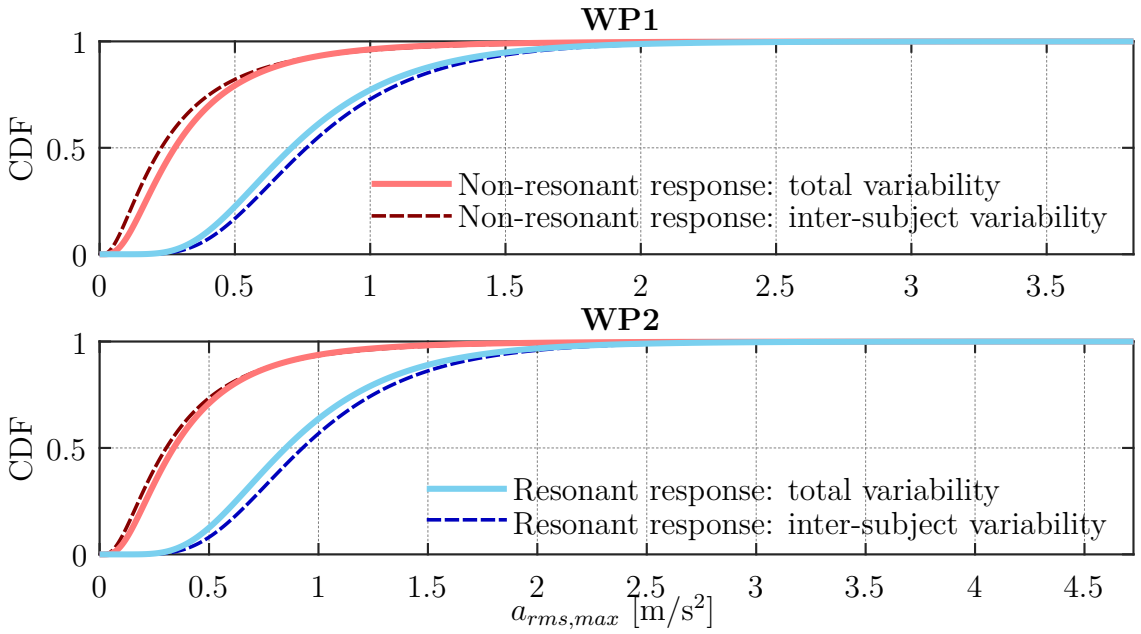

Figure 9.15: CDFs of non-resonant and resonant $a_{rms,max}$ considering total and inter-subject variability cases, for WP1 and WP2.

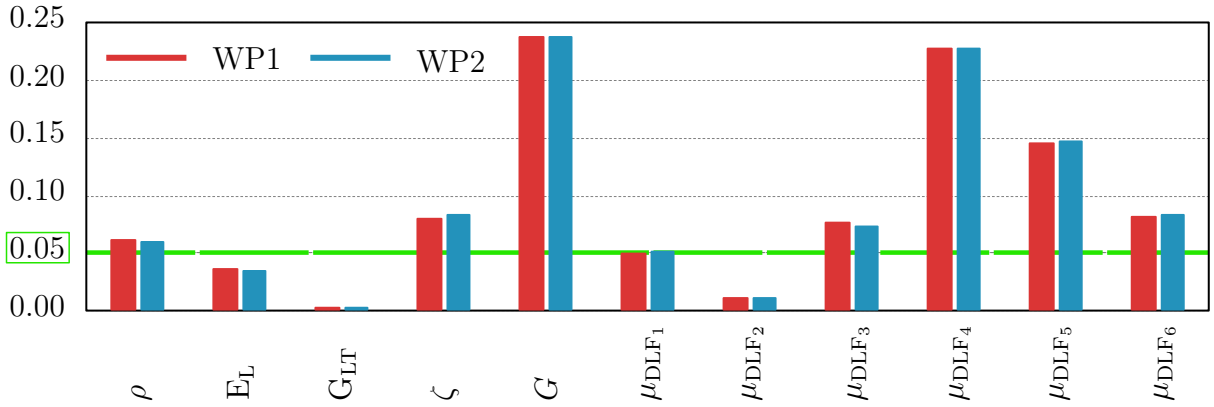

Figure 9.16: Normalised Shapley effects of the 11 uncertain input parameters for the resonant responses along WP1 and WP2, considering only inter-subject variability.

depend on the natural frequencies of the floor (Table 7.4). The natural frequencies are themselves uncertain, as they depend on timber density, the longitudinal modulus of elasticity and the shear modulus. Consequently, the probability distributions from which μ_{Ieff} and σ_{Ieff} should be sampled are not known at the beginning of a simulation, but only after the structural parameters have been sampled and the corresponding natural frequencies have been evaluated. Therefore, μ_{Ieff} and σ_{Ieff} cannot be sampled together with the remaining uncertain inputs at the start of the analysis.

Furthermore, treating μ_{Ieff} and σ_{Ieff} as uncertain inputs would also create an ambiguity in the subsequent SA. Their variability would then contain two conceptually different contributions. The first arises from the variability of μ_{Ieff} and σ_{Ieff} for a given natural frequency. The second arises indirectly from the structural parameters: changes in timber density, E_L and G_{LT} alter the natural frequencies and thereby shift the probability distributions of μ_{Ieff} and σ_{Ieff}. If the physical values of μ_{Ieff} and σ_{Ieff} were used directly as SA inputs, these two sources of variability would be mixed, making their Shapley effects difficult to interpret. In particular, part of the influence originating from the structural parameters through their effect on the natural

frequencies could be attributed to the effective-impulse parameters instead of being retained as part of the structural contribution.

To address these two issues, two auxiliary random variables, $Z_{\mu_{\text{Ieff}}}$ and $Z_{\sigma_{\text{Ieff}}}$, are introduced and used as the actual uncertain inputs. These variables do not represent physical quantities. Instead, they specify the relative position of a realisation within the probability distribution of μ_{Ieff} or σ_{Ieff}. Both are assumed to follow standard normal distributions, $\mathcal{N}(0,1)$, and can therefore be sampled before the floor natural frequencies are known. A given value of an auxiliary variable always represents the same relative position within the relevant distribution, although the corresponding physical value may differ because the distribution itself changes with natural frequency.

At the beginning of each simulation, the structural parameters, pedestrian weight, mean and standard deviation of walking frequency and the auxiliary variables $Z_{\mu_{\text{Ieff}}}$ and $Z_{\sigma_{\text{Ieff}}}$ are sampled simultaneously. The sampled structural parameters are then used to evaluate the corresponding floor natural frequencies, which determine the appropriate probability distributions of μ_{Ieff} and σ_{Ieff}. Values of $Z_{\mu_{\text{Ieff}}}$ and $Z_{\sigma_{\text{Ieff}}}$ are subsequently mapped to the corresponding positions within these frequency-dependent distributions, yielding the physical values of μ_{Ieff} and σ_{Ieff}. Therefore, although all uncertain input variables are sampled together, the physical values of μ_{Ieff} and σ_{Ieff} are evaluated only after the natural frequencies are calculated.

Accordingly, $Z_{\mu_{\text{Ieff}}}$ and $Z_{\sigma_{\text{Ieff}}}$ remain the uncertain input variables used throughout the sampling procedure and SA, whereas μ_{Ieff} and σ_{Ieff} are derived, frequency-dependent physical quantities. This formulation allows the uncertainty associated with the effective-impulse parameters to be distinguished from the indirect effect of structural uncertainty.

As in the case of LFFs, two sets of vibration responses were calculated in the following subsections: one accounting for both intra- and inter-subject variability of the walking load, i.e. the total variability, and the other accounting only for inter-subject variability. Two WPs are considered and maximum one-second moving average RMS velocity ($v_{rms,max}$) is calculated in the receiver point (Figure 8.9).

9.4.1 Uncertainty analysis of transient response considering total load variability

The results of the UQ analysis of the $v_{rms,max}$, including the PDFs, CDFs and corresponding statistical properties for the two WPs, are presented in Figure 9.17. The mean value and standard deviation of $v_{rms,max}$ are approximately 10% higher for WP2 than for WP1, while the COV is the same for both WPs, at 68.5%. For both WPs, $v_{rms,max}$ is best fitted by a lognormal distribution. As in the case of non-resonant response, a long right tail of lognormal distribution is observed, meaning that there is small number of simulations that resulted in extremely high vibration responses.

Figure 9.18 presents the CDFs of the transient responses obtained for the two WPs, with the deterministic predictions based on CCIP-016 and the proposed simplified load model, previously calculated in Section 8.3, superimposed. These deterministic predictions were obtained using the 75th percentile of the effective impulse load. However, this percentile corresponds specifically to a walking frequency of 2.5Hz, meaning that the adopted effective impulse lies within the highest 25% of impulse values associated with that frequency. In the present analysis,

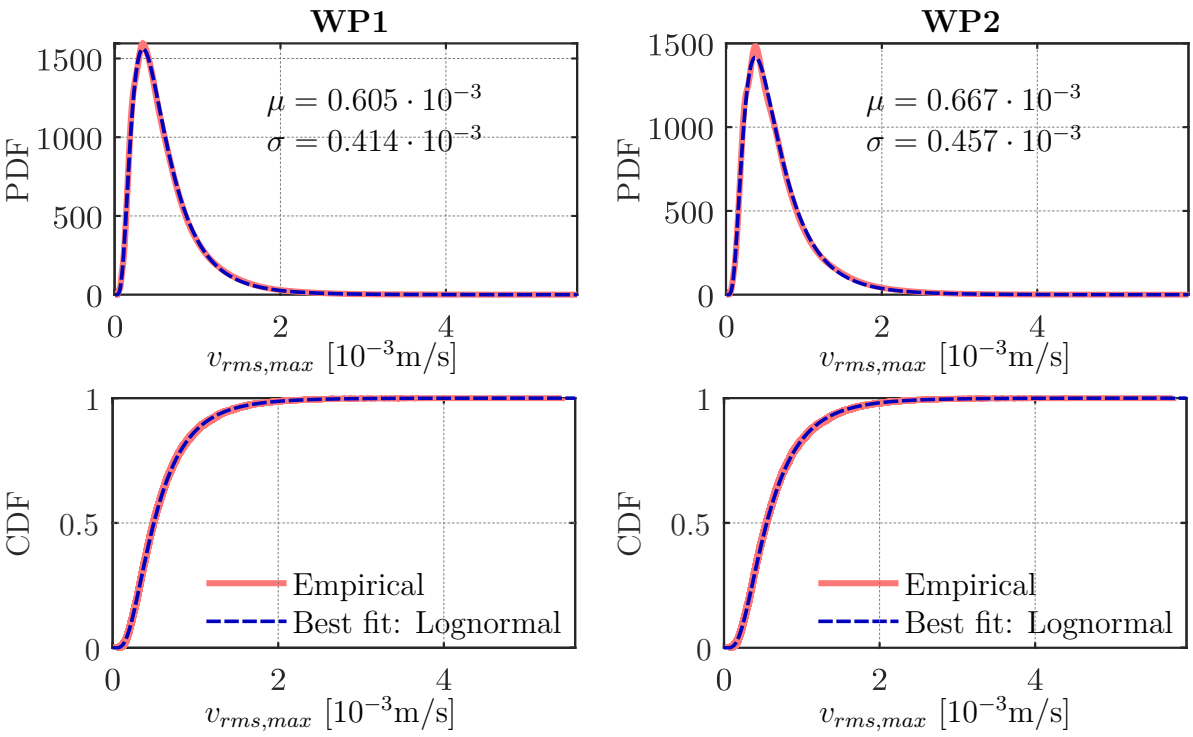

Figure 9.17: Empirical and best-fit distribution of transient $v_{rms,max}$ considering total variability for WP1 and WP2.

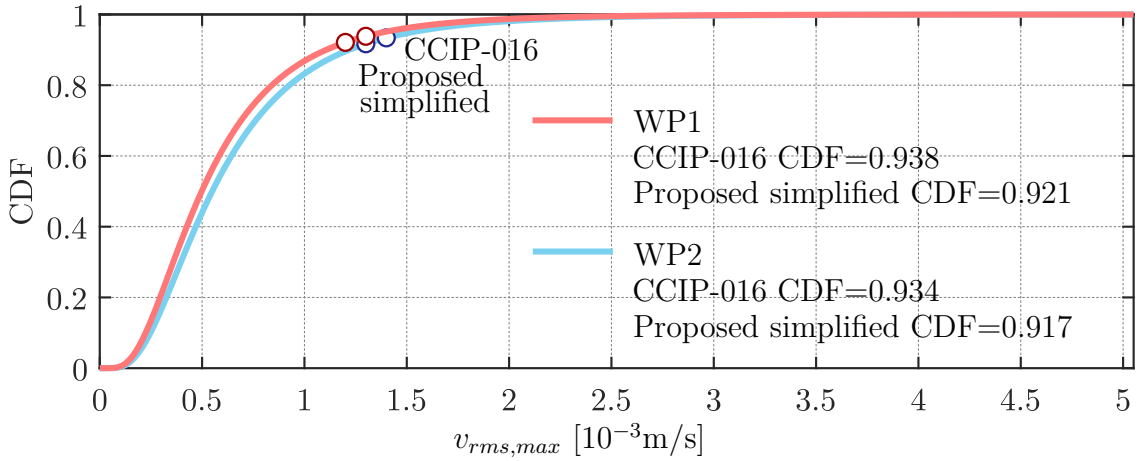

Figure 9.18: CDFs of transient $v_{rms,max}$ considering total variability for WP1 and WP2 with responses obtained deterministically using CCIP-016 and the proposed simplified load model.

however, the walking frequency varied according to its probability distribution, within which 2.5Hz is a relatively rare realisation, corresponding to the 98.8th percentile. Consequently, the deterministic predictions are located in the upper tail of the $v_{rms,max}$ response distributions. The responses predicted by CCIP-016 fall within the highest 6.2% and 6.6% of the simulated responses for WP1 and WP2, respectively, while those predicted by the proposed simplified model fall within the highest 7.9% and 8.3%, respectively.

The results of the SA, including the internal variability of the AR(1) load model and the nine normalised Shapley effects, are presented in Figure 9.19. As in the case of the LFF response, both WPs exhibit a very similar distribution of influence among the uncertain variables. The contribution of the internal variability is smaller than that obtained for the harmonic load model, accounting for approximately 2.5% of the total variance for WP1 and 1.8% for WP2. This could

be anticipated, as the effective impulse load model contains only two AR(1) representations, corresponding to f_p and I_{eff}, whereas the harmonic load model contains seven (f_p and six DLFs).

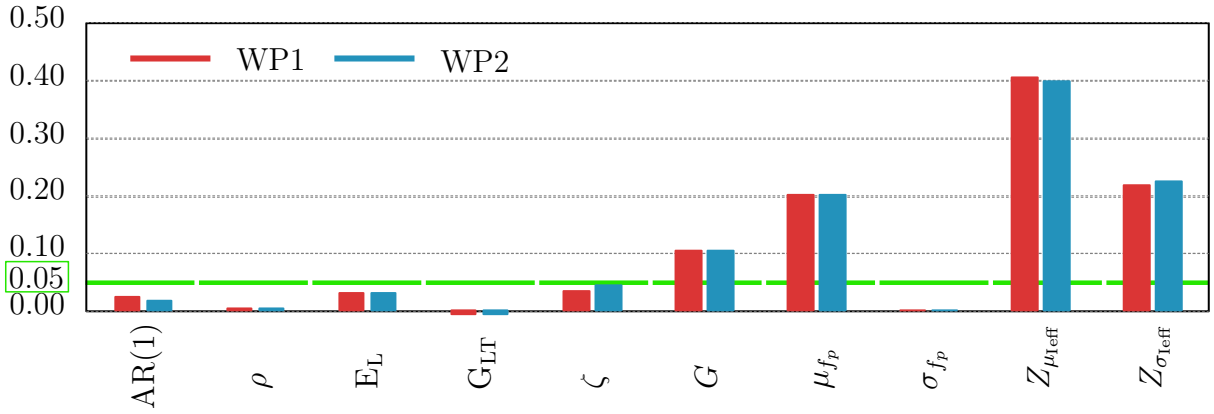

Figure 9.19: Internal AR(1) variability and normalised Shapley effects of the 9 uncertain input parameters for the transient responses along WP1 and WP2.

The largest contributions to the total response variance arise from the auxiliary random variables associated with the mean and standard deviation of I_{eff}, with normalised Shapley effects of approximately 0.40 and 0.22, respectively. Together, these variables account for approximately 62% of the total response variability, demonstrating that the uncertainty in the effective impulse is the dominant source of uncertainty in the HFF response. The mean walking frequency and pedestrian weight also have considerable influence, with normalised Shapley effects of approximately 0.20 and 0.10, respectively. In contrast, the standard deviation of the walking frequency has a negligible influence on the response variability.

The structural parameters make substantially smaller contributions to the response variance than the walking-load parameters, with all normalised Shapley effects below the adopted threshold of 0.05. The damping ratio and E_L account for approximately $3-4\%$ of the total variance each, whereas the contributions of timber density and shear modulus G_LT are bellow 1% of the total variance. Interestingly, despite the pronounced influence of timber density on the modal properties of the floor, its uncertainty does not contribute to the variability of the final HFF vibration response. This can likely be attributed to the mean effective impulse dependence on the floor natural frequency (Table 7.4), which introduces a compensating effect. A lower timber density reduces the modal mass and therefore tends to increase the vibration response. At the same time, however, the reduced density results in higher natural frequencies, for which the mean effective impulse is lower. These two opposing effects partially offset each other, thereby limiting the propagation of timber-density uncertainty to the final HFF response.

9.4.2 Uncertainty analysis of transient response considering only inter-subject load variability

The UQ analysis of the transient response $v_{rms,max}$ was repeated after removing the variables governing intra-subject variability, namely the standard deviation of f_p and the auxiliary variable $Z_{\sigma_{\text{Ieff}}}$. The resulting distributions are presented in Figure 9.20. For both WPs, $v_{rms,max}$ is best represented by a lognormal distribution. In this case, the mean response for WP2 is 4.4% higher than that for WP1, while the corresponding standard deviation is 6.8% higher. The resulting COVs are 74.2% and 72.4% for WP1 and WP2, respectively.

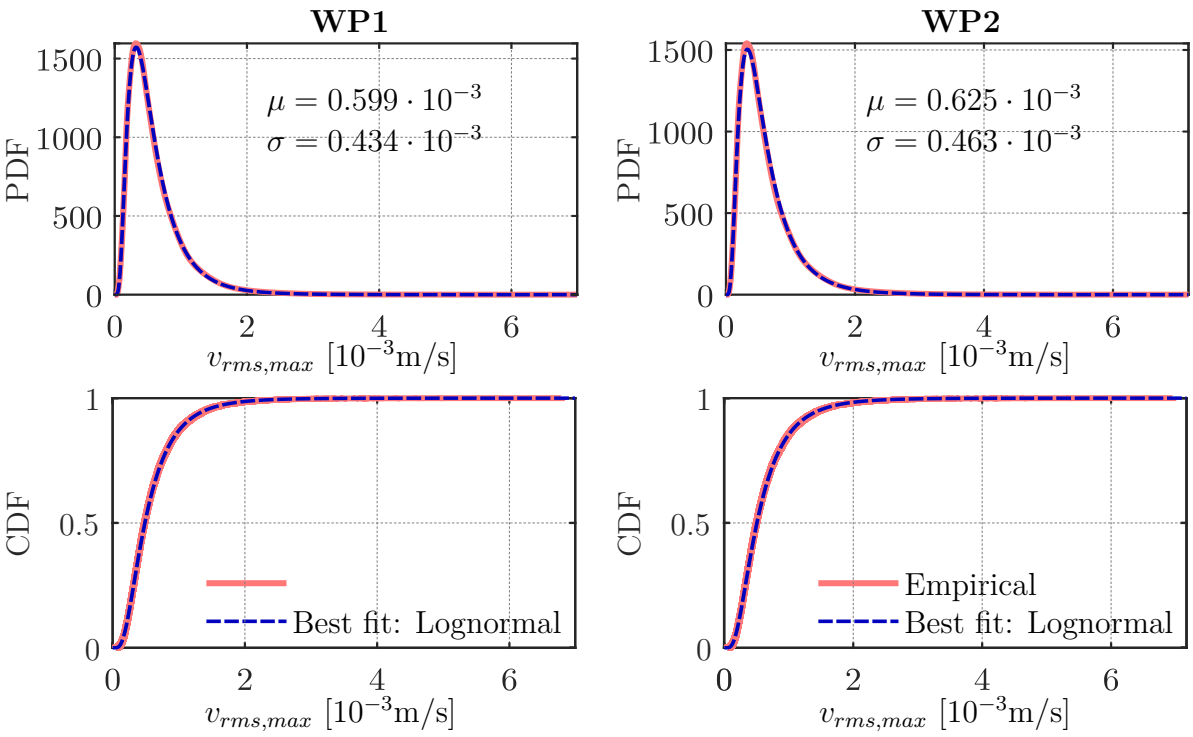

Figure 9.20: Empirical and best-fit distribution of transient $v_{rms,max}$ considering only inter-subject variability for WP1 and WP2.

Removing the variables governing intra-subject variability resulted in lower mean values of $v_{rms,max}$, by 1.0% for WP1 and 6.3% for WP2 (Figure 9.21). This caused the response distributions for WP2 to shift slightly to the left (Figure 9.22), while for WP1 stayed basically the same. In contrast, considering only inter-subject variability resulted in slightly higher standard deviations, by 4.7% and 1.4% for WP1 and WP2, respectively. Consequently, the corresponding COVs increased by 5.7% for WP1 and 8.2% for WP2.

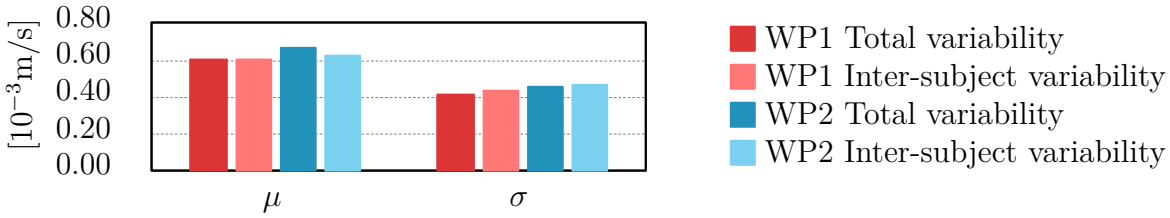

Figure 9.21: Mean values and standard deviation of transient $v_{rms,max}$, considering total and inter-subject variability cases, for WP1 and WP2.

It should be noted that the auxiliary input variable $Z_{\sigma_{\text{Ieff}}}$ exhibited a relatively high normalised Shapley effect when the total variability was considered (Figure 9.19). However, removing this variable did not result in a substantial reduction in the variance of the response. This indicates that its high Shapley effect is likely associated with its strong statistical dependence on other influential input variables, particularly μ_{Ieff} and μ_{f_p}, as demonstrated by the correlation coefficients presented in Figure 7.42. Thus, the relatively high Shapley effect of $Z_{\sigma_{\text{Ieff}}}$ should not be interpreted as an equally large direct contribution of the intra-subject variability of I_{eff} to the total response variance.

Finally, the results of the repeated SA, expressed through the normalised Shapley effects of the seven remaining input variables, are presented in Figure 9.23. The general trend observed for the total variability case is retained, with the walking-load parameters having a substantially

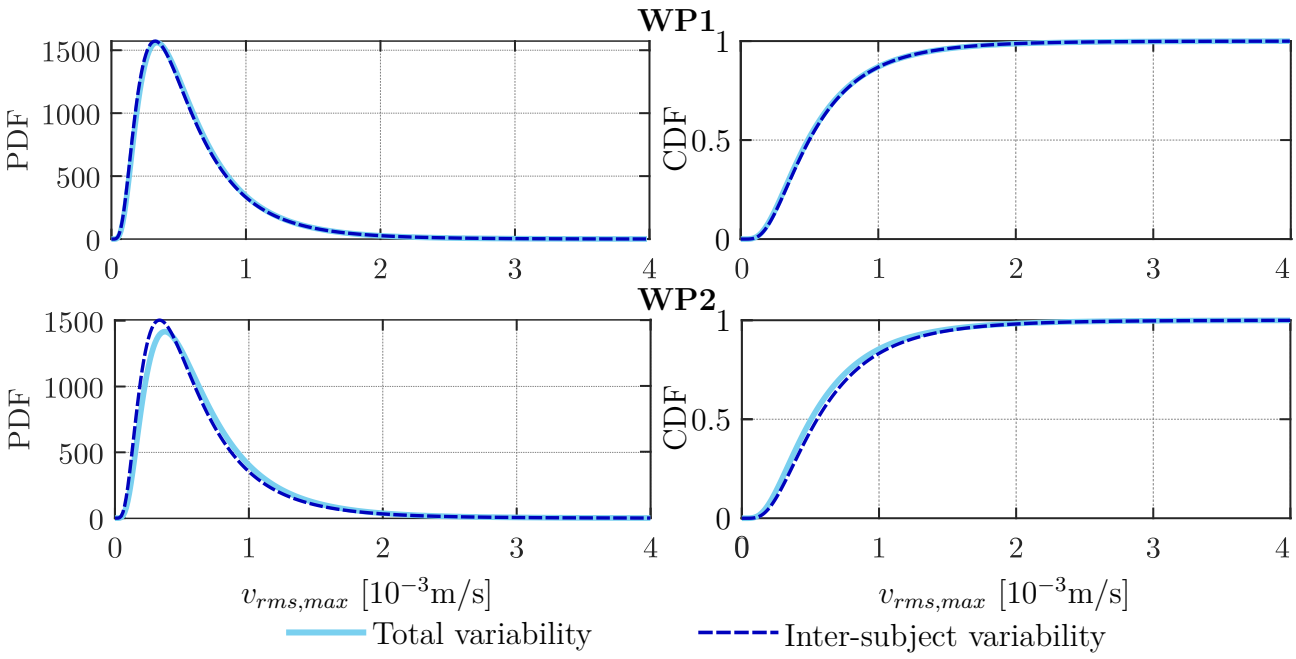

Figure 9.22: PDFs and CDFs of transient response $v_{rms,max}$ considering total and inter-subject variability cases for WP1 and WP2.

greater influence on the response variability than the structural parameters. The largest change is observed for the auxiliary input variable $Z_{\mu_{\text{Ieff}}}$, whose normalised Shapley effect increases from 0.40 to slightly above 0.50. Furthermore, the normalised Shapley effect of μ_{f_p} increases to approximately 0.26, compared with 0.20 when the total variability is considered. Among the structural parameters, only the damping ratio exhibited a sufficiently large increase in its Shapley effect to exceed the adopted 0.05 threshold and thus be considered influential.

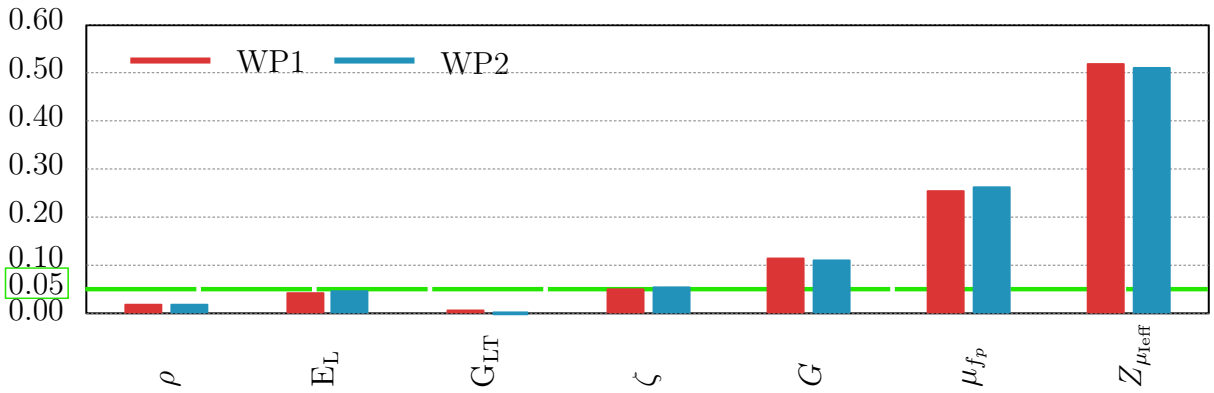

Figure 9.23: Normalised Shapley effects of the 7 uncertain input parameters for the transient responses along WP1 and WP2, considering only inter-subject variability.

9.5 Chapter summary

This chapter integrated the structural and load uncertainties into a holistic probabilistic framework for the uncertainty analysis of both low- and high-frequency CLT floor response. In addition to these uncertainties, the internal variability introduced by the AR(1) representation of load was also considered. This variability arises from the randomly modelled AR coefficients and the random noise term ε_t included in the AR(1) process. Its contribution to the total

response variance ranged from approximately 1.8% for the HFF response to as much as 8% for the LFF response.

UQ was performed using 10,000 MC simulations with particular attention devoted to assessing the influence of intra-subject variability of the walking load. Responses obtained considering both intra- and inter-subject walking-load variability were compared with those obtained when only inter-subject variability was retained. SA was conducted using Shapley effects, allowing the influence of highly correlated input variables to be quantified. A convergence study demonstrated that, for the most complex case involving 19 uncertain input parameters, 30,000 random permutations, corresponding to 1.6 million MC model evaluations, were sufficient to obtain stable and accurate estimates of the normalised Shapley effects.

For the LFF, two response types were analysed separately: non-resonant and resonant. In the former case, the walking frequency was sampled independently of the floor natural frequencies, allowing resonance to occur naturally in only a limited number of realisations. In the latter case, resonance was imposed in every simulation by selecting the walking frequency such that one of its harmonics coincided with the fundamental frequency of the floor.

UQ of the non-resonant responses produced lognormal distributions of $a_{rms,max}$ with pronounced right tails, reflecting the relatively rare occurrence of resonant and near-resonant conditions. Approximately 10% of the simulations fell into these conditions, producing exceptionally high $a_{rms,max}$ values and resulting in high variability with COVs of 77.0% and 73.4% for WP1 and WP2, respectively.

The experimentally measured $a_{rms,max}$ values obtained for the TSs walking freely along two WPs fell within the lower portion of the non-resonant response distributions. These comparatively low responses can be partly attributed to the relatively low weights of the TSs (48 and 51kg, corresponding to approximately 480 and 510N) compared with the mean pedestrian weight of 757N adopted in the probabilistic model. However, the available experimental dataset, comprising only two TSs and eight measurements across the two WPs, is insufficient for a statistically meaningful validation of the proposed framework.

SA revealed that the non-resonant response variance was governed primarily by the mean walking frequency, longitudinal modulus of elasticity and timber density, with normalised Shapley effects of 0.18, 0.15, and 0.13, respectively. Particular combinations of these three parameters can lead to resonant or near-resonant conditions and, consequently, exceptionally high values of $a_{rms,max}$. Pedestrian weight and the mean values of DLF_4–DLF_6 also showed non-negligible contributions, with normalised Shapley effects ranging from 0.05 to 0.09, while the influence of all remaining variables was comparatively small or negligible. The greater influence of μ_{DLF_6}–μ_{DLF_6} compared with the lower harmonics is attributed to the fact that the fourth to sixth harmonics fall within the frequency range of the fundamental mode of the considered floor. For floors with lower fundamental frequencies, lower-order harmonics would therefore be expected to show a greater influence on the response variance.

When resonance was imposed in every LFF simulation, the mean responses were more than twice those obtained for the non-resonant case, while the corresponding COVs were approximately 40% lower (43% for both WPs). This reduction in relative variability results from eliminating the uncertainty associated with the occurrence of resonance.

Although the deterministic responses predicted by CCIP-016 and the proposed simplified load model are based on the 75th percentile of the DLFs, they fall within approximately the highest

13% and 17% of the simulated resonant responses, respectively. This illustrates that the percentile assigned to an input load parameter does not translate directly into the same percentile of the resulting vibration response, since the response is governed by the combined influence of several uncertain structural and load parameters. Furthermore, these results are consistent with the deterministic assessment. For the considered floors, both CCIP-016 and the proposed simplified load models produced responses of a similar order, with the proposed formulations offering greater flexibility and a broader range of applicability.

SA of the resonant response showed that the response variance was governed primarily by the harmonic load parameters. The most influential variables were pedestrian weight and the mean values of DLF_4 and DLF_5, with normalised Shapley effects of 0.22, 0.19, and 0.11, respectively. Moderate contributions were observed for the mean values of DLF_3 and DLF_6, as well as for the damping ratio, each with a normalised Shapley effect of 0.07. Timber density exhibited a smaller but still non-negligible contribution, with a normalised Shapley effect of 0.05, while the remaining parameters had no statistically significant influence on the response variance.

Therefore, the dominant sources of uncertainty in the LFF vibration response depend on the response condition. For non-resonant excitation, the response variability is primarily governed by the interaction between pedestrian pacing rate and the structural parameters that determine the floor natural frequencies. Under resonant conditions, the influence of most structural parameters is reduced, except for damping, while pedestrian weight and the amplitudes of the relevant harmonics become the principal contributors to response variability.

Removing intra-subject variability reduced the mean non-resonant response $a_{rms,max}$ by 9.78% for WP1 and 5.09% for WP2. At the same time, the corresponding standard deviations increased by 4.66% and 3.61%, resulting in COVs that were 15.7% and 9.3% higher, respectively. Without step-to-step variability in walking frequency, each simulation tends to remain either away from resonance or close to it throughout the walking session. This reduces the mean response in realisations with harmonic excitation far away from the floor natural frequency. On the other hand, it produces a small number of persistently resonant, exceptionally high responses that increase the overall dispersion. For the resonant response, removing intra-subject variability enables maintaining resonance throughout the walking session, resulting in increased mean $a_{rms,max}$ by 7.12% for WP1 and 8.26% for WP2 and increased standard deviations by 4.41% and 5.01%, respectively. As a result, the COV decreased by approximately 3% for both WPs. Despite these changes, the overall pattern and ranking of the Shapley effects remained similar for both non-resonant and resonant responses compared with the corresponding cases including total walking-load variability. For design applications, where the resonant response is relevant, neglecting intra-subject variability therefore leads to slightly higher predicted response levels. Accordingly, considering only inter-subject variability may be regarded as a conservative simplification for the assessment of resonant LFF response. Given its limited influence on the predicted response and the additional complexity required for its explicit representation, modelling intra-subject variability is unlikely to be justified in routine engineering practice.

When the total walking-load variability was considered, the transient HFF response exhibited a COV of approximately 68.5% for both analysed WPs, indicating substantial variability in $v_{rms,max}$. Removing the variables governing intra-subject variability resulted in only minor changes in the response distributions. The mean response decreased by 1.0% for WP1 and 6.3% for WP2, while the corresponding COVs increased slightly, by 8.3 and 5.7%, respectively. These results indicate that explicitly modelling intra-subject variability has only a limited influence on the overall statistical properties of the HFF response.

The deterministic predictions obtained using CCIP-016 and the proposed simplified load model were located in the upper tail of the probabilistic response distributions, within approximately the highest 9% of the calculated responses. This is primarily associated with the deterministic adoption of a walking frequency of 2.5Hz, which corresponds to the 98.8^{th} percentile of the walking-frequency distribution. Since walking frequency and effective impulse are strongly correlated, with higher frequencies generally associated with larger impulses, such high impulse values become even less probable when the full distribution of walking frequencies is considered.

The SA demonstrated that the variability of the HFF response is governed predominantly by the walking-load parameters. The auxiliary variables associated with the mean and standard deviation of I_{eff} were the most influential, followed by the mean walking frequency and pedestrian weight, with normalised Shapley effects of approximately 0.40, 0.22, 0.20, and 0.10, respectively. The relatively high Shapley effect of the auxiliary variable associated with the standard deviation of I_{eff} appears to arise primarily from its strong statistical correlation with the mean I_{eff} and the mean walking frequency, rather than from a direct contribution to the vibration-response variance. By contrast, the structural parameters had only minor effects: the damping ratio and longitudinal modulus of elasticity showed small contributions, while the effects of timber density and shear modulus were negligible.

Overall, results from this chapter demonstrate that uncertainty in pedestrian loading is the principal source of uncertainty in the predicted vibration response of CLT floors. The importance of individual parameters, however, depends on the response case and on whether resonance is present. The comparison between total and inter-subject-only variability further indicates that the explicit representation of intra-subject variability has a limited effect on the overall response statistics, supporting the possibility of simplifying probabilistic load models for more practical VSA.

10 Concluding remarks

The vibration response of CLT floors due to people walking is subject to uncertainties arising from both the structural properties of the floor system (timber material, inter-panel connections, damping) and the characteristics of walking-induced loading. This dissertation studies how these uncertainties influence the vibration response and contribute to its variability. The uncertainty analysis combines uncertainty quantification (UQ) to characterise and propagate the input uncertainties with sensitivity analysis (SA) to identify the parameters that govern the resulting response variability. The uncertainty-based framework presented in this dissertation was developed through five research phases (Section 10.1), each providing a distinct contribution towards achieving the overall research aim. Main scientific contributions of this dissertation are presented in Section 10.2, while practical recommendations for the vibration serviceability assessment (VSA) of CLT floors are provided in Section 10.3. Finally, recommendations for future research are summarised in Section 10.4.

10.1 Dissertation summary and outputs

Phase 1

The first phase involved the development and calibration of FE models of the investigated multi-panel CLT floor, with particular attention to modelling the inter-panel connections. The reference structure was a full-scale 5×6m CLT floor comprising three five-ply panels connected by half-lapped joints. The connections were represented by *equivalent elastic strips* rigidly connected to the adjacent panels. Values of the timber material properties and the parameters defining the equivalent elastic strips were calibrated using experimentally measured modal properties obtained within the Substrate4CLT research project.

A three-step FE model updating procedure based on the Harmony Search Algorithm was applied. The measured modal properties of the single-panel floor were first used to identify the elastic support and timber material properties, followed by identification of the inter-panel connection parameters using the two-panel floor. The resulting model was finally validated against the measured modal properties of the three-panel floor. The identified equivalent-strip parameters indicate that rotational stiffness derived from static tests should not be directly transferred to vibration analysis. At the much smaller displacement amplitudes associated with floor vibrations, the rotational stiffness was found to be substantially lower. At the same time, the identified shear stiffness of the strip is equal to that of the full CLT cross-section.

A computationally efficient 2D model was shown to provide accuracy comparable to the detailed 3D model and was therefore adopted for the subsequent uncertainty analyses. A corresponding high-frequency floor (HFF) model was obtained by reducing the span and increasing the ply thickness of the low-frequency floor (LFF) configuration.

Phase 2

The second phase studied the influence of structural uncertainties on the natural frequencies and modal masses of the LFF and HFF. The considered uncertainties included timber material and inter-panel connection properties, with their ranges and probability distributions defined from the available literature. Due to insufficient data for reliably characterising statistical dependence between these parameters, they were assumed to be statistically uncorrelated. Mode shapes were not analysed directly as uncertain outputs. Instead, their sensitivity to the considered structural parameters was assessed indirectly through the modal masses, which depend on both timber density and mode shapes. Timber density was the only uncertain parameter directly affecting the mass matrix, while the remaining structural parameters could influence the modal masses only through changes in the mode shapes. SA of the modal masses was therefore used as an indirect measure of mode-shape variability.

To make the stochastic analyses computationally efficient, the 2D FE models were replaced by Polynomial Chaos Expansion (PCE) metamodels. The metamodels were developed using a training sample of 128 FE model realisations and validated against 10,000 FE realisations.

Both floor configurations exhibited similar uncertainty patterns. The COVs of the natural frequencies were approximately 7−9%, while those of the modal masses were approximately 10−14%. SA based on Sobol' indices identified timber density ρ, longitudinal modulus of elasticity E_L and shear modulus G_{LT} as the dominant parameters governing the modal properties relevant to human-induced vibrations. Additionally, results indicated that the mode shapes can be treated as effectively deterministic. Reduced metamodels retaining only ρ, E_L and G_{LT} were developed for the subsequent response analyses.

Phase 3

The third phase had two closely related objectives pertinent to the walking load models of LFF and HFF. First, the variability of the parameters defining the harmonic load model for LFFs and the effective impulse load model for HFFs was characterised using a database of 744 continuously recorded vertical walking-force signals. Second, these results were used to extend the CCIP-016 load models into probabilistic and simplified deterministic formulations.

The harmonic model was extended from four to six harmonics, allowing resonant excitation to be represented over a wider frequency range and increasing the LFF/HFF boundary from 10 to 14Hz. Walking frequency and harmonic amplitudes were allowed to vary between successive steps according to first-order auto-regression (AR(1)) processes, thereby accounting for intra-subject variability.

The analysis showed substantial variability in the parameters defining the harmonic load. Across the complete database, the mean walking frequency was approximately 1.9Hz, with a COV of about 14%. Within individual walking records, the COV of walking frequency generally

ranged from 1 to 10%. Among the DLFs, DLF_1 exhibited the lowest intra-subject variability, with COVs of approximately $3-24\%$, while the remaining DLFs generally showed considerably greater variability, with COVs reaching up to approximately 80%. The mean DLFs, particularly DLF_1, also showed a pronounced dependence on walking frequency, and considerable statistical dependence was identified between DLFs of different harmonic orders.

Based on these findings, the probabilistic harmonic model was formulated using 15 primary force parameters describing pedestrian weight, mean value and standard deviation of walking frequency and the six DLFs. Their variability was represented by fitted probability distributions, their mutual dependence by experimentally derived correlations and their temporal dependence by AR(1) coefficients. The resulting formulation therefore accounts for both inter- and intra-subject variability.

For HFFs, effective impulses were identified from the responses of SDOF oscillators with natural frequencies between 14 and 40Hz. This enabled characterisation of both the dependence of the effective impulse amplitude on structural natural frequency and its step-to-step variability. The effective impulse exhibited high variability, with mean COVs of approximately $25-35\%$, depending on structural natural frequency.

The probabilistic effective impulse model was described by five parameters representing pedestrian weight, mean and standard deviation of walking frequency and mean and standard deviation of effective impulse. Their probability distributions, statistical correlations and temporal dependencies were characterised from the experimental database. A correction factor was additionally introduced to extend the formulation beyond the 3% reference damping ratio used during impulse identification.

Finally, simplified deterministic versions of both models were proposed for routine VSA. These retain the main experimentally identified dependencies while avoiding the computational complexity of full probabilistic simulations. In both formulations, the selected CDF level of the DLFs or I_{eff} is introduced as an input parameter, allowing the load magnitude to be defined according to a chosen probability level.

Phase 4

The fourth phase focused on deterministic calculation of the vibration response, as this represents the standard approach in routine VSA. The modal-analysis-based VSA framework recommended in CCIP-016 was adopted without modification and first applied using the original CCIP-016 walking-load models. The same calculation procedure was then repeated by replacing only the walking-load models with the simplified harmonic and effective impulse formulations proposed in Chapter 7. The complete response calculation procedure was implemented in Hindu, a Python-based application that models pedestrian walking along a prescribed walking path and calculates the resulting vibration response from imported (numerical or experimental) modal properties.

The proposed simplified and original CCIP-016 formulations were assessed for non-resonant and resonant LFF responses and for the HFF response. Their deterministic predictions were compared with corresponding probabilistic responses obtained using the probabilistic force models developed in Chapter 7, as well as with responses generated using measured walking-force signals. In all probabilistic response calculations, the floor modal properties were kept deterministic.

For the non-resonant LFF case, both deterministic approaches generally produced responses of the same order as the probabilistic and measured-force results, with differences ranging from approximately 1.6 to 24%, depending on the walking path and reference response. Furthermore, comparison with the available experimental floor measurements showed good agreement for one test case but considerably larger discrepancies for the other. Since successive walking trials by the same pedestrian cannot produce identical force histories or vibration responses, reliable validation requires a sufficiently larger number of repeated tests to establish the experimental response distribution rather than comparison with individual measurements.

Under resonant LFF excitation, the proposed simplified model overestimated the 75th-percentile probabilistic response by approximately 16.5%, compared with approximately 25% for CCIP-016. Agreement with the measured-force responses was also better for the proposed model, with maximum differences of 9.2%, compared with 17.7% for CCIP-016. For the HFF, both deterministic formulations underestimated the measured-force and probabilistic responses, with differences of approximately $23-27\%$ for the proposed model and $17-21\%$ for CCIP-016.

Overall, the proposed simplified models provided response predictions comparable in magnitude and accuracy to those obtained using CCIP-016, while offering greater flexibility. The harmonic formulation allows resonant excitation to be represented over a wider frequency range, the effective impulse formulation accommodates different damping ratios and both models allow the load magnitude to be selected at different percentiles of the corresponding probability distributions. These extensions address several limitations of the CCIP-016 formulations while retaining the simplicity required for routine engineering VSA.

Phase 5

The fifth and final phase integrated the structural and pedestrian-load uncertainties characterised in the preceding phases into a unified probabilistic framework for VSA of CLT floors. The results showed that both the magnitude and the sources of vibration-response uncertainty depend strongly on the response case and, particularly for LFFs, on the occurrence of resonance.

For the LFF, the non-resonant response exhibited substantial variability, with COVs of approximately $73-77\%$. This was largely caused by resonant and near-resonant conditions occurring in approximately 10% of the simulations and producing exceptionally high responses. SA showed that the mean walking frequency was the most influential parameter, followed by the longitudinal modulus of elasticity and timber density. Interaction between these three parameters governs the occurrence of resonance. Therefore, the high response variability is primarily associated with uncertainty in whether the floor approaches resonance, rather than with variability in the load magnitude alone.

When resonance was imposed in every LFF simulation, the mean response more than doubled, while the COV decreased to approximately 43%. Pedestrian weight and the amplitudes of the harmonics participating in resonance became the dominant sources of response variability, while damping remained the most influential structural parameter. For the analysed floor, DLF_4 and DLF_5 were the dominant harmonics, while for floors with different natural frequency ranges, the dominant harmonic orders will change accordingly.

The HFF response also exhibited substantial variability, with a COV of approximately 68.5%. In contrast to the LFF, this variability was governed predominantly by pedestrian-load parameters, particularly mean value and standard deviation of the effective impulse, followed by

mean walking frequency and pedestrian weight. Structural parameters had only minor effects. The deterministic HFF predictions were located within approximately the highest 9% of the probabilistic response distributions, largely because the adopted walking frequency of 2.5Hz corresponds to the 99th percentile of the walking-frequency distribution and is associated with relatively large effective impulses.

Finally, intra-subject variability had a secondary influence compared with inter-subject variability and did not substantially alter the sensitivity rankings. For the LFF, neglecting intra-subject variability reduced the mean non-resonant response by up to approximately 10%, but increased the mean resonant response by about $7-8\%$. Since resonance represents the critical design condition, considering only inter-subject variability may therefore provide a reasonable and slightly conservative simplification for probabilistic resonant LFF assessment. A similarly limited influence of intra-subject variability was observed for the HFF.

10.2 Main contributions

This dissertation establishes a unique uncertainty-based framework for VSA of CLT floors subjected to pedestrian loading. The framework integrates uncertainties associated with the structural system and the walking load and quantifies how their combined variability propagates to the resulting vibration response. By combining UQ with global SA, the proposed approach provides information on both the range of possible responses and the parameters responsible for their variability. Within the broader scope of this principal contribution, several additional contributions were made.

A modelling approach for multi-panel CLT floors using an equivalent elastic strip to represent inter-panel connections was adopted. The parameters of the equivalent strip were efficiently identified through a three-step FE model updating procedure. Although the approach was demonstrated for the half-lapped joints, it can be applied to other connection types by appropriately calibrating the equivalent strip properties. Furthermore, a 2D model was shown to reproduce the modal properties relevant to human-induced vibrations with accuracy comparable to that of a detailed 3D model, while substantially reducing the computational cost.

For uncertainty analysis, the FE models were replaced by PCE metamodels, allowing UQ and SA to be carried out efficiently by post-processing the expansion coefficients. The results identified timber density, longitudinal modulus of elasticity and shear modulus as the main structural parameters governing the natural frequencies and modal masses of the analysed floors relevant to human-induced vibrations. These parameters should therefore be treated as uncertain variables, while the remaining material and connection parameters may be represented deterministically in probabilistic analyses.

Another major contribution is the experimentally based probabilistic characterisation of pedestrian loading. The analysis of 744 continuous walking-force records quantified the variability of the parameters defining both harmonic and effective impulse load models, including differences between pedestrians, step-to-step variability within individual walks, statistical dependence between parameters and temporal dependence between successive steps. This characterisation enabled the existing CCIP-016 harmonic and effective impulse models to be extended from deterministic descriptions to probabilistic formulations that account for the experimentally observed variability and dependence of the load parameters.

A further contribution is the identification of the parameters that govern the variability of the vibration response under different response conditions. For non-resonant LFF response, mean walking frequency, longitudinal modulus of elasticity and timber density are the most influential parameters, as their interaction controls whether the floor approaches resonance. Under resonant conditions, pedestrian weight and the amplitudes of the relevant force harmonics become dominant, while damping remains the most influential structural parameter. For HFFs, response variability is governed primarily by the mean value and standard deviation of effective impulse, mean walking frequency and pedestrian weight. The contribution from structural parameters is only minor. Across all response cases, inter-subject variability is found to be considerably more important than step-to-step variability within an individual walk.

Another contribution is the development of simplified harmonic and effective impulse load models suitable for routine VSA. For the analysed floors, these models produced response of a similar magnitude and accuracy to those obtained using CCIP-016, while offering a broader range of applicability. Although 14Hz was adopted as the boundary between LFFs and HFFs, the proposed six-harmonic formulation can represent resonant excitation up to 15Hz, corresponding to the sixth harmonic of the maximum considered walking frequency of 2.5Hz. Consequently, both the harmonic and effective impulse formulations are applicable within the $14-15$Hz range. Within this overlap range, both resonant and transient responses should be evaluated, and the larger response should be used for the VSA. Proposed effective impulse formulation can account for a wider range of damping ratios than CCIP-016, while both proposed harmonic and effective impulse load models allow the load level to be selected through the corresponding probability distributions.

Finally, the deterministic VSA framework and the proposed simplified load models were implemented in the bespoke Python-based software Hindu. The application integrates modal floor properties, moving pedestrian loads, walking paths, receiver locations and response evaluation within a single computational environment. It therefore provides a practical implementation of the methodological developments proposed in this dissertation and a basis for their further extension towards probabilistic VSA.

10.3 General implications for vibration serviceability assessment of CLT floors

The findings of this dissertation provide several recommendations regarding modelling CLT floors, the representation of pedestrian loading and the treatment of their uncertainty.

For numerical modelling of CLT floors, detailed 3D FE models do not appear to be necessary for VSA. The investigated 2D model reproduced the floors modal properties with accuracy comparable to that of the detailed 3D representation, while requiring substantially lower computational effort.

Inter-panel connections should be represented explicitly. They affect the natural frequencies, modal masses and mode shapes of multi-panel CLT floors, and neglecting them may therefore lead to inaccurate predictions of these modal properties. The equivalent elastic-strip approach adopted in this dissertation provides a simple and practical representation of connection behaviour that can be readily implemented in general-purpose FE software. At the same time, the uncertainty analyses showed that variability in the connection parameters contributes little to

the variability of the modal properties relevant to human-induced vibrations and, consequently, to the variability of the resulting vibration response. Therefore, the connections should be modelled realistically, but their parameters do not generally need to be treated as uncertain variables in probabilistic VSA.

Among the considered timber and connection parameters, only timber density, longitudinal modulus of elasticity and shear modulus had a significant influence on the variability of the modal properties relevant to human-induced vibrations. Probabilistic modelling may therefore be concentrated on these parameters, while those shown to have negligible influence can be represented deterministically. Damping should be considered separately, since its importance increases under resonant conditions.

For LFFs, resonant response remains the critical condition for design. However, when walking frequency was sampled independently of the floor natural frequencies, only approximately 10% of the analysed realisations approached resonant or near-resonant conditions. Although relatively infrequent, these cases produced disproportionately high responses and therefore remain important for VSA. A deterministic resonant calculation should consequently be interpreted as the assessment of a critical response condition rather than as a response representative of every walking event.

Once resonance is established, the response variability is governed predominantly by the pedestrian weight and the amplitudes of the relevant harmonics. Damping is also an influential parameter, while the impact of the remaining structural parameters decreases considerably. Although modal mass directly affects the magnitude of the resonant response, its contribution to response variability is relatively small compared with those of the other influential parameters. This is because the variability of timber density, which governs modal-mass variability, is considerably lower than that of the pedestrian-load parameters.

For HFFs, response variability was also governed predominantly by pedestrian-load parameters, particularly mean value and standard deviation of effective impulse and mean value of walking frequency, while structural uncertainties had substantially smaller effects. Therefore, improvements in HFF probabilistic response assessment should primarily focus on a realistic representation of pedestrian loading rather than on more detailed characterisation of uncertainty in the floor material properties.

The explicit representation of intra-subject variability appears to be of secondary importance for practical probabilistic assessment. For resonant LFF response, excluding intra-subject variability resulted in slightly higher mean responses, indicating that retaining only inter-subject variability may provide a reasonable and slightly conservative simplification. For HFFs, intra-subject variability likewise had only a limited influence on the overall response statistics. Its explicit representation may therefore be omitted in simplified probabilistic VSA without substantially affecting the predicted response variability.

Although probabilistic analysis provides a more complete description of vibration response and its variability, its modelling and computational requirements make it impractical for routine engineering calculations. Deterministic VSA therefore remains appropriate for the design of both LFFs and HFFs, particularly since the deterministic predictions examined in this dissertation were generally located in the upper tails of the corresponding probabilistic response distributions and thus had relatively low probabilities of exceedance. Probabilistic analysis is more valuable as an advanced assessment tool when the likelihood of different response levels needs to be quantified, when deterministic predictions are close to acceptance limits, or when the

influence of individual uncertainties needs to be identified. Rather than replacing deterministic VSA, the probabilistic framework developed in this dissertation can therefore be used to inform and calibrate simplified deterministic or semi-probabilistic design procedures.

10.4 Recommendations for future work

Several limitations of the present study should be acknowledged when interpreting the results and extending the proposed framework to other CLT floor systems.

The study was based on a limited number of floor configurations derived from the same reference multi-panel CLT floor. The adopted representation of the inter-panel connection was calibrated for the half-lapped joints used in the investigated floor. The applicability of the conclusions to other connection types, numbers of panels, boundary conditions and floor geometries therefore requires further verification. In addition, although both LFF and HFF behaviour were considered, the HFF configuration was obtained numerically by modifying the span and ply thickness of the reference LFF rather than from a separately tested full-scale floor. Future studies should apply and validate the proposed modelling strategy on a broader range of full-scale CLT floors with different geometries, panel arrangements, connection types and boundary conditions.

The investigated floors represented bare structural CLT systems. In completed buildings, non-structural components such as floor finishes, screeds, ceilings, partitions and furniture may considerably alter the mass, stiffness and particularly the damping of the floor. These components may therefore influence both the magnitude and variability of the vibration response. Further experimental and probabilistic studies should include completed floor systems to determine how non-structural components affect the governing uncertainties and the resulting vibration response.

The uncertainties assigned to the timber material and inter-panel connection parameters were defined from data available in the literature. Due to insufficient information on their statistical dependence, these parameters were assumed to be uncorrelated. More extensive experimental datasets are therefore required to establish representative probability distributions and possible correlations between structural parameters. Particular attention should also be given to damping, which showed an important influence under resonant conditions but remains one of the least well characterised structural parameters.

The pedestrian-load formulations also provide several directions for further development. This dissertation follows the traditional distinction between LFFs and HFFs, applying harmonic load models to the former and effective impulse models to the latter. Future work should investigate a unified pedestrian-force model applicable across the full range of floor frequencies, thereby eliminating the need for this division. For LFFs, the harmonic formulation could also be extended to include the phase angles of the individual harmonics, enabling a more complete representation of the measured walking-force signal and its variability. The walking-force database used in this dissertation was obtained from treadmill measurements, which may not fully represent the variability of forces generated during walking on an actual floor. Future development of load models should therefore include continuous force measurements collected during walking on real floor structures to assess and, if necessary, correct for the influence of the measurement environment.

Experimental validation of both the proposed probabilistic and simplified load models remains limited. For the LFF, only a small number of measurements from two test subjects were available, while no corresponding full-scale vibration measurements were available for the HFF. A broader experimental programme involving a larger number of pedestrians, repeated walking tests, different walking paths, and a wider range of LFF and HFF systems is therefore required for more robust validation of the predicted probabilistic response distributions. In addition, experiments conducted at controlled pacing rates would allow the deterministic predictions to be validated more systematically and could support refinement of the selected load percentiles and their relationship to target response probabilities.

Finally, the computational tools developed within this dissertation provide a basis for further advancement towards more efficient and practical VSA. The current version of Hindu represents an initial implementation of the deterministic assessment procedure. Future extensions could include direct calculation of floor modal properties, automated training and validation of metamodels and implementation of the probabilistic framework developed in this dissertation, enabling fully integrated UQ and SA. Such developments would allow the proposed methodology to progress from a research-oriented framework towards a comprehensive computational tool for uncertainty-informed VSA in engineering practice.

Bibliography

[1] United Nations Environment Programme (UNEP) and Global Alliance for Buildings and Construction (GlobalABC). *Global Status Report for Buildings and Construction 2024/25: Not Just Another Brick in the Wall*. Tech. rep. United Nations Environment Programme (UNEP), Global Alliance for Buildings, and Construction (GlobalABC), 2025.

[2] International Energy Agency and UN Climate Change High-Level Champions. *Buildings – Breakthrough Agenda Report 2024*. Tech. rep. Paris, France: International Energy Agency and UN Climate Change High-Level Champions, 2024.

[3] European Environment Agency. *Buildings and construction*. 2024.

[4] C. Li et al. "Carbon footprint of the construction sector is projected to double by 2050 globally". In: *Communications Earth & Environment* 6.1 (2025), p. 831. DOI: 10.1038/s43247-025-02840-x.

[5] A. M. Harte. "Mass timber the emergence of a modern construction material". In: *Journal of Structural Integrity and Maintenance* 2.3 (2017), pp. 121–132. DOI: 10.1080/24705314.2017.1354156.

[6] A. Faircloth et al. "Global state of knowledge on human-induced sound and vibration events: defining future research directions for mass timber products". In: *Journal of Wood Science* 71 (2025), p. 71. DOI: 10.1186/s10086-025-02247-4.

[7] O. Espinoza et al. "Cross-laminated timber". In: *BioResources* 11.1 (2016), pp. 281–295.

[8] R. Brandner et al. "Cross laminated timber (CLT): overview and development". In: *European Journal of Wood and Wood Products* 74.3 (2016), pp. 331–351. DOI: 10.1007/s00107-015-0999-5.

[9] TallWood Design Institute. *Cross-Laminated Timber: Introduction and Background (Info Sheet)*. Tech. rep. TallWood Design Institute, 2019.

[10] R. Brandner. "Production and Technology of Cross Laminated Timber (CLT): A state-of-the-art Report". In: *Focus Solid Timber Solutions - European Conference on Cross Laminated Timber (CLT)*. 2014, pp. 3–36. ISBN: 1 85790 181 9.

[11] C. Silva, J. M. Branco, and P. B. Lourenco. "A project contribution to the development of sustainable multistorey timber buildings". In: *Portugal SB13 - Contribution of Sustainable Building to Meet EU 20-20-20 Targets*. 2013.

[12] J. W. V. D. Kuilen et al. "Very tall wooden buildings with Cross Laminated Timber". In: *Procedia Engineering* 14 (2011), pp. 1621–1628. DOI: 10.1016/j.proeng.2011.07.204.

[13] J. W. van de Lindt et al. "Experimental seismic behavior of a two-story CLT platform building". In: *Engineering Structures* 183 (Dec. 2019), pp. 408–422. DOI: 10.1016/j.engstruct.2018.12.079.

[14] L. Muszyski et al. “Fire resistance of unprotected cross-laminated timber (CLT) floor assemblies produced in the USA”. In: *Fire Safety Journal* 107 (Apr. 2019), pp. 126–136. DOI: 10.1016/j.firesaf.2018.12.008.

[15] A. Younis and A. Dodoo. “Cross-laminated timber for building construction: A life-cycle-assessment overview”. In: *Journal of Building Engineering* 52 (2022), p. 104482. DOI: 10.1016/j.jobe.2022.104482.

[16] Y. Dong et al. “Assessment of energy saving potential by replacing conventional materials by cross laminated timber (CLT)-A case study of office buildings in China”. In: *Applied Sciences* 9.5 (2019), pp. 1–20. DOI: 10.3390/app9050858.

[17] R. N. Passarelli. “The environmental impact of reused CLT panels: Study of a single-storey commercial building in Japan”. In: *Proceedings of the World Conference on Timber Engineering (WCTE 2018)*. Aug. 2018.

[18] A. Aloisio et al. “Vibration issues in timber structures: A state-of-the-art review”. In: *Journal of Building Engineering* 76 (2023), p. 107098. DOI: 10.1016/j.jobe.2023.107098.

[19] V. Racic. “Emerging research on vibration serviceability assessment of pedestrian structures”. In: *Building Materials and Structures* 66.2 (2023), pp. 85–92. DOI: 10.5937/grmk2300001r.

[20] V. Racic, A. Pavic, and J. M. W. Brownjohn. “Experimental identification and analytical modelling of human walking forces: Literature review”. In: *Journal of Sound and Vibration* 326.1–2 (2009), pp. 1–49. DOI: 10.1016/j.jsv.2009.04.020.

[21] J. M. W. Brownjohn, V. Racic, and J. Chen. “Universal response spectrum procedure for predicting walking-induced floor vibration”. In: *Mechanical Systems and Signal Processing* 70-71 (2016), pp. 741–755. DOI: 10.1016/j.ymssp.2015.09.010.

[22] E. Ussher, K. Arjomandi, and I. Smith. “Status of vibration serviceability design methods for lightweight timber floors”. In: *Journal of Building Engineering* 50 (2022), p. 104111. DOI: 10.1016/j.jobe.2022.104111.

[23] D. Casagrande et al. “Analytical, numerical and experimental assessment of vibration performance in timber floors”. In: *Engineering Structures* 168 (July 2018), pp. 748–758. DOI: 10.1016/j.engstruct.2018.05.020.

[24] K. Lewis et al. “The use of cross-laminated timber for long-span flooring in commercial buildings”. In: *Proceedings of the World Conference on Timber Engineering (WCTE 2016)*. 2016, pp. 4813–4821.

[25] S. Zhang, J. Zhou, and Y. H. Chui. “Deflection criteria for controlling timber floor vibrations: A 200-year evolution”. In: *Engineering Structures* 326 (Aug. 2025), p. 119370. DOI: 10.1016/j.engstruct.2024.119370.

[26] E. Bayat and F. Tubino. “Human-induced vibrations of floors: A probabilistic approach”. In: *Engineering Structures* 300 (Nov. 2024), p. 117198. DOI: 10.1016/j.engstruct.2023.117198.

[27] S. Živanović and A. Pavic. “Probabilistic Modeling of Walking Excitation for Building Floors”. In: *Journal of Performance of Constructed Facilities* 23.3 (2009), pp. 132–143. DOI: 10.1061/(ASCE)CF.1943-5509.0000005.

[28] P. Castera and P. Morlier. “Variability of the mechanical properties of the wood: randomness and determinism”. In: *Proceedings of the NATO Advanced Research Workshop on PROBAMAT: Probabilities and Materials - Test, Models and Applications, Cachan, France*. 1993. ISBN: 978-94-010-4500-1. DOI: 10.1007/978-94-011-1142-3.

[29] L. Chen, G. Tamagnone, and L. Wan-Wendner. "Review of wood species and material characteristics of mass timber for structural applications". In: *Low-Carbon Materials and Green Construction* 4.1 (2026), p. 8. DOI: 10.1007/s44242-026-00104-1.

[30] A. Filiatrault, B. Folz, and F. R.O. "Finite-Strip Free-Vibration Analysis of Wood Floors". In: *Journal of Structural Engineering* 116.8 (1990), pp. 2127–2142.

[31] J. Jonasson, P. Persson, and H. Danielsson. "Mitigating footfall-induced vibrations in cross-laminated timber floor-panels by using beech or birch". In: *Journal of Building Engineering* 86 (Aug. 2024), p. 108751. DOI: 10.1016/j.jobe.2024.108751.

[32] T. Furtmüller, M. Kendlbacher, and F. Huber. "Influence of shrinkage on the dynamic properties of a cross-laminated timber panel". In: *Results in Engineering* 24 (2024), p. 103140. DOI: 10.1016/j.rineng.2024.103140.

[33] M. Milojević et al. "Influence of inter-panel connections on vibration response of CLT floors due to pedestrian-induced loading". In: *Engineering Structures* 277 (2023), p. 115432. DOI: 10.1016/j.engstruct.2022.115432.

[34] A. S. Mohammed, A. Pavic, and V. Racic. "Improved model for human induced vibrations of high-frequency floors". In: *Engineering Structures* 168 (May 2018), pp. 950–966. DOI: 10.1016/j.engstruct.2018.04.093.

[35] G. Stefanou. "The stochastic finite element method: Past, present and future". In: *Computer Methods in Applied Mechanics and Engineering* 198.9–12 (2009), pp. 1031–1051. DOI: 10.1016/j.cma.2008.11.007.

[36] R. F. Ling and R. Y. Rubinstein. "Simulation and the Monte Carlo Method." In: *Journal of the American Statistical Association* 78.382 (1983), p. 511. DOI: 10.2307/2288699.

[37] B. Sudret. "Meta-models for Structural Reliability and Uncertainty Quantification". In: *Proceedings of the 5th Asian-Pacific Symposium on Structural Reliability and its Applications (APSSRA 2012)*. Ed. by K. K. Phoon et al. Singapore: Research Publishing Services, 2012, pp. 53–76. ISBN: 978-981-07-2219-7. DOI: 10.3850/978-981-07-2219-7_p321.

[38] L. L. L. Gratiet, S. Marelli, and B. Sudret. "Metamodel-based sensitivity analysis: Polynomial chaos expansions and Gaussian processes". In: *Handbook of Uncertainty Quantification*. Ed. by R. Ghanem, D. Higdon, and H. Owhadi. Cham, Switzerland: Springer, 2017, pp. 1289–1325. DOI: 10.1007/978-3-319-12385-1_38.

[39] V Racic and A Pavic. "Mathematical model to generate near-periodic human jumping force signals". In: *Mechanical Systems and Signal Processing* 24.1 (2010), pp. 138–152. DOI: 10.1016/j.ymssp.2009.07.001.

[40] V. Racic and J. M. W. Brownjohn. "Stochastic model of near-periodic vertical loads due to humans walking". In: *Advanced Engineering Informatics* 25.2 (2011), pp. 259–275. DOI: 10.1016/j.aei.2010.07.004.

[41] M. R. Willford and P Young. *A Design Guide for Footfall-Induced Vibration of Structures*. Tech. rep. CCIP-016. UK: The Concrete Centre, 2006.

[42] M. Milojević et al. "Software for calculation of pedestrian-induced vibration of floors". In: *Proceedings of the 16th Congress hosted by Association of Structural Engineers of Serbia*. Aranelovac, Serbia, 2022, pp. 256–265. ISBN: 9788675182276.

[43] S. Živanović, A. Pavic, and P. Reynolds. "Vibration serviceability of footbridges under human-induced excitation: A literature review". In: *Journal of Sound and Vibration* 279.1–2 (2005), pp. 1–74. DOI: 10.1016/j.jsv.2004.01.019.

[44] T. A. Wyatt. *Design Guide on the Vibration of Floors*. Tech. rep. P076. Ascot, UK: Steel Construction Institute, 1989, p. 43.

[45] J. M. Brownjohn and C. J. Middleton. "Procedures for vibration serviceability assessment of high-frequency floors". In: *Engineering Structures* 30.6 (2008), pp. 1548–1559. DOI: 10.1016/j.engstruct.2007.10.006.

[46] J. Blanchard, B. L. Davies, and J. W. Smith. "Design Criteria and Analysis for Dynamic Loading of Footbridges". In: *Proceeding of a Symposium on Dynamic Behaviour of Bridges at the Transport and Road Research Laboratory*. Crowthorne, Berkshire, England, 1977, pp. 90–106.

[47] H Bachmann and W Ammann. *Vibrations in Structures: Induced by Man and Machines*. International Association for Bridge and Structural Engineering, 1987.

[48] J. H. Rainer, G. Pernica, and D. E. Allen. "Dynamic loading and response of footbridges". In: *Canadian Journal of Civil Engineering* 15.1 (1988), pp. 66–71. DOI: 10.1139/188-007.

[49] S. C. S. Kerr. "Human induced loading on staircases". PhD thesis. London: University of London, 1998.

[50] M. Willford, P. Young, and C. Field. "Improved methodologies for the prediction of footfall-induced vibration". In: *Buildings for Nanoscale Research and Beyond*. Vol. 5933. SPIE, Aug. 2005, 59330R. DOI: 10.1117/12.615417.

[51] A. Pavic and M. Willford. *Technical Report 43: Post-Tensioned Concrete Floors Design Handbook – Appendix G*. Tech. rep. Technical Report 43, Appendix G. Slough, UK: Concrete Society, 2008.

[52] C. J. Middleton and J. M. Brownjohn. "Response of high frequency floors: A literature review". In: *Engineering Structures* 32.2 (2010), pp. 337–352. DOI: 10.1016/j.engstruct.2009.11.003.

[53] S. Zivanovic, A. Pavic, and P. Reynolds. "Probability-based prediction of multi-mode vibration response to walking excitation". In: *Engineering Structures* 29.6 (2007), pp. 942–954. DOI: 10.1016/j.engstruct.2006.07.004.

[54] Y Matsumoto et al. "Dynamic design of footbridges". In: *IABSE proceedings*. 1978, P–17.

[55] Y. Matsumoto et al. "A study on dynamic design of pedestrian over-bridges in consideration of characteristics of pedestrians". In: *Proceedings of the Japan Society of Civil Engineers* 1972.205 (Mar. 1972), pp. 63–70. DOI: 10.2208/jscej1969.1972.205_63.

[56] S. C. Kerr and N. W. M. Bishop. "Human induced loading on flexible staircases". In: *Engineering Structures* 23.1 (2001), pp. 37–45. DOI: 10.1016/S0141-0296(00)00020-1.

[57] A. Pachi and T. Ji. "Frequency and velocity of people walking". In: *The Structural Engineer* 83.3 (2005), pp. 36–40.

[58] C. Sahnaci and M. Kasperski. "Simulation of random pedestrian flow". In: *Proceedings of the 8th International Conference on Structural Dynamics (EURODYN 2011)*. July 2011, pp. 1040–1047.

[59] J. M. Brownjohn, A. Pavic, and P. Omenzetter. "A spectral density approach for modelling continuous vertical forces on pedestrian structures due to walking". In: *Canadian Journal of Civil Engineering* 31.1 (2004), pp. 65–77. DOI: 10.1139/103-072.

[60] J. Chen, G. Ding, and S. Živanović. "Stochastic Single Footfall Trace Model for Pedestrian Walking Load". In: *International Journal of Structural Stability and Dynamics* 19.3 (2019), pp. 1–25. DOI: 10.1142/S0219455419500299.

[61] A. Magdaleno et al. “Generating vertical ground reaction forces using a stochastic data-driven model for pedestrian walking”. In: *Journal of Computational Science* 88 (2025), p. 102602. DOI: 10.1016/j.jocs.2025.102602.

[62] S. V. Ohlsson. “Floor vibrations and human discomfort”. 1 volume (various pagings). PhD thesis. Goteborg, Sweden: Chalmers University of Technology, 1982.

[63] P. Eriksson. “Vibration of Low-Frequency Floors - Dynamic Forces and Response Prediction”. PhD thesis. Goteborg, Sweden: Chalmers University of Technology, 1994.

[64] G. Piccardo and F. Tubino. “Equivalent spectral model and maximum dynamic response for the serviceability analysis of footbridges”. In: *Engineering Structures* 40 (2012), pp. 445–456. DOI: 10.1016/j.engstruct.2012.03.005.

[65] A. Ferrarotti and F. Tubino. “Generalized Equivalent Spectral Model for Serviceability Analysis of Footbridges”. In: *Journal of Bridge Engineering* 21.12 (2016), p. 04016091. DOI: 10.1061/(asce)be.1943-5592.0000963.

[66] J. Chen, J. Wang, and J. M. W. Brownjohn. “Power Spectral-Density Model for Pedestrian Walking Load”. In: *Journal of Structural Engineering* 145.2 (2019), p. 04018239. DOI: 10.1061/(asce)st.1943-541x.0002248.

[67] J. Wang et al. “Spectral Model for Crowd Walking Load”. In: *Journal of Structural Engineering* 146.3 (2020), p. 04019220. DOI: 10.1061/(asce)st.1943-541x.0002514.

[68] E. Bayat and F. Tubino. “Probabilistic assessment of the dynamic response of floors under multi-pedestrian walking loads”. In: *Mechanical Systems and Signal Processing* 213 (2024), p. 111363. DOI: 10.1016/j.ymssp.2024.111363.

[69] E. Ussher et al. “Predicting effects of design variables on modal responses of CLT floors”. In: *Structures* 11 (2017), pp. 40–48. DOI: 10.1016/j.istruc.2017.04.006.

[70] T. Asakura et al. “Prediction of low-frequency floor impact vibration of CLT structures using a single-layer FE model”. In: *Journal of Building Engineering* 98 (2024), p. 111336. DOI: 10.1016/j.jobe.2024.111336.

[71] E. Ussher et al. “Prediction of motion responses of cross-laminated-timber slabs”. In: *Structures* 11 (Jan. 2017), pp. 49–61. DOI: 10.1016/j.istruc.2017.04.007.

[72] J. Weckendorf and I. Smith. “Dynamic characteristics of shallow floors with cross-laminated-timber spines”. In: *World Conference on Timber Engineering 2012, WCTE 2012*. 2012, pp. 176–185.

[73] J. Weckendorf, E. Ussher, and I. Smith. “Dynamic response of CLT plate systems in the context of timber and hybrid construction”. In: *Composite Structures* 157 (2016), pp. 412–423. DOI: 10.1016/j.compstruct.2016.08.033.

[74] J. Weckendorf et al. “Vibration serviceability performance of timber floors”. In: *European Journal of Wood and Wood Products* 74.3 (2016), pp. 353–367. DOI: 10.1007/s00107-015-0976-z.

[75] K. Jarnero, A. Brandt, and A. Olsson. “Vibration properties of a timber floor assessed in laboratory and during construction”. In: *Engineering Structures* 82 (2015), pp. 44–54. DOI: 10.1016/j.engstruct.2014.10.019.

[76] S. Zhang et al. “Effect of end support restraints on vibration performance of cross laminated timber floors: An analytical approach”. In: *Engineering Structures* 189 (Jan. 2019), pp. 186–194. DOI: 10.1016/j.engstruct.2019.03.042.

[77] S. Zhang and Y. H. Chui. “Quantifying the effect of end support restraints on vibration serviceability of mass timber floor systems: Testing”. In: *Engineering Structures* 301 (2024), p. 117189. DOI: 10.1016/j.engstruct.2023.117189.

[78] S. Zhang and Y. H. Chui. "Quantifying the effect of end support restraints on vibration serviceability of mass timber floor systems: Analysis and design". In: *Engineering Structures* 339 (May 2025), p. 120643. DOI: 10.1016/j.engstruct.2025.120643.

[79] F. S. Lago and G. Doudak. "Vibration behaviour of low-frequency CLT floor systems: Influence of intermediate supports and panel-to-panel connections". In: *Engineering Structures* 353 (2026), p. 122351. DOI: 10.1016/j.engstruct.2026.122351.

[80] S. Zhang and Y. H. Chui. "Characterizing flexural behaviour of panel-to-panel connections in cross-laminated timber floor systems". In: *Structures* 28 (Oct. 2020), pp. 2047–2055. DOI: 10.1016/j.istruc.2020.10.040.

[81] M. Sadeghi et al. "Bending properties of connections in cross laminated timber". In: *IABSE Conference, Nara 2015: Elegance in Structures - Report*. May 2015, pp. 366–367. ISBN: 9783857481383. DOI: 10.2749/222137815815775402.

[82] M. Kawrza, T. Furtmüller, and C. Adam. "Experimental and numerical modal analysis of a cross laminated timber floor system in different construction states". In: *Construction and Building Materials* 344 (2022), p. 128032. DOI: 10.1016/j.conbuildmat.2022.128032.

[83] A. Paolini et al. "A high-order finite element model for vibration analysis of cross-laminated timber assemblies". In: *Building Acoustics* 24.3 (2017), pp. 135–158. DOI: 10.1177/1351010X17727126.

[84] E. Macpherson et al. "The rotational stiffness of cross-laminated timber half-lap joints". In: *World Conference on Timber Engineering WCTE 2018*. Seoul, Republic of Korea, 2018.

[85] E. Ussher et al. "Effect of partition walls on the vibration serviceability of cross-laminated timber floors". In: *Journal of Building Engineering* 95 (July 2024), p. 110001. DOI: 10.1016/j.jobe.2024.110001.

[86] B. K. Schwendy. "Effects of Heavy Topping on Vibrational Performance of Cross- Laminated Timber Floor Systems". PhD thesis. Clemson University, Aug. 2020.

[87] M. Salehi et al. "Experimental investigations of the effect of furniture on the vibration performance of lightweight timber floors". In: *Journal of Building Engineering* 125 (2026), p. 116034. DOI: 10.1016/j.jobe.2026.116034.

[88] S. Malek et al. "Vibration performance of CLT and CLT-concrete composite floors supported by glulam beams under human activity in mass timber office buildings". In: *Engineering Structures* 330 (2025), p. 119918. DOI: 10.1016/j.engstruct.2025.119918.

[89] International Organization for Standardization. *Bases for design of structures – Serviceability of buildings and walkways against vibrations*. Tech. rep. ISO 10137:2007. Geneva, Switzerland: International Organization for Standardization, 2007.

[90] British Standards Institution. *Guide to evaluation of human exposure to vibration in buildings (1 Hz to 80 Hz)*. Tech. rep. BS 6472:1992. London, UK: British Standards Institution, 1992.

[91] R. Sachse. "The Influence of Human Occupants on the Dynamic Properties of Slender Structures". PhD thesis. University of Sheffield, 2002.

[92] S. Živanović, A. Pavic, and P. Reynolds. "Human-structure dynamic interaction in footbridges". In: *Proceedings of the Institution of Civil Engineers – Bridge Engineering* 158.4 (2005), pp. 165–177. DOI: 10.1680/bren.2005.158.4.165.

[93] H. V. Dang. "Experimental and Numerical Modelling of Walking Locomotion on Vertically Vibrating Low-Frequency Structures". PhD thesis. University of Warwick, 2014.

[94] European Committee for Standardization. *Eurocode 5: Design of timber structures – Part 1-1: General – Common rules and rules for buildings*. Tech. rep. EN 1995-1-1:2004. Brussels, Belgium: European Committee for Standardization, 2004.

[95] RISE Research Institutes of Sweden. *The CLT Handbook*. Tech. rep. RISE Research Institutes of Sweden, 2019.

[96] E. Karacabeyli and S. Gagnon. *Canadian Cross-Laminated Timber Handbook: 2019 Edition*. Pointe-Claire, Quebec, Canada: FPInnovations, 2019. ISBN: 978-0-86488-590-6.

[97] P. Hamm, A. Richter, and S. Winter. "Floor vibrations - New results". In: *Proceedings of the 11th World Conference on Timber Engineering (WCTE 2010)*. Vol. 4. 2010, pp. 2765–2773.

[98] I. Abeysekera et al. "Development of a floor vibration design method for Eurocode 5". In: *New Zealand Timber Design Journal* 27.1 (2018).

[99] W. Schirén and T. Swahn. "Vibrations in residential timber floors A comparison between the current and the revised Eurocode 5". In: *25. Internationales Holzbau-Forum IHF*. 2019, pp. 1–12.

[100] A. L. Smith, S. J. Hicks, and P. J. Devine. *Design of Floors for Vibration: A New Approach*. Tech. rep. P354. Steel Construction Institute, Feb. 2009.

[101] B. M. Basaglia et al. "Response Prediction to Walking-Induced Vibrations of a Long-Span Timber Floor". In: *Journal of Structural Engineering* 147.2 (2021), pp. 1–15. DOI: 10.1061/(asce)st.1943-541x.0002888.

[102] S. Breneman et al. *U.S. Mass Timber Floor Vibration Design Guide*. Tech. rep. First edition, revised. WoodWorks – Wood Products Council, May 2021.

[103] X. Wei et al. "Influence of mechanical uncertainties on dynamic responses of a full-scale all-FRP footbridge". In: *Composite Structures* 223 (May 2019), p. 110964. DOI: 10.1016/j.compstruct.2019.110964.

[104] X. Wei et al. "Sensitivity Analysis for Pedestrian-Induced Vibration in Footbridges". In: *Buildings* 12.7 (2022), p. 883. DOI: 10.3390/buildings12070883.

[105] B. Chocholaty et al. "Vibration response of a hybrid steeltimber building element with uncertain material and joint parameters". In: *Archives of Civil and Mechanical Engineering* 24.1 (2024), p. 22. DOI: 10.1007/s43452-023-00819-z.

[106] S. Dey, T. Mukhopadhyay, and S. Adhikari. "Metamodel based high-fidelity stochastic analysis of composite laminates: A concise review with critical comparative assessment". In: *Composite Structures* 171 (2017), pp. 227–250. DOI: 10.1016/j.compstruct.2017.01.061.

[107] D. Zeng, H. Wang, and J. Chen. "Influence of uncertainties on dynamic properties and responses of human-structure coupled system under bouncing excitations". In: *Probabilistic Engineering Mechanics* 75 (2024), p. 103593. DOI: 10.1016/j.probengmech.2024.103593.

[108] K. V. Nimmen et al. "Pedestrian-Induced Vibrations of Footbridges: An Extended Spectral Approach". In: *Journal of Bridge Engineering* 25.8 (2020), pp. 1–15. DOI: 10.1061/(asce)be.1943-5592.0001582.

[109] P. Persson and O. Floden. "Effect of material parameter variability on vibroacoustic response in wood floors". In: *Applied Acoustics* 146 (2019), pp. 38–49. DOI: 10.1016/j.apacoust.2018.10.034.

[110] C. Qian et al. “Development of a vibroacoustic stochastic finite element prediction tool for a CLT floor”. In: *Applied Sciences* 9.6 (2019), pp. 1–25. DOI: 10.3390/app9061106.

[111] H. U. Lim et al. “Uncertainty quantification of wood floor system modal frequencies resulting from variable densities in members”. In: *Structures* 53 (Nov. 2023), pp. 1425–1434. DOI: 10.1016/j.istruc.2023.04.111.

[112] Q. Ge et al. “Investigation on the propagation of uncertainties of a timber floor under human excitation”. In: *Structural Safety* 111 (June 2024), p. 102519. DOI: 10.1016/j.strusafe.2024.102519.

[113] M. Milojević et al. “Effects of material uncertainties on vibration performance of cross laminated timber floors”. In: *Building Materials and Structures* 64.3 (2021), pp. 153–157. DOI: 10.5937/grmk2103153m.

[114] H. Huang, Y. Gao, and W. S. Chang. “Human-induced vibration of cross-laminated timber (CLT) floor under different boundary conditions”. In: *Engineering Structures* 204 (2020), p. 110016. DOI: 10.1016/j.engstruct.2019.110016.

[115] C. Wang et al. “Predicting the human-induced vibration of cross laminated timber floor under multi-person loadings”. In: *Structures* 29 (2021), pp. 65–78. DOI: 10.1016/j.istruc.2020.10.074.

[116] A. Aloisio et al. “Vibration serviceability of hybrid CLT-steel composite floors based on experimental and numerical investigations using random walk models”. In: *Engineering Structures* 304 (Dec. 2024), p. 117600. DOI: 10.1016/j.engstruct.2024.117600.

[117] T. J. Sullivan. *Introduction to Uncertainty Quantification*. Vol. 63. Texts in Applied Mathematics. Cham, Switzerland: Springer, 2015. ISBN: 978-3-319-23394-9. DOI: 10.1007/978-3-319-23395-6.

[118] R. Ghanem, D. Higdon, and H. Owhadi, eds. *Handbook of Uncertainty Quantification*. 1st. Cham, Switzerland: Springer, 2017. ISBN: 978-3-319-12384-4. DOI: 10.1007/978-3-319-12385-1.

[119] A. Pereira and R. Broed. *Methods for Uncertainty and Sensitivity Analysis. Review and recommendations for implementation in Ecolego*. Tech. rep. Stockholm, Sweden: Stockholm University, Jan. 2006.

[120] B. Sudret. “Global sensitivity analysis using polynomial chaos expansions”. In: *Reliability Engineering & System Safety* 93.7 (2008), pp. 964–979. DOI: 10.1016/j.ress.2007.04.002.

[121] B. Sudret, M. Berveiller, and M. Lemaire. “A stochastic finite element procedure for moment and reliability analysis”. In: *European Journal of Computational Mechanics* 15.7–8 (2006), pp. 825–866. DOI: 10.3166/remn.15.825-866.

[122] A. Saltelli et al. *Global Sensitivity Analysis: The Primer*. Chichester, UK: Wiley, 2008. ISBN: 978-0-470-72517-7. DOI: 10.1002/9780470725184.

[123] I. M. Sobol. “Sensitivity Estimates for Nonlinear Mathematical Models”. In: *MMCE* 1.4 (1993), pp. 407–414.

[124] L. S. Shapley. “A Value for n-Person Games”. In: *Contributions to the Theory of Games, Volume II*. Ed. by H. W. Kuhn and A. W. Tucker. Princeton, New Jersey, USA: Princeton University Press, 1953, pp. 307–318. ISBN: 9781400881970. DOI: 10.1515/9781400881970-018.

[125] A. B. Owen. “Sobol indices and shapley value”. In: *SIAM-ASA Journal on Uncertainty Quantification* 2.1 (2014), pp. 245–251. DOI: 10.1137/130936233.

[126] E. Song, B. L. Nelson, and J. Staum. "Shapley effects for global sensitivity analysis: Theory and computation". In: *SIAM-ASA Journal on Uncertainty Quantification* 4.1 (2016), pp. 1060–1083. DOI: 10.1137/15M1048070.

[127] B. Iooss and C. Prieur. "Shapley effects for sensitivity analysis with correlated inputs: comparisons with Sobol' indices, numerical estimation and applications". In: *International Journal for Uncertainty Quantification* 9.5 (2019), pp. 493–514. DOI: 10.1615/Int.J.UncertaintyQuantification.2019028372.

[128] M. I. Idrissi, V. Chabridon, and B. Iooss. "Developments and applications of Shapley effects to reliability-oriented sensitivity analysis with correlated inputs". In: *Environmental Modelling & Software* 143 (2021), p. 105115. DOI: 10.1016/j.envsoft.2021.105115.

[129] A. B. Owen and C. Prieur. "On shapley value for measuring importance of dependent inputs". In: *SIAM-ASA Journal on Uncertainty Quantification* 5.1 (2017), pp. 986–1002. DOI: 10.1137/16M1097717.

[130] J. Castro, D. Gómez, and J. Tejada. "Polynomial calculation of the Shapley value based on sampling". In: *Computers & Operations Research* 36.5 (2009), pp. 1726–1730. DOI: 10.1016/j.cor.2008.04.004.

[131] R. Teixeira, M. Nogal, and A. O'Connor. "Adaptive approaches in metamodel-based reliability analysis: A review". In: *Structural Safety* 89 (2021), p. 102019. DOI: 10.1016/j.strusafe.2020.102019.

[132] R. H. Myers, D. C. Montgomery, and C. M. Anderson-Cook. *Response Surface Methodology: Process and Product Optimization Using Designed Experiments*. 3rd. Hoboken, New Jersey, USA: John Wiley & Sons, 2009. ISBN: 978-0-470-17446-3.

[133] L. Zhang, Z. Lu, and P. Wang. "Efficient structural reliability analysis method based on advanced Kriging model". In: *Applied Mathematical Modelling* 39.2 (2015), pp. 781–793. DOI: 10.1016/j.apm.2014.07.008.

[134] J. H. Friedman. "Multivariate Adaptive Regression Splines". In: *The Annals of Statistics* 19.1 (Mar. 1991), pp. 1–67. DOI: 10.1214/aos/1176347963.

[135] R. L. Hardy. "Theory and applications of the multiquadric-biharmonic method 20 years of discovery 1968-1988". In: *Computers & Mathematics with Applications* 19.8–9 (1990), pp. 163–208. DOI: 10.1016/0898-1221(90)90272-L.

[136] K. Hornik, M. Stinchcombe, and H. White. "Multilayer feedforward networks are universal approximators". In: *Neural Networks* 2.5 (1989), pp. 359–366. DOI: 10.1016/0893-6080(89)90020-8.

[137] A. J. Smola and B. Schölkopf. "A tutorial on support vector regression". In: *Statistics and Computing* 14.3 (2004), pp. 199–222. DOI: 10.1023/B:STCO.0000035301.49549.88.

[138] N. Wiener. "The Homogeneous Chaos". In: *American Journal of Mathematics* 60.4 (1938), pp. 897–936.

[139] D. Xiu and G. E. Karniadakis. "The Wiener-Askey polynomial chaos for stochastic differential equations". In: *SIAM Journal on Scientific Computing* 24.2 (2002), pp. 619–644. DOI: 10.1137/S1064827501387826.

[140] J. Feinberg and H. P. Langtangen. "Chaospy: An open source tool for designing methods of uncertainty quantification". In: *Journal of Computational Science* 11 (2015), pp. 46–57. DOI: 10.1016/j.jocs.2015.08.008.

[141] G. van Rossum and the Python Development Team. *Python Tutorial, Release 3.12.3*. Python Software Foundation. 2024.

[142] M. Milojević et al. "Characterization of inter-panel connections in CLT floors using finite element model updating". In: *Journal of Building Engineering* 97 (Sept. 2024), p. 110682. DOI: 10.1016/j.jobe.2024.110682.

[143] Hottinger Brüel & Kjær. *Hottinger Brüel & Kjær*.

[144] *ARTeMIS Modal Pro*. Structural Vibration Solutions A/S. Aalborg, Denmark, 2022.

[145] *Abaqus/Standard User's Manual*. Dassault Systèmes Simulia Corp. Providence, Rhode Island, 2009.

[146] T. A. Bui et al. "Vibration-based numerical identification of effective orthotropic elastic properties for finite element model of cross-laminated timber panel". In: *Engineering Structures* 291 (Apr. 2023), p. 116480. DOI: 10.1016/j.engstruct.2023.116480.

[147] A. Bohman et al. "Vibration reduction in cross-laminated timber panels using various lamination materials and integrated elastomer layers". In: *Journal of Building Engineering* 118 (2026), p. 115037. DOI: 10.1016/j.jobe.2025.115037.

[148] M. Wallner-Novak, J. Koppelhuber, and K. Pock. *Cross-Laminated Timber Structural Design: Basic design and engineering principles according to Eurocode*. Tech. rep. pro-Holz Austria, 2014.

[149] M. Pastor, M. Binda, and T. Hararik. "Modal assurance criterion". In: *Procedia Engineering* 48 (2012), pp. 543–548. DOI: 10.1016/j.proeng.2012.09.551.

[150] S. D. Garvey, J. E. Penny, and M. I. Friswell. "The relationship between the real and imaginary parts of complex modes". In: *Journal of Sound and Vibration* 212.1 (1998), pp. 75–83. DOI: 10.1006/jsvi.1997.1377.

[151] S. Ereiz, I. Duvnjak, and J. F. Jiménez-Alonso. "Review of finite element model updating methods for structural applications". In: *Structures* 41 (2022), pp. 684–723. DOI: 10.1016/j.istruc.2022.05.041.

[152] M. I. Friswell and J. E. Mottershead. *Finite Element Model Updating in Structural Dynamics*. Vol. 38. Dordrecht: Springer Science & Business Media, 2013. ISBN: 978-90-481-4535-5. DOI: 10.1007/978-94-015-8508-8.

[153] J. F. Jimenez-Alonso et al. "Maximum Likelihood Finite-Element Model Updating of Civil Engineering Structures Using Nature-Inspired Computational Algorithms". In: *Structural Engineering International* (2020), pp. 1–13. DOI: 10.1080/10168664.2020.1768812.

[154] C. Audet and W. Hare. "Biobjective Optimization". In: *Derivative-Free and Blackbox Optimization*. Cham, Switzerland: Springer, 2017, pp. 247–262. ISBN: 978-3-319-68913-5. DOI: 10.1007/978-3-319-68913-5_14.

[155] F. Ponsi, E. Bassoli, and L. Vincenzi. "A multi-objective optimization approach for FE model updating based on a selection criterion of the preferred Pareto-optimal solution". In: *Structures* 33 (May 2021), pp. 916–934. DOI: 10.1016/j.istruc.2021.04.084.

[156] M. Dubey et al. "A Systematic Review on Harmony Search Algorithm: Theory, Literature, and Applications". In: *Mathematical Problems in Engineering* 2021 (2021), p. 5594267. DOI: 10.1155/2021/5594267.

[157] M. D. McKay, R. J. Beckman, and W. J. Conover. "A Comparison of Three Methods for Selecting Values of Input Variables in the Analysis of Output from a Computer Code". In: *Technometrics* 21.2 (1979), pp. 239–245. DOI: 10.2307/1268522.

[158] C. Gallegos-Calderon et al. "Identification of a human-structure interaction model on an ultra-lightweight FRP footbridge". In: *Applied Sciences* 11.14 (2021), pp. 1–22. DOI: 10.3390/app11146654.

[159] P. Niemz, A. Teischinger, and D. Sandberg, eds. *Springer Handbook of Wood Science and Technology*. 1st. Cham, Switzerland: Springer, 2023. ISBN: 978-3-030-81314-7. DOI: 10.1007/978-3-030-81315-4.

[160] T. Nguyen et al. "Mitigating footfall-induced vibration in long-span floors". In: *Australian Journal of Structural Engineering* 15.1 (2014), pp. 97–109. DOI: 10.7158/S12-061.2014.15.1.

[161] M. Milojevi, V. Racic, and M. Nefovska-Danilovi. "Uncertainty analysis of CLT floor vibrations due to inherent variability in structural properties". In: *Journal of Building Engineering* 113 (2025), p. 113725. DOI: 10.1016/j.jobe.2025.113725.

[162] U.S. Department of Agriculture, Forest Service, Forest Products Laboratory. *Wood handbook: wood as an engineering material*. Tech. rep. FPL-GTR-190. Madison, Wisconsin, USA: U.S. Department of Agriculture, Forest Service, Forest Products Laboratory, 2010, p. 509. DOI: 10.2737/FPL-GTR-190.

[163] B. Kasal and R. W. Anthony. "Semi-destructive techniques for in-situ evaluation of historic wood structures". In: *NSF/RILEM Workshop: In-Situ Evaluation of Historic Wood and Masonry Structures*. Prague, Czech Republic, 2006.

[164] Joint Committee on Structural Safety (JCSS). *JCSS Probabilistic Model Code, Part 3: Material Properties*. Tech. rep. Joint Committee on Structural Safety (JCSS), 2000.

[165] H. Lim, S. Tripathi, and M. Li. "Rolling shear modulus and strength of cross-laminated timber treated with micronized copper azole type C (MCA-C)". In: *Construction and Building Materials* 259 (2020), p. 120419. DOI: 10.1016/j.conbuildmat.2020.120419.

[166] Z. Wang et al. "Influence of technical characteristics on the rolling shear properties of cross laminated timber by modified planar shear tests". In: *Maderas: Ciencia y Tecnologia* 20.3 (2018), pp. 469–478. DOI: 10.4067/S0718-221X2018005031601.

[167] T. Yin et al. "Effect of lamination grade on bending and shear properties of CLT made from fast-growing Chinese fir". In: *Industrial Crops and Products* 207 (2024), p. 117741. DOI: 10.1016/j.indcrop.2023.117741.

[168] European Committee for Standardization. *Timber structures – Structural timber and glued laminated timber – Determination of some physical and mechanical properties*. Tech. rep. EN 408:2010+A1:2012. Brussels, Belgium: European Committee for Standardization, 2012.

[169] International Organization for Standardization. *Physical and mechanical properties of wood – Test methods for small clear wood specimens – Part 2: Determination of density for physical and mechanical tests*. Tech. rep. ISO 13061-2:2014. Geneva, Switzerland: International Organization for Standardization, 2014.

[170] A. Kareem and W. J. Sun. "Dynamic response of structures with uncertain damping". In: *Engineering Structures* 12.1 (1990), pp. 2–8. DOI: 10.1016/0141-0296(90)90032-N.

[171] B. Bondsman and A. Peplow. "Experimental Modal Analysis and variability assessment in Cross-laminated Timber". In: *Mechanical Systems and Signal Processing* 228 (2025), p. 112466. DOI: 10.1016/j.ymssp.2025.112466.

[172] M. Renardy et al. "To Sobol or not to Sobol? The effects of sampling schemes in systems biology applications". In: *Mathematical Biosciences* 337 (Apr. 2021), p. 108593. DOI: 10.1016/j.mbs.2021.108593.

[173] F. Cannavó. "Sensitivity analysis for volcanic source modeling quality assessment and model selection". In: *Computers & Geosciences* 44 (2012), pp. 52–59. DOI: 10.1016/j.cageo.2012.03.008.

[174] Y. Tang et al. "Advancing the identification and evaluation of distributed rainfall-runoff models using global sensitivity analysis". In: *Water Resources Research* 43.6 (2007), pp. 1–14. DOI: 10.1029/2006WR005813.

[175] D. Coppitters, W. D. Paepe, and F. Contino. "Surrogate-assisted robust design optimization and global sensitivity analysis of a directly coupled photovoltaic-electrolyzer system under techno-economic uncertainty". In: *Applied Energy* 248 (Apr. 2019), pp. 310–320. DOI: 10.1016/j.apenergy.2019.04.101.

[176] N. H. Hsieh et al. "Applying a global sensitivity analysis workflow to improve the computational efficiencies in physiologically-based pharmacokinetic modeling". In: *Frontiers in Pharmacology* 9 (June 2018), pp. 1–17. DOI: 10.3389/fphar.2018.00588.

[177] X. Y. Zhang et al. "Sobol sensitivity analysis: A tool to guide the development and evaluation of systems pharmacology models". In: *CPT: Pharmacometrics and Systems Pharmacology* 4.2 (2015), pp. 69–79. DOI: 10.1002/psp4.6.

[178] K. Chan, A. Saltelli, and S. Tarantola. "Sensitivity analysis of model output: Variance-based methods make the difference". In: *Proceedings of the 1997 Winter Simulation Conference*. Jan. 1997, pp. 261–268. DOI: 10.1109/WSC.1997.640407.

[179] G. E. Box et al. *Time Series Analysis: Forecasting and Control*. Fifth edition. Hoboken, New Jersey.: John Wiley & Sons, Inc., 2016. DOI: 10.1002/9781118619193.fmatter.

[180] F. J. J. Massey. "The Kolmogorov-Smirnov Test for Goodness of Fit". In: *Journal of the American Statistical Association* 46.253 (1951), pp. 68–78. DOI: 10.1080/01621459.1951.10500769.

[181] M. Herin et al. "Proportional Marginal Effects for Global Sensitivity Analysis". In: *SIAM-ASA Journal on Uncertainty Quantification* 12.2 (2024), pp. 667–692. DOI: 10.1137/22M153032X.

Biography

Marija Milojević was born in Pančevo, Serbia, in 1994. She completed primary school and Grammar School in Pančevo, receiving the Vuk Karadžić Diploma for outstanding academic achievement at both levels.

She received her BSc and MSc degrees in Civil Engineering from the University of Belgrade - Faculty of Civil Engineering in 2017 and 2018, respectively, with average grades of 9.61 and 9.71. During her studies, she received several awards for outstanding academic achievement, including the Award for the Best Student of the 2016/17 Generation in the Civil Engineering study programme.

Marija enrolled in the PhD programme at the University of Belgrade - Faculty of Civil Engineering in 2018 and completed all doctoral coursework with an average grade of 9.89. Since 2020, she has been employed as a Teaching Assistant at the Chair of Engineering Mechanics and Theory of Structures at the same Faculty.

Her research focuses on structural dynamics, vibration serviceability of cross-laminated timber floors, pedestrian-induced vibrations and uncertainty modelling. From 2022 to 2025, she participated in the Substrate4CLT project, funded by the Science Fund of the Republic of Serbia. In 2024, as a British Scholarship Trust scholar, she spent ten weeks at the University of Warwick, UK, conducting research under the supervision of Prof. Stana Živanović.

Marija has published five journal papers and sixteen papers in international conference proceedings. The list of publications related to this dissertation is provided in the Contributions section.

Contributions

International Journal Papers

1. **M. Milojević**, V. Racic, M. Nefovska-Danilović. "Uncertainty analysis of CLT floor vibrations due to inherent variability in structural properties". In: *Journal of Building Engineering* 113 (2025), p.113725. DOI: 10.1016/j.jobe.2025.113725 [M21a+]
2. **M. Milojević**, V. Racic, M. Nefovska-Danilović, S. Ereiz, I. Duvnjak. "Characterization of inter-panel connections in CLT floors usingfinite element model updating".In: *Journal of Building Engineering* 97 (2024), p.110682. DOI: 10.1016/j.jobe.2024.110682 [M21a+]
3. **M. Milojević**, V. Racic, M. Marjanović, M. Nefovska-Danilović. "Influence of inter-panel connections on vibration response of CLT floors due to pedestrian-induced loading". In: *Engineering Structures* 277 (2023), p.115432. DOI: 10.1016/j.engstruct.2022.115432 [M21a]
4. **M. Milojević**, E. Damnjanović, M. Nefovska-Danilović, M. Marjanović. "Effects of material uncertainties on vibration performance of cross laminated timber floors". In: *Building Materials and Structures* 64 (2021), pp.153–157. DOI: 10.5937/GRMK2103153M [M23]

International Conferences M33

1. **M. Milojević**, V. Racic, M. Nefovska-Danilović. "Impact of natural variability in structural properties on vibrations of CLT floors". In: *Proceedings of XIII International Conference on Structural Dynamics EURODYN 2026* (2026), pp. 2196–2206. DOI: 10.47964/1326.10819.098.
2. V. Racic, M. Nefovska-Danilović, **M. Milojević**, N. Simović, I. Glišović. "Impact of inter-panel connections on vibrations of CLT floors". In: *Proceedings of the World Conference on Timber Engineering WCTE 2025* (2025), pp. 5746–5751. DOI:10.52202/080513-0709.
3. M. Nefovska-Danilović, V. Racic, **M. Milojević**, Z. Mišković, S. Savatović. "Experimental analysis of cross-laminated timber floors". In: *Journal of Physics: Conference Series EURODYN 2023* 2647.13 (2023), p.132004. DOI: 10.1088/1742-6596/2647/13/132004.
4. **M. Milojević**, V. Racic, M. Marjanović, M. Nefovska-Danilović. "Vibration serviceability assessment of complex-shaped CLT floor". In: *Journal of Physics: Conference Series EURODYN 2023* 2647.13 (2023), p.132002. DOI: 10.1088/1742-6596/2647/13/132002.
5. M. Nefovska-Danilović, V. Racic, I. Glišović, M. Popović, M. Todorović, **M. Milojević**, R. Cvetković, N. Simović. "Experimental study of pedestrian-induced vibration of cross-laminated timber floors". In: *Proceedings of the International Symposium hosted by ASES* (2024), pp. 155–163.

6. V. Racic, M. Nefovska-Danilović, **M. Milojević**, M. Marjanović. "Effect of Inter-panel Connections on Modal Properties of Cross-Laminated Timber Floors". In: *Experimental Vibration Analysis for Civil Engineering Structures EVACES 2023. Lecture Notes in Civil Engineering* 432 (2023), pp. 589-598. DOI: 10.1007/978-3-031-39109-5_60.
7. **M. Milojević**, S. Ljaljević, V. Racic, M. Marjanović, M. Nefovska-Danilović. "Software for calculation of pedestrian-induced vibration of floor". In: *Proceedings of the 16th Congress hosted by ASES* (2022), pp. 256–265.
8. **M. Milojević**, E. Damnjanović, M. Nefovska-Danilović, M. Marjanović. "Effects of material uncertainties on vibration performance of cross laminated timber floors". In: *Proceedings of the International Symposium hosted by ASES* (2020).
9. **M. Milojević**, M. Nefovska-Danilović, S. Živanović, M. Marjanović. "Effects of mechanical uncertainties on dynamic properties of cross-laminated timber floors". In: *Proceedings of XI International Conference on Structural Dynamics EURODYN 2020* (2020), pp. 3519–3526.

образац изјаве о ауторству

Изјава о ауторству

Име и презиме аутора Марија Милојевић

Број индекса 905/18

Изјављујем

да је докторска дисертација под насловом

Uncertainty approach to modelling pedestrian-induced vibrations of CLT floors

Моделирање вибрација CLT међуспратних конструкција услед пешачког оптерећење применом анализе непоузданости

- резултат сопственог истраживачког рада;
- да дисертација у целини ни у деловима није била предложена за стицање друге дипломе према студијским програмима других високошколских установа;
- да су резултати коректно наведени и
- да нисам кршио/ла ауторска права и користио/ла интелектуалну својину других лица.

Потпис аутора

У Београду, 06.10.2026.

М.Милојевић

Изјава о истоветности штампане и електронске верзије докторског рада

Име и презиме аутора Марија Милојевић

Број индекса 905/18

Студијски програм грађевинарство

Наслов рада Uncertainty approach to modelling pedestrian-induced vibrations of CLT floors

Ментор проф. др Витомир Рацић, проф. др Марија Нефовска-Даниловић

Изјављујем да је штампана верзија мог докторског рада истоветна електронској верзији коју сам предао/ла ради похрањивања у **Дигиталном репозиторијуму Универзитета у Београду.**

Дозвољавам да се објаве моји лични подаци везани за добијање академског назива доктора наука, као што су име и презиме, година и место рођења и датум одбране рада.

Ови лични подаци могу се објавити на мрежним страницама дигиталне библиотеке, у електронском каталогу и у публикацијама Универзитета у Београду.

Потпис аутора

У Београду, 06.10.2026.

М.Милојевић

образац изјаве о коришћењу

Изјава о коришћењу

Овлашћујем Универзитетску библиотеку „Светозар Марковић“ да у Дигитални репозиторијум Универзитета у Београду унесе моју докторску дисертацију под насловом:

Uncertainty approach to modelling pedestrian-induced vibrations of CLT floors

Моделирање вибрација CLT међуспратних конструкција услед пешачког оптерећење применом анализе непоузданости

која је моје ауторско дело.

Дисертацију са свим прилозима предао/ла сам у електронском формату погодном за трајно архивирање.

Моју докторску дисертацију похрањену у Дигиталном репозиторијуму Универзитета у Београду и доступну у отвореном приступу могу да користе сви који поштују одредбе садржане у одабраном типу лиценце Креативне заједнице (Creative Commons) за коју сам се одлучио/ла.

1. Ауторство (CC BY)
2. Ауторство – некомерцијално (CC BY-NC)
3. Ауторство – некомерцијално – без прерада (CC BY-NC-ND)
4. Ауторство – некомерцијално – делити под истим условима (CC BY-NC-SA)
5. Ауторство – без прерада (CC BY-ND)
6. Ауторство – делити под истим условима (CC BY-SA)

(Молимо да заокружите само једну од шест понуђених лиценци.
Кратак опис лиценци је саставни део ове изјаве).

Потпис аутора

У Београду, 06.10.2026.

M Милојевић

1. **Ауторство**. Дозвољавате умножавање, дистрибуцију и јавно саопштавање дела, и прераде, ако се наведе име аутора на начин одређен од стране аутора или даваоца лиценце, чак и у комерцијалне сврхе. Ово је најслободнија од свих лиценци.

2. **Ауторство – некомерцијално**. Дозвољавате умножавање, дистрибуцију и јавно саопштавање дела, и прераде, ако се наведе име аутора на начин одређен од стране аутора или даваоца лиценце. Ова лиценца не дозвољава комерцијалну употребу дела.

3. **Ауторство – некомерцијално – без прерада**. Дозвољавате умножавање, дистрибуцију и јавно саопштавање дела, без промена, преобликовања или употребе дела у свом делу, ако се наведе име аутора на начин одређен од стране аутора или даваоца лиценце. Ова лиценца не дозвољава комерцијалну употребу дела. У односу на све остале лиценце, овом лиценцом се ограничава највећи обим права коришћења дела.

4. **Ауторство – некомерцијално – делити под истим условима**. Дозвољавате умножавање, дистрибуцију и јавно саопштавање дела, и прераде, ако се наведе име аутора на начин одређен од стране аутора или даваоца лиценце и ако се прерада дистрибуира под истом или сличном лиценцом. Ова лиценца не дозвољава комерцијалну употребу дела и прерада.

5. **Ауторство – без прерада**. Дозвољавате умножавање, дистрибуцију и јавно саопштавање дела, без промена, преобликовања или употребе дела у свом делу, ако се наведе име аутора на начин одређен од стране аутора или даваоца лиценце. Ова лиценца дозвољава комерцијалну употребу дела.

6. **Ауторство – делити под истим условима**. Дозвољавате умножавање, дистрибуцију и јавно саопштавање дела, и прераде, ако се наведе име аутора на начин одређен од стране аутора или даваоца лиценце и ако се прерада дистрибуира под истом или сличном лиценцом. Ова лиценца дозвољава комерцијалну употребу дела и прерада. Слична је софтверским лиценцама, односно лиценцама отвореног кода.